



Delft University of Technology

Cytoskeletal Cocktails

Reconstituting life with a taste of its mechanics

Istúriz Petitjean, I.

DOI

[10.4233/uuid:9e044fd3-5fa6-4cdb-be4e-f527e598a5cb](https://doi.org/10.4233/uuid:9e044fd3-5fa6-4cdb-be4e-f527e598a5cb)

Publication date

2024

Document Version

Final published version

Citation (APA)

Istúriz Petitjean, I. (2024). *Cytoskeletal Cocktails: Reconstituting life with a taste of its mechanics*. [Dissertation (TU Delft), Delft University of Technology]. <https://doi.org/10.4233/uuid:9e044fd3-5fa6-4cdb-be4e-f527e598a5cb>

Important note

To cite this publication, please use the final published version (if applicable).

Please check the document version above.

Copyright

Other than for strictly personal use, it is not permitted to download, forward or distribute the text or part of it, without the consent of the author(s) and/or copyright holder(s), unless the work is under an open content license such as Creative Commons.

Takedown policy

Please contact us and provide details if you believe this document breaches copyrights.

We will remove access to the work immediately and investigate your claim.

CYTOSKELETAL COCKTAILS

RECONSTITUTING LIFE WITH A TASTE OF ITS MECHANICS

CYTOSKELETAL COCKTAILS

RECONSTITUTING LIFE WITH A TASTE OF ITS MECHANICS

Dissertation

for the purpose of obtaining the degree of doctor
at Delft University of Technology
by the authority of the Rector Magnificus, prof. dr. ir. T.H.J.J. van der Hagen,
chair of the Board for Doctorates
to be defended publicly on Thursday 23 January 2025 at 10 o'clock

by

Irene ISTÚRIZ PETITJEAN

Master of Science in Nanoscience,
University of Copenhagen.

born in Barcelona (Catalunya, Spain).

This dissertation has been approved by the promotores.

Composition of the doctoral committee:

Rector Magnificus,	chairperson
Prof. Dr. G. H. Koenderink,	Technische Universiteit Delft, promotor
Prof. Dr. M. Dogterom,	Technische Universiteit Delft, copromotor

Independent members:

Prof. Dr. V. Garbin,	Technische Universiteit Delft
Prof. Dr. E. M. Hol,	University Medical Center Utrecht
Prof. Dr. S. Köster.	Georg-August-Universität Göttingen (Germany)
Prof. Dr. F. Lautenschläger,	Universität des Saarlandes (Germany)
Prof. Dr. C. Joo,	Technische Universiteit Delft, reserve member



ISBN 978-94-6496-324-3

An electronic version of this dissertation is available at
<http://repository.tudelft.nl/>.

À Mémé,
à Maman,
à toutes les femmes qui m'inspirent et que j'admire.

Aux Gris.

SUMMARY

Cells are the fundamental unit of life. All living matter is made of cells: from the small systems imperceptible to our eye, like bacteria or archaea; to bigger systems, like plants or magnificent trees, fungi, and animals - including ourselves: the humans. All these systems vary in size yet they are all alive. And the common element of these systems is that they are all composed of cells. Cells are therefore fundamental, but also very complex systems. One may say, broadly, that cells are a cocktail of subsystems that, in combination and in the right balance, can become this basic unit of life. Understanding cells, and their diverse mechanisms, would therefore imply that, eventually, curious scientists (like the author herself) may eventually be able to (better) understand life.

From a physics perspective, cells are fascinating because they constantly endure mechanical stresses and strains that challenge their survival, yet they also actively deform themselves. Our own cells exhibit remarkable deformability in response to external forces such as blood flow or muscle contraction. They also actively alter their own shape. During wound healing, cells in the skin for instance move as coherent cell sheets to heal wounds and renew tissue. And upon cellular division and differentiation, cells experience considerable shape transformations and therefore endure big deformations. Cell deformability is also an important factor in many diseases. During cancer metastasis, tumor cells for instance squeeze themselves through tissues and vessel and lymph node walls. All in all: cells are often pushed to deform, yet they somehow manage to endure those changes. So we may ask ourselves: How do they do this? To address this question, we can take a closer look at the units that form a cell.

As mentioned, cells are a complex cocktail of different elements: in this mixology, and, in the context of mammalian cells, cells have a crucial element that gives them shape: the cytoskeleton. The cytoskeleton, as its name indicates, is the skeleton of the cell. This cytoskeleton is composed of many different cytoskeletal proteins, that we group into three main categories or families: actin filaments, microtubules, and intermediate filaments. It is unclear how exactly the different cytoskeletal families collectively determine the mechanical properties of the cell, but it is clear that they interact. Historically in science, the three main cytoskeletal biopolymers have traditionally been regarded as independent systems with separate cellular tasks. However, growing evidence shows that their functions are coordinated and that this coordination is essential for many core cellular functions.

With this in mind, many scientists are currently studying the cytoskeleton, the collaboration and interaction between the cytoskeletal families (which we refer to as 'cytoskeletal crosstalk'), and the synergy that emerges from these interactions. There are several experimental approaches used for this purpose, but a very interesting approach is to study these cytoskeletal components outside of the cell in controlled environmental conditions: the cytoskeletal components are therefore purified and scientist investigate how they interact with each other. This minimalist approach, called *in vitro* reconsti-

tution, allows a more profound and fundamental understanding of how these different elements work and helps identify the components that are minimally required for cell-like mechanical functions to happen.

In this thesis, we first delve into the cytoskeleton and its role in the shape and function of the cell in **Chapter 1**. We do so with the intention to understand the different cytoskeletal families, their role in cell mechanics, and the role of auxiliary proteins in helping them interact. We discuss actin filaments, microtubules and intermediate filaments, and dive also into auxiliary proteins that link the cytoskeletal families (which we call 'crosslinkers'), like plectin. Finally **Chapter 1** summarizes the central aim and key objectives of the thesis.

In order to contextualize our research focus on cytoskeletal crosstalk, we next help the reader navigate through the existing literature on the role of cytoskeletal crosstalk in cell mechanics and cell migration, a process that involves major cell deformations as explained above. Cell migration is a fundamental process for life that depends on the dynamics and mechanics of actin, microtubules and intermediate filaments and their coordination. In **Chapter 2**, we summarize the literature in the context of cell migration, but we not only focus on bottom-up reconstitution (which we refer to as cell-free) as reported in this thesis, but also on top-down studies (live-cell studies). We summarize prior literature on cytoskeletal crosstalk and compare and confront the main findings from cell-free and live-cell experiments. We end with a perspective on how bridging the two approaches can help address the many open questions of how cytoskeletal crosstalk governs cell mechanics and makes cells move.

After this context on cytoskeletal crosstalk, in **Chapter 3** we employ *in vitro* reconstitution to combine actin and vimentin networks and study their interaction and mechanical crosstalk. We use a novel microrheology image analysis technique, Differential Dynamic Microscopy (DDM), as a proof-of-concept, to understand the spatiotemporal dynamics of these networks. In particular, we focus on a little explored system: the interaction of actin and vimentin and their composites. In our assays, in order to control the contributions of actin or vimentin to the composite's spatiotemporal dynamics, we vary the concentrations of actin and vimentin in such a way that the composite networks always have the same mesh size as single-filament control networks. Therefore we explore the contributions of actin and vimentin to the composite's mechanical crosstalk and observe that co-entangled actin-vimentin networks have additive properties when their mesh size is used as control parameter, and that no mechanical synergy emerges.

In **Chapters 4** and **5** we study the interaction of actin and vimentin mediated by a direct and controllable crosslinker. To this end, in **Chapter 4**, we engineer an actin-vimentin crosslinker that mimics and simplifies the biophysical role of plectin. We employ cloning techniques to select the domains of interest (a green fluorescent protein tag for fluorescent imaging, the actin binding domain of MACF1, a cortexillin coiled coil to mediate dimerization and the intermediate filament binding domain of plectin). We show that this crosslinker (which we refer to as 'ACTIF') is functional and binds to both actin and vimentin filaments. We show that it forms dimers via Interferometric Scattering Microscopy, similar to full-length plectin, and we characterize its biophysical properties: with Total Internal Reflection Microscopy we imaged co-localization of actin, ACTIF and vimentin and afterwards quantified the binding kinetics and affinities of ACTIF for

actin and vimentin. We also show, with Transmission Electron Microscopy, that ACTIF causes the formation of composite bundles of actin and vimentin filaments with a morphology that is dependent on ACTIF's concentration.

Having established a functional and well-characterized actin-vimentin crosslinker ACTIF, we move a big step further in **Chapter 5**: we crosslink actin and vimentin filaments in reconstituted cytoskeletal networks and we study their mechanical properties via bulk rheology. We compare the influence of ACTIF on the linear viscoelastic properties, strain-stiffening response and rupture behavior of actin or vimentin alone and in combination. We discovered that ACTIF introduces mechanical synergy in actin-vimentin composite networks and we quantify its (complex) dependence on ACTIF concentration. This Chapter sets a milestone in bottom-up cytoskeletal studies and an strong basis for further experimental and theoretical studies to better understand the interaction of the two semiflexible biopolymers and their role in the network's synergistic response to mechanical load.

To dissect the load-bearing roles of actin and vimentin in the cytoskeleton, it would be desirable to be able to measure load transmission within each individual network. Towards this goal, in **Chapter 6**, we develop force-sensing crosslinker proteins capable of reporting on local tension by changes in their fluorescence properties. Due to time constraints, we were able to develop only sensors for actin networks, but the modular design of the sensors should in future also allow for the creation of sensors for vimentin networks. All crosslinkers consist of two actin binding domains, so we can mediate actin-actin interactions, separated by a FRET (Förster resonance energy transfer) cassette and a force-sensing peptide. We chose tension-sensing peptides with force sensitivities relevant to the force range of actin-related processes in the cell, which were previously calibrated by our collaborators [1]. Moreover, we also engineered a no-force control and a donor-only control. We show that the engineered force-sensing crosslinkers are functional in the sense that they can crosslink actin networks: we use TIRF to image co-localization of actin filaments with the crosslinker and bulk rheology to assess the mechanical properties of actin networks crosslinked via the sensors. With a look on the future, we propose a potential experimental setup to validate the force sensors in reconstituted actin networks with forces generated internally by myosin motors.

In this thesis we focused on studying cytoskeletal crosstalk via *in vitro* reconstitution with a major emphasis on intermediate filaments. But as in any broad and multidisciplinary scientific project, many questions remain unanswered: How can we better understand the functional consequences of cytoskeletal crosstalk for cell mechanics? Can we do so by combining bottom-up research with simultaneous top-down studies in cells? How can we better understand the tissue-specific roles of the different intermediate filament proteins in different cell types? In **Chapter 7** we bring together a series of pilot projects that set the basis to approach these questions in future, with the ultimate goal to better understand cytoskeletal crosstalk and, in particular, the central role of intermediate filaments therein.

SAMENVATTING

Cellen zijn de fundamentele bouwsteen van alle levende organismen, van kleine eencellige organismen die onzichtbaar zijn met het blote oog, zoals bacteriën en archaea, tot grotere wezens, zoals planten, bomen, gisten en ook dieren – inclusief wij zelf: de mens. Cellen, hoe klein ook, zijn uiterst complexe systemen die op hun beurt een cocktail van subsystemen zijn. Het onderzoeken van cellen en hun werkingsprincipes zal uiteindelijk leergierige wetenschappers (zoals de auteur zelf) in staat stellen om leven (beter) te begrijpen.

Cellen zijn fascinerend vanuit een fysisch oogpunt omdat ze voortdurend mechanische spanningen en vervormingen moeten trotseren die hun voortbestaan bemoeilijken. Bovendien vertonen cellen een opmerkelijk vermogen om te vervormen als reactie op externe krachten, die bijvoorbeeld ontstaan door het stromen van het bloed in onze aderen of het samentrekken van onze spieren. Verder veranderen cellen ook actief hun eigen vorm. Huidcellen, bijvoorbeeld, bewegen als samenhangende lagen tijdens het helen van wonden en het vernieuwen van weefsel. Ook ervaren cellen flinke vormveranderingen tijdens de celdeeling en differentiatie. De vervormbaarheid van cellen is een belangrijk aspect in vele ziektes. Tijdens de uitzetting van tumoren, de zogeheten metastase, wringen kankercellen zich tussen weefsels en door de wanden van bloedvaten en lymfevaten. Op deze manier banen ze zich een weg door het lichaam. Kortom: cellen ondergaan vaak gedwongen vormveranderingen, maar weten toch deze veranderingen te verduren. We vragen ons dan ook af hoe cellen dit doen en om deze vraag te kunnen beantwoorden zullen we de onderdelen die een cel vormen in meer detail bestuderen.

Zoals eerder vermeld zijn cellen een complexe cocktail van verschillende elementen, waaronder, in de context van zoogdiercellen, het cytoskelet. Dit is een cruciaal element dat hen vorm geeft. Zoals de naam aangeeft is dit cytoskelet het geraamte van de cel. Het cytoskelet is opgebouwd uit veel verschillende eiwitten die we in drie voorname groepen of families categoriseren: actine filamenten, microtubuli, en intermediaire filamenten. Het is niet duidelijk hoe deze verschillende groepen samen de mechanische eigenschappen van de cel bepalen, maar we weten wel dat ze met elkaar interageren. Deze biopolymeren werden traditioneel gezien als onafhankelijke systemen met aparte taken in de cel. Er is echter steeds meer bewijs dat aantoon dat hun functies gecoördineerd zijn en dat deze coördinatie essentieel is voor verscheidene kerntaken in de cel.

Met dit in gedachten bestuderen op dit moment veel wetenschappers het cytoskelet, de samenwerking en de interacties tussen en de verschillende componenten van het cytoskelet en de synergie die hieruit ontstaat. Er zijn verschillende experimentele aanpakken mogelijk, maar een veelbelovende aanpak is het bestuderen van opgezuurde cytoskelet componenten buiten de cel in een gecontroleerde omgeving. Deze aanpak stelt onderzoekers in staat te bestuderen hoe de onderdelen met elkaar interageren. Deze minimalistische aanpak, de zogenaamde *in vitro* reconstructie, maakt een beter en

meer fundamenteel begrip van de werking van deze componenten mogelijk en helpt bij de identificatie van componenten die minimaal nodig zijn om celachtige mechanische functies te verkrijgen.

In dit proefschrift duiken we in **Chapter 1** eerst in de rol die het cytoskelet heeft in het vormgeven en functioneren van de cel. Dit doen we met de bedoeling om de verschillende cytoskelet families, hun rol in de mechanica van de cel en de rol die helpe-reiwitten hebben beter te begrijpen. We bespreken actine filamenten, microtubuli en intermediaire filamenten, en we behandelen ook de helpereiwitten die de verschillende componenten van het cytoskelet met elkaar verbinden (we noemen deze dan ook ‘crosslinkers’), zoals plectine. Uiteindelijk vat **Chapter 1** het centrale doel en de voornaamste doelstellingen van dit proefschrift samen.

We loodsen de lezer door de bestaande literatuur over de functie die cytoskelet kruis-communicatie speelt in cel mechanica en cel migratie. Dit laatste is een fundamenteel proces waarin cellen uitgesproken vorm-vervormingen ondergaan en dat afhangt van de dynamisch coördinatie en de mechanica van actine, microtubuli en intermediaire filamenten. In **Chapter 2** geven we een overzicht van de beschikbare literatuur in de context van cel migratie. We focussen niet enkel op “bottom-up” reconstitutie (een aanpak waarbij geen levende cellen aan te pas komen en die verder in dit proefschrift besproken wordt), maar ook op “top-down” studies (studies in levende cellen). We geven een overzicht van het reeds gepubliceerde werk over cytoskelet kruiscommunicatie en we vergelijken de voornaamste resultaten van ‘bottom-up’ en ‘top-down’ experimenten. We eindigen dit hoofdstuk door perspectief te bieden over we de beide benaderingen kunnen verbinden en hoe dit kan helpen om vragen te beantwoorden omrent de functie van cytoskelet kruiscommunicatie in cel mechanica en cel migratie.

Na deze duiding over cytoskelet kruiscommunicatie passen we in **Chapter 3** in vitro reconstitutie toe om actine en vimentine netwerken te combineren en hun mechanische interacties te bestuderen. We passen een nieuwe techniek, ‘Differential Dynamic Microscopy’ (DDM), toe als ‘proof-of-concept’ om de dynamica van deze netwerken zowel in de ruimtelijke en tijdsdimensie beter te begrijpen. We focussen specifiek op een nog maar weinig bestudeerd systeem, namelijk de interactie tussen actine en vimentine en hun composieten. In onze proeven variëren we de concentratie van actine en vimentine zodanig dat de grootte van de mazen in de composiet netwerken hetzelfde is als voor de controle netwerken die opgebouwd zijn uit slechts één type filament. Zodoende kunnen we de bijdragen van actine en vimentine aan de mechanische kruiscommunicatie van het composiet netwerk bepalen. We observeren dat verstrengelde actine-vimentine netwerken simpele additieve eigenschappen hebben als hun maasgrootte als controle parameter gebruikt wordt en dat geen mechanische synergie ontstaat.

In **Chapter 4** en **5** bestuderen we de interactie van actine en vimentine die gemedi-eerd wordt door een directe en controleerbare ‘crosslinker’. We ontwikkelen in **Chapter 4** een actine-vimentine ‘crosslinker’ die de biofysische rol van plectine uit cellen op een vereenvoudigde manier nabootst. Door middel van een klonering strategie selec-teren we de relevante domeinen (een groen fluorescent eiwit label voor de visualisatie, het actine-bindend domein van MACF1, een cortexilline ‘coiled coil’ om de dimerisatie te bevorderen en het intermediair filament bindend domain van plectine). We tonen aan dat deze ‘crosslinker’ (die we ‘ACTIF’ noemen) functioneel is en zowel aan actine als

vimentine filamenten bindt. We tonen ook aan via ‘Interferometric Scattering Microscopy’ dat ACTIF dimeren vormt, net zoals plectine, en we karakteriseren de biofysische eigenschappen ervan: we visualiseerden co-gelokaliseerd actine, ACTIF en vimentine met ‘Total Internal Reflection Microscopy’ en we kwantificeerden nadien de bindingskinetiek en affiniteit van ACTIF voor actine en vimentine. Verder tonen we ook met behulp van transmissie elektron microscopie aan dat ACTIF de vorming van actine-vimentine compositet bundels veroorzaakt, waarbij de morfologie van de bundels afhankelijk is van de ACTIF concentratie.

Na ACTIF, een functionele en goed gekarakteriseerde actine-vimentine ‘crosslinker’, te hebben ontwikkeld, nemen we een grote stap voorwaarts in **Chapter 5**: we linken actine en vimentine filamenten in gereconstrueerde cytoskelet netwerken en bestuderen de mechanische eigenschappen met behulp van bulk reologie. We vergelijken de invloed van ACTIF op de lineaire viscoelastische eigenschappen, de verstijving onder spanning en het scheuren van actine of vimentine, alleen of samen in een netwerk. We hebben ontdekt dat ACTIF mechanische synergie introduceert in actine-vimentine composit netwerken en we kwantificeren de (complex) ACTIF concentratie afhankelijkheid van deze netwerken. Dit hoofdstuk is een mijlpaal in ‘bottom-up’ cytoskelet studies en legt een sterke basis voor verder experimenteel en theoretisch onderzoek om zo de interacties van deze twee semiflexibele biopolymeren en hun rol in de synergistische respons van het netwerk op mechanische belasting beter te begrijpen.

Om de mechanische rol van actine en vimentine in het cytoskelet verder te doorgronden, zou men de transmissie van de belasting doorheen elk individueel netwerk moeten kunnen achterhalen. Daarom ontwikkelen we in **Chapter 6** kracht-detecterende ‘crosslinker’ eiwitten die het vermogen hebben om lokale spanningen aan te geven door middel van veranderingen in hun fluorescente eigenschappen. Als gevolg van tijdsgebrek hebben we enkel sensoren voor actine netwerken kunnen ontwikkelen, maar het modulaire ontwerp van de sensors maakt het in de toekomst ook mogelijk sensoren voor vimentine te ontwikkelen. Alle ‘crosslinkers’ bestaan uit twee actine bindende domeinen, zodat actine-actine crosslinking mogelijk is, gescheiden door een FRET (‘Förster resonance energy transfer’) cassette en een kracht-detecterend peptide. We kiezen voor spanning detecterende peptiden met een gevoeligheid die overeenkomt met de krachten die ontwikkeld worden door actine-gerelateerde processen in de cel. Deze peptiden zijn eerder gekalibreerd door onze partners [1]. Ook ontwikkelden we een ‘no-force’ controle en een ‘donor-only’ controle. We gebruiken TIRF om de co-lokalisatie van actine filamenten met de ‘crosslinker’ te visualiseren en we gebruiken bulk reologie om de mechanische eigenschappen van actine netwerken die met behulp van de sensor gelinkt zijn te analyseren. We tonen aan hiermee dat de sensors functioneel zijn: ze kunnen actine netwerken crosslinken. Met het oog op de toekomst stellen we ook een potentiële experimentele opzet voor om de sensoren te valideren in gereconstrueerde actine netwerken waarin intern krachten gegenereerd worden door myosine motoreiwitten.

In dit proefschrift hebben we de nadruk gelegd op het bestuderen van cytoskelet kruiscommunicatie via in vitro reconstructie, met daarbij een sterke nadruk op intermediaire filamenten. Maar, zoals in elk interdisciplinair wetenschappelijk project blijven veel vragen nog steeds onbeantwoord. Hoe kunnen we de functionele consequenties van cytoskelet kruiscommunicatie beter begrijpen? Kunnen we dit doen door ‘bottom-

up' en 'top-down' studies te combineren? Hoe kunnen we de weefselspecifieke functies van de verschillende intermediaire filamenten in verschillende celtypen beter begrijpen? In **Chapter 7** stellen we een reeks eerste experimenten voor die de basis vormen om deze vragen in de toekomst te kunnen beantwoorden, met als uiteindelijk doel een beter begrip te ontwikkelen van cytoskelet kruiscommunicatie en welke centrale rol intermediaire filamenten hierin spelen.

CONTENTS

Summary	7
Samenvatting	11
1 Introduction	19
1.1 The cell	20
1.2 The cytoskeleton	20
1.2.1 Actin filaments.	21
1.2.2 Intermediate filaments.	22
1.2.3 Microtubules.	23
1.2.4 Septins.	24
1.2.5 Plectin: a giant crosslinker	24
1.3 Focus of this thesis: cytoskeletal crosstalk.	25
1.4 Outline of this thesis	26
2 How cytoskeletal crosstalk makes cells move	29
2.1 Introduction	30
2.2 Cell deformability.	31
2.2.1 Live-cell studies	31
2.2.2 Cell-free reconstitution studies	34
2.3 Cell contractility	37
2.3.1 Live-cell studies	37
2.3.2 Cell-free reconstitution studies	38
2.4 Front-rear polarization	39
2.4.1 Live-cell studies	39
2.4.2 Cell-free reconstitution studies	41
2.5 Collective Migration & Intercellular Adhesions	42
2.6 Plasticity of cell migration.	43
2.6.1 Live-cell studies	43
2.6.2 Cell-free reconstitution studies	45
2.7 The road ahead	46
2.7.1 Increasing the complexity from the bottom-up	46
2.7.2 Reducing the complexity from the top-down	48
2.8 Acknowledgements	48
3 Spatiotemporal dynamics of co-entangled composite networks of F-actin and vimentin	49
3.1 Introduction	50
3.2 Principle of Differential Dynamic Microscopy	51

3.3	Results	53
3.3.1	Linear rheology of F-actin, vimentin and composites thereof	53
3.3.2	Spatiotemporal dynamics of F-actin, vimentin and composites thereof	54
3.4	Discussion	57
3.5	Conclusion	59
3.6	Acknowledgements	59
3.7	Materials and Methods	59
3.7.1	G-actin preparation	59
3.7.2	Vimentin purification	60
3.7.3	Tracer Particle Passivation	60
3.7.4	Sample Preparation for Differential Dynamic Microscopy	61
3.7.5	Image Acquisition for Differential Dynamic Microscopy	61
3.8	Appendix	63
3.8.1	Theoretical estimation of network mesh sizes	63
3.8.2	Appendix Tables and Figures	64
4	Cytolinker-mediated crosstalk between actin and vimentin	67
4.1	Introduction	68
4.2	Results	69
4.3	Discussion	83
4.4	Conclusions	86
4.5	Acknowledgements	86
4.6	Methods	86
4.6.1	Proteins	86
4.6.2	Total Internal Reflection Fluorescence Microscopy (TIRF-M)	92
4.6.3	Interferometric Scattering Microscopy	93
4.6.4	Transmission Electron Microscopy	94
4.6.5	Rheology	94
4.6.6	Data analysis	95
4.7	Appendix	96
4.7.1	Tables and figures	96
5	Crosslinker-mediated mechanical synergy of actin and vimentin	111
5.1	Introduction	112
5.2	Results	113
5.2.1	Impact of ACTIF on vimentin networks	114
5.2.2	Impact of ACTIF on F-actin networks	119
5.2.3	Impact of ACTIF on composite F-actin-vimentin networks	121
5.3	Discussion	124
5.4	Conclusion	126
5.5	Methods	126
5.5.1	Protein purification and reconstitution	126
5.5.2	Rheology	126
5.6	Acknowledgements	127
5.7	Appendix	128

6	Engineering a library of tension-sensing actin crosslinkers for molecular-scale force mapping within reconstituted actin networks	129
6.1	Introduction	130
6.2	Measuring the FRET efficiency of molecular tension sensors	131
6.3	Results	132
6.3.1	Engineering, purification and testing of the host actin-crosslinker vector	132
6.3.2	Design, cloning and optimization of force-sensing actin crosslinkers	135
6.3.3	Characterization of the actin-crosslinking FRET sensors	138
6.3.4	The actin-crosslinking FRET sensors indeed have crosslinking activity	139
6.4	Discussion	141
6.5	Conclusion	142
6.6	Acknowledgements	143
6.7	Methods	145
6.8	Appendix	149
6.8.1	Theoretical considerations for FRET pair design	149
6.8.2	Tables and figures	149
7	Outlook	159
7.1	Introduction	160
7.2	Bridging cell-free and cell-based studies of crosslinker-mediated cytoskeletal crosstalk	161
7.2.1	Expressing the engineered actin-vimentin crosslinker ACTIF in cells	161
7.2.2	Anillin-mediated crosslinking of actin and microtubules	162
7.3	Intermediate filaments: a long road of discoveries ahead	165
7.3.1	Peptides for targeting vimentin and interfering with its assembly	165
7.3.2	<i>In vitro</i> reconstitution of Glial Fibrillary Acidic Protein (GFAP)	168
7.4	Acknowledgements	170
References		173
Publications		217
Curriculum Vitae		219
Acknowledgments		221

1

INTRODUCTION

*The cell is the minimal living building block of life, found as simple unicellular organisms like bacteria but also in the most complex multicellular organisms like ourselves. Cells are constantly exposed to external stresses that deform them and challenge their survival. While bacterial and plant cells mainly rely on their cell wall for mechanical protection, cells in our body are able to sustain large deformations thanks to the cytoskeleton, which is composed of different families of cytoskeletal components. The mixing and dynamic interplay of the cytoskeletal components allow the cell to actively deform itself yet maintain its shape when subjected to external stresses. In this thesis we work with *in vitro* (cell-free) reconstituted cytoskeletal networks, where a controlled and fine-tuned combination of cytoskeletal components and tailored buffer conditions allow us to study the role of cytoskeletal crosstalk in the mechanical properties of the cytoskeleton. Hence the title of this thesis ('**Cytoskeletal Cocktails: Reconstituting Life with a Taste of Its Mechanics**'), which expresses the use of controlled mixing of cytoskeletal networks to ultimately help understand cells (i.e. life). This chapter serves as an introduction to the cytoskeleton and the different cytoskeletal families and to the concept of cytoskeletal crosstalk. At the end we explain the aim and central questions addressed in this thesis and briefly summarize the contents of the following chapters.*¹

¹In this Chapter we incorporated some adapted fragments of the following papers: a review co-written by Irene Istúriz, James Conboy, Anouk Van der Net and Gijsje Koenderink, published in Biophysics Reviews (2024); and a co-authored paper of Irene Istúriz and Duc Quang Tran, published in European Journal of Cell Biology (2024).

1.1. THE CELL

SINCE the very beginnings, humans have been intrigued by the complexity of life. The first microscopic observation of the cell by Robert Hooke in 1665 [2] was a pivotal moment in the history of science. Since then, the cell has become recognized as the basic building block of life. It is clear that in order to understand life, it is essential to understand the working principles of life's most minimal expression: the cell. From a physics point of view, cells are fascinating, since they constantly endure mechanical stresses and strains that challenge their survival yet they also actively deform themselves. Cells in our body for instance demonstrate significant deformability every time they divide. Also immune cells and metastatic cancer cells need to heavily deform themselves in order to squeeze through the small pores present in interstitial tissues [3, 4]. At the scale of a single cell, the extracellular matrix present in the tissue is highly irregular, requiring the cells to constantly adapt their shape for migration.

Now, we may ask ourselves the question: how can we better understand cells and their function? In the past decades, many scientist have focused on understanding the properties of cellular components via bottom-up reconstitution of cell-free systems. Bottom-up reconstitution (often referred to as *in vitro* reconstitution, although we note that the term *in vitro* also carries the connotation of laboratory cell culture) involves creating minimal systems by assembling purified components. This method allows researchers to determine which components and interactions are necessary and sufficient for particular cellular functions.

A crucial element of the cell is the cytoskeleton, which consists of a family of biopolymers that control the cell's shape and mechanical stability. In the area of cell mechanics, researchers have reconstituted the cytoskeletal proteins that form the fibrous network that controls cell shape and mechanics. The right temperature, pH and buffer conditions (like ionic strength) will induce the self-assembly of cytoskeletal proteins into polymers (a process that we refer to as polymerization). Therefore, reconstituting the cytoskeleton can be compared to fine-tuning the right balance of ingredients for a perfect recipe or a **perfect cytoskeletal cocktail**. The different elements (protein monomers, buffers, water) are mixed up and the reconstituted cytoskeletal elements emerge. In this thesis we use *in vitro* reconstitution as a tool to assess the individual contributions and synergy of different components of the cytoskeleton to the cell's overall mechanics.

1.2. THE CYTOSKELETON

As we mentioned, living cells possess both high mechanical strength and the remarkable capacity to deform during activities such as cell division and migration. This unique mechanical behavior is due to the cytoskeleton. Together with the enveloping plasma membrane, the cytoskeleton provides the cell with a well-defined shape and with mechanical stability. The cytoskeleton is composed of a network of biopolymers that occupy the cell's cytoplasm and connect to the plasma membrane and nucleus. The cytoskeleton allows the cell to deform but also makes it resilient to breakage. There are three main

cytoskeletal families: F-actin, intermediate filaments and microtubules (schematically represented in Figure 1.1A). Although not covered by the research described within this thesis, it is important to mention that in the recent years septins have also gained interest, and are starting to be mentioned as the fourth family of the cytoskeleton [5]. A brief introduction to all four cytoskeletal filament types follows below.

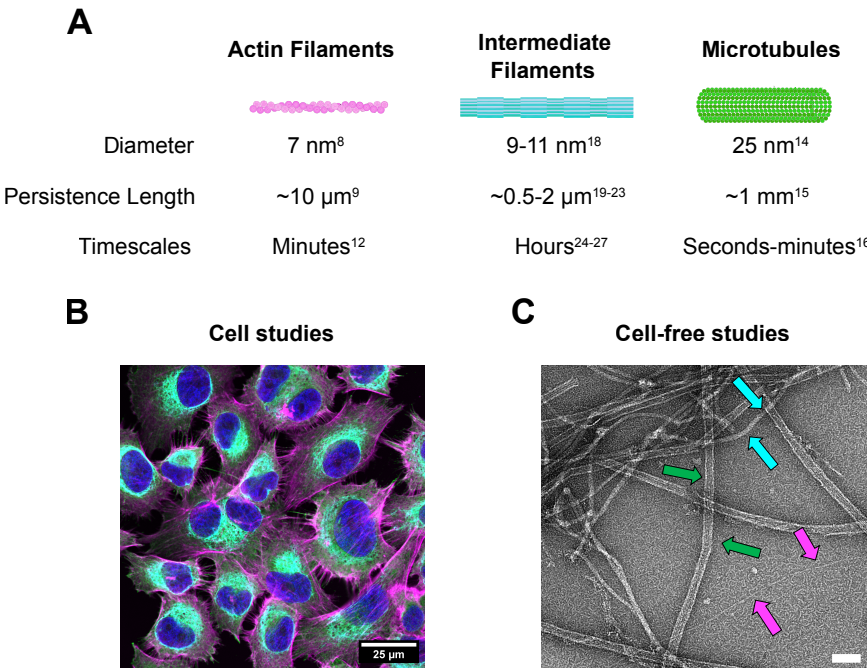


Figure 1.1: (A) Schematic of the three major cytoskeletal filament types and their distinctive physical properties. The fourth filament type (the septins) are not shown here. (B) Fluorescent confocal microscopy image of human melanoma (MV3) cells stained for α -tubulin (green), F-actin (magenta), and vimentin (cyan). The cell nuclei are shown in blue. (C) An electron microscopy image of an *in vitro* reconstituted three-component cytoskeletal network showing F-actin (magenta arrows), microtubules (green arrows) and vimentin (cyan arrows). Filaments were pre-polymerized separately at 1 μM . Actin and microtubules were polymerized in MRB0 buffer (80 mM PIPES pH 6.8, 1 mM EGTA and 4 mM MgCl₂) with 50 mM KCl, 1 mM DTT and 0.5 mM ATP), while vimentin was polymerized in V-buffer (40 mM PIPES pH 7, 1 mM EGTA and 4 mM MgCl₂, 100 mM KCl, 1 mM DTT). The filaments were combined in MRB80 buffer (with 50 mM KCl, 1 mM DTT and 0.5 mM ATP). Scale bar in C is 100 nm.

1.2.1. ACTIN FILAMENTS

An actin monomer is a globular protein with a molecular weight of ~42 kDa and diameter of approximately 5 nm. Actin filaments (F-actin) are double helices with a diameter of ~ 7 nm, made of two strands of globular monomers [6]. The filaments are semiflexible since their thermal persistence length $l_p = \kappa/k_B T$ (where κ is the bending rigidity and $k_B T$ thermal energy) is ~ 10 μm , of the same order as the filament contour length [7].

Actin filaments have an intrinsic structural polarity with a “barbed end” and a “pointed end”. Polymerization-linked ATP hydrolysis causes treadmilling, where the filaments grow at the barbed end and disassemble from the pointed end [8]. The polymerization of actin follows a nucleation-and-growth pathway: four monomers form a stable seed complex before filament growth begins. Filaments reconstituted from purified actin turn over slowly (one subunit every 3–4 s), but actin turnover in the cell is catalyzed by actin-binding proteins. Typical actin network turnover times are of order seconds in the leading edge of motile cells [9] to minutes in the actin cortex [10].

In the cell, different higher-order structures of actin are present. In adherent cells [11] and within membrane protrusions such as filopodia [12, 13] and stereocilia [14], actin filaments form rigid bundles. Additionally, actin forms a densely crosslinked network known as the actin cortex underneath the plasma membrane, capable of exerting contractile forces through myosin motor proteins [15]. Various F-actin-binding proteins, including filamin [16], alpha-actinin [17], fascin [18], and fimbrin [19], are responsible for forming these bundles and crosslinked networks. These proteins generally crosslink two actin filaments reversibly, with a typical crosslinking lifetime of a few seconds.

Actin networks are dynamically restructured by molecular motor proteins, such as myosin-2 [20]. Myosin-2 motors assemble into bipolar filaments that are small (tens of motors per filament) in non-muscle cells and much larger (hundreds of motors per filament) in muscle cells. These filaments feature motor domains at both ends, enabling myosin to move directionally along actin filaments and to slide these filaments past each other, thereby reorganizing actin networks. Together with myosin motor proteins, actin filaments form networks and bundles that generate contractile forces [15]. In muscle cells, myosin-2 facilitates macroscopic contraction [21], while in nonmuscle cells [22], it enables the contraction of the cell surface during cell division and the generation of tension in stress fibers to endure external forces.

1.2.2. INTERMEDIATE FILAMENTS

Intermediate filaments are homo-/heteropolymers made of rod-shaped proteins that are encoded by more than 70 genes in humans [23]. Intermediate filaments have been classified into six groups based on the similarities in their amino acid sequences. Types I and II include two groups of keratins [24, 25], which are expressed in epithelial cells [26]. Certain type I and II keratins, known as hard keratins, are utilized in the formation of structures like hair, nails, and horns [27]. In contrast, the other type I and II keratins, referred to as soft keratins, are prevalent in the cytoplasm of epithelial cells. The type III intermediate filament proteins include vimentin (present in fibroblasts and smooth muscle cells, among others). Other type III proteins are desmin [28], found in muscle cells, and glial fibrillary acidic protein (GFAP) [29], expressed in astrocytes. In this thesis we mostly focus on vimentin and briefly consider GFAP. The type IV intermediate filament proteins include neurofilament (NF) proteins [30, 31] (known as NF-L, NF-M, and NF-H for light, medium, and heavy, respectively). These proteins form the major intermediate filaments of many types of mature neurons. This group also includes α -internexin [32] (expressed at an earlier stage of neuron development than neurofilaments) and nestin [33] (expressed even earlier during neural development). The type V intermediate filament proteins are the nuclear lamins [34], which are found in all cells

in our body with a nucleus. They assemble into an orthogonal meshwork underlying the nuclear membrane that forms the scaffold of the nuclear envelope[35]. All intermediate filament **monomer proteins** have a central α -helical rod domain of approximately 310 amino acids (350 amino acids in lamins) [20]. This central rod domain is flanked by amino- and carboxy-terminal domains, which vary in sequence and length between the different intermediate filament proteins.

Intermediate filament proteins are expressed in a cell-type-specific manner. Mesenchymal cells for instance express vimentin, whereas epithelial cells express keratins [36, 37]. As we mentioned, all intermediate filament proteins share a common domain and secondary structure consisting of an alpha-helical rod domain flanked by intrinsically disordered head and tail domains. The initial stage of filament assembly involves the creation of **dimers**, where the central rod domains of two polypeptide chains intertwine into a coiled-coil structure [38, 20]. These dimers then align in a staggered antiparallel manner to form **tetramers**, which can connect end-to-end to generate **protofilaments**. The final **filaments** are composed of several protofilaments: for vimentin filaments, it has been shown that they are organized into five protofibrils [39]. In the case of keratin, K5/K14 filaments form a hollow cylinder with an internal electron dense core. The wall of the cylinder is constructed of a ring of six protofilaments [26]. Due to their assembly from antiparallel tetramers, the ends of intermediate filaments are identical, making them nonpolar (in contrast with the already described actin filaments and with microtubules, which are explained in the next section). Moreover, intermediate filaments are much more stable than actin filaments and microtubules, with slow subunit exchange along their length and annealing and fragmentation on hour time scales in reconstituted systems [40, 41] and in cells [42, 43].

Intermediate filaments are somewhat thicker (~ 10 nm) [44] than actin filaments, but they are nevertheless much more flexible ($l_p \sim 0.5 - 2 \mu\text{m}$, depending on intermediate filament composition and ionic strength [45, 46, 47, 48, 49]) because of their hierarchical rope-like structure. Another unique feature of intermediate filaments is their high extensibility in response to tensile loading: these filaments can tolerate tensile strains of up to 300% without breaking. By contrast, actin filaments and microtubules break at strains of less than 10% because they are built of weakly interacting globular subunits.

1.2.3. MICROTUBULES

Microtubules are cylindrical structures with a diameter of approximately 25 nm, formed by the polymerization of α - and β -tubulin subunits [50]. They extend throughout the cell, providing structural support and participating in various cellular functions. Microtubules are essential for cell division and play significant roles in cell motility, maintenance of cell shape, intracellular signaling, and the formation of specialized structures like cilia and flagella.

The polymerization of microtubules involves nucleation and elongation processes [51]. It begins with the formation of a stable seed structure that serves as a template for the addition of α - and β -tubulin dimers, which then arrange into protofilaments. Typically, 13 protofilaments align side-by-side to create a hollow tubular structure [52]. The microtubule elongates through the continued addition of tubulin subunits. Like actin filaments, microtubules are structurally polar, with the plus end growing faster than the

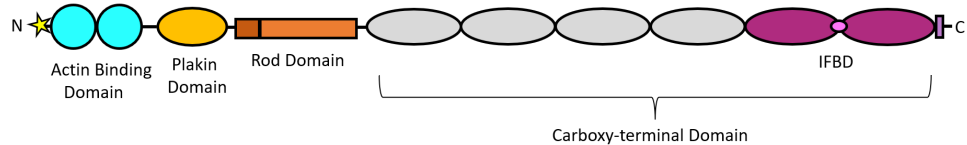


Figure 1.2: Schematic representation of full-length plectin. The isoform-specific N-terminal head domain is indicated by a star, followed by the actin-binding domain (ABD) (blue), an elongated plakin domain (yellow), a central alpha-helical rod domain (200 nm long) that mediates dimerization, six tandemly arranged plakin repeat domains separated by linker regions of variable length (the first four grey, the two related to the IFBD, violet), and finally, a short tail region containing Gly-Ser-Arg (GSR) repeats (pink square at the end).

minus end.

Polymerization is driven by the hydrolysis of guanosine triphosphate (GTP), which is bound to the β -tubulin subunits [53]. Tubulin dimers bound to GTP are more likely to be added to the growing microtubule, while those bound to GDP are more likely to dissociate [54]. As the microtubule grows, GTP bound to the tubulin dimers is hydrolyzed to GDP. When the concentration of GDP-bound tubulin reaches a critical level, a catastrophe event occurs, leading to rapid disassembly or shrinkage of the microtubule. This may be followed by a rescue event, where new GTP-bound tubulin subunits are added, allowing the microtubule to regrow. This stochastic alternation between growth and shrinkage is known as dynamic instability [55].

1.2.4. SEPTINS

Septins were recognized about a decade ago as the fourth component of the cytoskeleton [5]. They are a class of GTP-binding proteins found in all eukaryotic cells except for higher plants [56]. Septins can polymerize into nonpolar filaments of approximately 4 nm in thickness, which subsequently organize into diverse structures such as paired filaments, rings, and gauzes [57]. These proteins play multiple roles within the cell, including scaffolding for protein recruitment, forming barriers for subcellular compartmentalization, regulating cell division, and aiding in cell migration. Additionally, septins are implicated in host-microbe interactions [58] and are associated with various human diseases, including cancer and neurodegenerative disorders. Septins are not further covered in this thesis.

1.2.5. PLECTIN: A GIANT CROSSLINKER

In cells, intermediate filaments are crosslinked to F-actin and microtubules via large crosslinking proteins including members of the plakin family such as plectin [59, 60, 61]. Electron microscopy imaging and proximity ligation assays in cells have shown that besides forming crosslinks of intermediate filaments to F-actin and microtubules, plectin also forms crosslinks between intermediate filaments [62, 63, 64, 65, 66]. Vimentin filaments have been observed to closely associate with actin stress fibers [67], and there is evidence that this association depends on plectin [68, 66]. Plectin has also been implicated in crosslinking of vimentin to F-actin at the base of invadopodia [69, 70] and to the actin cortex of cells during mitosis [71].

The many splice isoforms of plectin share a conserved tripartite structure with a plakin domain, central rod domain, and C-terminal domain (Figure 1.2). Depending on the isoform, plectin can have up to seven functional domains. The N-terminal motif is isoform-specific and targets plectin to specific cellular locations such as the nucleus, hemidesmosomes, or focal adhesions [72]. Actin-binding is mediated by calponin homology domains that form an actin-binding domain (ABD) directly following the N-terminal motif [73, 74]. Intermediate filament binding is mediated by four domains at the C-terminus consisting of two plakin repeat domains (PRDs) separated by a linker region and a short C-terminal extremity containing Gly-Ser-Arg (GSR) repeats [59]. The PRDs and the linker region have a similar basic groove that binds the acidic coiled-coil rod domain of intermediate filaments [75, 76, 77, 78, 60]. Plectin depletion has been shown to alter the mechanical behavior of cells to varying degrees depending on cell type [79, 80, 81, 82, 83]. Moreover, plectin depletion impairs the mechanical stability of epithelial and endothelial cell sheets [84, 85]. Plectin mutations are associated with severe skin blistering disorders and muscular dystrophy. However, plectin's specific role in these mechanical abnormalities as a cytoskeletal crosslinker has been difficult to decipher since it has several other roles besides direct crosslinking: it also anchors intermediate filaments to cell-matrix and cell-cell adhesion receptor complexes [86, 87, 88, 89, 90], to LINC complexes in the nuclear envelope [91] and to mitochondria [72].

1.3. FOCUS OF THIS THESIS: CYTOSKELETAL CROSSTALK

It is unclear how exactly the different cytoskeletal families interact and how they collectively determine the mechanical properties of the cell. The three main cytoskeletal biopolymers have traditionally been regarded as independent systems with separate cellular tasks. However, growing evidence shows that their functions are coordinated and that this coordination is essential for many core cellular functions (see Chapter 2 for a detailed review). Directional cell migration, for instance, relies on F-actin to generate the driving force, but coordination with both microtubules and intermediate filaments is required to polarize the F-actin cytoskeleton and control the amplitude and directionality of force generation [68, 92, 93, 94, 95]. In dividing cells, F-actin/microtubule interactions control the correct placement of the division plane and F-actin/vimentin interactions at the cell cortex are essential for normal mitotic progression [96, 71]. These examples underscore the need to study the mechanisms that couple the activities of the three cytoskeletal systems. Despite the potential of *in vitro* reconstitution to understand cytoskeletal interactions and their role in cytoskeletal mechanics, there have been few reconstitution studies combining different cytoskeletal biopolymer families so far.

In this thesis we explore this direction of research, with a focus on combinations of two, rather than three, interacting subsystems for tractability. But then which two subsystems should we choose for our cytoskeletal cocktail? Upon starting this thesis, and having to decide which cytoskeletal composite system to focus on, I realized that in contrast to F-actin and microtubules, the properties of intermediate filaments received little scientific attention in the past, and their functions still remain enigmatic. Yet there

is strong evidence that they have a major impact on cell mechanics. Keratin filaments for instance have been shown to have a stronger impact on the stiffness of keratinocytes than the actin cortex [97, 98] and vimentin filaments have been shown to protect cells against large stresses and act as a 'safety belt' [99]: the fundamental role of intermediate filaments is undeniable. Therefore I decided to make intermediate filaments the main subject of interest for this thesis.

Upon looking up prior *in vitro* studies of vimentin reconstituted together with other cytoskeletal components, it became evident that the literature on actin-vimentin crosstalk reported some interesting contradictory results: Esue et al. [100] reported synergistic mechanical properties of actin and vimentin composite networks, meaning that composite networks had a higher stiffness than expected from a simple linear superposition of the two constituent networks. By contrast, Golde et al. [101] reported that no mechanical synergy emerged in these composites. Motivated by this controversy and by the clear importance of actin-vimentin interactions for cell mechanics, I therefore decided to add actin filaments as the second main ingredient in my cytoskeletal cocktails.

1.4. OUTLINE OF THIS THESIS

As motivated above, the aim of this thesis was to understand the crosstalk of F-actin and vimentin intermediate filaments. How do actin and vimentin interact? Can we control this interaction to better understand the contributions of each cytoskeletal filament to cytoskeletal mechanics? What are the mechanical properties that emerge from this interaction? To answer these main questions, and many more that arose during my scientific journey, in this thesis, we use *in vitro* reconstitution to study the crosstalk of actin and vimentin. For the benefit of the reader, we build up the complexity in each subsequent thesis chapter, starting with simple cocktails (no crosslinker) and slowly making our cocktail more complex (adding crosslinkers).

In **Chapter 2** we guide the reader through the existing literature on the role of cytoskeletal crosstalk in cell mechanics and migration. Cell migration, which is a fundamental process for life, depends on the dynamics and mechanics of actin, microtubules and intermediate filaments and their coordination. In this chapter we not only focus on bottom-up reconstitution (which we refer to as cell-free), but also on top-down studies (live-cell studies). We summarize prior literature on cytoskeletal crosstalk and compare and confront the main findings from cell-free and live-cell experiments. We end with a perspective on how bridging the two approaches can help address the open questions of how cytoskeletal crosstalk governs cell mechanics and makes cells move.

After this context on cytoskeletal crosstalk, in **Chapter 3**, we employ *in vitro* reconstitution to combine actin and vimentin and study their interaction and mechanical crosstalk. First, we use bulk rheology to measure the linear elastic properties of actin and vimentin, alone and in combination. We vary the concentrations of actin and vimentin in such a way that the composite networks always a comparable mesh size as the single-filament control networks. To check this, we use a novel microrheology image analysis technique known as Differential Dynamic Microscopy (DDM). Our rheology data reveal that co-entangled actin-vimentin networks have simple additive elastic properties when

their mesh size is used as control parameter and no mechanical synergy emerges, resolving the controversy in the literature explained above.

In **Chapters 4 and 5** we study the interaction of actin and vimentin mediated by a direct and controllable crosslinker. To this end, in **Chapter 4**, we engineer an actin-vimentin crosslinker that mimics and simplifies the biophysical role of plectin. We employ cloning techniques to select the domains of interest, namely a fluorescent protein tag for fluorescent imaging, the actin binding domain of MACF1, a cortexillin coiled coil to mediate dimerization and the intermediate filament binding domain of plectin. We show that this crosslinker (which we refer to as 'ACTIF') is functional and binds to both actin and vimentin filaments. We show that it forms dimers via Interferometric Scattering Microscopy, similar to full-length plectin. We next characterize its biophysical properties: with Total Internal Reflection Microscopy we imaged co-localization of actin, ACTIF and vimentin and afterwards quantified the binding kinetics and affinities of ACTIF for actin and vimentin. We also show, with Transmission Electron Microscopy, that ACTIF induces composite bundles of actin and vimentin filaments with a morphology that is dependent on ACTIF's concentration.

Having established a functional and well-characterized actin-vimentin crosslinker ACTIF, we move a big step further in **Chapter 5**: we crosslink actin and vimentin filaments in reconstituted cytoskeletal networks and we study their mechanical properties via bulk rheology. We compare the influence of ACTIF on the mechanical response of actin or vimentin alone and in combination. We show that ACTIF is capable of crosslinking both the single-polymer control networks and composite networks of actin and vimentin. Interestingly, we find that ACTIF introduces mechanical synergy in the composites, not present in absence of ACTIF. Finally, we show that different interactions compete to cause a very complex dependence of the nonlinear elastic response and rupture behavior of the crosslinked composites on the concentration of ACTIF. This Chapter sets a milestone in bottom-up cytoskeletal studies and an extensive basis for further experimental and theoretical studies to better understand the interaction of the two semiflexible biopolymers and their role in the network's synergistic response to mechanical load.

To dissect the load-bearing roles of actin and vimentin in the cytoskeleton, it would be desirable to be able to measure load transmission within each individual network. Towards this goal, in **Chapter 6**, we develop force-sensing crosslinker proteins capable of reporting on local tension by changes in their fluorescence properties. Due to time constraints, we were able to develop only sensors for actin networks, but the modular design of the sensors should in future also allow for the creation of sensors for vimentin networks. All crosslinkers consist of two actin binding domains, so we can mediate actin-actin interactions, separated by a FRET (Förster resonance energy transfer) cassette and force-sensing peptide. We chose peptides with force sensitivities relevant to the force range of actin-related processes in the cell, which were previously calibrated by our collaborators [1]. Moreover, we also engineered a no-force control and a donor-only control. We show that the engineered force-sensing crosslinkers are functional and can crosslink actin networks: we use TIRF to image co-localization of actin filaments with the crosslinker and bulk rheology to assess the mechanical properties of actin networks crosslinked via the sensors. With a look on the future, we propose a potential experimental setup to validate the force sensors in reconstituted actin networks with forces

generated internally by myosin motors.

In this thesis we focused on studying cytoskeletal crosstalk via *in vitro* reconstitution with a major emphasis on intermediate filaments. But as in any broad and multidisciplinary scientific project, many questions remain unanswered: How can we better understand the functional consequences of cytoskeletal crosstalk for cell mechanics? Can we do so by combining bottom-up research with simultaneous top-down studies in cells? How can we better understand the tissue-specific roles of the different intermediate filament proteins in different cell types? In **Chapter 7** we bring together a series of pilot projects that set the basis to approach these questions in future with the ultimate goal to better understand cytoskeletal crosstalk and, in particular, the central role of intermediate filaments therein.

2

HOW CYTOSKELETAL CROSSTALK MAKES CELLS MOVE

Cell migration is a fundamental process for life and is highly dependent on the dynamical and mechanical properties of the cytoskeleton. Intensive physical and biochemical crosstalk between actin, microtubules, and intermediate filaments ensures their coordination to enable cell migration. In this Chapter, the different mechanical aspects that govern cell migration are discussed. For each of these aspects, we provide a novel perspective by juxtaposing two complementary approaches to the biophysical study of cytoskeletal crosstalk: live-cell studies (which we here refer to as top-down studies) and cell-free studies (which we here refer to as bottom-up studies). We end with a perspective on how to better bridge the two perspectives in future to address the many open questions of how cytoskeletal crosstalk makes cells move. This Chapter sets a baseline to understand the scientific context of the cytoskeletal crosstalk studies presented in this thesis and the potential applications of our findings.¹

¹This chapter is co-authored with James Conboy, Anouk van der Net and Gijsje Koenderink and was published in Biophysics Reviews (2024).

2.1. INTRODUCTION

CELL migration is a process that is fundamental for life. It is a major contributor to tissue morphogenesis in developing embryos [102] and drives angiogenesis [103], bone formation [104], tissue repair [105] and immune surveillance [106]. On the flip side, however, cell migration is also responsible for pathological cell migration during chronic inflammation [107] and cancer metastasis [108]. Cell migration depends on the mechanical and dynamical properties of the cytoskeleton, a network of dynamic biopolymers that self-assemble from small protein building blocks. There are three main cytoskeletal biopolymers: actin filaments, microtubules, and intermediate filaments, as introduced in Chapter 1. They have markedly different structural, mechanical and dynamical properties. Note that in addition, septins are identified as the fourth cytoskeletal component [5] (we will return to this at the end of this chapter).

The physical properties of the cytoskeletal filaments are directly connected to their functions in cell migration. Actin, with its ability to generate protrusive and contractile forces, provides the main driving forces for polymerization-driven *mesenchymal migration* and bleb-based *amoeboid migration* [109, 110]. Meanwhile microtubules play a key role in establishing front-rear polarity and promoting persistent migration, aided by their large persistence length that is much longer than the size of the cell [111]. Finally, intermediate filaments, with their mechanical resilience, protect the migrating cell and its nucleus from mechanical damage, which is especially important when cells squeeze through confined environments [112, 113]. There is growing evidence that cell migration requires a dynamic interplay between the three cytoskeletal filament systems that depends on mechanical and signaling crosstalk. In mesenchymal migration, coupling of actin to microtubules and intermediate filaments is for instance essential to polarize the actin cytoskeleton and thereby control force generation [114]. In Table 2.1 we highlight examples of the different cytoskeletal crosstalk modalities.

In this chapter we review recent insights in the role of cytoskeletal crosstalk in cell migration. We focus on mechanical aspects, which are also the focus of the thesis. For more detailed cell biological insights, we refer the reader to several excellent reviews [114, 115, 116, 117]. We take a mainly experimental perspective and refer the reader to other reviews for more theoretically oriented perspectives [118, 119]. Throughout this review, we confront two opposite experimental approaches to studying the biophysics of cytoskeletal crosstalk: *live cell (top-down)* studies versus *cell-free (bottom-up)* studies of simplified model systems reconstituted from component parts. Live-cell studies have the benefit of physiological relevance, but mechanistic dissection can be challenging because of the cell's compositional complexity. Each cytoskeletal system exhibits enormous compositional diversity with different isoforms and posttranslational modifications [120]. Moreover, cytoskeletal coupling is mechanosensitive as a consequence of mechanosensory signalling loops and transcriptional regulation [121]. Cell-free studies (the focus of this thesis) provide a powerful approach to complement live-cell studies because they allow for highly controlled experiments from the level of single protein, to filaments, to networks.

Cytoskeletal crosstalk contributes to every aspect of cell migration (Figure 2.1). The

Modality	Cytoskeletal element #1	Cytoskeletal element #2	Mediator(s)	Function of the crosstalk
Direct interaction	Microtubules	Vimentin	Excluded volume	Promoted strain-stiffening ^{136, 137}
	Actin	Vimentin	Excluded volume	Mechanical synergy ¹³³
Crosslinker	Actin	Vimentin	Plectin	Force transmission to nucleus ¹⁴⁷
	Microtubule	Actin	ACF7/MACF	Guided filament growth ^{141, 193}
Molecular signalling	Actin	Microtubules	GEF-H1/RhoA	Detachment of leader cells ²³²
	Actin	Vimentin	RhoGTPases	Inhibition of stress fiber assembly ¹⁵⁶
Steric interaction	Actin	Microtubules	Electrostatic interactions	Promoting filament alignment ¹⁴¹

Table 2.1: Table highlighting the different cytoskeletal crosstalk modalities that are discussed in this chapter, each with an example from the text.

structure of this chapter follows these aspects: we cover cell deformability, front-back polarity, contractility and finally plasticity, which refers to the ability of cells to adapt their mode of migration to their environment [122]. We note that we only briefly cover adhesion control in collective cell migration, since this falls outside the scope of this thesis, but we refer the reader to a more complete overview in our original review [123]. At the end of the chapter, we provide a perspective on how connections can be made between cell-free and live-cell studies to address the many open questions on the role of cytoskeletal crosstalk in cell migration.

2.2. CELL DEFORMABILITY

2.2.1. LIVE-CELL STUDIES

MECHANICAL CHALLENGES IN CELL MIGRATION

Migrating cells must deform their nucleus and cytoskeleton, especially when they move through interstitial tissues that impose significant confinement. Depending on tissue type, cells encounter extracellular matrix (ECM) and interstices between tissues with sizes ranging between 2 and 30 μm , comparable to their own body and sometimes even nuclear size [124]. Metastasizing cancer cells have to overcome even more severe physical barriers as they intravasate across the endothelium into blood vessels or across epithelial tissues into lymphatic vessels. Cell deformability is therefore an important determinant of cell migration [125]. For many cancer cells, for instance, lower stiffness correlates with higher motility [126].

Migrating cells experience a complex combination of tensile, compressive and shear deformations of varying amplitude and rate. The effect of these mechanical parameters

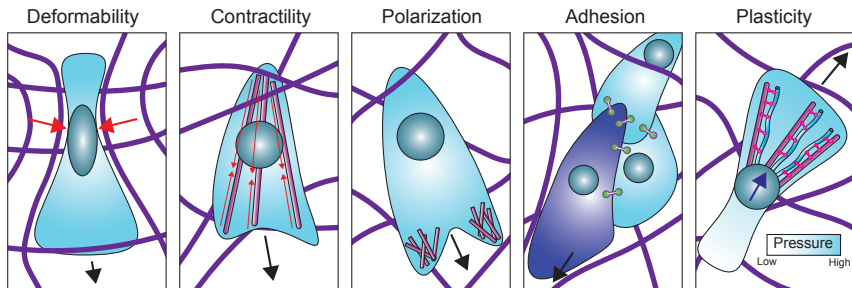


Figure 2.1: Cytoskeletal crosstalk contributes to every aspect of cell migration including: (1) Cell deformability that governs the ability of cells to migrate through confining environments. Red arrows show deformation caused by the cell migrating through the extracellular matrix. (2) Contractility as a major driver of cell motility. Red arrows show actin-myosin contraction. (3) Front-rear polarity for directional migration. (4) Cell-cell adhesions to coordinate collective migration. The leader cell is shown in dark blue. (5) Plasticity, the ability of cells to interconvert between different migration strategies in response to their environment, for example between mesenchymal and nuclear piston modes. Here the nucleus is pulled forwards (dark blue arrow). Black arrows show the direction of migration. Actin (magenta), vimentin (cyan), nucleus (teal), intercellular adhesions (green linkers), plectin (pink linkers) and extracellular matrix fibers (purple).

on cell deformability has been extensively characterized using quantitative biophysical techniques. To study the viscoelastic properties of cells without the impact of cell adhesion, cells can be detached from their substrate and measured in suspension by micropipette aspiration [127], optical stretching [128], parallel-plates rheometers [129], or high-throughput microfluidic methods [130]. These measurements are mostly relevant for amoeboid migration where cells exhibit only weak adhesion to their environment. For mesenchymal migration, it is more relevant to study mechanics on adherent cells. Whole-cell measurements of adherent cells can be done by monolayer rheology or stretching [131, 132, 133] or by single-cell atomic force microscopy [134, 135]. Localized measurements to resolve the mechanics of specific subcellular regions can be done by magnetic twisting cytometry [136], atomic force microscopy [137], optical or magnetic tweezers [138, 139], or particle tracking microrheology [140]. Some of these methods allow for *in situ* measurements in migrating cells [141, 142].

The nucleus is generally considered the stiffest and largest organelle with a stiffness reported to range from 0.1 to 10 kPa, dependent on cell-type [143] (although we note that recent data appear to challenge this notion, suggesting the nucleus may be softer than hitherto believed [144]). The main contributors to the rigidity of the nucleus are heterochromatin and the nuclear lamina (also termed the nucleoskeleton), which contains lamin intermediate filaments [145, 146, 147]. Intact nuclei *in situ* have a higher stiffness than isolated nuclei because the nucleus is coupled to the cytoskeleton through the LINC complex (composed of SUN-domain proteins and KASH-domain proteins, which physically connect the cytoskeleton to the nucleoskeleton) [148]. Since the nucleus is not only the stiffest but also the largest cellular organelle, it poses a major bottleneck for confined migration [149]. When cells are embedded in collagen networks or microfabricated microchannels, their migration velocity linearly decreases with decreasing pore

size until migration is physically blocked when the pore size reaches 10% of the nuclear cross section [150]. Under highly confined conditions, cells can only move if they are able to remove blocking ECM fibers with proteolytic enzymes [150, 151].

REGULATION OF CELL DEFORMABILITY THROUGH CYTOSKELETAL CROSSTALK

The actin cytoskeleton is often considered the main determinant of cell mechanics. Drug-induced depolymerization of actin filaments indeed significantly softens cells both under non-adherent and adherent conditions [152, 153]. An important contribution of the actin cytoskeleton to cell stiffness comes from contractile forces generated by actin-myosin stress fibers [154] and by the actin cortex [155].

Intermediate filaments form dense networks that are mainly perinuclear, so they contribute little to cortical stiffness but strongly affect the cytoplasmic shear modulus [156] and the resistance of cells to compression [135]. For leukocytes and tumor cells performing 3D migration, the intermediate filament cytoskeleton is a major determinant of cell deformability. Intermediate filament protein deletion or network disruption causes significant cell softening while at the same time enhancing cell migration [157, 158, 159, 113].

Microtubules generally do not contribute much to cell stiffness, with drugs that interfere with microtubule polymerization having minor effects on cell mechanics [160]. Recently, though, microtubules were shown to exhibit interesting mechano-responsive properties. Cytoskeletal compression induced by cyclic cell stretching or by confined migration was shown to stabilize deformed microtubules by triggering recruitment of the microtubule-binding protein CLASP2 [161]. When cells are transferred from rigid 2D substrates to softer 3D hydrogels, the mechanical contribution of microtubules becomes more important because actin stress fibers become less prominent. In cells migrating through collagen gels, microtubules for instance play a crucial role in mechanical support of cellular protrusions [162].

It remains an open question how the interactions between the three cytoskeletal biopolymers influence the mechanics of the composite cytoskeleton. Theoretical models predict that composite networks composed of interpenetrating networks of a rigid and a flexible polymer are substantially stiffer than expected from the sum of the moduli of the separate networks [163]. Rigid fiber networks by themselves are expected to be soft at low deformation because they deform in a non-affine manner, where the elasticity is governed by fiber bending [164]. The presence of a background network of flexible polymer suppresses these non-affine bending deformations [163]. Unfortunately this prediction is difficult to directly test in live-cell experiments because it is very challenging to specifically remove one cytoskeletal network without also affecting the others. Microtubule depolymerization is for instance well-known to activate acto-myosin contraction by the release of the microtubule-associated guanine nucleotide exchange factor GEF-H1 [165]. At large strains, though, there is some evidence of mechanical synergy between the cytoskeletal networks. Epithelial cell layers are able to undergo extreme stretching under constant tension ('active superelasticity') by strain-softening of the actin cortex followed by re-stiffening thanks to the keratin intermediate filament network [166]. Physical crosslinking between actin and keratin is essential for the maintenance of epithelial stability [85]. The ability of flexible polymers to suppress bending

deformations of rigid polymers has the interesting consequence that the rigid polymers are reinforced against compressive loads [167]. Under compressive loading, rigid polymers exhibit an Euler buckling instability at a critical compression force $f_c \sim 10\kappa/L^2$, where L is the polymer length. For microtubules, the critical compression force is only of order 1 pN [168]. In the cell, however, microtubules can bear 100-fold larger compression forces because the surrounding actin and intermediate filament cytoskeleton constrains microtubule buckling [169, 170]. This is consistent with the so-called tensegrity model, which states that cellular shape stability is achieved via a balance between actin filaments and intermediate filaments loaded under tension, and microtubules and thick actin bundles under compression [171].

2.2.2. CELL-FREE RECONSTITUTION STUDIES

Live-cell mechanical measurements can be difficult to interpret in quantitative terms because they are sensitive to the amplitude, type and rate of deformation, geometry of the mechanical probe, the probed location in the cell, and the cell's extracellular environment [172]. Cell-free reconstitution studies provide a useful complement because they permit quantitative measurements of the mechanical properties of isolated cytoskeletal components, both at the single filament and at the network level.

MECHANICAL PROPERTIES OF INDIVIDUAL CYTOSKELETAL FILAMENTS

At the single filament level, cytoskeletal biopolymers have been bent, stretched, compressed, and twisted using optical and magnetic tweezers [173, 174, 175, 176], atomic force microscopy [177, 178], and microfluidic devices [179]. Actin filaments and microtubules have a high bending and stretching rigidity, but they break at rather low tensile strains ($\sim 150\%$ strains) [180, 181]. Moreover, actin filaments become more fragile under torsion [180] and microtubules soften upon repeated bending [179]. This fragility is likely related to the fact that actin filaments and microtubules are made of globular subunits. By contrast, intermediate filaments are made of fibrous subunits held together by extensive lateral interactions. Intermediate filaments easily stretch and bend due to their open structure and they can withstand tensile strains of more than 200% before rupture [177]. Similar to a car's safety belt, intermediate filaments are soft under small and slow deformations but stiff under large and fast deformations [173]. Recent evidence suggests that different intermediate filament proteins respond differently to tensile loads. When subjected to stretch-relax cycles, keratin filaments elongate with every cycle but keep the same stiffness, whereas vimentin filaments soften with every cycle but always return to the same initial length [182]. It appears that vimentin stretches by monomer unfolding [183], whereas keratin filaments stretch by viscous sliding of subunits [182]. It will be interesting to see what further diversity may be generated by co-polymerization of different intermediate filament proteins and by post-translational modifications.

MECHANICAL PROPERTIES OF SINGLE-SUBSYSTEM CYTOSKELETAL NETWORKS

At the network level, mechanical properties are most conveniently probed by either bulk rheology or microrheology (see Chapter 3 for examples). In bulk rheology, cytoskeletal networks are sheared between the two parallel plates of a rheometer, providing a read-out of the macroscopic viscoelastic response [184]. Microrheology instead probes the localized viscoelastic response of a material by tracking the motion of embedded probe particles, either in response to thermal fluctuations (passive microrheology [185]) or to a force applied by optical or magnetic tweezers (active microrheology [186]).

The mechanical response of cytoskeletal networks is determined by an interplay of the stiffness of the filaments and their interactions. In absence of crosslinkers, actin filaments and microtubules form entangled networks that easily fluidize under shear due to filament disentanglement [187, 188, 189]. Crosslinker proteins prevent this fluidization and cause the networks to strain-stiffen. This strain-stiffening response is only moderate for microtubules because of their high rigidity and because shearing causes force-induced unbinding of crosslinks [187, 186]. Actin networks exhibit more pronounced strain-stiffening because their elasticity is affected by the entropic elastic response of the filaments to tensile loading [190]. Tensile loading reduces the conformational entropy of actin filaments, pulling out bending fluctuations, causing entropic strain-stiffening [191]. Increased crosslink densities shift the onset of strain-stiffening to smaller shear strains because less excess length is stored in bending fluctuations when the crosslinks are more closely spaced [190]. Some crosslinker proteins (most notably filamin) are so large that their compliance directly contributes to the network response. Crosslinker extensibility increases the rupture strain by postponing the point where the actin filaments experience tensile loading [192, 193]. Bundling of actin filaments, which is common at high concentrations of crosslinker proteins, suppresses entropic elasticity. Bundled actin networks still strain-stiffen [190], but by an enthalpic mechanism that involves a transition from soft bending modes at low strains to rigid stretching modes at high strain [194, 195]. Under compression, actin and microtubule networks soften due to filament buckling [135]. For branched actin networks, compressive softening has been shown to be reversible, likely because the buckled filaments are prevented from collapsing by their connections with the network [196].

The mechanical properties of intermediate filament networks differ in various respects from those of actin and microtubule networks. First, intermediate filaments form strain-stiffening networks even in absence of any crosslinker proteins, as demonstrated for vimentin, neurofilaments, desmin, and keratin [197, 198]. The filaments spontaneously form crosslinks mediated by electrostatic interactions between their disordered C-terminal tails. Upon tail truncation, the networks no longer strain-stiffen [199, 200, 201]. The effective crosslink density depends on the concentration of divalent cations such as Mg^{2+} , Ca^{2+} or Zn^{2+} [199, 198, 202, 203] and is sensitive to the buffer ionic strength and pH [204]. For keratins, there are additional hydrophobic interactions between the central rod domains that stiffen the networks [47]. Second, intermediate filament networks have much larger rupture strains than actin and microtubule networks as a consequence of the larger single-filament extensibility. This is reflected in the dependence of the elastic modulus K on the applied shear stress σ . While actin networks only exhibit an entropic strain-stiffening regime where K increases as $\sigma^{\frac{3}{2}}$, intermediate filament net-

works exhibit an additional enthalpic regime where K increases more weakly, reflecting strain-induced filament alignment [197]. After yielding, intermediate filament networks can even recover their initial shear modulus, likely by the re-establishment of tail-tail crosslinks [33, 200].

MECHANICAL PROPERTIES OF COMPOSITE CYTOSKELETAL NETWORKS

Recently there has been increasing attention for the mechanical properties of cytoskeletal composites. Reconstitution of composite networks requires careful tuning of the buffer conditions since the different cytoskeletal polymers are traditionally reconstituted in their own optimized buffer conditions. Intermediate filaments are especially sensitive to solution pH and ionic concentrations, forming filaments of different widths and protein mass-per-length ratios depending on the buffer [205]. Until now nearly all studies of composite networks have focused on two-component composites of cytoskeletal filaments co-polymerized in the absence of crosslinkers. At small strains, co-entangled composites (specifically combinations of actin/vimentin [101], actin/keratin [206, 207], actin/microtubules [208], and vimentin/microtubules [209] have generally been shown to exhibit a simple additive viscoelastic response. However, there is evidence for direct interactions of vimentin filaments with actin filaments [100] as well as microtubules [210], which could potentially influence the network rheology. These interactions could potentially lead to cell-type specific cytoskeletal crosstalk, since they are mediated by the C-terminal tail of intermediate filaments that shows large length and sequence variations between different intermediate filament proteins. It was furthermore shown that vimentin can impose steric constraints that hamper actin network formation and thus cause network weakening [211].

At large strains, there is evidence of synergistic enhancement of the mechanical properties in certain cytoskeletal composites. For actin/keratin composites, the strong strain-stiffening response of the keratin network was found to dominate the high-strain response of the composites [207]. For actin/microtubule composites, microtubules were shown to promote strain-stiffening of the actin networks, even at low density [212, 213]. This effect was explained by the ability of rigid microtubules to suppress nonaffine bending fluctuations of actin filaments. It will be interesting to explore how these synergies are modified in the presence of crosslinkers. Recent work showed that when actin filaments and microtubules are crosslinked to each other by biotin-streptavidin, the composite is more elastic than when both filaments are independently crosslinked [214].

To the best of our knowledge, there has so far been only one study of three-component networks combining actin, vimentin and microtubules [215]. It was shown by microrheology that the linear elastic modulus of the composite is dominated by actin, with little contribution from either microtubules or vimentin. Yet vimentin was shown to significantly extend the elastic regime to longer timescales. The authors proposed that the vimentin network that fills in the pore spaces of the actin network [67] slows stress relaxation by constraining actin reptation. More work is needed to systematically study cytoskeletal composites and to explore the impact of crosslinking with cytolinker proteins such as plectin. Due to their high molecular weight these proteins are difficult to purify. To circumvent this problem, one can engineer proteins that contain only the cytoskeletal binding domains separated by a spacer [216]. As described later in this the-

sis (see Chapters 4 and 5), we recently found that crosslinking with a plectin-mimetic crosslinker causes synergistic stiffening of actin-vimentin composites (see also [217]).

2.3. CELL CONTRACTILITY

2.3.1. LIVE-CELL STUDIES

ACTO-MYOSIN CONTRACTION IS THE DRIVING FORCE BEHIND CELL MIGRATION

The actin cytoskeleton is the engine behind cell migration [218]. Depending on the extracellular environment, cells can switch between different mechanisms that use actin-based forces in different ways [219]. Fibroblasts and other adherent cells perform *mesenchymal migration*, which relies on integrin-based adhesion to the extracellular matrix (ECM). The process occurs via a four-step cycle. First, actin polymerization pushes against the membrane at the leading edge, producing lamellipodia in cells migrating on flat rigid surfaces or pseudopodia in cells migrating in 3D extracellular matrices. Next, the cell generates integrin-based adhesions with the substrate that connect to the contractile machinery of acto-myosin stress fibres. Through a combination of pulling from the front and squeezing from the rear, the cell body moves forward. Finally, old adhesions are detached from the substrate or dissolved at the trailing edge [220]. The contractile forces involved in cell migration have been measured through the traction forces exerted on the substrate. This is usually done by adhering cells to a hydrogel substrate with known mechanical properties, such as polyacrylamide. By measuring the displacements of fluorescent tracer particles incorporated in the gel with fluorescence microscopy, one can computationally infer the traction forces using continuum mechanics models [221].

Adherent cells that experience strong confinement utilize a *nuclear piston* mechanism where actin-myosin contraction in front of the nucleus pulls the nucleus forward. Since the nucleus divides the cell in forward and rearward compartments, it acts as a piston that pressurizes the forward compartment and drives forward a cylindrical lobopodial protrusion [222]. Weakly adherent cells such as leukocytes and physically confined fibroblasts and cancer cells perform *amoeboid migration*, characterized by spherical membrane blebs at the leading edge (reviewed in [223]). Blebs are created by myosin-driven contraction of the actin cortex underneath the cell membrane, which builds up hydrostatic pressure in the cytoplasm. Local rupture of the actin cortex or its attachment to the membrane causes local membrane delamination, pushing forward a membrane bleb. Over time the actin cortex regrows under the bleb membrane and myosin contraction drives bleb retraction. Confinement can also induce other migration modes that require little substrate adhesion. Cells can move via friction generated by actin flows within the cortex based on myosin contraction and actin turnover [224], and some tumor cells can migrate by using active transport of water from the front to the back of the cell to propel themselves forward (*osmotic engine* model [225]).

THE ROLE OF MICROTUBULES AND INTERMEDIATE FILAMENTS IN CELL CONTRACTILITY

While not being components of the contractile machinery, both microtubules and intermediate filaments are important for regulating cell contraction. Microtubules negatively regulate the assembly and contractility of actin stress fibers by sequestering GEF-H1, an activator of the small GTPase Rho, in an autoinhibited state [226]. Microtubule depolymerization by nocodazole releases active GEF-H1, leading to a global increase of contractility as measured by traction force microscopy [227]. During both mesenchymal and amoeboid migration, microtubule depolymerization and consequent GEF-H1 is tightly regulated so that actin contractility can be precisely timed and localized in a mechanosensitive manner [228, 229, 230]. Besides biochemical regulation, it is likely that mechanical synergy is also involved in microtubule-based control of actin contractility, since microtubules are able to absorb some of the forces from the contractile actin cytoskeleton [171].

Intermediate filaments likewise regulate actin-based cell contraction by a combination of mechanical synergy and biochemical signaling. In cells migrating on flat surfaces, vimentin has been reported to inhibit stress fiber assembly and contractility through down-regulating GEF-H1 and RhoA [94]. Nevertheless, traction force measurements have shown that vimentin-null cells are less contractile than their wild-type counterparts [67]. Taken together with the observation that vimentin filaments orient traction stresses along the front-rear axis, this suggests a mechanical synergy where vimentin helps build up and transmit larger contractile forces [93]. Recently it was shown by structured illumination microscopy and electron microscopy that vimentin filaments are closely associated with actin stress fibers, forming meshworks that wrap around stress fibers or co-align with them [67, 121]. Physical coupling between the two systems is dependent on the cytolinker protein plectin [68]. Interestingly, it was recently shown that plectin binds vimentin in response to acto-myosin pulling forces [66]. The mechanism for this mechanosensitivity is unknown but could involve catch bonding [231]. Plectin-mediated coupling of actin and vimentin was recently shown to be essential for cells migrating via the nuclear piston mechanism [66]. The vimentin network helps transmit acto-myosin pulling forces to the nucleus, thus enhancing the pressure in the front of the nucleus. It is not yet known whether intermediate filaments also influence cell migration modes driven by contractile activity of the actin cortex, but recent observations that vimentin and F-actin are associated within the cell cortex suggest this is likely [67].

2.3.2. CELL-FREE RECONSTITUTION STUDIES

There is an extensive body of work using cell-free reconstitution to elucidate the mechanisms by which myosin II motor proteins contract actin networks (reviewed in [232]). The contraction mechanism has been found to depend on the actin network connectivity, which is controlled by filament length and by crosslinking. Well-connected networks of long filaments contract because myosins generate compressive stress that causes the actin filaments to buckle and break [233]. By contrast, when the filaments are short, myosins contract the network by polarity sorting, transporting and clustering actin filament plus ends to form polar actin asters [234]. In both cases, the length scale of con-

traction is set by the network connectivity. Global network contraction requires the actin network to be crosslinked above a critical percolation threshold [235]. However, excessive crosslinking will prevent contraction by making the network too rigid [236].

As described above, several cell migration mechanisms rely on myosin-driven contraction of the actin cortex. Recently several groups have been able to reconstitute biomimetic actin cortices by co-encapsulating actin and myosin inside cell-sized lipid vesicles. For weak actin-membrane attachment, the network detaches from the membrane upon contraction [237]. In case of stronger attachment, myosin contraction can cause membrane blebbing [238]. Cortical flows that are important for driving amoeboid migration require not only myosin activity, but also network remodeling through actin depolymerization [239]. Under particular conditions, crosslinked actin-myosin cortical networks in emulsion droplets have been observed to exhibit cortical flows [240], likely because myosin can promote actin turnover [241]. Cell extracts, which contain additional proteins to promote actin turnover, also exhibit cortical flows when encapsulated in emulsion droplets [242, 243, 244]. When these droplets are confined, the myosin-driven cortical flows can propel the droplets forward due to friction with the channel walls, mimicking amoeboid migration of nonadhesive cells [245].

So far only few studies have looked at the effect of intermediate filaments or microtubules on contraction of actin-myosin networks. The addition of a vimentin network that interpenetrates an actin network has been shown to promote myosin-driven contraction by increasing the network connectivity [215]. Similarly, also the addition of microtubules has been shown to promote uniform macroscopic myosin-driven contraction [246].

2.4. FRONT-REAR POLARIZATION

2.4.1. LIVE-CELL STUDIES

CROSSTALK BETWEEN ACTIN AND MICROTUBULES GOVERNS CELL POLARIZATION IN MIGRATION

Directed cell migration requires the breaking of cell symmetry to generate a cell front and a cell rear along an axis aligned with the direction of locomotion. Until now, the role of cytoskeletal crosstalk in front-rear polarity has mostly been studied in the context of 2D mesenchymal cell migration [247]. It is long known that the microtubule cytoskeleton is essential for maintaining a polarized distribution of actin-based forces with actin polymerization in the front and myosin II-based contraction forces in the cell body and rear [248]. Microtubules align along the axis of cell movement with their plus ends oriented towards the leading edge. They appear to stimulate actin-driven cell protrusion by multiple mechanisms. They activate Rac1 and inhibit Rho, therefore promoting actin polymerization and preventing myosin-II-driven contractility at the leading edge. Moreover, actin filaments have been observed to grow directly from microtubule tips toward the leading edge in growth cones of neurons, with the help of protein complexes involving APC and CLIP-170 [249, 250]. There is an interesting actin/microtubule reciprocity, though, since the microtubules require guidance along actin stress fibers to reach the

leading edge. This guidance requires actin-microtubule crosslinking, for instance by ACF7, Growth Arrest-Specific Proteins (Gas2L1), CLIP-associating proteins (CLASPs) or drebrins (reviewed in [251]). These proteins target growing microtubule plus ends by binding to EB (end-binding) proteins, and all of them except drebrin also possess a microtubule-lattice-binding domain. When these crosslinkers are depleted from cells, microtubules cease to grow along actin stress fibers and the microtubule array loses its front-rear polarity [252, 253]. Persistent cell migration is strongly hampered as a consequence, not only because actin-based protrusions are misregulated, but also because microtubules fail to reach cortical microtubule stabilizing complexes (CMSCs) that surround focal adhesions [254].

Microtubule dynamics have also been shown to regulate amoeboid cell migration by locally promoting the retraction of protrusions. In migrating dendritic cells, microtubule depolymerization within protrusions distant from the microtubule organizing center triggers actomyosin contractility, which is controlled by RhoA and its corresponding exchange factor Lfc [230]. Tethering and stabilization of microtubule plus ends by CMSC binding is required for microtubule-dependent focal adhesion turnover, which is essential for migration (reviewed in [117]).

It is not yet clear how these crosstalk mechanisms are modified when cells perform 3D mesenchymal migration, but likely the core mechanisms are shared. One important new factor in 3D migration is that microtubules have a more important mechanical role and are needed to support pseudopodia [162]. A second important new factor is that the rigidity of the nucleus hampers migration through small pores. It was recently shown that microtubules anchored to the nucleus play an important role in active transport of MT1-MMP, which degrades the extracellular matrix, to the cell surface where it drives extracellular matrix proteolysis in front of the nucleus [255].

INTERMEDIATE FILAMENTS CONTRIBUTE TO CELL POLARIZATION VIA CROSSTALK WITH ACTIN AND MICROTUBULES

Although intermediate filaments lack intrinsic polarity, they do contribute to directed mesenchymal migration [115]. When the vimentin network is disassembled using peptides or when vimentin expression is knocked down, cells lose their polarity and lamellipodia appear all around the cell [256]. Vimentin forms closely associated parallel arrays with microtubules in migrating cells [257, 92]. Experiments conducted using vimentin-deficient mouse embryonic fibroblasts attached to polarized and non-polarized protein micropatterns demonstrated that the lack of vimentin alters microtubule organisation, disrupting cell polarity [258]. The two cytoskeletal networks organize in an interdependent manner. The vimentin distribution is polarized by a collaboration between active motor-driven transport along microtubules and actin-driven retrograde flow [259]. Conversely, since the vimentin network is about 10-fold more long-lived than the microtubule network, it can serve as a template for guiding microtubule growth along previous microtubule tracks [92]. This provides a feedback mechanism to sustain front-rear polarity. Moreover, the alignment of the vimentin network with the polarity axis mechanically integrates actin-based forces and orients them to promote directional migration [93]. This mechanical integration is probably aided by vimentin-microtubule crosslinker

proteins such as plectin and APC [257].

In addition to this mechanical role, there is growing evidence for signalling functions of intermediate filaments in cell migration (reviewed in [114]). At the cell periphery, there is for instance Rac-mediated crosstalk between vimentin and actin, where Rac causes vimentin disassembly by controlling the phosphorylation of vimentin at Ser-38, a p21-activated kinase phosphorylation site, promoting actin-driven membrane protrusion [256]. Intermediate filaments also regulate focal adhesion clustering and turnover by binding integrins and via biochemical signalling [260].

2.4.2. CELL-FREE RECONSTITUTION STUDIES

POLARIZATION CROSSTALK STUDIES INVOLVING INTERMEDIATE FILAMENTS

Several studies have explored how interactions between two different cytoskeletal filament types may contribute to the front-rear polarity of migrating cells. These studies mostly used surface assays where one or both cytoskeletal filaments were surface-anchored to facilitate imaging and control the geometry of interaction. These assays straightforwardly allow to probe the crosstalk involved in filament polymerization, an essential component of cell polarization. Most of these studies focused on actin-microtubule crosstalk (see below), and just a few of them investigated the interplay of intermediate filaments with actin or microtubules. When surface-anchored microtubules were grown in the presence of an entangled vimentin network, they were found to be stabilized against depolymerization by direct interactions with vimentin filaments [210]. Vimentin attachment reduced the catastrophe frequency and induced rescue of depolymerizing microtubules. However, in the absence of crosslinker proteins, these interactions were found to be short and infrequent. It is likely that vimentin-microtubule crosslinkers such as APC and plectin create more drastic effects on vimentin and microtubule polymerization. Interestingly, the vimentin-binding region of APC by itself promotes vimentin polymerization [257], which may perhaps promote vimentin polymerization along microtubules. As we show in this thesis (Chapter 3), actin and vimentin filaments do not interact in the absence of crosslinkers, but when an engineered plectin-mimicking crosslinker is added, actin filaments polymerize along surface-anchored vimentin filaments (see also [217]).

POLARIZATION CROSSTALK STUDIES INVOLVING MICROTUBULES

A larger set of studies investigated the interplay of microtubules with different actin network structures designed to mimic structures found at the front of crawling cells. Branched or densely entangled actin network that mimic the dense actin array in the lamellipodium were shown to act as a steric barrier for microtubule growth [261, 262, 263]. However, when microtubules were crosslinked to actin by Tau protein, they were able to generate sufficient polymerization force to penetrate dense actin barriers [263]. By contrast, when actin was arranged in stiff bundles that mimic actin stress fibers or bundles in filopodia, steric interactions were instead found to promote alignment and growth of microtubules along the actin bundles [261, 263]. Actin-microtubule crosslinking proteins such as ACF7, Gas2L1, or CLASP2 were shown to promote actin-guided

microtubule growth by allowing growing microtubules to be captured by and zippered along the actin bundles [261, 263, 264, 265, 216, 266].

Conversely, microtubules can also influence actin polymerization. Microtubule-lattice binding crosslinkers can induce guided polymerization of actin filaments along microtubule [265, 267]. Microtubule-tip binding crosslinkers can induce active transport of actin filaments by the growing microtubule tip [216, 268]. Computer simulations and theoretical modeling showed that this transport is driven by the affinity of the crosslinker for the chemically distinct microtubule tip region [268]. These interactions may potentially enable growing microtubules to relocate newly nucleated actin filaments to the leading edge of the cell and thus boost migration.

Altogether, cell-free reconstitution studies suggest that coupled polarization of the three cytoskeletal filament systems observed in the cell can at least partly be understood on the basis of a mechanical interplay.

2.5. COLLECTIVE MIGRATION & INTERCELLULAR ADHESIONS

Below we briefly review cell-based studies of the role of cytoskeletal crosstalk in the regulation of intercellular adhesion dynamics and collective migration. For a more detailed overview, we refer the reader to our review [123].

In epithelial tissues, keratin intermediate filaments and actin jointly influence desmosomal and adherens junctions because they are crosslinked via plectin. Plectin organizes keratin into a rim-and-spoke configuration where contractile forces generated by acto-myosin are balanced by compressive elements provided by the keratin network, thus balancing internal tension and stabilizing cell-cell contacts [85]. Deletion of plectin therefore causes perturbations of both desmosomes and adherens junctions. Although endothelial cells do not have desmosomes, also here plectin-mediated crosslinking between F-actin and vimentin intermediate filaments regulates adherens junction strength and tissue integrity [84]. Migrating epithelial cells need to dynamically rearrange their adhesive contacts. Desmosome remodeling is dependent on both actin and keratin. Assembly of desmosomes at the leading edge and subsequent transport to the lateral sides is mediated through extensive actin remodelling, while more matured desmosomes are guided via keratins to the cell center to eventually disassemble [269]. Intermediate filaments have an important mechanical role in distributing actin-myosin based forces, similar to their role in single-cell migration. Collective movement of both embryonic cells and astrocytes with proper leader-follower dynamics was shown to be highly dependent on this mechanical synergy of actin and intermediate filaments [270, 89].

There is ample evidence that microtubule-actin crosstalk affects adherens junctions via mechanisms similar to those observed for focal adhesions. Adherens junctions contain multiple proteins that bind microtubule plus ends, including APC, ACF7 and CLASP [271, 272]. This allows microtubules to promote myosin II activation and local concentration of cadherin molecules [273] and facilitates trafficking of junctional components to the cell surface [274, 275]. At the same time, microtubules promote junctional actin assembly by promoting liquid-liquid-phase separation of the actin nucleator cor-

don bleu (Cobl) [276]. In studies of *in vivo* collective migration it was found that cell-cell contacts differed in their requirement for dynamic microtubules along the leader-follower axis [277]. Cells of the leading domain remained cohesive in the absence of dynamic microtubules, whereas dynamic microtubules were essential for the conversion of leader cells to epithelial followers. Interestingly, it was recently shown that physical confinement of collectively migrating cancer cells can induce the dissociation of leader cells by actin-microtubule crosstalk [278]. Confinement-induced microtubule destabilization releases and activates GEF-H1, which promotes RhoA activation and results in leader cell detachment.

2.6. PLASTICITY OF CELL MIGRATION

2.6.1. LIVE-CELL STUDIES

CELLULAR PLASTICITY IS MEDIATED THROUGH FOCAL ADHESIONS

Most terminally differentiated cells such as epithelial and stromal cells migrate only during morphogenesis. However, tissue injury can induce cell plasticity. Mature cells can re-enter the cell cycle and change their phenotype guided by paligenesis programs [279]. Unfortunately plasticity can also contribute to disease. For instance, malignant cancer cells are often hyperplastic, contributing to their invasiveness. A well-studied example of cell plasticity is epithelial-mesenchymal transition (EMT), a reversible process in which epithelial cells lose polarity through cytoskeletal remodelling, individualize and gain motility. EMT is a critical process in embryonic development and wound healing, but it also plays a key role in fibrosis and cancer invasion. EMT and the reverse mesenchymal-epithelial transition (MET) are influenced not only by biochemical cues, but also by mechanical properties of the ECM [280, 281].

Cells sense the mechanical properties of the ECM through their acto-myosin cytoskeleton at focal adhesions, mediating mechanotransduction and activating downstream plasticity mechanisms in response to environmental changes. Focal adhesions are based on integrin adhesion receptors that interact with the ECM through their extracellular domains and with the actin cytoskeleton through their cytoplasmic tails [282]. The actin-integrin connection is mediated through talin and kindlin (reviewed in [283]). Single integrins form small and transient junctions, but mechanical stimulation reinforces integrin adhesions by causing maturation into large focal adhesions. Upon mechanical stimulation, talin and kindlin undergo conformational changes that expose cryptic binding sites for additional cytoskeletal and signalling proteins [282]. Mechanical stimulation further reinforces focal adhesions by inducing actin polymerization [284]. Variations in the biochemical composition and physical properties of the ECM can elicit different 3D cell migration modes characterized by different amounts of cell-ECM adhesion [219, 285]. Highly crosslinked and dense matrices elicit lobopodial migration, characterized by a high number of focal adhesions and high actomyosin contractility. Less dense, fibrous environments elicit mesenchymal migration with a characteristic front-to-rear gradient of focal adhesions. In low-confining areas that lack adhesion sites, cells

depend on bleb formation to drive themselves forward, a mechanism that does not require focal adhesions [219].

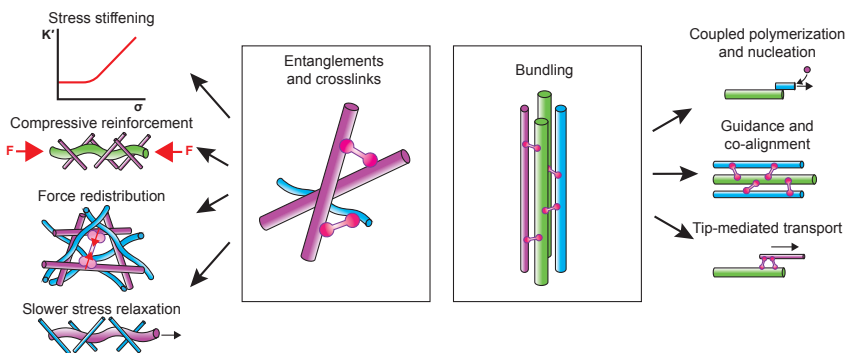


Figure 2.2: Schematic of the two general cytoskeletal crosstalk mechanisms and their effect on cytoskeletal biophysics. *Entanglements and crosslinks* regulate stress stiffening, compressive reinforcement, force distribution and slower stress relaxation (left). *Bundling* regulates coupled polymerization and nucleation, guidance and co-alignment, and tip-mediated transport of filaments (right). Color scheme: actin (magenta), microtubules (green), intermediate filaments (cyan) and crosslinkers (pink).

ROLE OF MICROTUBULES IN CELL MIGRATION PLASTICITY

Not much is known about the role of cytoskeletal crosstalk in migration plasticity. Microtubules are likely involved through their feedback interactions with actin near focal adhesions. It was recently shown that higher substrate rigidity promotes microtubule acetylation through the recruitment of α -tubulin acetyltransferase (α TAT) to focal adhesions by talin [121]. In turn, microtubule acetylation tunes the mechanosensitivity of focal adhesions by promoting the release of GEF-H1 from microtubules to activate RhoA, which in turn promotes actomyosin contractility [121]. In breast cancer cells, actin-microtubule crosstalk near focal adhesions via the scaffolding protein IQGAP1 was demonstrated to promote invasion in wound healing and transwell assays [286]. In fibrosarcoma cells, the microtubule-destabilizing protein stathmin was shown to influence migration mode switching [287]. Increased stathmin activity, and as a result less stable microtubule networks, promoted amoeboid-like migration, while phosphorylation of stathmin led to a more elongated migratory phenotype. Besides crosstalk near focal adhesions, microtubules can also influence migration mode switching through mechanical effects. In confined or compressed cells, microtubules are stabilized through CLASP2 localization to the lattice, providing a mechanosensitive pathways for cells to adapt to highly constricting environments [161].

ROLE OF INTERMEDIATE FILAMENTS IN CELL MIGRATION PLASTICITY

The intermediate filament protein vimentin is considered a key cellular plasticity regulator and marker of tumor cell malignancy, especially based on its general upregulation in

EMT and in motile cancer cells [288]. Carcinoma cells in addition express integrin $\alpha 6\beta 4$, which recruits vimentin to focal adhesions through its binding to plectin, promoting a 3D invasive phenotype switch [289]. Together with nuclear lamins, vimentin contributes to migration plasticity through regulation of nuclear deformation, for instance allowing for a transition towards amoeboid-like and faster migration in Hela cells and melanoma cells when encountering confinement [290, 113]. Moreover, cells migrating under high confinement use their nucleus as a piston to squeeze through small pores. This complicated pulling mechanism is regulated through crosstalk between the vimentin cage around the nucleus and actomyosin in front of the nucleus [222].

2.6.2. CELL-FREE RECONSTITUTION STUDIES

Understanding the molecular basis of migration plasticity is an enormous challenge since integrin-based matrix adhesions contain over 100 types of molecules that are potentially mechanosensitive [291].

One of the first mechanotransduction events during adhesion maturation is stretching of talin, followed by vinculin binding and activation. This core process was elegantly reconstituted by overlaying a network of actin-myosin bundles mimicking stress fibers on a talin-micropatterned surface [292]. It was shown that direct binding of the contractile actin-myosin network to talin was sufficient to stretch the protein and induce the association and activation of vinculin. Talin binding facilitates vinculin activation by allosterically weakening the head-tail interaction that keeps it in an auto-inhibited conformation [293]. Exposure of the actin-binding tail induces a positive feedback that reinforces the connection with actin [292]. Using the same assay, it was shown that activated vinculin can interact with Arp2/3 complex-mediated branched actin networks and modify their organization by crosslinking actin filaments into bundles [294]. This is likely an important step towards focal adhesion maturation. Single-molecule studies showed that vinculin forms a directionally asymmetric catch bond with F-actin [295]. In this way vinculin can organize the polarity of the actin cytoskeleton and contribute to front-rear asymmetry in migrating cells. Recently the interaction of integrins, talin and kindlin, another major focal adhesion regulator, was reconstituted on giant unilamellar vesicles [296]. It was shown that phosphoinositide-rich membranes recruit talin and kindlin, which then cause the formation of large integrin clusters that can recruit actin-myosin. Another study showed that membrane-bound talin can also activate vinculin and the two proteins together can link actin to the membrane [297].

Cell-free reconstitution studies suggest that the actin cytoskeleton itself also contains proteins that mediate mechanotransduction. An example is filamin A (FLNA), a large multi-domain scaffolding protein that cross-links actin filaments and binds numerous proteins via cryptic binding sites along its length. Using reconstituted actin networks crosslinked with FLNA, it was shown that mechanical strain on the FLNA crosslinks alters its binding affinity for its binding partners [298]. Both externally imposed bulk shear and contraction by myosin-II increased binding of the cytoplasmic tail of β -integrin while it weakened binding of FilGAP, a GTPase that inactivates Rac. Mechanical strain on FLNA can thus stabilize extracellular matrix binding and at the same time influence actin dynamics through Rac activity.

2.7. THE ROAD AHEAD

Cytoskeletal crosstalk is increasingly recognized as a major determinant of cell migration. Coupling between the actin, microtubule and intermediate filament cytoskeleton influences cell migration by regulating cell deformability, contractility, front-rear polarity and migration plasticity. Coupling of filaments through entanglements, crosslinking and bundling regulates a variety of mechanisms that mediate cellular mechanics and cytoskeletal dynamics involved in these migration strategies (Figure 2.2). To complicate matters, there is growing evidence that a fourth cytoskeletal protein family, the septins, also strongly impacts cell migration. Septins are well-equipped to mediate cytoskeletal crosstalk since they can bind to the cell membrane, actin and microtubules [299]. Recent research demonstrated roles of septins in mesenchymal and amoeboid single-cell migration [300, 301] and in the regulation of endothelial and epithelial cell-cell adhesion [302, 303].

Elucidating the biophysical mechanisms by which cytoskeletal crosstalk regulates cell migration is challenging due to the enormous molecular complexity of the cell and feedback between mechanical forces and biochemical signaling. Cell-free reconstitution provides a valuable complement to live-cell studies because it simplifies the challenge of separating biochemical and physical contributions to cytoskeletal crosstalk. Yet we do note that caution should be used when translating findings regarding cytoskeletal crosstalk from bottom-up studies to cells. Cell-free model systems present a highly simplified environment in terms of molecular complexity, crowding, ionic conditions, spatial heterogeneities, mechanical conditions, etcetera. Cytoskeletal interactions or mechanical effects observed in a cell-free system do not necessarily occur (in the same way) in the cellular environment. The power of cell-free studies is to develop and test hypotheses regarding possible interactions and their biophysical impact under well-controlled conditions. Using cell-based studies, one can then test how these findings carry over to the cellular environment.

2.7.1. INCREASING THE COMPLEXITY FROM THE BOTTOM-UP

Clearly there still remains an enormous gap between the complexity of cells and the simplicity of reconstituted systems. How can this gap be bridged? We propose different routes to bridge this gap (Figure 2.3). One obvious direction to bridge this gap is to enhance the complexity of cell-free assays. We would like to mention three aspects here.

First, it will be important to introduce **controlled interactions** between the cytoskeletal constituents. Most cell-free studies so far combined cytoskeletal filaments without any accessory proteins. Interestingly, this work showed that steric interactions alone suffice to give rise to nonlinear stiffening and enhanced compressive strength. There is some evidence that intermediate filaments directly interact with actin filaments and microtubules via electrostatic interactions [100, 210], but this could be an artefact of *in vitro* conditions. Single-molecule measurements of filament interactions within cells or cell lysates could shed light on this issue. An important next step to bridge the gap to the cell is to incorporate accessory proteins that mediate cytoskeletal coupling. Several studies have shown that crosslinking via cytolinkers is sufficient to give rise to cytoskele-

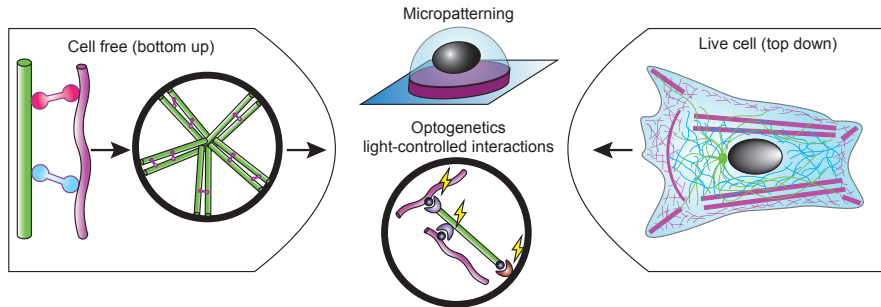


Figure 2.3: Our proposed route to bridge the gap between live cell (top down) and cell free (bottom up) approaches in the research of cytoskeletal crosstalk in cell migration. *Micropatterning* and *optogenetic tools* can be used to manipulate cytoskeletal interactions both in cell-free and live cell model systems. These approaches, together with other advances, can therefore help bridge the gap between the two research approaches. Color scheme: actin (magenta), microtubules (green), intermediate filaments (cyan) and crosslinkers (pink).

tal filament co-alignment and mechanical synergy (e.g. [216, 217]). More detailed investigations of the effects of cytolinkers, both *in vitro* and in cells, will be important to delineate their roles in cytoskeletal co-organization, mechanical synergy, and mechanotransduction. In this thesis we make first steps in this direction by exploring the impact of cytolinkers on the mechanical synergy of actin and vimentin using cell-free reconstitution (Chapters 4 and 5) and we explore the use of these cytolinkers in cells (Chapter 7).

Second, it will be important to introduce **cell-mimicking geometrical constraints**. In the cell, cytoskeletal crosstalk is guided by geometrical constraints provided by the cell membrane. The membrane organizes the cytoskeleton through spatial confinement and by providing adhesion sites where cytoskeletal filaments are nucleated or anchored. Reconstitution experiments have begun to recapitulate these constraints by encapsulating cytoskeletal proteins inside cell-sized emulsion droplets or lipid vesicles, including actin/microtubule and actin/keratin composites [206, 304]. These model systems could form a basis for reconstituting synthetic cells capable of migration. Adhesion-independent migration is probably easiest to reconstitute. Flow-driven confined migration was recently reconstituted, although based on a cell extract, so the minimal set of ingredients is not yet known [245]. It will be interesting to incorporate microtubules and/or intermediate filaments in this assay to control cell polarity and mechanics. Mesenchymal migration is likely more challenging to reconstitute because it requires coordinated actin polymerization, contraction, and cell-matrix adhesion. Motility driven by actin polymerization has been successfully reconstituted on the outer surface of lipid vesicles (reviewed in [305]), but motility of vesicles with actin polymerization inside will require substrate adhesion. Surface micropatterning provides an interesting approach to impose polarized shapes to synthetic cells by forcing them to adapt to the pattern shape and size [306].

Third, it will be important to introduce **symmetry-breaking cues**. One could for in-

stance use light-induced dimerization to induce spatial patterning and symmetry breaking of cytoskeletal networks. Light-inducible dimers (LIDs) come from photoactivatable systems naturally occurring in plants and allow for reversible photoactivation [307]. Recently it was for instance shown that microtubule-interacting proteins fused to opto-chemical dimerization domains can be used to drive symmetry breaking of microtubule networks inside emulsion droplets [308].

2.7.2. REDUCING THE COMPLEXITY FROM THE TOP-DOWN

The opposite direction to bridge the gap between live-cell and cell-free studies is to reduce the complexity of living cells. Some of the same techniques that can provide more control over cell-free systems can also provide control over the behavior of living cells.

Surface micropatterning for instance allows one to confine cells to adhesive islands with precisely controlled geometries, forcing the cells to adopt prescribed shape and corresponding cytoskeletal organizations. Imaging many cells adhered on the same pattern greatly facilitates quantification of cytoskeletal crosstalk [258]. Moreover, micropatterning can be used to investigate how cytoskeletal interactions affect single-cell and collective cell migration dynamics [309].

Light-inducible dimerization can be used to manipulate cytoskeletal interactions with high spatial and temporal control. It was for instance recently shown that F-actin can be crosslinked to microtubule plus ends by transfecting cells with an iLID-tagged EB-binding SxIP peptide and SspB-tagged actin-binding domains [310]. This could be an interesting tool to systematically study the crosstalk of microtubules with actin and intermediate filaments that takes place near cell adhesions.

Finally, molecular tension sensors provide a very interesting tool to selectively interrogate mechanical interactions between cytoskeletal networks. Tension sensors consist of two fluorescent proteins separated by a peptide with a calibrated mechanical compliance. Under strain, the fluorescent proteins are separated, decreasing fluorescence energy transfer (FRET) between them. By embedding a tension sensor in the actin crosslinker FLNA, it was recently shown that molecular tension can be measured within the actin cytoskeleton [311]. It will be interesting to use a similar approach to measure tension within the intermediate filament cytoskeleton and test force transmission between the actin and intermediate filament cytoskeleton. In this thesis we make first steps in this direction in Chapter 6, where we develop tension-sensing proteins that crosslink F-actin.

2.8. ACKNOWLEDGEMENTS

I would like to thank Anouk Van der Net and James Conboy for their awesome literature-review work and great discussions and working on the corrections during my travels. I would also like to thank Gisje Koenderink for great feedback and helping us with narrowing the content of the review.

3

SPATIOTEMPORAL DYNAMICS OF CO-ENTANGLED COMPOSITE NETWORKS OF F-ACTIN AND VIMENTIN

Cell shape and deformability are determined by the cytoskeleton, which consists of an interpenetrating network of actin filaments, microtubules, and intermediate filaments. In mesenchymal cells, interactions between actin and vimentin, a type of intermediate filament, contribute to vital cellular processes such as cell division and migration. However, the molecular nature of these interactions and the resulting mechanical synergy between actin and vimentin remain poorly understood. A few prior studies have used in vitro reconstitution to test for mechanical synergy in composite networks of actin and vimentin, but there is contradictory evidence whether or not these filaments combine to give synergistic mechanical enhancement. In this Chapter we revisit this question using bulk rheology measurements in which we compare co-entangled actin-vimentin composites with single-component networks of actin or vimentin. We choose protein concentrations such that the network mesh sizes should be comparable, an assumption that we validate by Differential Dynamic Microscopy (DDM) measurements of the mobility of embedded tracer particles. We show by bulk rheology that the linear viscoelastic properties of co-entangled actin-vimentin networks are a simple superposition of the properties of the two component networks, suggesting that no mechanical synergy emerges in absence of accessory proteins.

3.1. INTRODUCTION

THE mammalian cell cytoskeleton is a scaffold made up of different filamentous proteins, including actin, microtubules, and intermediate filaments (IFs). The interactions among these cytoskeletal components are crucial for controlling the cell's overall shape and internal structure and for regulating basic cellular functions. For example, the combined actions of filamentous (F-)actin and microtubules influence cell shape and polarity [251] (F-actin/microtubule crosstalk), while the organization and transport of vimentin networks (an intermediate filament protein expressed in mesenchymal cells) depend on their interactions with microtubules [43] (vimentin/microtubule crosstalk). Recently, vimentin and actin were shown to form an interpenetrating network structure within the cell cortex that is important for cell division in confined environments [67, 215]. Moreover, high resolution imaging of mouse embryonic fibroblasts revealed coupling between actin and vimentin structures within the cortex as well as in stress fibers [67] (F-actin/vimentin crosstalk).

Previous studies on cell mechanics have overwhelmingly focused on the individual contribution of each cytoskeletal system, obtained by measuring the change in cell stiffness or contractile force generation upon genetic or pharmacological manipulations. These studies have been complemented by mechanical studies on individually reconstituted cytoskeletal components [312]. Based on these studies, intermediate filaments are thought to mainly govern cell strength, while F-actin is thought to mainly govern cell stiffness and contractility [313, 314]. However, the mechanical properties of the cytoskeleton as a whole, resulting from the combination of different cytoskeletal subsystems, remains poorly understood.

In recent years there has been a shift towards a more comprehensive approach that considers interactions between different cytoskeletal subsystems. For instance, experimental and theoretical studies have revealed substantial alterations in the nonlinear viscoelastic behavior of filamentous (F-)actin networks as soon as even a small density of microtubules are incorporated [212]. Several studies have addressed reconstituted networks of F-actin and vimentin, but there is contradictory evidence whether or not these filaments combine to give synergistic mechanical enhancement. One study reported a synergistic stiffness enhancement for co-polymerized networks of actin and vimentin at a total protein monomer concentration of $24 \mu\text{M}$, compared to their single-component counterparts, each at a monomer concentration of $24 \mu\text{M}$ [100]. The authors proposed that the filaments experience direct interactions facilitated by the disordered C-terminal tail domains of vimentin, which decorate the surface of vimentin filaments. They showed that synergistic stiffening was indeed absent in composite networks reconstituted using a tail-truncated vimentin mutant. While this finding is suggestive of direct F-actin/vimentin interactions, the precise physical origin and binding strength remained elusive. Moreover, later work showed that when the mesh size of the networks was kept constant instead of the concentration, composite actin-vimentin networks exhibited a rheological response that was a simple superposition of the response of the single-component networks [101]. Note that, due to the different monomer molecular weight (42 kDa) and filament width of F-actin (double-stranded helices [6]) versus vi-

mentin (53.6 kDa monomer molecular weight, 32 monomers per cross-section [315]), networks of the same protein molar concentration have a different mesh size. The mesh size reflects the average spacing between neighboring filaments, which is the main determinant of the concentration-dependent rheology of semiflexible polymer networks [316]. When the mesh size is held constant, any differences in network properties between composite versus single-component networks should reflect filament interactions, whereas when the monomer concentration is held constant, these differences will be impacted by a different filament spacing.

In this chapter, in part motivated by the disparity from these previous studies, we aim to better understand what are the dynamic and mechanical properties that emerge from combining F-actin and vimentin filaments in reconstituted networks. It is important to note that in the cell the interaction between F-actin and vimentin is regulated by crosslinker proteins like plectin [61] (see Chapters 4 and 5 of this thesis). In this chapter, we limit ourselves to the more basic reconstitution of just F-actin and vimentin filaments without any additional crosslinker protein. To study the network dynamics and mesh size, we performed passive microrheology, a method that relies on the quantification of the thermal fluctuations of embedded probe particles [317]. Instead of single-particle tracking, which has been used extensively in prior studies of actin and vimentin networks [215, 197, 318], we use Differential Dynamic Microscopy (DDM). DDM has the advantage that it does not require localization and tracking of individual particles. Instead, images are analyzed in Fourier space to extract the characteristic decorrelation times of density fluctuations across a span of wave vectors. One thus obtains information equivalent to light scattering but with real-space images acquired on a microscope [319, 320]. Recently a few labs picked up on this method in the context of cytoskeletal networks *in vitro* [321, 246, 322] and in cells [323]. In our study, we extend an existing analysis pipeline [324] with custom-written Python modules for data analysis. In parallel, we also study the stress relaxation dynamics of the networks by small amplitude oscillatory shear measurements. The DDM measurements reveal that the spatiotemporal dynamics of the F-actin-vimentin composites reflect a superposition of the F-actin and vimentin network dynamics. In line with this finding, the bulk linear viscoelastic properties for composite networks are a simple superposition of the two networks when compared at constant mesh size. We conclude that there is no significant mechanical synergy between F-actin and vimentin networks in the absence of crosslinking.

3.2. PRINCIPLE OF DIFFERENTIAL DYNAMIC MICROSCOPY

Differential dynamic microscopy (DDM) is an analytical technique that allows for the quantification of the decorrelation rate of structural features within a system based on time lapse sequences of two-dimensional microscopy images, $I(x, y, t)$, where I is the intensity in each pixel (x, y) [319, 320]. Here we used either bright field or wide field fluorescence imaging of tracer particles embedded within the reconstituted cytoskeletal network. However, we note that the method is very general and also extends to alternative imaging modalities such as dark field microscopy [325] and to alternative probes such as the cytoskeletal filaments themselves [326].

A fundamental step in DDM involves subtracting frames separated by a lag time Δt : this process eliminates the time-independent signal, thus revealing the displacements of mobile tracer particles. At a lag time characteristic of the system, the difference images become statistically indistinguishable. This occurs when the tracer particles have moved sufficiently far from their original positions, eliminating correlation with the image at the initial time, t_0 . The next step in the DDM analysis entails a 2D Fourier transform of the difference image of each pair of images separated by Δt , which is then squared, producing the image structure function:

$$D(\vec{q}, \Delta t) = \langle |I(\vec{q}; \Delta t + t_0) - I(\vec{q}; t_0)|^2 \rangle_{t_0} \quad (3.1)$$

$D(\vec{q}, \Delta t)$ depends on the lag time and on the wave vector \vec{q} . This wavevector corresponds to a spatial frequency, $\lambda = \frac{2\pi}{q}$. For each q -value, $D(\vec{q}, \Delta t)$ probes movement at a specific length scale. If the particle dynamics are isotropic, as is the case for reconstituted solutions of cytoskeletal filaments, the image structure function can be radially averaged, using the magnitude of \vec{q} . Furthermore, in case of random tracer particle movement driven by thermal fluctuations, subtracting images separated by the same time lag at different times yields statistically identical Fourier transforms. Thus, to enhance statistical accuracy, Fourier transforms for all image pairs with equal Δt were averaged.

The image structure function can be related to the intermediate scattering function (ISF), which contains information about the underlying dynamics of the sample [319]:

$$D(\vec{q}, \Delta t) = A(\vec{q})[1 - f(\vec{q}, \Delta t)] + B(\vec{q}) \quad (3.2)$$

Here, $f(\vec{q}, \Delta t)$ is the ISF, and $A(\vec{q})$ and $B(\vec{q})$ are dependent on the optical properties of the microscope and the sample. $B(\vec{q})$ is the background, which depends on the noise in the images, while $A(\vec{q})$ is the amplitude, associated with the static scattering of the sample [327]. These parameters can be determined by fitting the data with $D(\vec{q}; \Delta t \rightarrow 0) = B(\vec{q})$. When the tracer particles are immersed in a simple Newtonian fluid, the ISF starts at a value of 1 at zero lag time and decays to a final value of 0 as correlation within the system is entirely lost. Decorrelation is more rapid for large q -values, which corresponds to small wavelengths in real space. When the tracer particles undergo simple Brownian motion, the ISF is expected to decay exponentially [319]:

$$f(\vec{q}, \Delta t) = e^{-\Delta t/\tau(\vec{q})}, \quad (3.3)$$

where $\tau(\vec{q})$ is the characteristic decay time of the system, which governs the diffusion coefficient D of the particles.

For particles embedded in more complex non-Newtonian materials such as a cytoskeletal protein network, particle motion becomes subdiffusive due to particle confinement [328]. The particle confinement will depend on the tracer particle size relative to the network mesh size. Particles that are similar-sized or larger than the meshes will be strongly hindered in their diffusion [329]. When the particles are larger than the meshes, their diffusion coefficient is mainly dependent on the linear viscoelastic properties of the network. This is the basis for microrheology, where the network rheology is inferred from the ISF (or in the time domain, the mean squared displacement of the particles)

by generalizing the Stokes-Einstein relation and replacing the solvent viscosity by the complex shear modulus [330, 331].

3.3. RESULTS

3.3.1. LINEAR RHEOLOGY OF F-ACTIN, VIMENTIN AND COMPOSITES THEREOF

We first revisited earlier contradictory findings summarized in the Introduction regarding mechanical synergy in composite networks of F-actin and vimentin. We polymerized actin (24 μM), vimentin (18 μM), or composite actin-vimentin networks (24 μM actin + 18 μM vimentin) between the cone-and-plate of a rheometer and performed linear viscoelastic measurements. We chose the actin and vimentin monomer concentrations such that we expected a similar average mesh size of 300 nm as estimated based on the protein concentration and the known mass-per-unit length of the filaments (see detailed explanation in Appendix 3.8.1). We performed the experiments with two different batches of vimentin: one batch that was also used for DDM later in this chapter (Figure 3.1A), and another batch that was used in the later Chapters 4 and 5 (Figure 3.1B). In both cases, we applied small amplitude oscillatory shear with a strain amplitude of 1% while varying the frequency logarithmically and determined the network elastic (storage) shear modulus, G' , and viscous (loss) modulus, G'' , from the stress response.

In case of the vimentin batch used for DDM measurements, the elastic moduli were comparable for F-actin (blue curve), vimentin (pink curve) and actin+vimentin (black), with values of ~ 4 Pa (Figure 3.1A (top)). The vimentin network (pink curve in Figure 3.1A (bottom)) was slightly more solid-like than the F-actin network (blue curve), as characterized by a slightly smaller loss tangent $\tan(\delta) = \frac{G''}{G'}$. The composite network had a loss tangent intermediate between that of F-actin and vimentin. The frequency dependencies of the elastic modulus and loss tangent were similar for all three networks, suggesting similar stress relaxation dynamics. These results indicate that there is no mechanical enhancement between the two subsystems upon co-polymerization.

In case of the vimentin batch used in later chapters (Chapters 4 and 5), the F-actin network (blue curve) was softer than the vimentin network (pink curve) (see Figure 3.1B (top)). The F-actin network had an elastic modulus of ~ 1.5 Pa, whereas the vimentin network had an elastic modulus of ~ 3 Pa. The stiffness of the F-actin/vimentin composite network (black curve) was approximately equal to the sum of the elastic moduli of the two isolated networks (more details are discussed in Chapter 4). The loss tangent of the networks (Figure 3.1B (bottom)) was quite noisy but showed F-actin-vimentin composite networks (black curve) to be in-between the single-filament networks of vimentin (pink curve) and F-actin (blue curve). These observations again indicate that the viscoelastic properties of F-actin/vimentin composites are a simple superposition of two non-interacting networks.

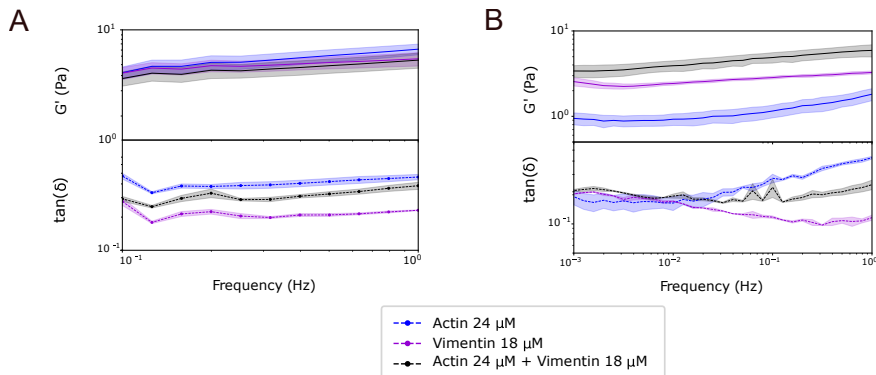


Figure 3.1: Linear bulk rheology of F-actin (24 μ M), vimentin (18 μ M) and 24 μ M actin + 18 μ M vimentin composites. The color code is the same in both panels (see legend at the bottom). (A) Data obtained with the vimentin batch also used for DDM assays. (Top) Frequency dependence of the storage modulus G' of F-actin-vimentin composite network (black curve) and of one-component F-actin (blue curve) and vimentin (pink curve) networks. (Bottom) Corresponding loss tangents, defined as the ratio of the loss modulus G'' to the storage modulus G' (same color code). Note that the loss tangent is noisy because the applied strain and the shear moduli (especially G'') are small, so the stress is close to the sensitivity limit of the rheometer. Also note that $\tan\Delta$ is dimensionless. (B) Corresponding data obtained with the vimentin batch used in Chapters 4 and 5.

3.3.2. SPATIOTEMPORAL DYNAMICS OF F-ACTIN, VIMENTIN AND COMPOSITES THEREOF

In order to compare the spatiotemporal dynamics of F-actin, vimentin and composite F-actin-vimentin networks, we performed comparative microrheology measurements on the three types of networks using DDM analysis of time-lapse movies of tracer particles embedded in the networks. These measurements provide an indirect way to test the theoretical estimates of the network mesh size. As explained in Appendix 3.8.1, estimating the mesh size from the protein monomer concentrations assumes that the networks are isotropic and uniform. To test the validity of this assumption, we used tracer beads with two different sizes (0.6 μ m or 1.1 μ m) and networks with four different estimated mesh sizes (0.25 μ m, 0.3 μ m, 0.4 μ m and 0.5 μ m). A detailed overview of the parameters we explored is shown in Appendix Tables 3.1 and 3.2 for F-actin and vimentin networks, respectively. We made sure to perform this systematic series of experiments all with the same batch of dialyzed vimentin and G-actin, to minimize any influence of batch-to-batch variations (see below). We expect the particles to become strongly hampered in their motion when their diameter becomes comparable to the mesh size [329]. We quantified the dynamics of the particles through the intermediate scattering function (ISF), which is shown for a constant q -value of 4.65 μ m⁻¹, an intermediate value where the ISF is minimally affected by noise or drift [332]. We adjusted the particle concentrations such that the number of particles was between 5-10 in the field of view for all the samples, with the help of calibration samples of particles in glycerol/water solutions at different dilutions (see Appendix Figure 3.4).

We first studied the dynamics of tracer particles with two different sizes (0.6 or 1.1

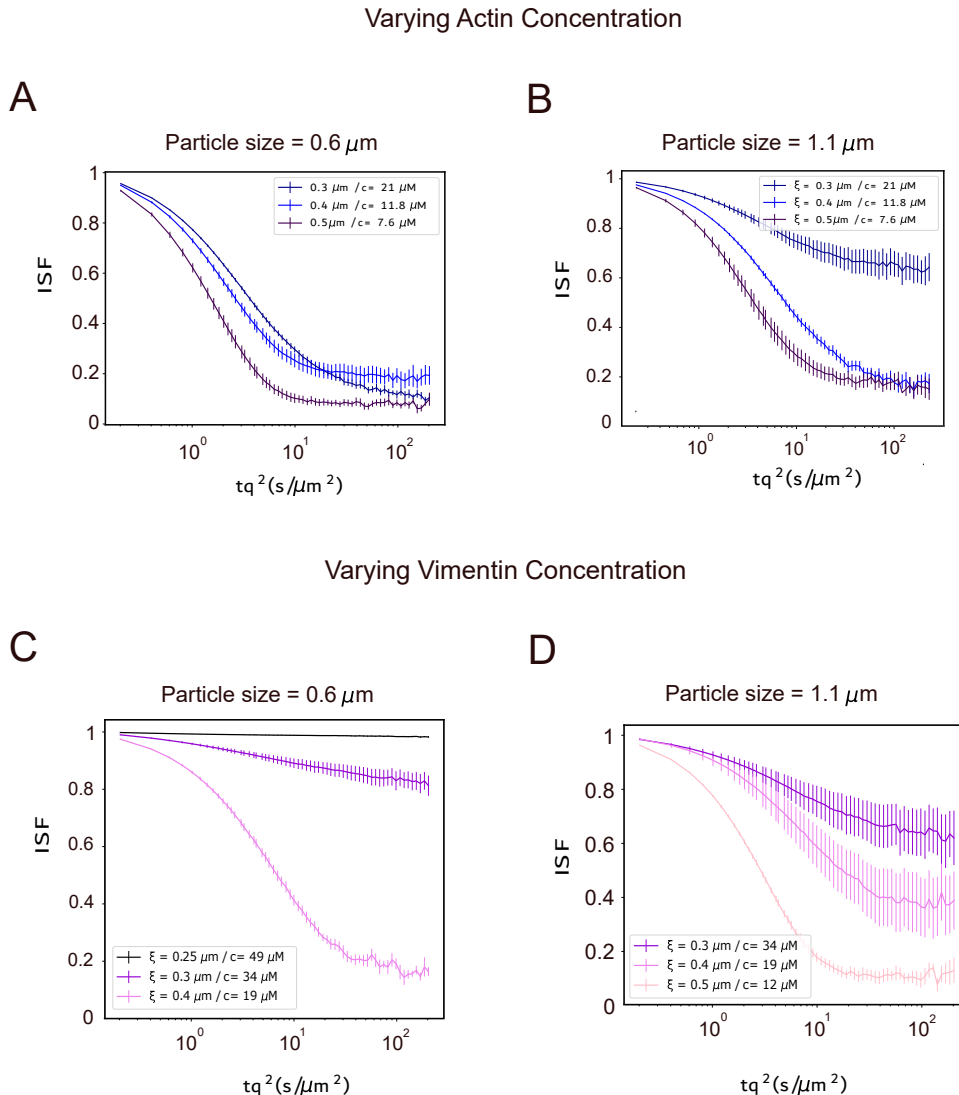


Figure 3.2: DDM data showing the intermediate scattering function (ISF) for tracer particles in F-actin and vimentin networks as a function of particle size and network mesh size. (A) Series of ISF data for tracer particles with a diameter of $0.6 \mu\text{m}$ in actin networks prepared at different concentrations corresponding to theoretical mesh sizes of $0.3 \mu\text{m}$ (dark blue curve), $0.4 \mu\text{m}$ (blue curve) or $0.5 \mu\text{m}$ (dark violet curve). (B) Corresponding series of ISF data for tracer particles with a diameter of $1.1 \mu\text{m}$ in actin networks (same color code as in A). (C) Series of ISF data for tracer particles with a diameter of $0.6 \mu\text{m}$ in vimentin networks prepared at different concentrations corresponding to theoretical mesh sizes of $0.25 \mu\text{m}$ (black curve), $0.3 \mu\text{m}$ (violet curve) and $0.4 \mu\text{m}$ (pink curve). (D) Series of ISF data for tracer particles with a diameter of $1.1 \mu\text{m}$ in vimentin networks prepared at different concentrations corresponding to theoretical mesh sizes of $0.3 \mu\text{m}$ (violet curve), $0.4 \mu\text{m}$ (pink curve) and $0.5 \mu\text{m}$ (salmon curve). All ISF data were obtained at a constant q value of $4.65 \mu\text{m}^{-1}$. Note that the ISF is dimensionless.

μm) in F-actin networks. For the smaller particles ($0.6 \mu\text{m}$, Figure 3.2A), we observed decorrelation of the ISF with a slowing down when the mesh size was decreased from $0.5 \mu\text{m}$ (dark violet curve) to $0.4 \mu\text{m}$ (blue curve) and $0.3 \mu\text{m}$ (dark blue curve). The ISF curves did not decorrelate to zero, as expected in case of free diffusion. However, we note that even in simple water-glycerol mixtures, our ISF curves did not decorrelate fully to zero (see Appendix Figure 3.4). We hence suspect that this effect reflects problems with the background estimation, where we probably used inaccurate estimates of $A(q)$ and B in the calculation needed to determine the ISF from the DDM matrix (see Equation 3.2). It has been reported previously that B can be overestimated in this approach [324]. The DDM data show that the tracer particles were not immobilized in any of the F-actin networks, even though the ratio of particle size to the average estimated mesh size was larger than 1 in all cases ($R_{0.3A} = 2$, to $R_{0.4A} = 1.5$, and $R_{0.5A} = 1.2$). Since we anticipate a distribution of mesh sizes, this is not unexpected. For the larger particles ($1.1 \mu\text{m}$), we observed similar dynamics as for the smaller particles in networks with the two largest mesh sizes ($0.4 \mu\text{m}$ (blue curve) and $0.5 \mu\text{m}$ (dark violet curve), corresponding to particle size/mesh size ratios of $R_{0.4A} = 2.75$ and $R_{0.5A} = 2.2$, respectively). However, the ISF showed significantly slower and incomplete relaxation when the particles were embedded in the F-actin network with the smallest mesh size ($0.3 \mu\text{m}$ (dark blue curve), corresponding to $R_{0.3A} = 3.6$). These observations suggest that the theoretical mesh size estimates for F-actin networks provide a reasonable proxy of the average interfilament spacing.

Next we performed similar measurements with the same two particle sizes for vimentin networks. For the smaller particles ($0.6 \mu\text{m}$ diameter, Figure 3.2C), we observed a strong impact of the vimentin concentration on particle mobility. For the largest mesh size (pink curve, $0.4 \mu\text{m}$, corresponding to $R_{0.4V} = 1.5$), the ISF fully decorrelated, just like in F-actin networks at $R_{0.4A} = 1.5$. In this case the tracer particles are hence unconstrained by the network. However, when the mesh size was reduced to $0.3 \mu\text{m}$ (violet curve), corresponding to $R_{0.3V} = 2$, the ISF no longer fully decorrelated to zero, indicating hindrance of particle motion. When the mesh size was further reduced to $0.25 \mu\text{m}$ (black curve), corresponding to $R_{0.25V} = 2.4$, the ISF did not correlate at all on the experimental time scale, indicating particle caging. For the larger particles ($1.1 \mu\text{m}$ diameter, Figure 3.2D), we qualitatively observed a similar concentration-dependent increase in particle hindrance as the particle/mesh size ratio increased from $R_{0.5V} = 2.2$ (light pink curve) to $R_{0.4V} = 2.75$ (pink curve) and $R_{0.3V} = 3.6$ (violet curve). Altogether, these observations suggest that the theoretical mesh size estimates also provide a reasonable proxy of the average interfilament spacing for vimentin.

The trend of increased particle hindrance with increasing particle size-to-mesh size ratio is consistent between the F-actin and vimentin networks. Interestingly, however, in this series of measurements the extent of particle hindrance is larger in vimentin networks than in F-actin networks when we compare ISF curves for the same particle/mesh size ratio. Strong hindrance of the particles already occurred at particle/mesh size ratios above 2 in vimentin, whereas this required a particle/mesh size ratio of 3.6 in F-actin. This difference could of course be simply due to inaccuracies in the key assumptions (network uniformity and isotropy) or numbers (filament mass-length ratio) that enter the theoretical mesh size calculation. However, the larger hindrance by vimentin

as compared to F-actin could also be an effect of the larger flexibility of vimentin filaments (with a persistence length of 0.5-1 μm) as compared to actin filaments (with a persistence length of 10 μm). Previous microrheology measurements reporting heat maps of the probability distributions of particle positions for 1 μm particles indeed also indicated more constrained motion in vimentin (9 μM , $R_{Vimentin} = 1.6$) as compared to F-actin networks (24 μM , $R_{Actin} = 3.5$) and attributed this to the larger flexibility of vimentin filaments [215].

Finally we compared the dynamics of the single-component networks with the dynamics of composite F-actin-vimentin networks prepared at the same (theoretical) mesh size of 0.4 μm , using tracer particles with a diameter of either 0.6 μm (Figure 3.3A) or 1.1 μm (Figure 3.3B). In both cases we tested composites with two different compositions: either with F-actin being the dominant component (actin concentration 2-fold larger than the vimentin concentration, dark blue curves in Figure 3.3A and B)) or with vimentin being dominant (vimentin concentration 2.2-fold larger than the actin concentration, violet curves). We note that this series of experiments was performed with a different batch of dialyzed G-actin from the one used above. For both composites, the ISF curves are intermediate between the curves for F-actin and vimentin networks. This observation suggests that the spatiotemporal dynamics of the composite reflects a simple combination of the dynamics of the separate components. We furthermore see that for both particle sizes, the ISF decorrelated fastest for vimentin and slowest for F-actin. We note that this observation is opposite to the data presented in Figure 3.2A,B, where vimentin caused more hindrance than F-actin networks in slightly denser (mesh size of 0.4 μm) networks. In particular the particle dynamics in F-actin networks are slower in the data set in Figure 3.3A,B as compared to the data set in Figure 3.2A,B. This discrepancy reflects the pronounced variability we observed between experiments performed on F-actin networks on different days (see Appendix Figure 3.5). However, sample preparation required dialysis of the G-actin stock solution into fresh buffer (see Methods 3.7.1), which could introduce variations. For instance, differences in the activity of dithiothreitol (DTT), which is included in the buffer to prevent G-actin oxidation [333], could lead to variations in actin polymerization/depolymerization and crosslinking [334].

3.4. DISCUSSION

To better understand what are the spatiotemporal and mechanical properties that emerge from combining F-actin and vimentin filaments, we performed bulk rheology and tracer particle microrheology on *in vitro* reconstituted networks of F-actin, vimentin and composites thereof. This chapter was partly motivated by contradictory evidence from earlier studies where one study claimed that vimentin filaments bind to actin filaments via their C-terminal tails leading to mechanical enhancement in vimentin-F-actin composites [100], whereas later work concluded that the mechanical properties of vimentin-F-actin composites are a simple superposition of noninteracting networks [101]. Despite a slight batch-to-batch variability, our bulk rheology measurements indicate that F-actin-vimentin composite networks display a mechanical response that is simply a superposition of the two constituents. Consistent with this, Differential Dynamic Microscopy

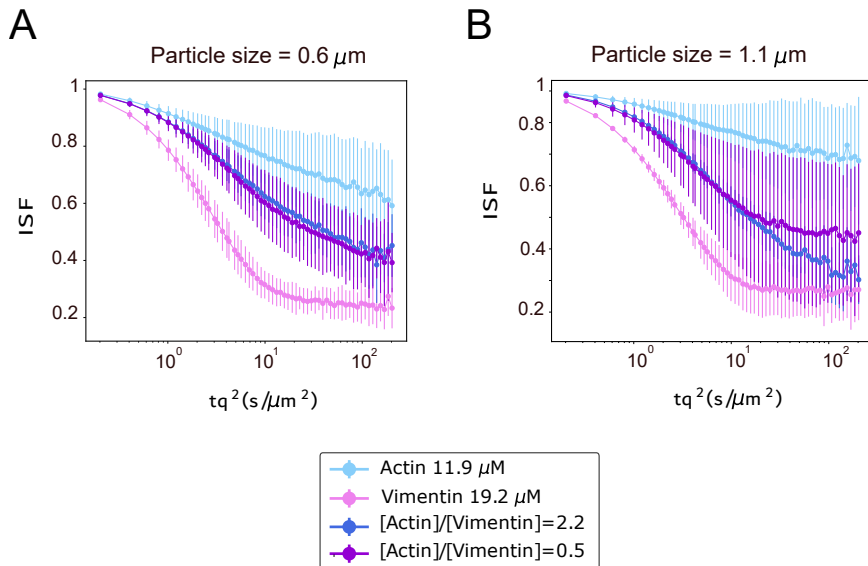


Figure 3.3: DDM data comparing the ISF curves for tracer particles embedded in either vimentin networks (pink curve), F-actin networks (blue curve), or two different composites, with either $c_{\text{actin}} > c_{\text{vimentin}}$ (dark blue curve) or $c_{\text{vimentin}} > c_{\text{actin}}$ (violet curve). In all cases, the (theoretical) average mesh size is 0.4 μm . (A) ISFs for tracer particles with a diameter of 0.6 μm . (B) ISFs for tracer particles with a diameter of 1.1 μm . All ISF curves were obtained at the same q value of 4.65 μm^{-1} . Note that the ISF is dimensionless.

(DDM) measurements showed that the dynamics of tracer particles in composite F-actin-vimentin networks was inbetween the dynamics observed in single-component F-actin or vimentin networks. Neither F-actin nor vimentin appeared to dominate the composites' dynamics, again suggesting that there is no mechanical synergy in co-entangled F-actin-vimentin composites.

Importantly, in our comparative measurements, we aimed to prepare F-actin and vimentin networks at the same mesh size, which we estimated from the monomer concentration using a calculation that assumes that the networks are uniform and isotropic. To validate this assumption, we employed Differential Dynamic Microscopy (DDM) measurements where we systematically varied the particle size and the network mesh size. We acknowledge that tracer particle mobility is an indirect measure of the network microstructure. However, unfortunately more direct measurements of the mesh size by confocal fluorescence microscopy are exceedingly challenging because the mesh sizes are comparable to the diffraction limit and actin and vimentin filaments exhibit significant thermal bending undulations. By tracking the change in mobility of the tracer particles with variations in the ratio of particle size-to-mesh size, we confirmed that the theoretically calculated mesh sizes were in reasonable agreement with the apparent mesh sizes as experienced by the tracer particles. In a series of experiments where we systematically varied the network mesh size, we found that the particles were more constrained in vimentin as compared to F-actin networks for the same the particle size/mesh size ratio, which could reflect the larger flexibility of vimentin filaments [215]. However, we

note that in a different experiment performed only at a single mesh size, the particles were more constrained by F-actin than by vimentin. This discrepancy points to experimental variability in the actin dynamics whose exact source we could not yet pinpoint.

Our conclusion that co-entangled F-actin-vimentin networks do not display any mechanical enhancement is consistent with prior rheological evidence [101] and is also supported by evidence which we will present in Chapter 4, where we visualize mixtures of actin and vimentin filaments via TIRF microscopy. It is important to remind the reader that the fact that we did not find any mechanical synergy between actin and vimentin in co-entangled composite networks does not exclude the possibility of mechanical synergy in the cell, where accessory proteins may introduce interactions.

3.5. CONCLUSION

The measurements we performed with Differential dynamic microscopy show that the spatiotemporal dynamics of the actin and vimentin composites are a superposition of the F-actin and vimentin network dynamics. Consistent with this conclusion, we found that the linear viscoelastic properties of composite networks are a simple superposition of the two networks when compared at constant mesh size. We conclude that there is no significant mechanical synergy between F-actin and vimentin in *in vitro* reconstituted networks (in the absence of crosslinking).

3.6. ACKNOWLEDGEMENTS

I would like to note that the time-lapse experiments used for the DDM analysis here presented were performed by Hannah Verwei. Also, I would like to thank Stijn Heinen for his valuable help and contribution to the Scripts for DDM data analysis. I would also like to thank Kabir Razack and Lucia Baldauf for the collaboration in our actin-vimentin project, mostly not shown here, and Jeffrey den Haan for protein purification.

3.7. MATERIALS AND METHODS

All chemicals were bought from Sigma Aldrich unless specified otherwise.

3.7.1. G-ACTIN PREPARATION

Lyophilized monomeric (G)-actin (42 kDa) isolated from rabbit skeletal muscle was procured from HYPERMOL (α -actin, cat. #: 8101-03). One milligram of the lyophilized protein was reconstituted in 250 μ M of milliQ water, resulting in a final concentration of 4 mg/mL G-actin in G-buffer with additives (namely 2 mM Tris-Cl pH 8.2, 0.4 mM ATP, 0.1 mM DTT, 0.08 mM CaCl₂ and 0.2% unspecified disaccharides). To remove the additives, we dialyzed the G-actin solution against 200 mL of G-buffer (5 mM Tris-HCl pH 7.8, 0.2 mM CaCl₂, 0.2 mM Na₂ATP, 1 mM DTT) at 4 °C overnight using a 20 kDa molecular

weight cut-off dialysis cassette (Slide-A-Lyzer™ MINI Dialysis Device, 20K MWCO, 0.5 mL, Thermo Scientific, cat. #: 88402). The following day, the dialysis buffer was replaced and the protein was dialyzed for an additional 24 hours. To remove any protein aggregates, the dialyzed G-actin was airfuged using an Air-Driven Ultracentrifuge (Beckman Coulter) at 30 psi (148,000g) for 1 hour. The rotor was pre-cooled to 4 °C, but the Airfuge itself is not actively cooled. If any pellet was observed post-centrifugation, it was resuspended and the solution was subjected to another 24 hours of dialysis in fresh G-buffer, followed by centrifugation. The final G-actin concentration was determined by measuring the UV absorbance at 290 nm using a Nanodrop spectrophotometer, assuming an extinction coefficient of $\epsilon = 0.62 \text{ cm}^{-1} \text{mg}^{-1} \text{mL}$ [335]. The dialyzed G-actin was aliquoted, snap-frozen in liquid N₂, and stored at -80 °C. Before use, snap-frozen aliquots were thawed on ice or at 4 °C for at least 2 hours.

3.7.2. VIMENTIN PURIFICATION

For vimentin purification, we refer the reader to the Methods section in Chapter 4. For experiments, about 100 μL denatured vimentin aliquots were transferred to dialysis tubing (Servapor, molecular weight cut off at 12 kDa) and vimentin was renatured by step-wise dialysis from 8 M, 6 M, 4 M, 2 M, 1 M, to 0 M urea and transferred by dialysis into sodium phosphate buffer (pH 7.0, 2.5 mM sodium phosphate, 1 mM DTT) at room temperature with at least 15 minutes for each step. The final dialysis step was performed overnight at 4 °C in 2 L of the sodium phosphate buffer. The vimentin concentration was determined by UV-VIS absorbance measurements using a molecular weight of 53.65 kDa and extinction coefficient at 280 nm of 22,450 $\text{M}^{-1} \text{cm}^{-1}$ [200].

3.7.3. TRACER PARTICLE PASSIVATION

Spherical polystyrene particles with diameters of 0.6 and 1.1 μm (Sigma Aldrich) were passivated against protein interactions according to a protocol refined by Jansen et al. [336], drawing upon a protocol devised by Kim et al. [337]. We first sonicated 15 μL aliquots of the particle suspensions for 5 minutes to disperse any aggregates. Subsequently, the suspensions were centrifuged at 16000 rcf to precipitate the particles. The pellet was isolated by aspirating the supernatant and resuspended and incubated for 10-minutes in 100 μL of a 1% (w/w) F-127 Pluronic solution (Sigma Aldrich). Next, 40 μL of anhydrous toluene (99.8%) was introduced in order to swell the beads, which facilitates insertion of the Pluronic polymers. The solution was allowed to incubate for 3 hours at room temperature on a wheel spinning at 20 rpm. The toluene was then evaporated off by placing the Eppendorf tubes in a heating block at 98 °C. To remove excess Pluronic molecules, the bead suspensions were subjected three times to a cycle of vortexing, sonication (10 min), and centrifugation (5 minutes per iteration). After each centrifugation step, the supernatant was carefully decanted and the volume was replenished with Milli-Q water to *sim* 0.5 mL. The 1.1 μm particles were prepared within one month before utilization and were stored refrigerated. The 0.6 μm particles were prepared one week to three months before use.

3.7.4. SAMPLE PREPARATION FOR DIFFERENTIAL DYNAMIC MICROSCOPY

Thin high-precision coverslips ($170 \pm 5\mu\text{m}$) and thicker coverslips underwent a rigorous cleansing procedure involving ethanol and isopropanol, followed by rinsing with Milli-Q water. Next, the coverslips were dried with a nitrogen gun. Parafilm strips were placed between the coverslips and melted using a hotplate, generating 6-8 thin rectangular imaging chambers per coverslip. These chambers were passivated with a 0.1 mg/ml solution of Poly (L-lysine) polyethylene glycol biotin (PLL-PEG-bio) in MiliQ to avert non-specific interactions with the glass surface. The passivated coverslips were stored refrigerated between 2 to 48 hours before sample loading. Prior to sample loading, the chambers were thoroughly flushed with an assembly buffer containing 40 mM Piperazine-N,N'-bis(2-ethane sulfonic acid) (PIPES) (pH=7.4), 70 mM KCl, 4 mM MgCl₂, and 1 mM EGTA.

Samples were prepared on ice in assembly buffer supplemented with 1 mM DTT and 0.5 mM MgATP. The final sample volume was standardized to 15 μL . We prepared two to three independent samples per condition, except for some controls. Particles and proteins were introduced separately in each independent replicate. For composite samples, vimentin tetramers and G-actin were homogeneously mixed in a separate Eppendorf tube before being introduced into the sample mixture. Prior to addition to the sample, particles were sonicated for 10-minutes to disperse any aggregates. The particle volume was empirically determined based on the number of particles per region of interest (ROI) observed during imaging. We aimed for a target range of 5-20 particles per ROI to prevent artifacts arising from particles moving out of frame: this range was established experimentally and does not exclude other particle concentrations to be used for the assays. Subsequently, actin and/or vimentin were introduced and the mixture was slowly but thoroughly resuspended immediately before sample loading. After sample loading into the chambers, we immediate sealed the channels with vacuum grease. Samples were incubated at room temperature in a Petri dish enveloped with wet tissues and sealed with parafilm to prevent drying. Incubation times ranged from 15 minutes to 4 hours.

Calibration samples for DDM with particles in Newtonian fluids of varying viscosity were prepared by mixing glycerol (99.9%) with Mili-Q water at different volume ratios (0, 0.5, 1, and 1.5). Particles were subsequently resuspended in the glycerol-water mixture. For samples containing only water, a higher particle volume fraction was used to counteract settling to the surface.

3.7.5. IMAGE ACQUISITION FOR DIFFERENTIAL DYNAMIC MICROSCOPY

Videos were recorded in bright field mode on an inverted Nikon Ti-Eclipse microscope utilizing a 100x oil oil immersion objective with a numerical aperture of 1.4. Videos were recorded with a CMOS camera (Hamatsu, Orca-Flash 4.0). We imaged a region of interest (ROI) with dimensions of 1024x1024 pixels. With 2x2 binning, this resulted in a final ROI of 512 x 512 pixels, corresponding to 66.56x66.56 μm . The focal plane was held in focus using the Perfect Focus option of the microscope. The objective was centered in the middle of the imaging chamber, and the image plane was positioned at least 20 μm above the surface, marked by the edge of the channel. The autoexposure time was set to 10 ms, resulting in an effective frame rate of 99.9 fps. Two to three videos, each com-

prising 5000 loops, were generated for each sample without any delay between frames. The ROI was chosen to ensure that there were at least 5 particles in view and maximum 20, as discussed in Section 3.7.4, preferably away from the edges of the field of view to ensure they stayed in view. Ideally, the imaged regions were randomly selected areas in the middle of the imaging chamber, each containing approximately 5-20 particles.

3.8. APPENDIX

3.8.1. THEORETICAL ESTIMATION OF NETWORK MESH SIZES

Consistent with earlier work exploring mechanical synergy in F-actin-vimentin composite networks [101], we decided to compare composite networks with single-polymer networks at a constant network architecture, i.e., with the same mesh size ζ and hence the same typical separation between adjacent filaments [316]. Since we were unable to measure the mesh size directly by imaging (the mesh size being smaller than the diffraction limit), we estimated the average mesh size from the protein concentrations by a simple calculation assuming that the networks are isotropic and uniform. The calculation furthermore assumes that the filaments (at least at the scale of the mesh size) are rigid rods, forming geometric cubes [338]. If the monomer molecular weight and the mass-per-unit filament length are known, the mesh size can be correlated with protein concentration, making it an experimentally adjustable parameter:

$$\zeta = \sqrt{3 \frac{m_L}{c}}, \quad (3.4)$$

where c denotes the protein monomer concentration in units of g m^{-3} . The mass-per-unit length (m_L) is $2.66 \times 10^{-11} \text{ g m}^{-1}$ for actin filaments (based on their known double-helical structure) and $5.48 \times 10^{-11} \text{ g m}^{-1}$ for vimentin (based on scanning transmission electron microscopy data [339]). Based on Equation (3.4), we can for example calculate that, to achieve a theoretical mesh size of $0.4 \mu\text{m}$, one requires $19.2 \mu\text{M}$ vimentin or $11.9 \mu\text{M}$ G-actin.

For composite F-actin-vimentin networks, we computed the average mesh size as a geometric mean of the actin and vimentin contributions [101]:

$$\begin{aligned} \zeta^{-3} &= \zeta_{\text{Actin}}^{-3} + \zeta_{\text{Vimentin}}^{-3} \\ \zeta^{-3} &= \left(\frac{3 \cdot m_{L_{\text{Actin}}}}{c_{\text{Actin}}} \right)^{-\frac{3}{2}} + \left(\frac{3 \cdot m_{L_{\text{Vimentin}}}}{x c_{\text{Actin}}} \right)^{-\frac{3}{2}} \end{aligned} \quad (3.5)$$

In order to calculate the monomer concentrations of actin (c_A) and vimentin (c_V) needed to obtain a specific mesh size from Equation 3.5, we use an additional equation to impose constraints on the ratio of c_V and c_A . Specifically we chose two conditions, $c_V = 2.2c_A$ (vimentin dominant) and $c_V = 0.5c_A$ (actin dominant). For example, to achieve an average mesh size of $0.4 \mu\text{m}$, this yields $12.5 \mu\text{M}$ vimentin with $7.2 \mu\text{M}$ actin for the first condition and $4.3 \mu\text{M}$ vimentin with $11.0 \mu\text{M}$ actin for the second condition.

3.8.2. APPENDIX TABLES AND FIGURES

Actin networks		
Particle diameter (μm)	Mesh size (μm)	Ratio Particle/Mesh size
0,6	0,3	2
0,6	0,4	1,5
0,6	0,5	1,2
Particle diameter (μm)	Mesh size (μm)	Ratio Particle/Mesh size
1,1	0,3	3,6
1,1	0,4	2,75
1,1	0,5	2,2

Table 3.1: Overview of the parameters explored in DDM experiments with different tracer particle sizes and different actin concentrations. The table shows the theoretically estimated mesh size for each actin network and corresponding particle size/mesh size ratio.

Vimentin networks		
Particle diameter (μm)	Mesh size (μm)	Ratio Particle/Mesh size
0.6	0.25	2.4
0.6	0.3	2
0.6	0.4	1.5
Particle diameter (μm)	Mesh size (μm)	Ratio Particle/Mesh size
1.1	0.3	3.6
1.1	0.4	2.75
1.1	0.5	2.2

Table 3.2: Overview of the parameters explored in DDM experiments with different tracer particle sizes and different vimentin concentrations. The table shows the theoretically estimated mesh size for each vimentin network and corresponding particle size/mesh size ratio.

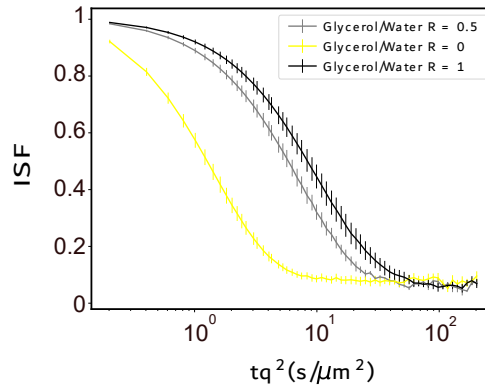


Figure 3.4: DDM data comparing the ISF curves for tracer particles ($0.6 \mu\text{m}$ of diameter) embedded in different glycerol/water ratios, used as a control of the method and to estimate particle count within the frames. The studied glycerol/water ratios are R=0 (yellow curve), R=0.5 (grey curve) and R=1 (black curve).

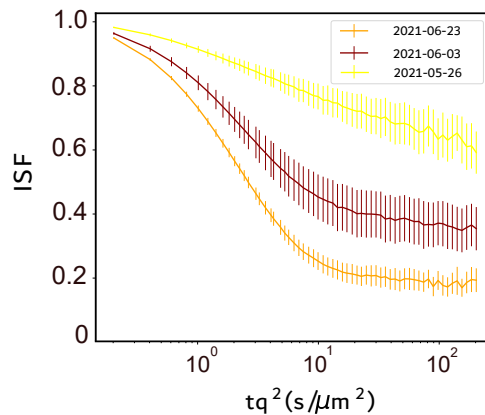


Figure 3.5: DDM data comparing the ISF curves for tracer particles ($0.6 \mu\text{m}$ of diameter) embedded in different actin networks, all with a theoretical mesh size of $0.4 \mu\text{m}$. The different datasets correspond to different dates of experiments. These are shown to display the variability issues we had regarding F-actin network dynamics. Orange curve corresponds to the data shown for the single networks (see Figure 3.2) and yellow curve corresponds to the data shown in the composite networks (see Figure 3.3).

4

CYTOLINKER-MEDIATED CROSSTALK BETWEEN ACTIN AND VIMENTIN

Cell shape and motility are determined by the cytoskeleton, an interpenetrating network of actin filaments, microtubules, and intermediate filaments. The biophysical properties of each filament type individually have been studied extensively by cell-free reconstitution. By contrast, the interactions between the three cytoskeletal networks are relatively unexplored. They are coupled via crosslinkers of the plakin family such as plectin. These are challenging proteins for reconstitution because of their giant size and multidomain structure. In this chapter we engineer a recombinant actin-vimentin crosslinker protein which we call 'ACTIF' that provides a minimal model system for plectin, recapitulating its modular design with actin-binding and intermediate filament-binding domains separated by a coiled-coil linker for dimerisation. We show by fluorescence and electron microscopy that ACTIF has a high binding affinity for vimentin and actin and creates mixed actin-vimentin bundles. Finally, we demonstrate the modularity of this approach by creating an ACTIF variant with the intermediate filament binding domain of Adenomatous Polyposis Coli. Our protein engineering approach provides a new cell-free system for the biophysical characterization of intermediate filament-binding crosslinkers and for understanding the mechanical synergy between actin and vimentin in mesenchymal cells.¹

¹This chapter's first authorship is co-authored with Quang D.Tran and was published in European Journal of Cell Biology (2024).

4.1. INTRODUCTION

THE cytoskeleton serves multiple crucial functions within mammalian cells. It defines cell shape [340], provides mechanical stability [341], drives cell movement and division [342], connects cells within tissues [343], and influences intracellular signaling processes [344]. As explained in Chapter 1, the cytoskeleton is a network of three primary types of biopolymers: actin filaments (F-actin), microtubules (MTs), and intermediate filaments (IFs), each playing distinct roles in various cellular activities. F-actin and MTs have been widely studied for their roles in regulating cell mechanics and essential processes such as cell division and migration [251]. Both biopolymers form dynamic networks that can generate forces by active (de)polymerization and by the activity of molecular motor proteins. F-actin networks drive different modes of cell migration and also drive membrane constriction in dividing cells by forming a contractile ring. At the same time, F-actin is an important determinant of cell stiffness and strength [340]. MTs build the mitotic spindle that drives chromosome segregation in dividing cells, while also contributing to the overall mechanical integrity of the cytoskeleton [251].

By contrast, much less is known about the role of IFs in cell function. Traditionally, they are considered mostly as a kind of “cellular safety belt” that protects cells against large mechanical stresses [99, 135, 345]. Indeed IFs can stretch to more than 3 times their rest length because they are built up of fibrous subunits that can unfold [346, 347]. However, in the past years, many additional non-mechanical functions of IFs have been discovered [348]. IF networks contribute to the functioning of several cellular organelles [349, 350] and regulate signaling pathways that control cell survival, growth, and differentiation [351, 288]. This raises the interesting possibility that IFs confer cell-type-specific functions. The two most well-studied IFs are keratins, expressed in non-motile epithelial cells, and vimentin, expressed in motile mesenchymal cells. Recent biophysical studies indicate that keratin and vimentin have distinct mechanical properties tailored to their cellular functions [182].

Cytoskeletal coupling is known to involve a combination of biochemical coupling via signaling loops and transcriptional regulation [352] and physical coupling via crosslinking proteins [85], motor proteins [114], and joint connections to adhesion receptor complexes in the plasma membrane [84] and to LINC complexes in the nuclear envelope [353]. This complexity makes it difficult to understand the mechanisms of cytoskeletal coupling in cells. As argued in Chapter 2, cell-free reconstitution can provide a way to overcome this challenge. In this reductionist approach, components of the cytoskeleton are purified and studied in isolation or together with a limited set of regulatory proteins. In the past, cell-free reconstitution of isolated cytoskeletal biopolymers has successfully delivered quantitative models explaining how F-actin drives cell motility [354], how MTs organize the mitotic spindle [355], and how IFs provide mechanical resilience [313]. However, coupling between different cytoskeletal subsystems has only recently begun to be investigated by reconstitution. Most of the available work has focused on F-actin/MT coordination, with studies of molecular motor motility at F-actin-MT crossings [356, 357], interdependent F-actin/MT polymerization [358, 359, 268], and mechanical synergy in F-actin/MT composites [208, 213, 360]. There are even fewer

studies of cytoskeletal composites involving IFs. A few studies have investigated the collective viscoelastic properties of two-component (IF/F-actin) [100, 211, 101] and three-component composite networks [215] and the interactions between single IFs and MTs [210]. In all these studies, the cytoskeletal filaments were combined in the absence of any cytolinkers.

There is hence a need for reconstitution studies where plectin's crosslinking role can be studied in isolation from its other functions. Unfortunately, plectin is a challenging protein for reconstitution because of its giant size (500 kDa) and multidomain structure. Full-length plectin can in principle be obtained from mammalian cells [63], but it is difficult to obtain proteins in high yield and purity using this strategy.

Here we engineer a recombinant actin-vimentin crosslinker that we call 'ACTIF', which is designed to crosslink F-actin and IFs in a similar manner as plectin. The engineered linker has a modular design with an N-terminal Green Fluorescent Protein (GFP) tag and actin-binding domain, a C-terminal IF-binding domain, and a coiled-coil linker to induce parallel dimerisation. Its small (138 kDa) size allows for convenient recombinant expression in bacteria. We demonstrate by imaging and rheology that ACTIF with the plectin intermediate filament binding domain (IFBD) efficiently crosslinks vimentin intermediate filaments to F-actin. Using Total Internal Reflection Fluorescence (TIRF) imaging, we quantitatively characterize the binding kinetics for the plectin-derived ACTIF crosslinker. Finally, we demonstrate the modularity of our approach by creating an alternative ACTIF variant with an IFBD based on the armadillo repeats of the tumor suppressor protein Adenomatous Polyposis Coli (APC) [257]. Our work provides a powerful new reconstitution platform to study the biophysical mechanisms that contribute to the functional coupling of the F-actin and IF cytoskeleton that controls cell mechanics and migration.

4.2. RESULTS

ACTIF CROSSLINKS F-ACTIN AND VIMENTIN AND MEDIATES CO-LOCALIZATION

Full-length plectin (Fig. 4.1(top)) is a giant (> 500 kDa) multidomain cytolinker protein [61]. The isoform-specific N-terminal head domain (indicated by a star in Fig. 4.1, top schematic) is followed by the actin-binding domain (ABD), an elongated plakin domain [361, 362, 363], a central alpha-helical rod domain (200 nm long) that mediates plectin dimerization, six tandemly arranged plakin repeat domains (PRDs, ~300 residues each) separated by linker regions of variable length, and finally, a short tail region containing Gly-Ser-Arg (GSR) repeats. The first four PRD domains do not contribute to IF-binding [364, 365]. The last two PRD domains contribute together with the PRD5-PRD6 linker region (~50 residues) and the GSR-containing C-terminal extremity to ensure efficient IF binding [59]. The linker region is essential but not sufficient for strong IF-binding [364, 76, 59]. In addition, a sequence of approximately 50 amino acid residues (4262-4316) within one-third of the PRD5 is indispensable for filament association [364].

We generated a minimal crosslinker protein designed to model the crosslinking activity of plectin (Fig. 1 (bottom)), which we call ACTIF. We based the design on an earlier

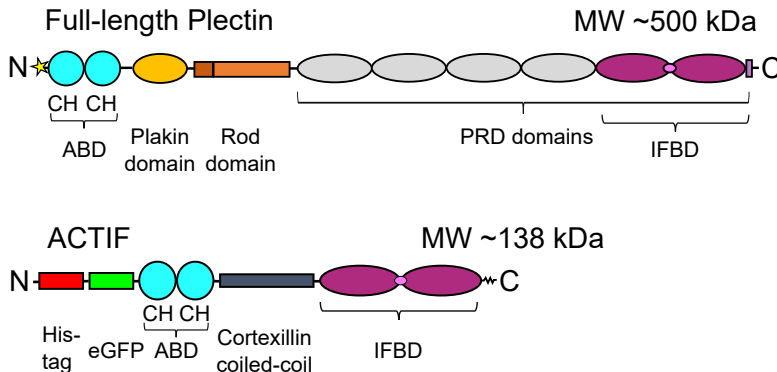


Figure 4.1: (Top) Domain structure of full-length plectin. (Bottom) Domain structure of ACTIF with the actin binding domain (ABD) composed of tandem calponin homology (CH) domains from MACF and the intermediate filament binding domain (IFBD) from plectin. Note that plectin has a larger spacer consisting of a plakin domain, rod domain, and plectin repeat (PRD) domains. These domains are replaced altogether by a cortexillin coiled-coil domain in ACTIF. The star in the top schematic stands for plectin's isoform-specific head domain. The approximate molecular weight (MW) of both proteins is specified above the schematics.

engineered cytolinker called TipAct that models the actin-microtubule cytolinker protein MACF/ACF7 [359, 268]. The TipAct protein consisted of an N-terminal green fluorescent protein (GFP) tag, followed by the F-actin binding domain of MACF, a coiled-coil spacer domain, and a C-terminal microtubule-binding domain. We retained this domain structure but replaced the microtubule-binding domain with the C-terminal intermediate filament binding domain (IFBD) of plectin. To ensure robust IF-binding, we included the last two PRD domains (PRD5 and PRD6) and their connecting linker [364]. The ABD from MACF consists of a tandem of two calponin-homology (CH) domains and resembles the ABD of plectin [73, 366, 367]. The coiled-coil spacer domain separating the ABD and IFBD was taken from cortexillin I, in order to mimic plectin's dimeric state by inducing parallel dimerization of ACTIF [368]. By removing the large plakin rod and the first four PRD domains of plectin, we obtained an actin-IF cytolinker protein with a molecular weight of only 138 kDa, enabling us to express the protein in bacteria.

We first tested the purity and oligomeric state of the purified ACTIF protein. To test the protein purity, we performed SDS-PAGE analysis after the final gel filtration chromatography step (see Appendix Figure 4.13). As shown in Fig. 4.2A, the SDS-PAGE gel shows a major band localized at the expected molecular weight of 138 kDa and smaller bands indicative of protein degradation. Densitometry analysis showed that full length ACTIF made up 64% of the protein preparation (Appendix Figure 4.14).

To test whether the smaller molecular weight products are degradation products of ACTIF, we tested for the presence of the N-terminal eGFP tag in the bands by fluorescence imaging of the gels using a Typhoon imager (Appendix Figure 4.15) and by Western blot analysis using antibodies to detect GFP (Appendix Figure 4.16). Both experiments showed that all the proteins present in the ACTIF preparation contained eGFP, indicating that the lower molecular weight products are indeed degradation products of ACTIF.

Finally, we performed liquid chromatography–mass spectrometry (LC–MS) analysis of the ACTIF preparation (Appendix Figure 4.17). This analysis confirmed that the most

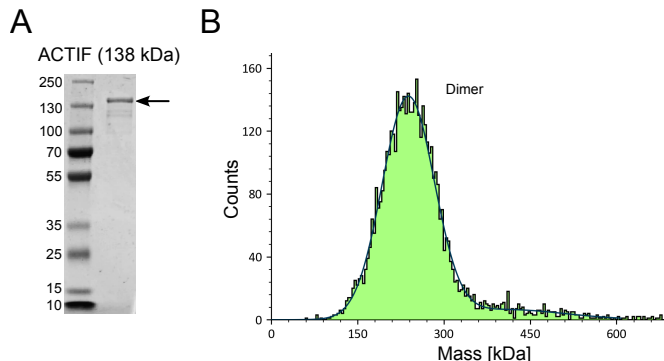


Figure 4.2: (A) SDS-PAGE of ACTIF purification after gel filtration. 10 μ L of proteins at 10 μ M were loaded and stained with InstantBlue Coomassie Protein Stain for polyacrylamide gels. (B) Interferometric scattering microscopy (iSCAT) of ACTIF preparation (50 nM in F-buffer buffer) shows a peak at a molecular weight of 243 kDa, indicating that ACTIF forms a dimer.

abundant protein in the sample had a molecular weight compatible with the expected value for ACTIF at 138,747 Da, with a precision of about 1 Da. Putative identification of some of the mass peaks allowed us to identify ACTIF fragments, consistent with the conclusion from Typhoon and Western blot analysis that these proteins result from partial proteolysis of ACTIF. To check the oligomeric state of the ACTIF protein in solution, we performed interferometric scattering (iSCAT) microscopy [369]. With iSCAT the light scattering of molecules near a surface is amplified with reference light, typically the reflection of the laser on the bottom of the glass slide (Appendix Figure 4.12). Background subtraction makes it possible to detect the molecules landing on or moving away from the surface. The detected signal is directly proportional to the molecular weight of the proteins [369]. As shown in Fig. 4.4C), the mass histogram confirms that the crosslinker is dimeric, as shown by the peak of 98% of signal counts being centered around 243 ± 73 kDa, about twice the molecular weight of the monomer. Note that this peak likely includes dimers of full length ACTIF as well as dimers of the degradation products.

Before testing the crosslinking activity of ACTIF, we first wanted to test whether F-actin and vimentin have any direct interactions under our experimental conditions. This idea was motivated by earlier findings that vimentin can bind F-actin with its C-terminal tails [100]. To test for interactions, we used a TIRF microscopy assay (Fig. 4.3A). We prepared a microfluidic flow chamber made of coverglass treated with vimentin antibodies that securely trap vimentin filaments, and with passivation agents including pluronic F127 and bovine serum albumin (BSA), to prevent unwanted protein binding to the substrate. Pre-assembled vimentin filaments fluorescently labeled with Alexa Fluor 555 were next introduced into the chamber and allowed to adhere to the substrate. Next, we flowed in ATTO-647-labeled G-actin monomers in F-buffer supplemented with 0.2 % methylcellulose, to polymerize F-actin directly in the chamber. Methylcellulose was used to force the growing F-actin filaments close to the substrate with vimentin. As shown in Fig. 4.3B, we did not observe any signs of co-localization between F-actin

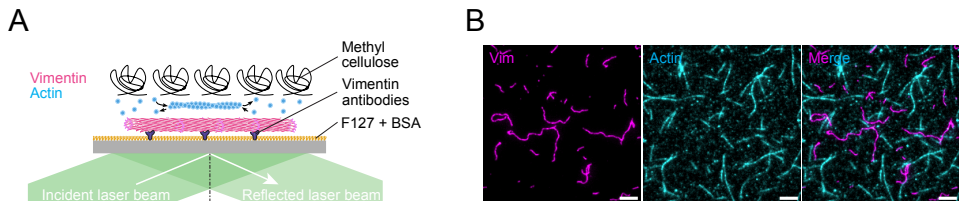


Figure 4.3: (A) Schematic of control experiment with TIRF microscopy to probe for interactions between vimentin filaments, immobilized on the microscope coverslip using vimentin antibodies, and F-actin polymerized from 1 μ M G-actin in solution. Methylcellulose (0.2 %) was added to push F-actin down toward the surface. (B) Images showing no co-localization between the filaments, suggesting there are no interactions.

and the fixed vimentin filaments from the beginning of the F-actin polymerization until they became long filaments. Time-lapse movies confirmed that the F-actin filaments are freely moving (Supporting Movie S1). We conclude that vimentin and F-actin do not interact directly under the conditions of our assay. Moreover, since G-actin co-existed with F-actin during the *in situ* assembly, the absence of colocalization of actin and vimentin signals suggested that neither G-actin nor F-actin bind vimentin filaments in our experimental conditions, although we cannot rule out that transient weak interaction may take place.

Having established that vimentin and F-actin do not significantly interact, we could then test whether ACTIF induces interactions. We again used a TIRF imaging assay where we sequentially flushed in the different components (Fig. 4.4A). We first flushed in 37 nM of pre-assembled vimentin and allowed these filaments to adhere to the vimentin antibodies on the substrate. We previously showed that vimentin attachment to a glass surface through antibodies has minor impact on the structural organization of the filaments [183]. When we next flushed in 5.3 nM of ACTIF, we observed that it rapidly bound to the vimentin filaments as seen by co-localization (Fig. 4.4B (middle)). Finally, we flushed in 0.1 μ M of pre-assembled F-actin. Note that as the F-actin was diluted 100-fold just before use from a stock solution of 10 μ M F-actin pre-polymerized for 1 h, we assumed the concentration of G-actin to be in the nM range (100 times smaller than the critical concentration for actin polymerization), thus providing minimal contribution to the fluorescent signal in the actin channel.

Over time, we observed that the actin filaments settled and remained on top of the vimentin filaments (Fig. 4.4B (right)). At steady state, F-actin, vimentin, and ACTIF co-localized, as shown in the merged image (Fig. 4.4B (far right)). Following the maximum intensity of the F-actin signal along a cross-section drawn perpendicularly to the vimentin filaments, we could follow the time evolution of successive F-actin binding events, which appeared as intensity steps (Fig. 4.4C). By quantifying pixel fluorescence intensities in the F-actin channel along vimentin filaments at steady states (\sim 150 filaments from 2 independent experiments), we observed a complex distribution with multiple peaks indicating the presence of multiple actin filaments (Fig. 4.4D), different from the single peak distribution obtained with vimentin only (Appendix Figure 4.18). As the intensity of the first peak matched the intensity expected for single F-actin, we estimated that an average of 3 actin filaments and up to 7 actin filaments could bind a vimentin fil-

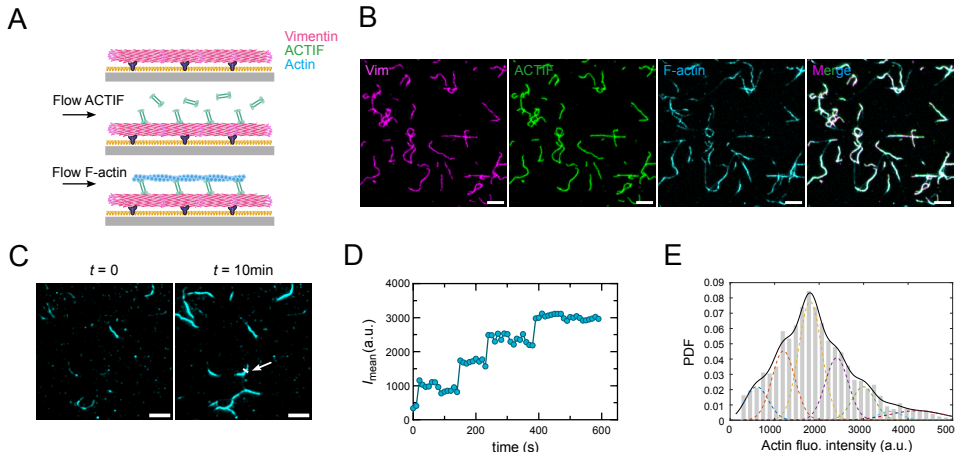


Figure 4.4: (A) Schematic of sequential steps in the TIRF experiments to probe ACTIF-mediated binding of F-actin to vimentin filaments (left). First ACTIF preparation (5 nM in F-buffer) was flushed into the channel containing surface-bound vimentin filaments for 15 min. Next pre-formed F-actin (0.1 μM in F-buffer) was flushed in. (B) Images showing vimentin-ACTIF-F-actin colocalization (C) Images of F-actin attachment over time on top of ACTIF-bound vimentin filaments. (D) Mean intensity over time of a representative F-actin at the cross-section marked by the white line in (C), showing multiple actin filaments recruited on top of ACTIF-bound vimentin. (E) Distribution of pixel fluorescence intensities in the F-actin channel along vimentin filaments (~ 150 filaments from 2 independent experiments) at steady state. The probability distribution function (PDF) was fitted by a multiple Gaussian, with the peak positions constrained to be multiples of the position of the first peak, and common width for all the peaks except the last one. The first peak was estimated at an intensity ~ 600 , as expected for single F-actin imaged in similar conditions. Scale bar: 5 μm .

ament through ACTIF crosslinking at steady state (Fig. 4.4E). These observations prove that ACTIF is capable of binding both F-actin and vimentin and of crosslinking the two filament types.

ACTIF ROBUSTLY BINDS AND COUPLES VIMENTIN AND F-ACTIN FILAMENTS

We performed a series of TIRF microscopy assays to validate the efficiency of ACTIF in crosslinking actin and vimentin filaments in real-time. In the similar TIRF microscopy and flow chamber setup as shown in Fig. 4.4(A and B), we flowed ACTIF at a low concentration of $c \approx 5$ nM into a channel with surface-bound vimentin filaments (Fig. 4.5A). We observed rapid co-localization of ACTIF with vimentin within 10 min (Fig. 4.5B). Using the coloc 2 plugin from Fiji, we quantified the colocalization between the different components and obtained Manders coefficients of $M1 = 0.978$ and $M2 = 0.984$ for the colocalization of ACTIF vs. vimentin and $M1 = 0.972$ and $M2 = 0.987$ for the colocalization of F-actin and vimentin. Fluorescence quantification showed that ACTIF bound to vimentin with a reaction rate $K \approx 0.0140 \pm 0.0024 \text{ s}^{-1}$ (mean \pm SD, averaged over 3 independent repeats) obtained by fitting the kinetics of association with a single exponential (Fig. 4.5D).

Once the ACTIF signal reached a steady state (after 10 minutes), we performed a Fluorescence Recovery After Photobleaching (FRAP) assay (Fig. 4.5A) to measure the ACTIF

unbinding rate, assuming that the recovery is reaction-limited [370]. As shown in Fig. 4.5C and quantified in Fig. 4.5E, we observed about 30 % of ACTIF is mobile ($N = 3$ independent repeats). We presume that the mobile fraction corresponds to dimeric ACTIF and the immobile fraction to higher oligomerization of ACTIF induced by attachment to vimentin, which increases protein avidity. By fitting the recovery curve to a single exponential, we estimated the unbinding rate of the mobile fraction of ACTIF from vimentin filaments of $k_{\text{off}} \approx 0.0032 \pm 0.0012 \text{ s}^{-1}$ (mean \pm SD, $N = 3$ repeats). Moreover, according to densitometry and Typhoon assays (Appendix Figure 4.14 and 4.15), only 64 % of the ACTIF preparation was full-length with a functional IFBD domain, which reduced the binding efficiency of ACTIF on vimentin filaments. With the assumption of a first-order reaction with binding efficiency of 65 % and assuming that 30 % of ACTIF is mobile, the rate K of association kinetics can be approximated by: $K = 0.65 k_{\text{on}} c + f_m k_{\text{off}}$, where k_{on} is the binding rate and f_m is the mobile fraction. From the concentration c , the rate K and the unbinding rate k_{off} estimated by FRAP, we estimated the binding rate of ACTIF to vimentin $k_{\text{on}} \approx (3.7 \pm 0.7) \cdot 10^6 \text{ M}^{-1}\text{s}^{-1}$ (mean \pm SD, $N = 3$ repeats), and the affinity described by a dissociation equilibrium constant $K_d \approx 0.9 \pm 0.4 \text{ nM}$ ($N = 3$ repeats).

We next tested the F-actin crosslinking ability of the vimentin-bound ACTIF by flowing in pre-assembled F-actin in a buffer without methylcellulose. We observed that the F-actin filaments quickly attached and localized along vimentin filaments, forming composites of F-actin-ACTIF-vimentin (Fig. 4.6A). Interestingly, once the composites were established, ACTIF was fixed inside the composites as its fluorescence intensity remained constant over time when we flushed in a solution that contained F-actin but no ACTIF (Fig. 4.6B, green curve). We verified that ACTIF partially dissociated from vimentin in the absence of F-actin when the ACTIF soluble pool was flushed out (Fig. 4.6B, orange curve), indicating that ACTIF is stabilized on vimentin through its binding to actin. Note that this experiment also demonstrates that the incomplete fluorescence recovery seen in FRAP experiments is not due to any protein alteration by bleaching. Our findings suggest strong binding of ACTIF to vimentin filaments and stable crosslinking between vimentin and F-actin filaments.

To study the binding and unbinding rates of ACTIF on F-actin, we modified the experimental setup by immobilizing pre-assembled biotinylated actin filaments on the surface of the flow chamber, which had been coated with neutravidin, and the passivation agents F127 and BSA, respectively. Next, we flowed in ACTIF to characterize the kinetics of association to F-actin, then performed FRAP to measure the unbinding rate from F-actin and deduce the binding rate to F-actin, and finally flowed in vimentin filaments to create F-actin-ACTIF-vimentin composites (Fig. 4.7A and Figure 4.8A). When we flowed in ACTIF at the same concentration of $\sim 5 \text{ nM}$, as in the earlier experiment with immobilized vimentin, we did not observe any signs of binding to the immobilized F-actin (Fig. 4.7(B (Top), D) after 10 minutes. To our surprise, we needed to flow in $c \approx 500 \text{ nM}$ of ACTIF to achieve a final ACTIF fluorescence intensity equivalent to its intensity on vimentin achieved with a 100-fold lower ACTIF concentration (Fig. 4.7B(Bottom)). Although it is expected that the number of binding sites for ACTIF on F-actin is not the same as that on vimentin (see Discussion), the difference by a factor of 100 in concentration indicates the binding rate is much lower on actin than on vimentin. By fitting the time-dependent increase of the ACTIF fluorescence intensity to

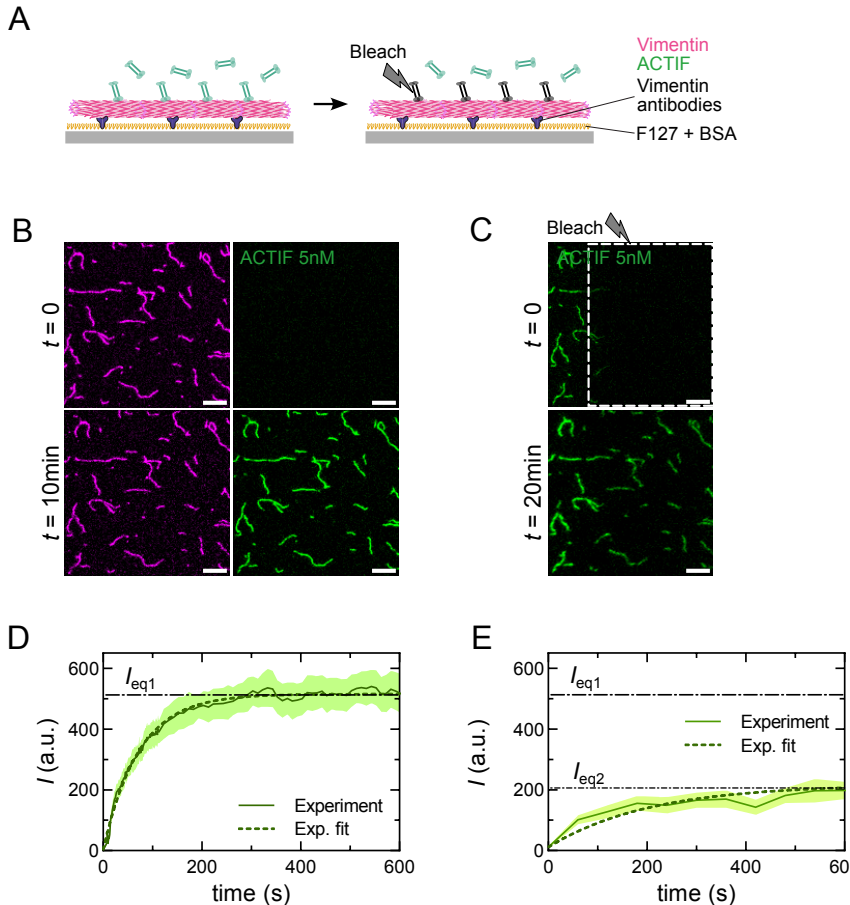


Figure 4.5: TIRF microscopy experiment to elucidate the crosslinking efficiency of ACTIF. A) Assay to measure the binding rate of ACTIF to surface-bound vimentin by imaging (left) and the unbinding rate by FRAP (right). B) Still images at $t = 0$, directly after flushing in 5 nM ACTIF preparation, and at $t = 10\text{ min}$, showing ACTIF (green) co-localizing with vimentin filaments (magenta). C) Images showing the recovery of ACTIF fluorescence at $t = 20\text{ min}$ after photobleaching the region boxed by white dashed lines at $t = 0$. D) Mean fluorescence intensity of ACTIF on vimentin filaments (averaged over 30 filaments) over time, obtained from the representative repeat shown in B. The data is fitted by an exponential equation, $I = I_{\text{eq}1}(1 - e^{-Kt})$. E) Recovery of fluorescence intensity of ACTIF on vimentin filaments (mean fluorescence averaged over 30 filaments) over time after photobleaching, obtained from the representative repeat shown in C. The data is fitted by an exponential equation, $I = I_{\text{eq}2}(1 - e^{-k_{\text{off}}t})$.

a single exponential, we obtained a reaction rate $K \approx 0.0080 \pm 0.0013\text{ s}^{-1}$ (mean \pm SD, $N = 3$ repeats) (Fig. 4.7D). FRAP measurements on the actin-bound ACTIF allowed us to estimate the mobile ACTIF unbinding rate of $k_{\text{off}} \approx 0.0064 \pm 0.0011\text{ s}^{-1}$ from F-actin, and a mobile fraction of about 48 % ($N = 3$) (Fig. 4.7C, E). The binding efficiency of ACTIF on F-actin is not affected by the 65 % purity of the protein since the ABD domain on the N-terminus is always intact (See Appendix Figure 4.15). Hence, the association kinetics

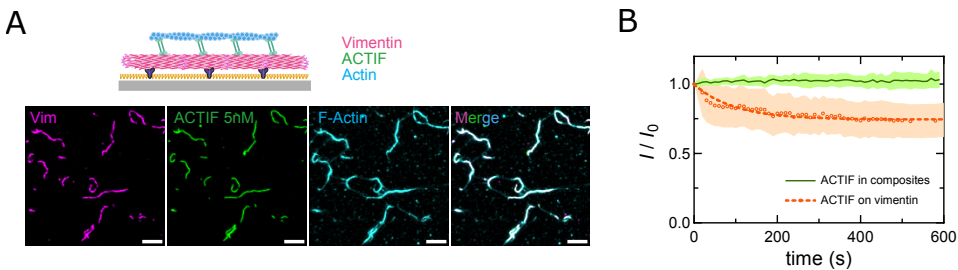


Figure 4.6: (A) Assay and images of steady-state vimentin-ACTIF-F-actin composites with surface-bound vimentin. (B) Normalized fluorescence intensity of ACTIF in the actin-vimentin composites (green) over time after flushing in a solution containing F-actin but no ACTIF (averaged over 30 and 50 filaments respectively).

(at $t = 0$), and on vimentin (orange) over time after flushing out solution-phase ACTIF (averaged over 30 and 50 filaments respectively).

Table 4.1: Summary of (un)binding rate constants and affinities of ACTIF towards vimentin and actin filaments measured by TIRF imaging and FRAP assays. Values shown in Repeat 1-3 are means averaged over 30 filaments calculated for each independent repeat experiment. The combined “Mean \pm SD” represents the averaged mean from 3 repeats with SD being the standard deviation of the means.

	Repeat #	K (s^{-1})	k_{on} ($\text{M}^{-1} \text{s}^{-1}$)	% mobile f_m	Mobile fraction	
					k_{off} (s^{-1})	K_d (nM)
ACTIF on vimentin $c = 5.3 \text{ nM}$	1	0.0111	$3.1 \cdot 10^6$	25 %	0.0023	0.75
	2	0.0170	$4.7 \cdot 10^6$	27 %	0.0025	0.53
	3	0.0138	$3.4 \cdot 10^6$	40 %	0.0049	1.43
	Mean \pm SD	0.0140 ± 0.0024	$(3.7 \pm 0.7) \cdot 10^6$	$(31 \pm 7) \%$	0.0032 ± 0.0012	0.9 ± 0.4
ACTIF on F-actin $c = 530 \text{ nM}$	1	0.0079	$7.7 \cdot 10^3$	56 %	0.0068	883
	2	0.0096	$13.6 \cdot 10^3$	32 %	0.0075	551
	3	0.0065	$7.2 \cdot 10^3$	55 %	0.0049	681
	Mean \pm SD	0.0080 ± 0.0013	$(9.5 \pm 2.9) \cdot 10^3$	$(48 \pm 11) \%$	0.0064 ± 0.0011	705 ± 137

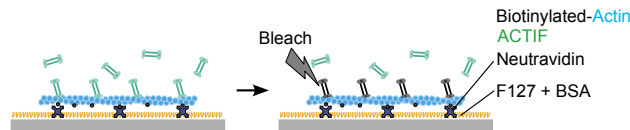
of ACTIF on F-actin is estimated by $K = k_{\text{on}} c + f_m k_{\text{off}}$. From the values of K , c , k_{off} and f_m , we estimated the binding rate to F-actin $k_{\text{on}} \approx (9.5 \pm 2.9) \cdot 10^3 \text{ M}^{-1} \text{s}^{-1}$ and the affinity to F-actin described by $K_d \approx 705 \pm 137 \text{ nM}$.

When we finally flushed in pre-assembled vimentin filaments, we again obtained colocalization of the vimentin filaments with the ACTIF-saturated F-actin, reaffirming the robust formation of the composite (Fig. 4.8A). Time-lapse imaging also again showed the ACTIF signal in the composite structure to be constant, even though no ACTIF was supplied in the solution (Fig. 4.8B). Overall, our results indicate the binding of ACTIF to F-actin is about 700 times lower than its affinity to vimentin (summary in Table 4.1).

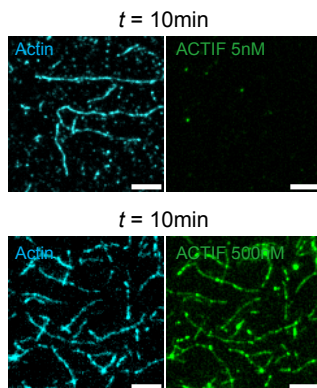
THE PLECTIN IFBD INDUCES VIMENTIN BUNDLING

To test whether the isolated plectin IFBD domain is capable of binding or bundling vimentin, we expressed and purified this domain, comprising PRD 5 and PRD 6 and the intervening linker region that provides the major IF-binding site of plectin [364]. iSCAT imaging showed the isolated IFBD to form mostly monomers with a small (13%) fraction

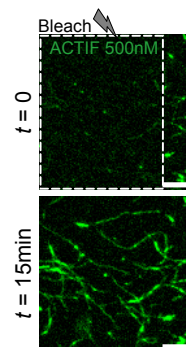
A



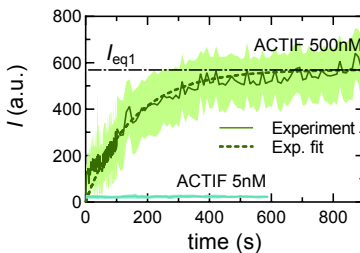
B



C



D



E

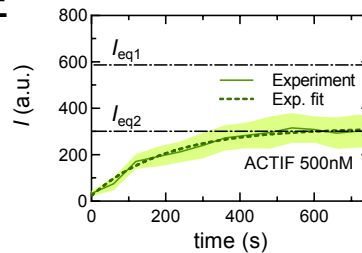


Figure 4.7: (A) Assay to measure the binding rate of ACTIF to surface-bound F-actin by imaging (left) and the unbinding rate by FRAP (right). I, (B) Images of ACTIF (green) co-localizing with actin filaments (cyan) at $t = 10$ min after flushing in ACTIF at a concentration of ~ 5 nM (Top) and ~ 500 nM (Bottom). (C) Images showing the recovery of ACTIF fluorescence at 500 nM on F-actin at $t = 15$ min after photobleaching the region boxed by white dashed lines at $t = 0$. (D) Fluorescence intensity of ACTIF preparation at concentrations of 5 nM and 500 nM on F-actin (both conditions averaged over 30 filaments) over time. The data is fitted by an exponential equation, $I = I_{\text{eq}1} (1 - e^{-Kt})$. (E) Recovery of fluorescence intensity of ACTIF preparation at 500 nM on F-actin (averaged over 30 filaments) over time after photobleaching. The data is fitted by an exponential equation, $I = I_{\text{eq}2} (1 - e^{-k_{\text{off}}t})$.

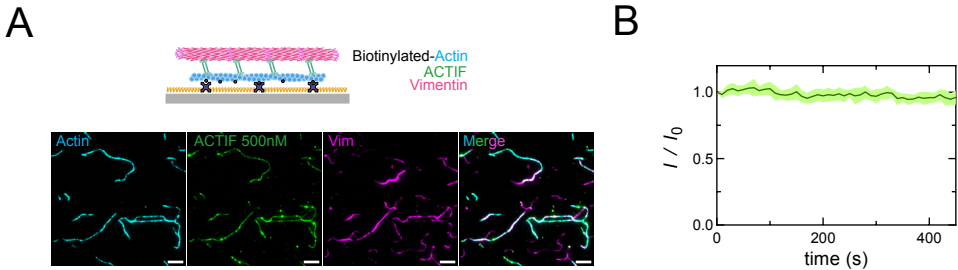


Figure 4.8: (A) Assay and images of steady-state actin-ACTIF-vimentin composites with surface-bound F-actin. (B) Normalized fluorescence intensity of ACTIF in the composites over time, after flushing in F-actin while flushing out solution-phase ACTIF at $t = 0$ (averaged over 30 filaments). Shaded areas in all the graphs show the standard deviations over 30 to 50 filaments. Dashed lines show exponential fits for the kinetics of association and for FRAP recovery curves. Scale bars: 5 μ m.

of dimers (Appendix Figure 4.19A) and SDS-PAGE analysis showed a major band at the expected molecular weight of 71 kDa (Appendix Figure 4.19B). Next, we co-polymerized the IFBD with vimentin filaments at different IFBD:vimentin molar ratios, always keeping the vimentin molar concentration fixed at 4 μ M, and imaged the mixtures by electron microscopy (EM). EM provides higher spatial resolution than TIRF imaging and allows us to resolve filament and bundle morphologies and widths.

Vimentin filaments reconstituted in the absence of the IFBD were visible in EM images as semiflexible filaments (Fig. 4.9A (left)). To determine the filament widths, we plotted intensity profiles perpendicular to the segment of interest at multiple locations along the filament contours. We then measured the width of the bright area between the darker borders, which corresponds to the filament diameter. We observed an average filament width of ~ 10 nm (Appendix Figure 4.20), in agreement with previous literature [371]. Surprisingly, when vimentin was co-polymerized with the IFBD at a molar ratio of IFBD:vimentin of 1:10 (0.4 μ M of IFBD), it formed thin bundles (see Fig. 4.9A (middle)). Bundles often contained around three to four distinguishable filaments. Using the same procedure as described above to determine the bundle widths, we found that the bundles had a variable width with an average bundle size of 33 ± 12 nm (Fig. 4.9B). Upon increasing the IFBD:vimentin molar ratio to 1:1 (4 μ M of IFBD), vimentin filaments formed straight and well-aligned bundles (Fig. 4.9A (right)) of an average diameter of 58 ± 22 nm (Fig. 4.9B). The bundles formed at a 1:1 IFBD:vimentin ratio were significantly thicker than those formed at a 1:10 ratio ($p < 0.0001$, calculated by a statistical unpaired t-test). We conclude that the IFBD domain can by itself bundle vimentin filaments at high (> 400 nM) concentrations. Presumably, bundling requires dimerization or clustering of the IFBD domain, which we showed to be mostly monomeric (with only 13 % dimeric) in iSCAT measurements performed at a concentration of 40 nM (Appendix Figure 4.19A). Potentially, at the high (> 400 nM) concentrations used in the EM assays, the IFBD domain can oligomerize even more. As a control, we also tested co-polymerized actin and IFBD. In this case, EM images showed no signs of actin bundling, but plectin was present in the form of dense globular structures, suggesting that the IFBD can cluster at high concentrations (Appendix Figure 4.22).

ACTIF FORMS BUNDLES OF F-ACTIN AND VIMENTIN FILAMENTS

With the certainty based on EM data that the IFBD from plectin can bind vimentin filaments, we next imaged mixtures of F-actin and vimentin filaments with and without ACTIF, always keeping the monomer concentrations at 1 μM for actin and 1 μM for vimentin. In the absence of ACTIF, actin filaments can be distinguished from vimentin filaments by their smaller diameter (8 nm vs 10 nm) [371]) and by their larger persistence length (10 μm vs 1 μm [371]). As shown in Figure 4.9 C(left) and Supplemental Figure 4.23, the two filament types can indeed be easily distinguished.

Upon adding ACTIF in a molar ratio of 1:100 to the sum of the vimentin and actin molar concentrations, we found that tightly packed bundles formed (Fig. 4.9C (middle)) with an average diameter of 66 ± 34 nm (Fig. 4.9D). Note that bundling of actin and vimentin by ACTIF occurs at a much lower crosslinker:monomer ratio than bundling of vimentin by the IFBD domain, consistent with ACTIF being a parallel dimer presenting two actin-binding domains on one end and two IF-binding domains on the other end.

At a ten-fold larger ACTIF:monomer ratio of 1:10 (0.2 μM of ACTIF), even thicker bundles were observed that consisted of a larger number of filaments (Fig. 4.9C (right)). The average bundle size was significantly larger (131 ± 66 nm) than for the bundles formed at the 1:100 molar ratio (Fig. 4.9D), $p < 0.00001$. Interestingly, the bundle widths showed an apparently bimodal distribution at the 1:10 ACTIF:monomer ratio, with the first peak centered around a similar width of 70 nm as observed at 1:100. This observation suggests a hierarchical bundling process, where thinner bundles can get connected into thicker bundles. Many bundles were too dense to observe their constituent filaments, but in some cases we could observe bundles clearly consisting of a mixture of actin and vimentin filaments (Appendix Figure 4.24A), some bundles eventually splitting into two or more sub-bundles (Appendix Figure 4.24B) and some bundles apparently consisting only of actin filaments (Appendix Figure 4.24C).

We note that the presence of 36 % of truncated ACTIF that does not bind vimentin may impact the morphology and composition of actin bundles. We furthermore conclude that ACTIF drives the formation of mixed actin-vimentin bundles in a concentration-dependent manner.

COMPOSITE F-ACTIN/VIMENTIN NETWORKS STIFFEN UPON CROSSLINKING WITH ACTIF

To test whether ACTIF is capable of crosslinking F-actin and vimentin in dense networks, we used shear rheology to measure the viscoelastic properties of composite networks formed with or without ACTIF. The viscoelastic response of cytoskeletal networks is known to be sensitive to the presence of crosslinkers, which tend to enhance the elastic modulus and suppress viscous dissipation [372]. We polymerized actin (24 μM), vimentin (18 μM), or composite actin-vimentin networks between the plates of a rheometer. We did not observe any major differences in the polymerization kinetics between one-component versus two-component networks (Appendix Figure 4.25). After 2 hours, when network formation was completed, we measured the linear viscoelastic response by applying small amplitude oscillatory shear with a strain amplitude of 1% while varying the frequency logarithmically between 0.001 and 10 Hz. We determined the network

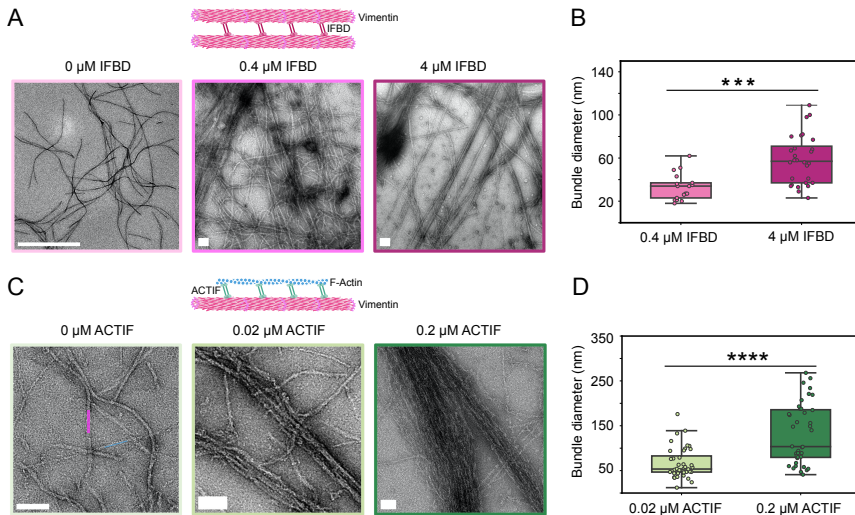


Figure 4.9: Electron microscopy (EM) to test binding and crosslinking activities of ACTIF preparation and its plectin IFBD. A) EM images of reconstituted vimentin filaments alone (left) or co-polymerized with 0.4 μM (middle) or 4 μM (right) of IFBD (schematic on top). Enlarged versions are shown in Appendix Figure 4.21). Corresponding box plots of vimentin bundle widths, with 17 bundles measured for 0.4 μM of IFBD and 28 bundles measured for 4 μM of IFBD. Two independent sample replicates per condition were imaged.. *** $p < 0.001$ from unpaired t -test. C) EM images of co-polymerized F-actin (cyan) and vimentin filaments (pink) without ACTIF preparation (left) or with 0.02 μM (middle) or 0.2 μM (right) of ACTIF preparation (schematic on top). D) Corresponding box plots of the F-actin/vimentin co-bundles. **** $p < 0.0001$ from unpaired t -test. For both conditions, 40 bundles were measured. Two independent sample replicates per condition were imaged.

elastic (storage) shear modulus, G' , and viscous (loss) modulus, G'' , from the stress response. In the absence of ACTIF, the composite networks had a small elastic modulus of order ~ 10 Pa that increased very weakly as an approximate power law with frequency with an exponent of 0.07 (grey curve in Fig. 4.10A). In the presence of ACTIF (4.2 μM), the networks were more than an order of magnitude stiffer (green curve in Fig. 4.10A), as summarized in Fig. 4.10B. The frequency dependence for the crosslinked network again followed a weak power law with an exponent of 0.07. Simultaneously, the network with ACTIF was more solid-like, as characterized by a smaller loss tangent, $\tan(\delta) = \frac{G''}{G'}$, compared to the corresponding network without ACTIF (Fig. 4.10B)). The rheology measurements hence prove that ACTIF crosslinks the composite network.

To test whether there is mechanical synergy upon combining actin and vimentin, we also performed rheology measurements for isolated actin networks (blue curve in Fig. 4.10A) and vimentin networks (pink curve in Fig. 4.10A). The stiffness of the actin/vimentin composite network formed without ACTIF was approximately equal to the sum of the elastic moduli of the two isolated networks (Fig. 4.10A). Interestingly, when actin was polymerized in the presence of ACTIF (4.2 μM), it formed stiffer networks than in the absence of ACTIF (Appendix Figure 4.26A), indicating that ACTIF is capable of crosslinking actin filaments. By contrast, when vimentin was polymerized in the presence of ACTIF,

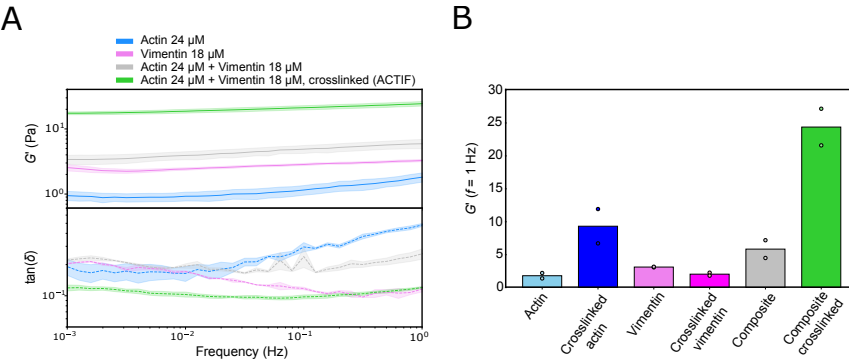


Figure 4.10: Rheology on crosslinked actin and vimentin composites via ACTIF. (A) (Top) Frequency dependence of the storage modulus of crosslinked (green) and non-crosslinked (grey) actin/vimentin composite networks and of one-component actin (blue) or vimentin (pink) networks. Protein concentrations: 24 μ M F-actin, 18 μ M vimentin. (Bottom) Corresponding loss tangents, defined as the ratio of the loss modulus G'' to the storage modulus G' (same color code). Note that the loss tangent is noisy because the applied strain and the shear moduli (especially G'') are small, so the stress is close to the sensitivity limit of the rheometer. B) Bar plots comparing the elastic modulus G' at a frequency of 1 Hz of entangled and crosslinked networks of actin, vimentin, and actin/vimentin composites. Protein concentrations: 24 μ M F-actin, 18 μ M vimentin, 4.2 μ M ACTIF preparation. For each condition, $N = 2$, circles are individual data points. All scale bars are 100 nm, except in the far left image of panel A, where the scale bar is 1000 nm.

it formed a slightly softer network than in the absence of ACTIF (Appendix Figure 4.26B). This suggests that ACTIF may partially disrupt crosslinking by vimentin's C-terminal tail domains [200] or that ACTIF generates network inhomogeneities by bundling vimentin filaments. Interestingly, the stiffness of the crosslinked actin/vimentin composite network is larger than the sum of the moduli of the two isolated networks (Fig. 4.10B), suggesting the presence of some form of mechanical synergy. We will explore this mechanical synergy and the suggested competition between ACTIF and vimentin's C-terminal tails in more depth in Chapter 5.

ACTIF CROSSLINKER VARIANT WITH THE IFBD OF APC

The engineered ACTIF crosslinker has a modular design such that its functional modules can be swapped for alternative domains. To prove the benefit of this modularity, we swapped the IFBD from plectin for an alternative IFBD, taken from the Adenomatous Polyposis Coli (APC) protein. APC was reported to directly bind vimentin filaments in astrocytes, leading to crosslinking and elongation of vimentin filaments along microtubules [257]. IF-binding was traced to the N-terminal Armadillo repeats of APC via biochemical assays with truncated APC proteins. We hence engineered an ACTIF variant where the IFBD from plectin was substituted by the armadillo repeats of APC, specifically, the region referred to as APCn2 [257]. The ACTIF-APCn2 crosslinker therefore consisted of an N-terminal GFP-tag, followed by the F-actin binding domain of MACF2, the cortexillin I coiled-coil to induce dimerization, and finally a C-terminal region containing the armadillo repeats of APC (Fig. 4.11A). We performed iSCAT to check the

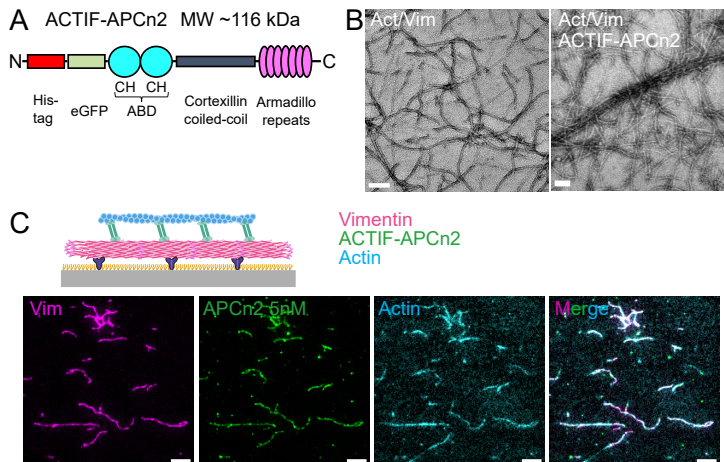


Figure 4.11: ACTIF crosslinker with the IFBD of APC binds and crosslinks F-actin and vimentin. A) Schematic representation of the engineered crosslinker ACTIF-APCn2, which is identical to ACTIF aside from its IFBD domain consisting of the armadillo repeats of APC. B) EM image of actin 1.5 μ M and vimentin 1.5 μ M co-polymerized in the absence (left) and presence (right) of 0.3 μ M ACTIF-APCn2. ACTIF-APCn2 forms thick straight bundles. Scale bars: 100 nm. C) Schematic and fluorescent images from the TIRF microscopy assay following the same protocol as Fig. 4.4(E), showing F-actin was added in solution and recruited on top of ACTIF-APCn2-bound vimentin after ACTIF-APCn2 at ~5 nM was flushed into the chamber with vimentin filaments on the substrate. Scale bars: 5 μ m.

oligomeric state of the ACTIF-APCn2 crosslinker and found it to be dimeric (Appendix Figure 4.19C). To test the protein purity, we performed SDS-PAGE analysis after the final gel filtration chromatography step. As shown in Appendix Figure 4.19D, the SDS-PAGE gel shows a major band localized at the expected molecular weight of 116 kDa and a smaller second band at ~80 kDa indicative of some protein degradation.

We first performed EM assays to test the ability of ACTIF-APCn2 to crosslink F-actin and vimentin filaments. We compared actin and vimentin mixtures co-polymerized in the absence (Fig. 4.11B (left)) and presence (Fig. 4.11B (right)) of 0.3 μ M of ACTIF-APCn2. ACTIF-APCn2 caused the formation of thick straight bundles of F-actin and vimentin filaments, showing that it is capable of crosslinking the two filament types. ACTIF-APCn2 induces bundles that are strikingly long (Appendix Figure 4.27A) and that are thinner than ACTIF-induced bundles (average width of 58 \pm 8 nm at 0.3 μ M of ACTIF-APCn2, Appendix Figure 4.27B). We next performed TIRF microscopy to validate the efficacy of ACTIF-APCn2 in crosslinking actin and vimentin filaments in real-time. After immobilizing vimentin filaments on a substrate as described earlier, we sequentially flushed in ACTIF-APCn2 (~5 nM) for 10 min, then pre-assembled F-actin. We observed binding of ACTIF-APCn2 to vimentin and progressive recruitment of F-actin on top of the ACTIF-APCn2-decorated vimentin filaments (Fig. 4.11C), forming a stable actin-ACTIF-APCn2-vimentin composite. Quantitative colocalization analysis gave Manders coefficients of $M1 = 0.932$ and $M2 = 0.929$ for the colocalization of ACTIF-APCn2 on vimentin and $M1 = 0.906$ and $M2 = 0.916$ for the colocalization of actin on vimentin, similar to the values observed with ACTIF. When we characterized the ACTIF-APCn2 association

on vimentin at a similar concentration as for ACTIF (5 nM), we noted that ACTIF-APCn2 associated at a rate about 60 times lower than ACTIF during the initial phase of fluorescence intensity increase (Appendix Figure 4.28). We conclude that the type of IFBD impacts the association rate of the ACTIF on vimentin.

4.3. DISCUSSION

In this work, we reconstituted specific interactions between actin and vimentin filaments by engineering a cytolinker protein that recapitulates the crosslinking activity of plectin. We found that the engineered cytolinker protein, which we named ACTIF, has a high binding affinity ($K_d \approx 1.4$ nM) for vimentin and lower binding affinity for actin ($K_d \approx 0.7$ μ M). TIRF imaging showed that ACTIF molecules very stably crosslink actin and vimentin filaments since we did not observe any dissociation when we removed the soluble ACTIF pool, while ACTIF partially dissociated when only attached to vimentin. ACTIF is thus able to form long-lived composite actin-vimentin bundles.

The affinity of ACTIF on vimentin and on actin was estimated from the mobile fraction of ACTIF in FRAP experiments, which we believe is dimeric (~30% on vimentin and ~50% on actin). We presume that the high proportion of immobile ACTIF results from oligomerization induced by the high density of ACTIF on the filaments, which increases the strength of the bond between the oligomers and the filaments. This could explain why we only observed one population of dimers of ACTIF with the iSCAT experiments in similar conditions (concentration and buffer), but two populations on filaments (dimers and oligomers induced by the high density on filaments). We believe that the ACTIF immobile fraction is more important on vimentin than on F-actin due to the higher density of binding sites on vimentin (at least 800 per micron length of vimentin filaments made of 10 tetramers per cross-section [39] and an axial repeat of 50 nm [183], compared to 360 per micron length of F-actin [373] if we assume one ACTIF per monomer of vimentin or actin).

The high affinity of ACTIF for vimentin is qualitatively consistent with previous biochemical measurements using different plectin fragments, showing that the PRD5 and PRD6 domains and intervening linker constitute the main vimentin binding site. In quantitative terms, ACTIF under the conditions of our assays had a higher binding affinity for vimentin as compared to values reported previously for these fragments, specifically fragments consisting of the PRD5 domain and linker ($K_d = 50$ nM) [364], the PRD5-PRD6 (including the linker region) ($K_d = 0.15 - 0.3$ μ M) [374], or the entire C-terminus starting from the PRD5 domain ($K_d = 135$ nM) [59]. Variants of ACTIF with IFBDs composed of different combinations of domains could be used in the future to sort out the contribution and synergy of the different domains of plectin implicated in controlling its affinity for vimentin. Also, ACTIF variants could be used for testing the binding affinity and crosslinking efficiency of PRD and linker domains from other plakin proteins. Sequence analysis has shown that these domains differ in the number of basic residues in their IF-binding groove, suggesting that they present a spectrum from weak to strong binding affinities [60]. The lower binding affinity of ACTIF's ABD for F-actin is consistent with previous measurements for TipAct [359], the engineered actin-microtubule

crosslinker that formed the template for ACTIF. ACTIF has the same MACF-derived ABD as TipAct and its affinity for actin was measured at about 5 μ M by a co-sedimentation assay in MRB40 buffer. Since both ACTIF and TipAct are dimers, this also further validates our assumption that the ACTIF mobile fraction is dimeric. Sequence analysis shows a 73.8% overlap between the ABD of MACF and the ABD of plectin (see sequence alignment in Appendix Figure 4.29). Both ABDs consist of two calponin homology (CH) domains in tandem. The isolated CH1 supports binding to actin, albeit with a lower affinity than the tandem; in contrast, CH2 domain has a weaker affinity. The tandem binds at full capacity and has three conserved actin binding sites [375]. The plectin ABD, with its CH domains in a closed conformation, has also been reported to have structural similarity with fimbrin [367], despite dissimilar sequences. Observations of plectin localization in cells suggest that the high binding affinity for vimentin and low affinity for actin of ACTIF are physiologically relevant. EM images showed that in IF-containing cells, plectin co-localized largely with the vimentin network, whereas in IF-deficient cells, it became mainly associated with the actin cytoskeleton [64].

We showed by electron microscopy that ACTIF induces the formation of crosslinked actin/vimentin bundles and networks already at rather low molar ratios of just 1 ACTIF molecule per 100 actin/vimentin monomers. The isolated IFBD domain could induce bundling of vimentin filaments, but only at much higher (1:1) molar ratios of IFBD:monomer. This finding is consistent with previous work showing that the PRD5 domain by itself can crosslink vimentin (and cytokeratin) filaments [376]. However, we note that contrary to that study, we did not observe any negative effect of the isolated IFBD domain on vimentin filament formation. The fact that the IFBD domain alone can bundle vimentin filaments suggests that it may oligomerize. Indeed in EM images of actin filaments mixed with the IFBD domain, we observed globular structures (non-interacting with F-actin), indicating the presence of IFBD clusters. Oligomerization of full-length plectin has been previously observed by electron microscopy images of rotary-shadowed samples, where filament-bound plectin structures were shown to be oligomeric [63]. It would be interesting for future studies to investigate the ultrastructure of the bundles formed by ACTIF crosslinking by thin-section EM or cryo-electron tomography.

ACTIF not only forms crosslinks between actin and vimentin filaments, but it also forms crosslinks between actin filaments. This finding is consistent with previous work showing that the ABD of plectin by itself can bundle actin filaments [73]. In this earlier study, actin bundling relied on dimerization of the ABD. In the case of ACTIF, we enforced dimerization using a cortexillin coiled-coil spacer domain. We cannot exclude that, additionally, interactions between the ABD domains may also contribute to the observed ACTIF-mediated F-actin bundling. In this study we focused on cytolinker-mediated interactions of vimentin and actin in their filamentous forms. In the future it will be interesting to also test interactions between filamentous and soluble forms (G-actin and vimentin tetramers or unit-length filaments). It was recently shown in cells that the vimentin network obstructs G-actin diffusion, possibly due to transient attractive interactions or binding between the two proteins that contributes to the reduced motion [67].

The modular engineered cytolinkers we introduced here can provide a strong basis for understanding the regulation and functions of cytolinker-mediated actin/intermediate filament crosslinking in cells. Using cell-free assays, one can test the interactions of cy-

tolinkers with actin and intermediate filaments under well-controlled conditions. Using cell-based studies, one can then test how these findings carry over to the cellular environment, which is much more complex due to effects such as molecular crowding, nonequilibrium activity, etc. To connect cell-free studies to cell-based studies, it will be important to test the effect of cytolinker size, and more specifically the effect of spacer length. In cell-free studies, the effect of spacer length could be studied by purifying full length plectin or APCn2 or engineered variants with different spacer domains from insect or mammalian cells. In cell-based studies, the effect of spacer length could be studied by transfecting cells with knockouts for endogenous cytolinkers with engineered cytolinker constructs. We note that previous work from our lab with an engineered actin-microtubule crosslinker mimicking ACF7/MACF showed that short constructs with the same spacer domain as ACTIF behaved identically to full-length ACF7/MACF in cell-free assays [266].

Several important open questions could be addressed using our engineered cytolinkers. First, it will be interesting to compare binding and crosslinking by ACTIF and ACTIF-APCn2 with different types of intermediate filaments (IFs), given that the expression pattern of IF proteins is cell-type specific and may convey cell-specific cellular functions. Plectin and other plakins have been shown to possess a broad binding specificity towards different types of IFs, including not only vimentin, which we studied in this work, but also cytokeratins, desmin, GFAP and neurofilaments [63, 376, 76, 89], because they recognize the conserved rod domain of IF proteins. By contrast, APC was reported to interact with vimentin and GFAP, but not with keratin, although the structural basis for this is still unknown [257]. Our system makes it possible to perform quantitative comparisons of the kinetic (un)binding rates and the crosslinking efficiency of different IF types. Second, it is also relevant to uncover how posttranslational modifications (PTMs) of IFs such as phosphorylation [377], glycosylation [378] and electrophilic or oxidative modifications [379] may affect interactions with ACTIF and ACTIF-APCn2. Conversely, it would also be interesting to test how PTMs of plectin regulate its interactions with IFs. Cell studies have shown evidence for regulation by phosphorylation of sites like serine 4642 in the C-terminal extremity [380, 381, 382] and by oxidation and nitrosylation of cysteines in plectin's IFBD [374]. Finally, a recent study showed that the association between plectin and vimentin is mechanosensitive and requires actomyosin contractility [66]. Our reconstitution assay could be used to test whether this mechanosensitivity is intrinsic to plectin, for instance to its force-sensing plakin domain [383].

Our work also provides an interesting proof-of-concept for constructing cytoskeletal systems to be applied in active matter model systems [384, 385] or in synthetic cells [386, 387]. In these systems, designer crosslinkers like ACTIF could be used to manipulate the material's mechanical properties and associated dynamics. An interesting expansion of our work would be to engineer a light-activatable cytolinker variant, where the crosslinking effect can be spatiotemporally controlled by illumination. Other interesting modular options to tune cytoskeletal crosstalk are to add tubulin-binding sites or binding sites for actin- or microtubule-based motor proteins.

4.4. CONCLUSIONS

Our results reveal specific crosslinking of actin and vimentin filaments mediated by the engineered crosslinker ACTIF. Actin and vimentin filaments form composite bundles and stiff networks upon crosslinking via ACTIF. This engineered crosslinker enables biochemical, structural, and biophysical studies of crosslinker-mediated cytoskeletal interactions. The crosslinker's modular design provides an opportunity to test different IF binding domains to better understand intermediate filament binding, as demonstrated by our proof of concept comparing the IFBDs from plectin and APC. This approach also provides the opportunity to unravel the effect that actin-vimentin crosstalk exerts on the mechanical properties of the cytoskeleton, either in a simplified *in vitro* system as reported here, or directly in cells.

4.5. ACKNOWLEDGEMENTS

I would like to thank Quang D. Tran and Cécile Leduc for hosting us in Paris to help Jeffrey den Haan and myself with vimentin purification, bringing a happy end to a period of protracted experimental issues for us. I would also like to thank them for their essential help with the TIRF microscopy experiments, analysis, and interpretation. Thank you as well to Angeliki Goutou and Zima Kabir for their massive efforts with ACTIF cloning and purification optimization, which was fundamental in the success of this chapter! Thank you to Gerhard Whiche for valuable discussions about plectin's cellular functions and for providing constructs that formed the basis for our ACTIF design. I would also like to thank Jeffrey de Haan and Sonam Marapin for protein purification and Eli van der Sluis for great teaching and discussions about cloning techniques. Also, I would like to thank Sonam Marapin for the Western blot analysis, as well as Guillaume Chevreux, Jean-Michel Camadro and Marie Ley (IJM proteomics platform) for the LS-MS analysis. Thank you as well to Sandrine Etienne-Manneville for the APCn2 construct and the entire Romet-Lemonne/Jégou lab for purification and labeling of the actin used in the TIRF experiments as well as technical help and stimulating discussions during my visit to Paris.

4.6. METHODS

4.6.1. PROTEINS

ACTIF PLASMID CONSTRUCTION

ACTIF was designed to contain an enhanced Green Fluorescent Protein (eGFP) tag followed by the ABD from MACF, the coiled-coiled linker of Cortexillin I, and the IFBD of plectin. We inserted additional residues for flexibility between the different domains, as shown in Appendix Figure 4.30. As a vector, we used the TipAct construct [359]. For the IFBD insert, we used a plasmid corresponding to residues 4030-4631 aa of the isoform

Q9QXS1-1 of mouse plectin, a region that contains the plakin repeat domains 5 and 6 and intervening linker[364]. The two fragments (vector and insert) were amplified using the primers indicated in Appendix Table 4.2. PCR amplification was performed using KOD Xtreme Hot start DNA polymerase (#1975). The PCR products were run on a 1% agarose gel (Biorad #1613100EDU) and cleaned using the Wizard® SV Gel and PCR Clean-Up System A9281. For electrophoresis, samples were prepared with TrackIt™ Cyan/Yellow Loading Buffer (Invitrogen #10482035), and TrackIt™ 1 Kb Plus DNA Ladder (Invitrogen #10488085) was used as a ladder. The electrophoresis gel was run at 100V for 20 minutes (Biorad #1613100EDU). Next, the fragments were assembled using the Gibson assembly, following the instructions of NEBuilder HiFi DNA Assembly Cloning Kit (#E5520S). Afterward, the sample was transformed into *Dh5α* competent *E. coli* cells (#C2987). To determine if the plasmid contained the insert, a miniprep was performed for sequencing via Macrogen. The miniprep was performed using the PureYield™ Plasmid Miniprep System A1222. After sequencing, the plasmid was transformed into *E. coli* BL21 (NEB #C2527).

ACTIF PROTEIN PURIFICATION

A pre-culture of *E. coli* BL21 cells expressing ACTIF was grown from a glycerol stock in Luria-Bertani (LB) medium containing 1:1000 diluted kanamycin at 37 °C. Growth was upscaled to a total of 12 liters (separated in 4 cultures of 3 L each), adding 1:1000 diluted kanamycin, and 25 mL of ACTIF preculture. The cultures were incubated at 37 °C in flasks on a shaker platform at 200 rpm. When the Optical Density (OD) reached 0.9, we cooled the 4 cultures down in an ice bath for 30 minutes, then induced overnight expression with 1 mM Isopropyl β -D-1-thiogalactopyranoside (IPTG #11411446001) at 16 °C. The cultures were harvested by a 15 min centrifugation in the Avanti JLA8.1000 fixed angle rotor at 4000 rpm at 25 °C. The supernatant was discarded, and the cell pellets were combined in one 50 mL falcon tube. The cells were resuspended with lysis buffer (20 mM sodium phosphate pH 7.4, 10 % glycerol, 5 mM 2-mercaptoethanol, 500 mM NaCl, 45 mM imidazole), supplemented with cCompleteTM EDTA-free protease inhibitor cocktail (SigmaAldrich, St. Louis, MO, USA #11836153001) and 1 mg/mL of lysozyme from chicken egg white (Sigma Aldrich #10837059001). The cell solution was incubated on ice for 30 minutes. The lysate was passed through the French press three times at 20 kpsi and next centrifuged at 17,000 \times g for 1 hour and 20 minutes at 4 °C (Avanti JXN-26). The supernatant was collected and incubated with 1 mL pre-washed nickel-IMAC resin (Thermo Fisher Scientific #88221) overnight at 4 °C. The beads were pre-washed with wash buffer (20 mM sodium phosphate pH 7.4, 10% glycerol, 5 mM 2-mercaptoethanol, 500 mM NaCl, 45 mM imidazole) in an empty column (Econo-Pac® Chromatography Columns #7321010). The lysate was passed through the disposable column for gravity flow purification. The flow-through was collected and kept at 4 °C. The column was washed three times with wash buffer. To elute the protein from the column, the column was incubated with elution buffer (20 mM sodium phosphate pH 7.4, 10% glycerol, 5 mM 2-mercaptoethanol, 500 mM NaCl, 200 mM imidazole) for 20 minutes at 4 °C. Afterward, an analysis of protein yield and purity for the eluate was performed by SDS-PAGE analysis. To improve the protein purity, a final size exclusion chromatography step was performed on a Superdex 200 10/300 prep grade (Cytiva) column.

The column was previously stored in ethanol, and it was washed with $1.5 \times$ column volume of MiliQ and then with $1.5 \times$ column volume of MRB40 buffer (40mM piperazine-N,N'-bis(2-ethanesulfonic acid) (PIPES) pH 7.0, 4 mM MgCl₂, and 1 mM Ethylene glycol tetraacetic acid (EGTA)). After the column was equilibrated, we injected the sample through the 5 mL loop and ran it at a flow rate of 0.5 mL/min, while collecting 0.3 mL fractions. The fractions of interest as judged from the absorbance at 280 nm were pooled and analyzed by SDS-PAGE gel electrophoresis. The sample was aliquoted at the desired molar concentration, calculated using values for the molecular weight and extinction coefficient of 138 kDa and 101,245 M⁻¹ cm⁻¹, respectively, which were theoretically estimated with Expasy analysis tool [388]. The aliquots were stored at -80 °C. We typically obtained 7 mg from 12 L of bacterial cell culture at a concentration of about 7 mg/mL.

By quantifying the intensity of the protein bands observed on the SDS-page gel in Appendix Figure 4.14 using the plugin called "Gels" on Fiji, we estimated the purity of ACTIF at 64%. To test whether the lower-molecular weight bands are degradation products of ACTIF, we performed fluorescence imaging of the SDS-page gels using a Typhoon (Appendix Figure 4.15). The most prominent bands in the SDS-page gel displayed a fluorescent GFP signal, indicating that these bands indeed result from partial proteolysis of ACTIF. Western blot analysis where we stained the bands with anti-GFP antibodies confirmed this conclusion (Appendix Figure 4.16). Finally, we also performed liquid chromatography-mass spectrometry (LC-MS) to assess the purify of the ACTIF preparation. LC-MS analysis showed that the most abundant protein in the sample had a molecular weight of 138 kDa, as expected from the amino-acid sequence of ACTIF (Appendix Figure 4.17). Putative identification of the main peaks of the LS-MS chromatogram allowed us to identify degraded fragments of ACTIF sample.

IFBD(PLECTIN) CONSTRUCTION

The IFBD(plectin) construct consisted of an N-terminal His6-tag followed by the region of the isoform Q9QXS1-1 of mouse plectin of 4030-4631 aa, corresponding to the plakin repeat domains 5 and 6 and intervening linkers, as shown in Appendix Figure 4.31. The plasmid assembly was performed as reported for ACTIF, and the used primers are presented in Appendix Table 4.4.

ACTIF-APCn2 CONSTRUCTION

ACTIF-APCn2 was designed as a variant of ACTIF, with the plectin-derived IFBD replaced by the armadillo repeats of APC, again using the TipAct construct [359, 268] as a vector. For the insert, we used a plasmid courtesy of Sandrine Etienne-Manneville that corresponded to the APCn2 fragment of APC, specifically from residue 334 to 740 [257]. The assembly was performed as reported for ACTIF using the primers presented in Appendix Table 4.3. The final sequence is shown in Appendix Figure 4.32.

IFBD(PLECTIN) PROTEIN PURIFICATION

IFBD(plectin) was purified following the same protocol as for ACTIF but no gel filtration was required. In order to calculate the final concentration of the purified sample, the

respective molecular weight and extinction coefficients are 71 kDa and $48,165 \text{ M}^{-1} \text{ cm}^{-1}$, which were calculated based on the protein sequence with the Expasy analysis tool [388]. We typically obtained 5 mg from 6 L of bacterial cell culture.

ACTIF-APCn2 PROTEIN PURIFICATION

ACTIF-APCn2 was purified following the exact same protocol as ACTIF until the lysis step. Culture pellets were resuspended in 40 mL of lysis buffer (20 mM sodium phosphate pH 7.4, 500 mM NaCl, 45 mM imidazole, 5 mM bME, 10 % v/v glycerol), 1 cComplete™, EDTA-free Protease Inhibitor Cocktail (Roche) and 1 mg/mL of lysozyme from chicken egg white (Sigma Aldrich). Lysis of the spun down cultures was performed by sonication, using a 422A tip, with a protocol following amplitude 40 %, 10 seconds on, 10 seconds off, for a duration of 10 minutes. Afterwards, the lysate was centrifuged using TI45 40,000 rpm, for 30 min at 4 °C. The supernatant was loaded on a 5mL HisTrap FF column (Cytiva) and the purification was performed using the AKTA system. The column was washed with 50 mL lysis buffer and was eluted with 50 mL lysis buffer supplemented with 200mM imidazole. The flow rate of the buffers was 1 mL/min. Fractions with the clean protein based on the SDS-gel were pooled. In order to calculate the final concentration of the purified sample, the respective molecular weight and extinction coefficients are 116 kDa and $94,770 \text{ M}^{-1} \text{ cm}^{-1}$, which were theoretically estimated with Expasy analysis tool [388]. We typically obtained 6-8 mg from 12 L of bacterial cell culture at a concentration of 6-8 mg/mL. By quantifying the intensity of the protein bands observed on the SDS-page gel, we estimated a purity of 72% (Appendix Figure 4.14).

ACTIN PURIFICATION

For EM and rheology experiments, lyophilized rabbit alpha-skeletal muscle actin was purchased from Hypermol EK. Actin was dialyzed against G-buffer (pH 7.8) comprising 5 mM Tris-HCl, 0.1 mM MgCl₂, 0.2 mM ATP and 5 mM DTT. After dialysis, G-actin was aliquoted, flash-frozen in liquid nitrogen and stored at -80 °C. The final actin concentration was measured by UV-VIS absorbance measurements using an extinction coefficient at 290 nm of $26,600 \text{ M}^{-1} \text{ cm}^{-1}$ and molecular weight of G-actin of 42 kDa [335].

For TIRF experiments, alpha-skeletal actin was purified from rabbit muscle acetone powder following a protocol in ref. [389] that was based on an earlier protocol [390]. G-actin was fluorescently labeled on accessible surface lysines using ATTO-643 succinimidyl ester (Life Technologies) as described previously [391]. Similarly, actin was labeled with biotin using biotin succinimidyl ester (Life Technologies). An SDS-page gel showing the purity of the actin preparation is provided in Appendix Figure 4.14.

VIMENTIN PURIFICATION

Wild-type human vimentin was purified from TG1 *E. coli* bacteria (Sigma-Aldrich) following an earlier protocol [392]. In brief, we started the induction when the OD reached 1.2, and cultured the bacteria in Terrific Broth medium overnight at 37 °C. Then, we collected the bacterial cells by centrifuging the culture medium, and lysed them with lysozyme, together with DNase (Roche), RNase (Roche), and protease inhibitors (Pef-

bloc and PMSF) in a 50 mM TRIS buffer pH 8. We washed the released inclusion bodies 5 times in the presence of DTT, and protease inhibitors: first with 200mM NaCl, 1% sodium desoxycholate, 1% NP40, 20mM TRIS pH 7.5, 2mM EDTA; second with 10mM TRIS pH 8, 0.5% Triton X 100; third with 10 mM TRIS pH 8, 0.5% Triton X 100 and 1.5M KCL; fourth with 10 mM TRIS pH 8, 0.5% Triton X 100; and finally with 10 mM TRIS, 0.1 mM EDTA pH 8 and 20 μ l DTT. Washing includes successive steps of incubation on ice for 20 min, centrifugation at 8000 rpm for 10 min at 4 degrees Celsius, and resuspension using a cooled douncer. After washing, we resuspended the inclusion bodies in a denaturing buffer (8 M urea, 5 mM Tris pH 7.5, 1 mM EDTA, 1 mM DTT, 1 % PMSF) and centrifuged them at high speed (100000 \times g) for 1 h. Upon collecting the supernatant, we conducted vimentin purification by two sequential steps of exchange chromatography, using first an anionic (DEAE Sepharose, GE Healthcare) and then a cationic (CM Sepharose, GE Healthcare) column in a buffer of pH 7.5 containing 8 M urea, 5 mM TRIS, 1 mM EDTA, and 0.1 mM EGTA. We collected the vimentin protein in 2 mL Eppendorf tubes and monitored the protein concentration by Bradford assay. Only the most concentrated fractions were selected and pooled together. We stored the vimentin at -80 °C with an additional 10 mM methylamine hydrochloride solution. An SDS-page gel showing the purity of the vimentin preparation is provided in Appendix Figure 4.14.

For experiments, about 100 μ L denatured vimentin aliquots were transferred to dialysis tubing (Servapor, molecular weight cut off at 12 kDa) and vimentin was renatured by stepwise dialysis from 8 M, 6 M, 4 M, 2 M, 1 M, 0 M urea into sodium phosphate buffer (pH 7.0, 2.5 mM sodium phosphate, 1 mM DTT) at room temperature with at least 15 minutes for each step. The final dialysis step was performed overnight at 4 °C in 2 L of the sodium phosphate buffer. The vimentin concentration was determined by UV-VIS absorbance measurements using a molecular weight of 53.65 kDa and extinction coefficient at 280 nm of 22,450 M⁻¹ cm⁻¹ [200].

FLUORESCENT LABELING OF VIMENTIN

We labeled vimentin proteins by coupling an Alexa Fluor 555 dye to cysteine-328, as described previously [393, 394]. In short, denatured vimentin stored in 8 M urea was dialyzed for 3 h in a labeling buffer of pH 7.0 containing 50 mM sodium phosphate and 5 M urea. Next, the fluorescent dye (AF-555 C2 maleimide, ThermoFisher) dissolved in DMSO was added in a molar ratio of 5:1 of (dye:vimentin). The solution was gently mixed for 1 h at room temperature, and the reaction was then quenched by the addition of 1 mM DTT. We used a Dye Removal Column (#22858, ThermoFisher) to remove excess dye. Finally, we renatured the labeled vimentin by stepwise dialysis from 8 M, 6 M, 4 M, 2 M, 1 M, 0 M urea to sodium phosphate buffer (pH 7.0, 2.5 mM sodium phosphate, 1 mM DTT). The final product was stored at 4 °C and used within 10 days.

SDS-PAGE GELS

We used 10% Mini-PROTEAN TGX precast polyacrylamide gels with 10 wells (Bio-rad). We loaded 10 μ L of proteins at 10 μ M mixed in a 3:1 ratio with 4X Laemmli Buffer Sample (Bio-rad) provided with 10% DTT. We ran the gels for 1h at 120 V with Tris/Glycine/SDS buffer (Bio-rad) and stained the gels with InstantBlue protein stain (Expedeon) for 1h.

To assess purity before and after gel filtration of ACTIF, we used a 4-15% Mini-PROTEAN TGX Precast Protein Gels, 15-well, 15uL (Bio-rad). We loaded 10 μ L of protein mixed in a 1:1 ratio with Laemmli 2x Concentrate (Merck). The gel was ran for 35min at 200V with Tris/Glycine/SDS buffer (Bio-rad) and stained with InstantBlue Coomassie Protein Stain (Cat # Ab119211) for 2 hours. Gel imaging was performed using a ChemiDoc Imaging System (Bio-rad). The intensity of the bands observed on the SDS-page gels were analyzed using the plugin "Gels" from Fiji [395].

TYPHOON IMAGING

An SDS-PAGE gel with the samples of interest was prepared. The proteins were diluted with 2x Laemmli Sample buffer (2x Laemmli Sample Buffer S3401-1VL). 10 μ L of proteins (at concentrations of 53 μ M for ACTIF, 30 μ M for GFP and 122 μ M for VCA) were loaded onto the Mini-Protean TGX Gels. The gels were ran for 35 min at 200 V in 1x Tris/Glycine/SDS buffer from Bio-Rad. Gels were afterwards washed with demi-water and imaged with the Amersham Typhoon. The wavelengths for Cy2, Cy3 and Cy5 were chosen, according to the marker (Colorcoded Prestained Protein Marker Broad Range (10-250kDa) Lot4 74154S). Images of the three wavelengths were combined using ImageQuant TL.

WESTERN BLOT

The samples were boiled at 95°C for 5 min in 3:1 Laemmli sample/loading buffer provided with 10% DTT. These samples were spun down for 5 min at 16000g before loading 10 μ L into 10% Mini-PROTEAN TGX precast gels (Bio-Rad). The gel was run on gel electrophoresis at 150 V for 1 h. After the run was complete, we performed a wet transfer to a nitrocellulose membrane (Bio-Rad) for 1h at 0.09 A at room temperature. The membrane was then blocked with 4% milk solution diluted in TBS 1X provided with 0.5% Tween 20 (TBS-T) for 30 minutes. After the blocking, the membrane was incubated with 10 mL of anti-GFP primary antibodies (Roche, Cat.#11814460001) at a concentration of 1 μ g/mL in 4% milk/TBS-T for 1h. The membrane was then washed three times for 15 min with TBS-T on a shaker. For the secondary antibody staining, the membrane was incubated with 10 mL TBS-T with secondary antibodies Mouse HRP at a dilution of 1:5000 (Jackson ImmunoResearch, Cat.#715-035-151) for 45 min at room temperature on a shaker. After incubation, the membrane was washed 3 times for 15 min in TBS-T. We used a ChemiDoc Imaging System (Bio-rad) to image the western blot. Activation of the HRP was done using an ECL Western Blotting Substrate detection kit (Pierce, Cat.#PI32106).

LIQUID CHROMATOGRAPHY-MASS SPECTROMETRY (LC-MS)

Intact protein analysis by LC-MS was performed as described previously [396]. Samples were injected onto a custom made BioResolve RP (450 \AA , 2.7 μ m, 0.3 mm \times 150 mm) Polyphenyl Column (Waters, Milford, MA, USA) using an Acquity M-Class chromatographic system from Waters. Mobile phases A and B were H₂O and H₂O/acetonitrile 20/80, respectively, acidified with 0.1 % (v/v) Difluoroacetic Acid. Samples were eluted at a flow rate of 6 μ L/min using the following slope change points: 0-5 min hold at 12.5 %

B, 10 min gradient to 25 % B, 40 min gradient to 50% B, 10 min wash at 80 % B and finally 5 min hold at 12.5 % B. The eluent was sprayed using the conventional ESI ion source of a Waters Cyclic IMS SELECT SERIES mass spectrometer operating in the positive ion mode. 500ng were injected on the column. The time of flight was operated in V-mode with a resolution specification of 60,000 FWHM at a mass range of m/z 50-4000.

4.6.2. TOTAL INTERNAL REFLECTION FLUORESCENCE MICROSCOPY (TIRF-M)

ASSEMBLY OF FLUORESCENT VIMENTIN AND ACTIN FILAMENTS

Prior to the experiment, we polymerized vimentin filaments from AF-555-labeled vimentin (with 10 % labeling fraction) at a concentration of 3.7 μ M in V-buffer (2.5 mM sodium phosphate, pH 7.0, 100 mM KCl) for 3 h at 37 °C using a water bath. We also polymerized F-actin from 10 μ M G-actin labeled with ATTO-643 (10 % labeling fraction) in F-buffer (20 mM Tris-HCl, pH 7.4, 50 mM KCl, 2 mM MgCl₂, 0.5 mM ATP) for 1 h at room temperature. In experiments that required F-actin immobilization, we assembled biotinylated F-actin from 10 μ M G-actin labeled with both ATTO-643 (10 % labeling fraction) and biotin (1 % labeling fraction) in F-buffer for 1 h at room temperature. We note that labeling fractions of 10 % do not impact the assembly of actin [397] nor vimentin [394].

TIRF-M EXPERIMENTAL SETUP

We assembled the composites of vimentin, F-actin and ACTIF in a flow chamber. The flow chamber was constructed from silanized coverslips following a previously described protocol [398, 394]. Briefly, we incubated cleaned coverslips with dichlorodimethylsilane 0.05 % in trichloroethylene for 1 h at room temperature. We sonicated the coverslips 3 times in methanol, each for 15 min, to wash off the excess silane. We then heated up two silanized coverslips compressing pieces of parafilm in between to 50 °C on a hot plate. This made the parafilm melt and attach to the two coverslips, resulting in a flow chamber with a volume of about 10 microliters.

For the control experiment to test the actin-vimentin direct interaction, we first flowed vimentin antibodies (SC666260, Santa Cruz Biotechnology) at a concentration of 2 μ g/mL in F-buffer into the chamber and incubated for 5 min. We passivated the flow chamber by flowing Pluronic F127 1 % in F-buffer and incubating for 15 min. We continued flowing bovine serum albumin (BSA) 5 % in F-buffer and incubated for 15 min. Finally, we thoroughly rinsed the chamber by flowing an extensive amount of F-buffer. We prepared ATTO-643-labeled G-actin (10 % labeling fraction) at 1 μ M in F-buffer supplemented with an oxygen scavenger mixture (glucose 1.2 mg/mL, glucose oxidase 40 μ g/mL, glucose catalase 8 μ g/mL, DTT 1 mM) and 0.2 % methylcellulose 4000 cP, and gently flowed them into the chamber with vimentin filaments on substrate. We captured images of the whole process of F-actin polymerizing from G-actin and rapidly elongating to long filaments while freely moving close to the vimentin filaments.

For the TIRF-M assay in which vimentin filaments were attached to the substrate, we used a similar protocol to have the flow chamber coated with vimentin antibodies

and passivated with F127 and BSA as described in the control experiment above. We then began the composite assembly by diluting pre-assembled vimentin filaments 100 times in F-buffer (final concentration: 37 nM), then flowing them into the chamber and incubating for 5 min for filament attachment onto the vimentin antibodies. Next, the chamber was rinsed, and ACTIF diluted in F-buffer supplemented with the oxygen scavenger mixture to a final concentration of 5.3 nM was flushed into the chamber while imaging had started in advance in order to capture the early state of protein attachment to vimentin filaments. After 15 min, we performed FRAP assay by photo-bleaching a region of ACTIF binding to vimentin filaments and observing the fluorescence recovery over 20 min. Finally, pre-assembled actin filaments were diluted 100 times in F-buffer with an oxygen scavenger (final concentration: 0.1 μ M) and flushed into the chamber, forming vimentin-ACTIF-actin composites.

For the assay with immobilized F-actin, we flowed neutravidin (Cat. #31000, ThermoFisher) at a concentration of 10 μ g/mL in F-buffer into the chamber and incubated for 5 min. We again passivated the flow chamber with Pluronic F127 1 % in F-buffer and BSA 5 % in F-buffer, and thoroughly rinsed the chamber afterward, similar to the previous assay. Here, our first step in the composite assembly was diluting pre-assembled biotinylated F-actin 100 times in F-buffer (final concentration: 0.1 μ M), then flushing them into the chamber, and incubating for 5 min. F-actin with biotin was constrained on the substrate due to the neutravidin coating. Then, we rinsed the chamber and flowed in diluted ACTIF at 5.3 nM or at 530 nM in F-buffer with oxygen scavenger while imaging the binding reaction for 15 min. We also performed a FRAP assay by photo-bleaching a region of ACTIF on F-actin and recording the recovery for 20 min. Finally, pre-assembled vimentin filaments diluted 100 times in F-buffer with oxygen scavenger (final concentration: 37 nM) were flowed into the chamber for the formation of actin/vimentin composite bundles.

TIRF microscopy was performed on a Nikon Eclipse *Ti* inverted microscope controlled by MicroManager, equipped with a 60 \times oil-immersion objective and a Kinetix sCMOS Camera (Photometrics). The TIRF illumination was performed using an Ilas2 module (GATACA Systems). The experiment temperature was maintained at 25 °C using objective and microscope stage temperature controllers.

4.6.3. INTERFEROMETRIC SCATTERING MICROSCOPY

Interferometric Scattering Microscopy (iSCAT) experiments were conducted with a OneMP Mass Photometer (Refeyn). The instrument was equipped with a 525 nm laser for illumination. iSCAT measurements were carried out using CultureWell gaskets (Cat. #GBL103250, Grace Biolabs) affixed to #1.5 coverslips (Cat. #13296788, Corning). To prepare the coverslips for optimal protein adhesion, a meticulous stepwise sonication cleaning process was employed. The coverslips were sonicated sequentially in MilliQ water, 50% isopropanol, and again in MilliQ water, each for a duration of 5 minutes. Following the cleaning process, the coverslips were incubated with a poly-L-lysine solution (PLL, Cat. #P4832, Merck) for 30 seconds. Subsequently, the coverslips were rinsed with MilliQ water and dried under a stream of N₂ gas. The treated coverslips were stored upright in a Teflon rack within a covered beaker to protect them from dust. They were utilized within a week to maintain their cleanliness. During the iSCAT measurements, videos

were recorded with a field of view measuring $10 \times 10 \mu\text{m}$. The recording duration ranged from 6000 to 15000 frames, with a frame rate of 300 frames per second. This ensured a minimum count of 1000 particles per video. Maintaining a dilute solution of proteins is crucial to ensure well-separated scattering patterns with no overlap. Hence protein concentrations (in the range of 10 nM to 50 nM, dilution with F-buffer from the stock concentration of the protein) were chosen to achieve adequate separation of landing events while still collecting sufficient statistics within a maximum of 15000 frames to limit data volume. The iSCAT video analysis was executed using the DiscoverMP software, a commercial software package provided by Refeyn.

4.6.4. TRANSMISSION ELECTRON MICROSCOPY

Electron microscopy analysis was conducted on samples deposited on Cu400 carbon support grids (Quantifoil, Cat. #N1-C73nCu40-01) with a JEM-1400Plus transmission electron microscope (JEOL) operating at an acceleration voltage of 120 kV. Imaging was carried out using a TemCam-F416 CMOS camera (TVIPS) with a resolution of $4\text{k} \times 4\text{k}$ pixels. The sample preparation protocol was as follows: Initially, the Cu400 grids underwent a glow discharge treatment in an oxygen plasma using the GloQube-D instrument provided by Quorum Technologies Ltd. This procedure was essential to enhance protein adsorption. Subsequently, a $4 \mu\text{L}$ droplet of the protein sample was delicately deposited onto the grid and allowed to adsorb for 1 to 2 minutes. To eliminate any surplus protein and salt, the samples underwent three washes with MilliQ water with careful blot-drying after each wash. Finally, the samples were stained for 25 seconds with a 2% aqueous solution of uranyl acetate from Electron Microscopy Sciences. Following staining, the samples were meticulously blot-dried once again to eliminate any remaining liquid. We made two independent repeats per sample condition. For each independently prepared sample we usually prepared 2 grids (in case one would be broken or overstained). To study the samples of vimentin and IFBD, we took a total of 100 images depicting all conditions. To study the samples of actin, vimentin and ACTIF, we took a total of 180 images depicting all conditions. To study the samples of actin, vimentin and ACTIF-APCn2, we took a total of 100 images depicting all conditions. Many bundles were imaged twice, since we looked at different magnifications to inspect different regions of the bundles in detail. Upon measuring bundle widths for statistics, we carefully avoided measuring the same bundle.

4.6.5. RHEOLOGY

Rheological measurements were conducted using a stress-controlled KinexusMalvern Pro rheometer equipped with a stainless steel cone-plate geometry. The cone had a radius of 20 mm and an angle of 1° . The temperature was maintained at 37°C by Peltier plates. F-actin-vimentin networks were polymerized between the plates of the rheometer by loading $40 \mu\text{l}$ of the sample directly after mixing the proteins into the polymerization buffer (F-buffer). To prevent solvent evaporation during the experiment, a thin layer of mineral oil Type A was carefully applied around the sample edge. Progress of network formation was monitored by applying a small oscillatory shear with a fixed strain amplitude of 0.5% and an oscillation frequency of 0.5 Hz for 2 hours. Following the 2-hour

polymerization period, a frequency sweep was conducted in the range of 0.01 to 10 Hz at a small strain amplitude of 1%, sampling 10 data points per decade. Data taken at frequencies exceeding 3 Hz had to be discarded because they were dominated by inertial effects from the rheometer. For each curve, we took an average over $N = 2$ independently prepared samples.

4.6.6. DATA ANALYSIS

All quantitative analysis of TIRF imaging data was performed using Fiji. The images were pre-processed with background subtraction and image registration. To quantify colocalization of F-actin, vimentin, and the cytolinkers, we used the coloc2 plugin from Fiji to perform a pixel intensity correlation over space. To retrieve reaction rates of ACTIF on vimentin filaments (or on F-actin), we manually extracted the intensity values over time in the ACTIF channel along 30 to 50 vimentin filaments. In this experiment, we performed 3 independent repeats with one field of view for each repeat. In each repeat, we calculated the mean and standard deviation of ACTIF intensity over 30 - 50 ROIs and fitted the intensity curves using GraphPad Prism. To retrieve the number of actin filaments attached to vimentin through ACTIF, we quantified the pixel fluorescence intensities in the F-actin channel along vimentin filaments (~ 150 filaments, $N = 2$ independent experiments) and plotted the distribution of intensities. This distribution displayed multiple peaks, with the first peak at an intensity of ~ 600 a.u., as expected for single F-actin in these imaging conditions. The distribution was fitted by a multiple Gaussian, with the peak positions constrained to be multiples of the position of the first peak, and common width for all the peaks except the last one.

To obtain the unbinding rate of ACTIF from vimentin filaments (or from F-actin) from FRAP data, we again first performed background subtraction and image registration. Then, we again selected 30 ROIs following shapes of vimentin filaments (or F-actin) from a pre-bleached image. The selected filaments needed to be inside the photo-bleaching region. Then we extracted the intensity value of ACTIF over time from the selected ROIs. In this experiment, we also performed 3 independent repeats with one field of view for each repeat. In each repeat, we obtained the mean and standard deviation of the ACTIF intensity over 30 ROIs and fitted the intensity curves using GraphPad Prism.

For TEM microscopy, image analysis was performed by Fiji. In order to determine the filament widths, intensity profiles perpendicular to the segment of interest were plotted at multiple locations along the filament contours. The filament diameter was determined from the width of the bright area between the darker borders. For copolymerized vimentin and IFBD, $N = 28$ bundles were measured for the 1:10 IFBD:vimentin molar ratio and $N = 17$ bundles for the 1:1 IFBD:vimentin molar ratio. For copolymerized actin and vimentin with ACTIF, $N = 40$ bundles were measured for each ACTIF:monomer ratio.

For shear rheology, data was extracted from the rSpace Software (NETZSCH Analyzing and Testing). Custom Python scripts were used to plot G' and $\tan(\delta)$ as a function of oscillation frequency. We calculated an average of $N = 2$ curves of independently prepared experiments per condition.

4.7. APPENDIX

4.7.1. TABLES AND FIGURES

Table 4.2: Primers used for Gibson Assembly of ACTIF construct.

Construct	Fragment	Forward primer	Reverse primer
ACTIF	Vector	5'-TGAGATCCGGCTGCTAACAAAGCC-3'	5'-CCCTCTGATTCCTGGTGGCTTCGAT-3'
	Insert	5'-AAAGTCTCTGAGGGTGGAGAAAGGAAAGCTCGTTAGAGAGTAGCAA-3'	5'-TTGTTGTCGAGTTTGATTTTCATCGATGGCTCAGCTA ATTTCAA-3'

Table 4.3: Primers used for Gibson Assembly of ACTIF-APCn2 construct.

Construct	Fragment	Forward primer	Reverse primer
ACTIF-APCn2	Vector	5'-GAAAATCAAACCTCGAACAAACAA-3'	5'-CCCTCTCCACCCCTCAGGAACCTT-3'
	Insert	5'-ATCGAAGGCCACCGAACATCAGAGGCTAGCTATGCTAGCTCCAAGAC-3'	5'-GGCTTTGTTAGCAGCCGGATCTCAGGCATCCTGIACTTCGAGGCCCT-3'

Table 4.4: Primers used for Gibson Assembly of IFBD(plectin) construct.

Construct	Fragment	Forward primer	Reverse primer
IFBD	Vector	5'-GATCCGGCTGCTAACAAAGCCGA-3'	5'-GCGACCCATTTCGCTGTCACCACTG-3'
	Insert	5'-ACTGGTGGACAGCAAATGGGTCGCATCGAACGCCACAGAATCAGAGGG-3'	5'-TCGGGCTTGTAGCAGCCGGATCTCAGGGCTCGAGGCCAGAGCCACT-3'

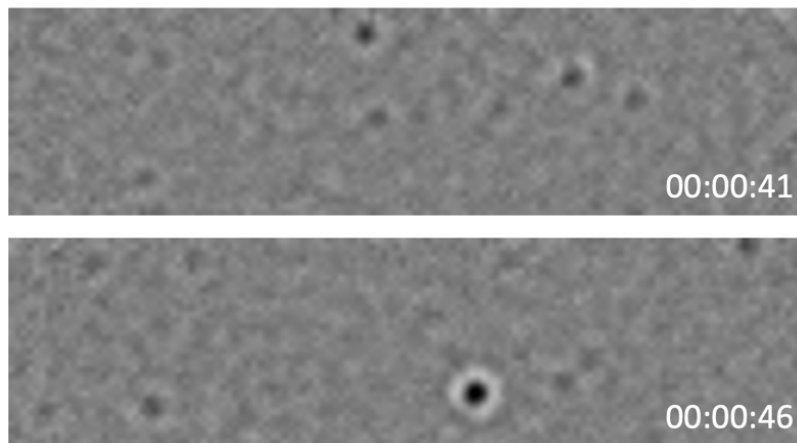


Figure 4.12: Frames from a time-lapse video recorded for interferometric scattering microscopy of a sample of 40nM ACTIF. Different time frames are shown in seconds. The area of detection shown is 18 μm^2 .

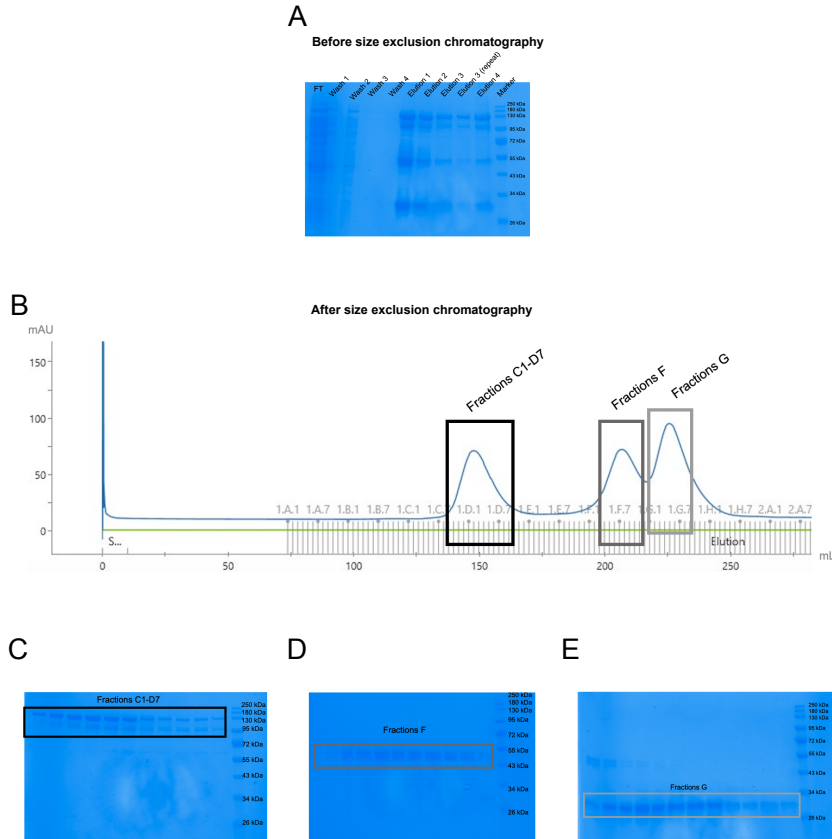


Figure 4.13: Gel filtration purification of ACTIF (A) SDS-PAGE gel of ACTIF fractions obtained by His-tag protein purification. The lanes show the flowthrough (FT), fractions from the wash steps, and fractions from the elution steps. On the right, the molecular weight reference. (B) Chromatogram of the size exclusion purification with the pooled fractions (C1-D7 fractions, F fractions and G fractions) marked by the rectangles. The first peak corresponds to the expected molecular weight of ACTIF (138 kDa). (C) SDS-PAGE gel of the pooled fractions C1-D7, corresponding to the first peak in the chromatogram. (D) SDS-PAGE gel of the pooled fractions F, corresponding to the second peak in the chromatogram. (E) SDS-PAGE gel of the pooled fractions G, corresponding to the third peak in the chromatogram.

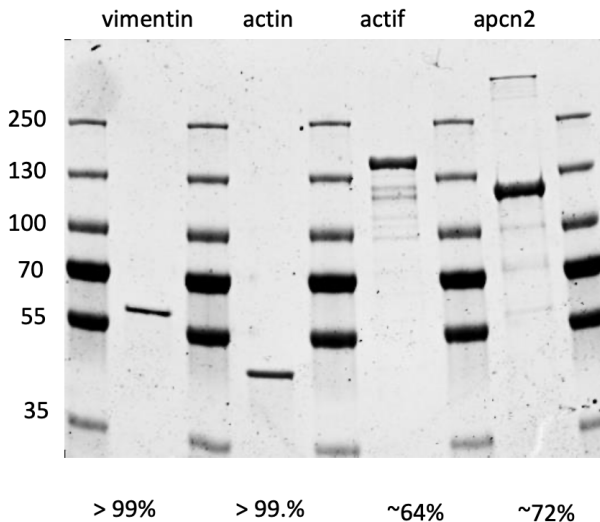


Figure 4.14: SDS-PAGE gel of purified vimentin, G-actin, ACTIF and ACTIF-APCn2. The purities of the full-length products as determined by densitometry analysis of the gel are specified at the bottom.

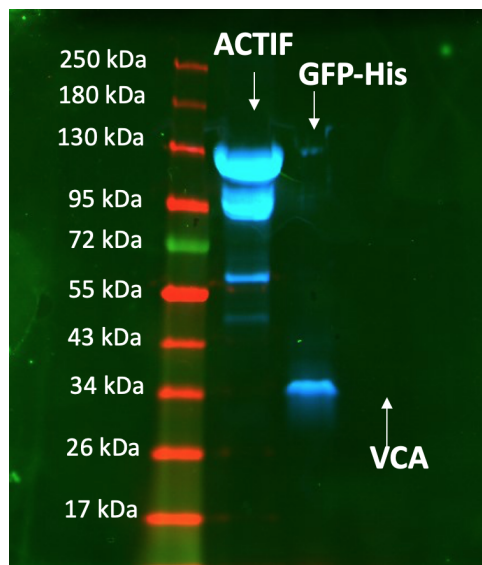


Figure 4.15: Typhoon fluorescence imaging of an SDS-PAGE gel containing ACTIF, His-tagged GFP (as a positive control) and VCA (non-fluorescent control protein). Green fluorescent signal is detected for full-length ACTIF and the lower bands (indicating proteolysis) and for the His-tagged GFP control sample. No fluorescent signal is detected for VCA.

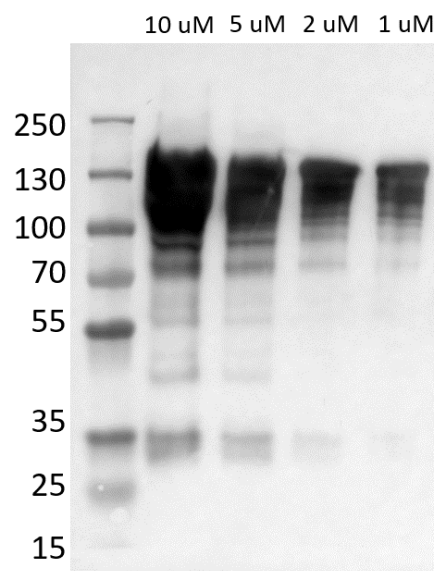


Figure 4.16: Western blot analysis of an ACTIF preparation with mouse anti-GFP antibodies. Blot imaging of activated secondary antibody labeled with HRP overlayed with a colorimetric image of the protein ladder. The different lanes correspond to different ACTIF dilutions, and the protein concentration is written on top of the lanes. 10 μ L of protein/Laemli was loaded by lane.

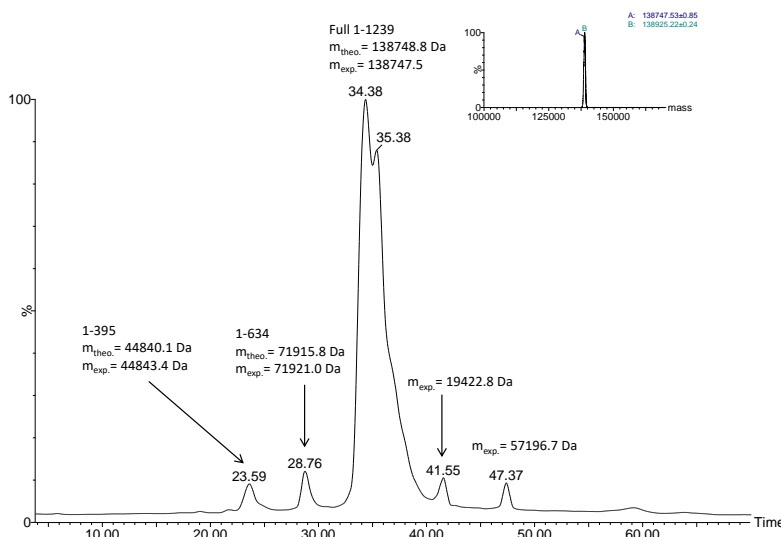


Figure 4.17: Liquid chromatography–mass spectrometry (LC–MS) analysis of ACTIF. Putative identification of the peaks in the mass spectrogram is indicated on the graph with the size of the corresponding ACTIF fragment, the theoretical mass and experimental mass. Inset: Deconvolved mass spectra of the most abundant proteins with masses of 138747.5 Da and 138925.2 Da, corresponding to full length ACTIF with N-gluconylation (+178 Da), a standard post-translational modification obtained for N-terminally His-tagged proteins expressed in E.Coli.

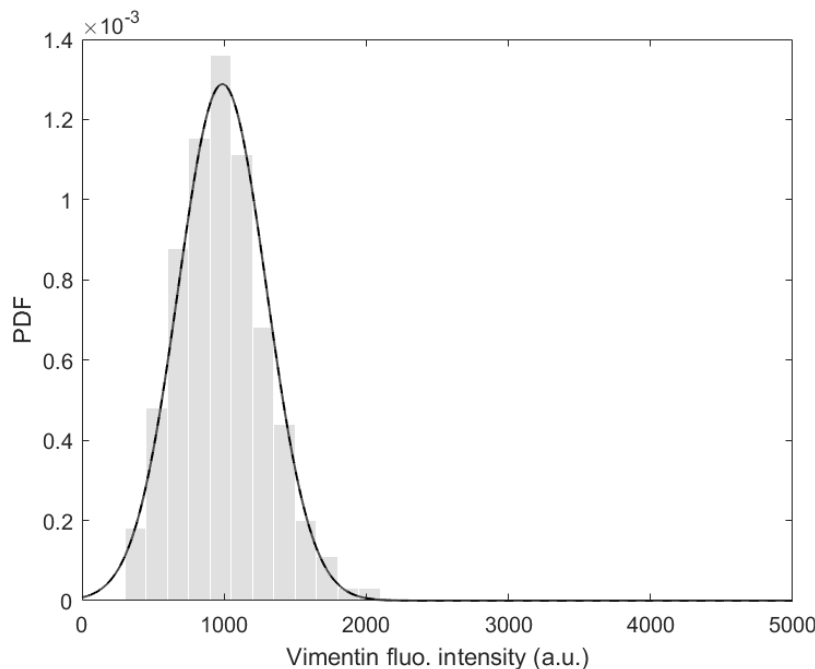


Figure 4.18: Distribution of pixel fluorescence intensities along vimentin filaments. The distribution appears as a single peak with the average intensity expected for single filaments under these imaging conditions, indicating that vimentin exists mainly as single filaments when attached to the substrate. Sample size, 100 filaments. PDF, Probability density function.

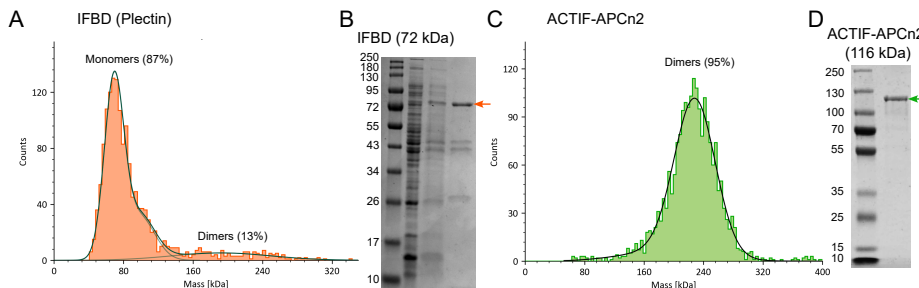


Figure 4.19: iSCAT and SDS-PAGE of ACTIF-APCn2 and IFBD. (A) iSCAT histogram count of IFBD (plectin), portraying a mostly monomeric population with a 13% dimeric population count. (B) SDS-PAGE of the pooled fractions of IFBD(plectin) after purification, with an arrow marking the band of interest. (C) iSCAT histogram count of APCn2, portraying a 95% dimeric population. (D) SDS-PAGE of the pooled fractions of APCn2, with an arrow marking the band of interest. For the gels, 10 μ L of proteins at 10 μ M were loaded and stained with Coomassie.

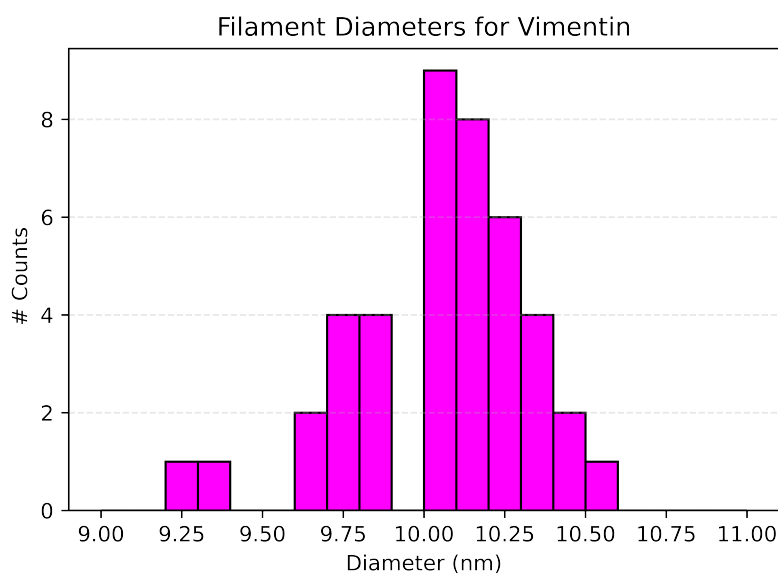


Figure 4.20: Histogram of diameters of randomly sampled vimentin filaments ($N = 50$).

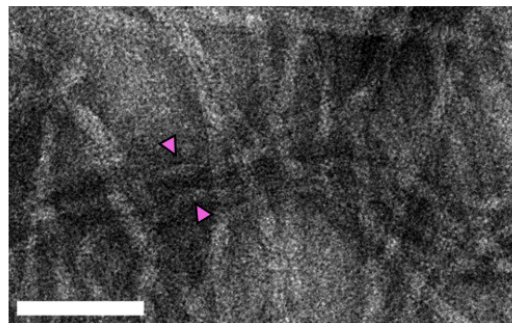
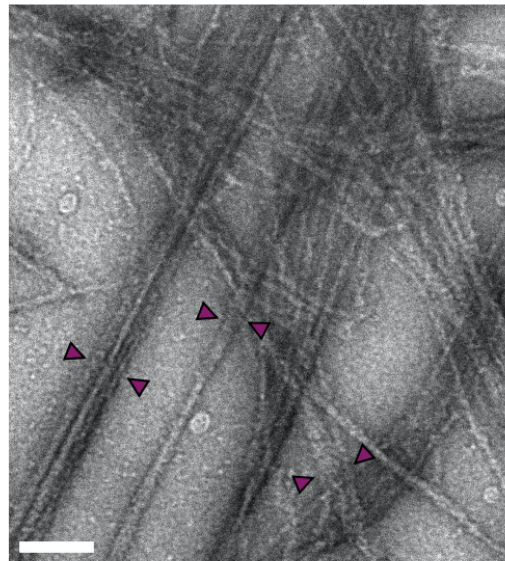
A**B**

Figure 4.21: Zoomed-in transmission electron microscopy images of $4 \mu\text{M}$ of vimentin filaments bundled with (A) $0.4 \mu\text{M}$ IFBD or (B) $4 \mu\text{M}$ IFBD. The arrows indicate examples of measured bundles. Scale bars indicate 100 nm.

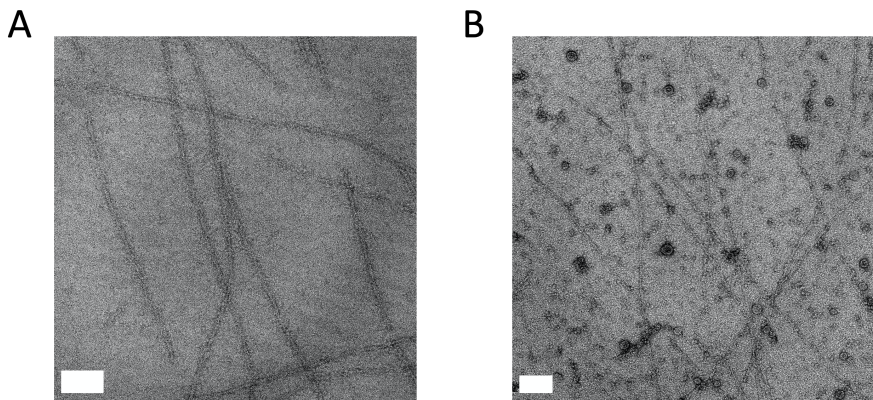


Figure 4.22: Transmission electron microscopy images of actin filaments at 2 μM concentration (A) polymerized without IFBD or (B) with 20 μM IFBD (from plectin). The IFBD tends to oligomerize (see globular structures present in (B) but not in (A)). We do not observe evidence for any interactions between actin and the globular IFBD structures. Scale bars indicate 100 nm.

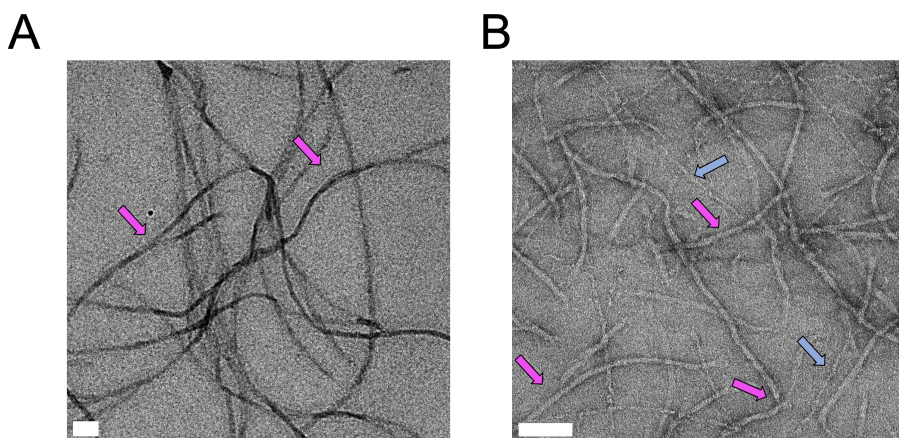


Figure 4.23: Zoomed-in electron microscopy images comparing vimentin and co-polymerized vimentin-actin composites. (A) 4 μM vimentin filaments. (B) 1 μM vimentin and 1 μM F-actin. Pink arrows indicate vimentin filaments, which are recognizable based on their larger diameter and smaller persistence length as compared to F-actin. Blue arrows in B indicate F-actin. Scale bars indicate 100 nm.

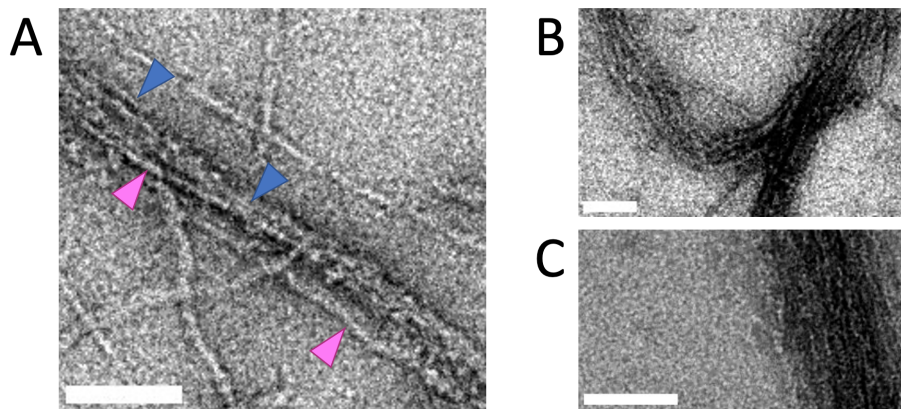


Figure 4.24: Transmission electron microscopy of copolymerized actin, vimentin and ACTIF showing detailed views of the bundles. (A) Mixed actin and vimentin within a bundle (blue arrows for actin, magenta for vimentin). (B) Another example, showing variations in bundle packing along the bundle length. (C) Bundle where we only observe actin filaments, based on their diameter. Scale bars indicate 100 nm.

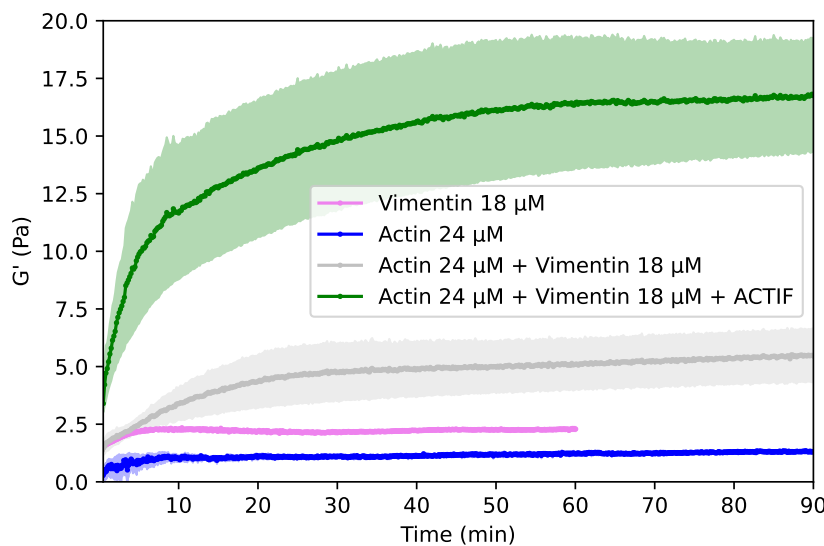


Figure 4.25: Polymerization curves for different reconstituted networks recorded by small amplitude oscillatory shear measurements. Actin (24 μ M, blue), vimentin (18 μ M, pink), actin and vimentin composite (24 μ M actin, 18 μ M vimentin, grey), and actin and vimentin composite crosslinked with 4.2 μ M ACTIF (green). Curves averaged over $N=2$ measurements.

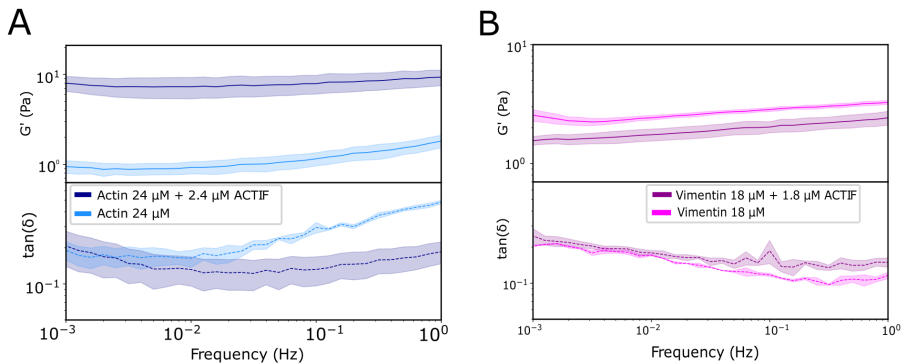


Figure 4.26: (A) Frequency sweep for an actin network (24 μ M) and for a crosslinked actin network (24 μ M actin + 2.4 μ M ACTIF), showing the elastic and viscous shear moduli (top) and corresponding loss tangents (bottom). (B) Frequency sweep for a vimentin network (18 μ M) and for a crosslinked vimentin network (18 μ M + 1.8 μ M ACTIF) showing the elastic and viscous shear moduli (top) and corresponding loss tangents (bottom).

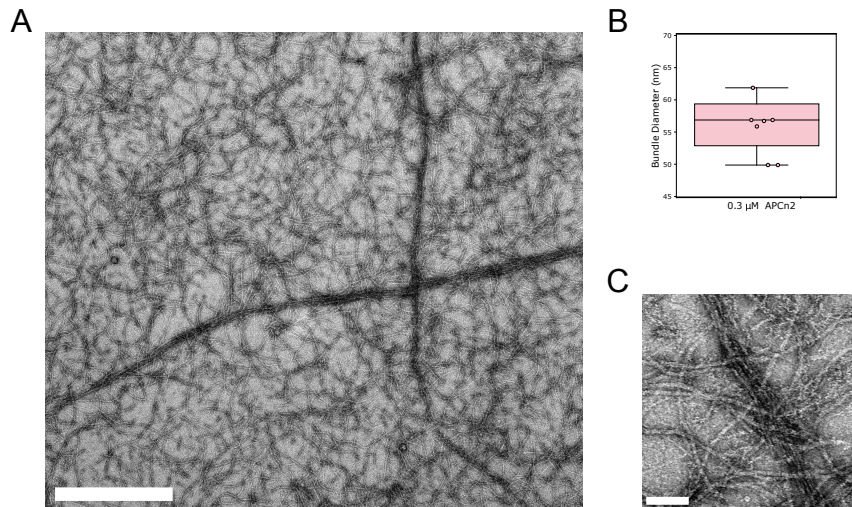


Figure 4.27: Transmission electron microscopy images of bundles of F-actin and vimentin formed with ACTIF-APCn2. (A) Overview of copolymerized actin (1.5 μ M) and vimentin (1.5 μ M) bundles formed with 0.3 μ M of ACTIF-APCn2. Scale bar 1 μ m. (B) Box plot depicting the bundle widths of 7 bundles from 2 independently prepared EM grids. (C) Zoomed-in image of a bundle. Scale bar 100 nm.

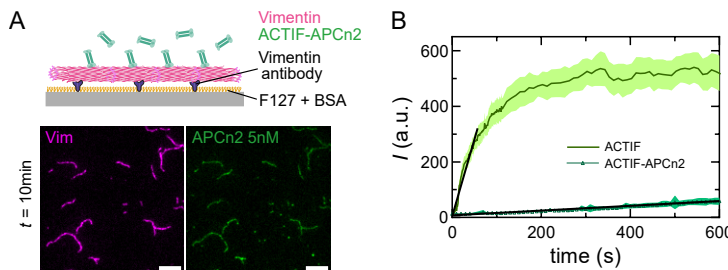


Figure 4.28: Binding affinity of ACTIF-APCn2 for vimentin filaments. (A) Schematic of the binding assay and images of ACTIF-APCn2 (green) at 5 nM co-localized with vimentin filaments (magenta) attached to the substrate, at $t = 10$ min after flushing ACTIF-APCn2 into the chamber. (B) Fluorescence intensity of ACTIF-APCn2 at 5 nM (dark green), in comparison with ACTIF at the same concentration of 5 nM (light green), on vimentin filaments over time (averaged over 30 filaments). Black lines represent linear regression of the curves. The shaded area represents standard deviations. Scale bar: 5 μ m.

PLEC	1	RVQKKTFTKVVNKHLIKAQRHISDLYEDLRDGHNLISLLEVLSGDSLPREKGRMRFHKLQ	60
ACTIF	1	RVQKKTFTKVVNKHL MKV RKHINDLYEDLRDGHNLISLLEVLSG I KLPREKGRMRFH R LQ	60
PLEC	61	NVQIALDYLRLHRQVKLVNIRNDDIADGNPKLTLGLIWTIILHFQ-----MTAK	108
ACTIF	61	NVQIALDFL K QRQVKLVNIRNDDITDGNPKLTGGLIWTIILHFQ I SDIYISGESGDMSAK	120
PLEC	109	EKLLLWSQRMVEGYQGLRCDNFNTSSWRDGRLFNAIHRHKPLLIDMNKVYRQTNLENLDQ	168
ACTIF	121	EKLLLWTQ K VTA G TG I KCTNFSSC W D G K M FNALI H R Y R P D L V D M E R V Q I Q SNRENLEQ	180
PLEC	169	AFSVAERDLGVTRLLDPEDVDVPQPDEKSIIITYVSSLYDAMP	210
ACTIF	181	A FEVAER- L GVTRLLD A EDVDV P SPDEKS V ITYVSS I YDAFP	221

Figure 4.29: Sequence alignment of the calponin homology domains of plectin (top) and ACTIF (bottom), where the CH tandem of ACTIF has been taken from MACF (Q9QXZ0, 78-298 aa). In red, sequence differences.

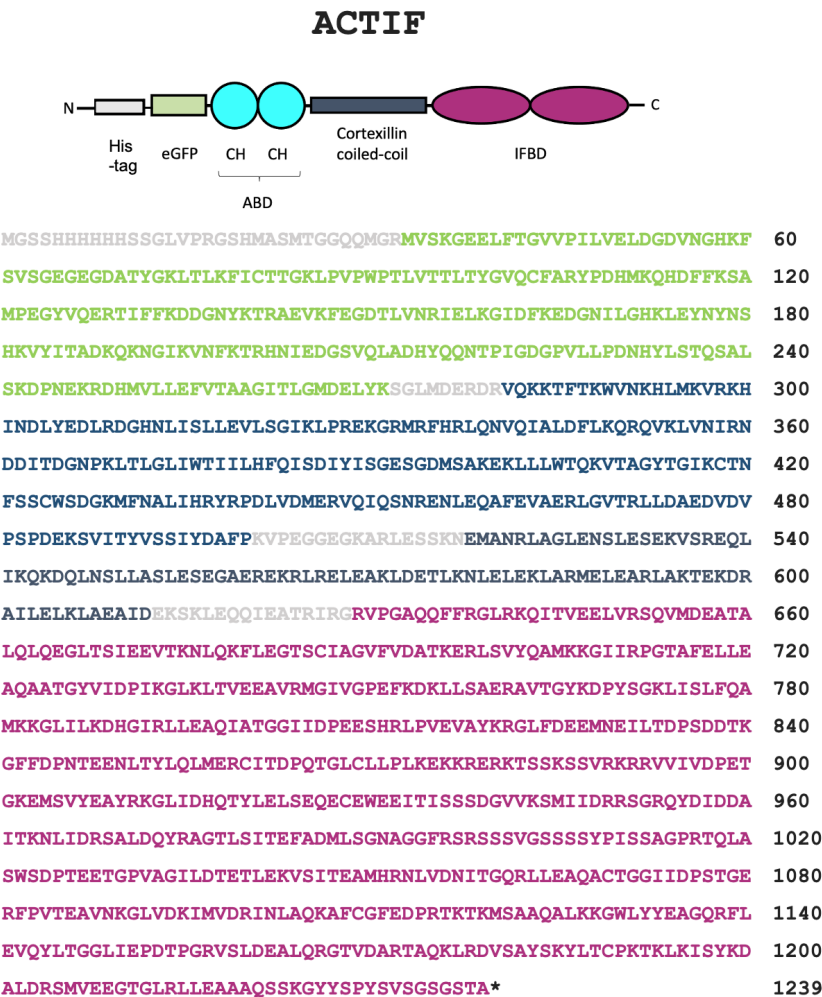
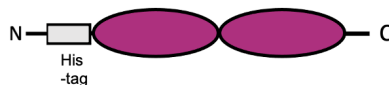


Figure 4.30: ACTIF's amino-acid sequence and domain organization. (A) ACTIF domain organization with the amino-acid numbers indicated from the sequence in (B). eGFP, enhanced green fluorescent protein; ABD, actin-binding domain; CC, coiled-coil; IFBD, intermediate filament binding domain (B) Amino-acid sequence of ACTIF. The color code corresponds to the domains indicated on the diagram in (A) and the spacers between domains are indicated in light grey letters.

IFBD (plectin)



MGSSH HHHHHSSGLVPRGSH MASMTGG QOMGRIEATRIRG RV VPGAQ QFFRGLRKQITVEE	60
LVR SQVMDEATALQ I QEGLTSIEEVTKNLQKFLEG TSCIAGV FV DATKERLSVY QAMKKG	120
I IRPGTAFELLEAQ ATGYV IDPIKGLKL TVEEAVRM GIVGPEFKDKL LSAERAVTGY KD	180
P YSGKLISLFQAMKKGLIL KDH DHGIRL LEAQ IATGGI IDPEE SHRLP VE VAYK RGLF DEEM	240
NEIL TDPSSDTKGFFDPNT EEENLTYL QLMERC ITDPQTGLCLLP KEKKR ERKTSSK SSV	300
R KRRVVIVDPETGKEM SV YEAYRKGLIDH QTY LEL SE QECE WEE ITISSDGVVKS MI ID	360
RRSGR QYDIDDAITKNLIDRS ALD QYRAGTLSITEFADMLSGNAGGFR RSRSSVG SSSSY	420
P ISSAGPRTQLASWSDP TEETGP VAGILD TE TETLEKVSITEAMHRN LVD LITG QRL LEAQ	480
CTGG IIDPSTGERFPVTEAVNKGLVDKIMVDRINLAQKAF CGF PRTK TKMSAAQ ALKK	540
GWLY YEAGQRFL E EVQYL T GGLIE P DTPG R VSL DE ALQ RG TV DART AQ KL RDV SAY SKY LT	600
CP KTKL KIS YKD ALDR SMVEEGT GL RLLEAA AQSS KGYYSPY S VSGSGSTA *	651

Figure 4.31: IFBD's domain organization and amino-acid sequence. (A) Domain organization of IFBD (plectin). (B) Amino-acid sequence of IFBD (plectin) domain. The color code corresponds to the domains indicated on the diagram in (A).

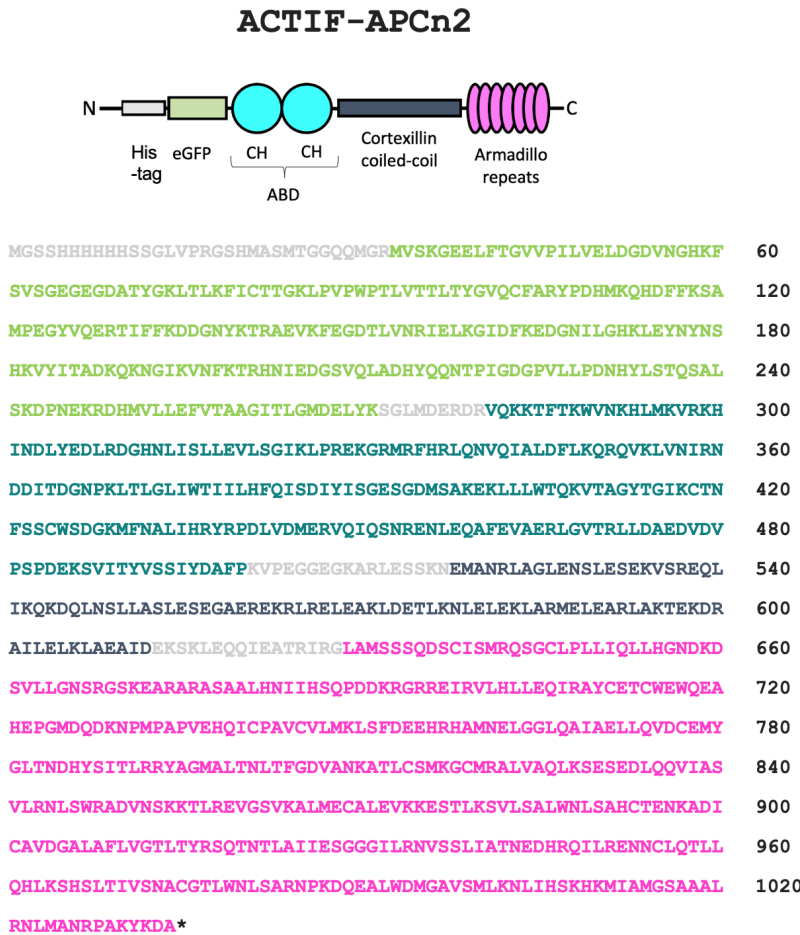


Figure 4.32: ACTIF-APCn2's amino-acid sequence and domain organization. (A) Amino-acid sequence of ACTIF-APCn2. The color code corresponds to the domains indicated on the diagram in (B) and the spacers between domains are indicated in light grey letters. (B) ACTIF-APCn2 domain organization with the amino-acid numbers indicated from the sequence in (A). His-tag, grey; eGFP, enhanced green fluorescent protein; ABD, actin-binding domain; CC, coiled-coil; armadillo repeats.

5

CROSSLINKER-MEDIATED MECHANICAL SYNERGY OF ACTIN AND VIMENTIN

Cells mechanically interact with their environment through the cytoskeleton, a dynamical scaffold consisting of protein polymers and their associated proteins including crosslinkers. The cytoskeleton is composed of three different cytoskeletal filament families (F-actin, intermediate filaments and microtubules), in constant interaction. The impact of these interactions on the mechanical properties of the cytoskeleton are relatively unexplored. In this Chapter we focus on the mechanical consequences of F-actin-intermediate filament interactions mediated by the plectin-mimicking crosslinker protein ACTIF presented in Chapter 4. This engineered crosslinker has a modular design, with F-actin-binding and intermediate filament-binding domains separated by a spacer that mediates dimerization. We show that ACTIF can crosslink F-actin networks as well as vimentin intermediate filament networks, likely due to its dimeric state. Moreover, we find that ACTIF causes a strongly synergistic enhancement of the stiffness of composite F-actin-vimentin networks as compared to the co-entangled (non-crosslinked) composites studied in Chapter 3. Our findings set the basis for future studies of composite biopolymer materials and for understanding the contribution of crosslinking of the different cytoskeletal subsystems to cell mechanics.¹

¹This chapter is co-authored with Iain Muntz and is the basis for a manuscript in progress.

5.1. INTRODUCTION

CELLS mechanically interact with their environment through the cytoskeleton, a highly interconnected polymeric network composed of three distinct cytoskeletal protein subsystems: filamentous (F)-actin, microtubules and intermediate filaments. The cytoskeleton subsystems each have distinct functions, but they exert these functions in a coupled manner to provide mechanical stability and function to the cell. The actin and intermediate filament cytoskeletal networks have for instance been shown to contribute in a collaborative manner to several essential cellular processes. In astrocytes, vimentin regulates cell migration by restricting myosin-driven actin flow and aligning traction stress [399]. During mitosis of mesenchymal cells, vimentin filaments interact with the actin cortex, allowing cell division [96]. In adherent cells, actin stress fibers interact with vimentin intermediate filaments and promote their retrograde flow in a plectin-dependent manner [68, 94]. Yet, despite this evidence for functional crosstalk, the specifics on the interplay between F-actin and vimentin are still unknown.

Previous cell-free studies of the interaction of F-actin and vimentin have focused on composites formed in the absence of crosslinkers. In 2006, Esue et al. [100] reported that actin and vimentin filaments exhibit interactions mediated via the tail domain of vimentin, which also mediates crosslinking between vimentin filaments [200, 199, 202]. However, this finding was contradicted by a later study in 2018 by Golde et al. [101], who found that composite networks reconstituted from F-actin and vimentin exhibit mechanical properties that are simply a superposition of two non-interacting scaffolds. Important to note is that the two studies used a different experimental design: Esue et al. used the molar ratio of actin and vimentin monomers as a control parameter to compare composite networks against single-component control networks, whereas Golde et al. compared composite and control networks at the same mesh size. Comparisons at the same mesh size are more insightful since this parameter, expressing the average space between neighboring filaments, is the main determinant of the concentration-dependent rheology of semiflexible polymer networks [316]. The mesh size has a different dependence on the monomer concentration for actin and vimentin since the filaments differ in their protein mass-per-length ratio. In Chapter 3 we confirmed via bulk rheology that actin-vimentin composite networks exhibit simple additive properties when the mesh size is used as a control parameter.

Importantly, the fact that we did not find any mechanical synergy between F-actin and vimentin in co-entangled composite networks does not exclude the possibility of mechanical synergy in the cell. As discussed in more detail in Chapter 4, F-actin and vimentin networks are crosslinked to each other by accessory proteins including the giant protein plectin. Plectin is a crosslinker from the plakin family [61] whose functions have so far been mostly studied in cells. Unfortunately plectin is a challenging protein for cell-free reconstitution because of its giant molecular weight (500 kDa) and multidomain structure. Accordingly there have been very few studies on crosstalk between different cytoskeletal families by plectin [82].

Previous cell-free studies of the impact of crosslinker proteins on the mechanical properties of cytoskeletal networks have mainly focused on F-actin networks. A large

body of work has revealed that F-actin networks exhibit a strongly nonlinear response to shear, which depends on the nature of the crosslinker protein. In case of crosslinker proteins that are small and noncompliant such as scruin, the nonlinearity arises from the entropic strain-stiffening of the actin filaments [190, 400]. By contrast, compliant crosslinker proteins such as filamin A introduce a more complex strain-stiffening mechanism where the crosslinker compliance dominates at small strain and the more rigid actin filaments dominate at larger strain [401, 402]. To our knowledge, there have not been any systematic experimental studies of the mechanics of crosslinked F-actin-vimentin composite networks.

In this chapter we reconstitute crosslinked F-actin-vimentin composite networks utilizing the engineered plectin-mimicking crosslinker ACTIF developed in Chapter 4 and study the mechanical properties of these networks. Since our biophysical characterization in Chapter 4 showed that ACTIF can also crosslink single-component F-actin or vimentin networks [217], we systematically compare the impact of ACTIF on F-actin networks, vimentin networks, and finally F-actin-vimentin composites. Specifically, we measured the elastic response of the networks to small as well as large deformations for different crosslinker/filament concentration ratios. Our results reveal that ACTIF strongly stiffens F-actin networks but has a minor effect on vimentin networks, likely due to competition with tail-mediated vimentin-vimentin crosslinking. We further show that crosslinking F-actin and vimentin results in composite networks with strongly enhanced elastic properties, pointing to crosslinker-mediated mechanical synergy between the two semiflexible polymers. These results set the basis for further understanding the mechanical properties of crosslinked semiflexible biopolymers of different persistence lengths and for understanding the contribution of crosslinker-mediated cytoskeletal crosstalk to cell mechanics.

5.2. RESULTS

We designed the ACTIF crosslinker such that it dimerizes via a cortexillin coiled-coil domain, in order to mimic the dimeric state of plectin. Its dimeric nature implies that ACTIF has two potential binding domains available for vimentin as well as for F-actin. We therefore first checked the ability of ACTIF to crosslink vimentin and F-actin in single-filament type networks. We reconstituted vimentin and F-actin networks at the same monomer concentration of $18 \mu\text{M}$ and $24 \mu\text{M}$, respectively, with a range of ACTIF:vimentin crosslinking ratios. In the here presented study we do not use the mesh size as a control parameter due to the crosslinker ACTIF having different binding affinities for actin and vimentin [217] and the potential architectural homogeneities that may emerge from its crosslinking activity (making a mesh size control not our main premise for the study). Afterwards we reconstituted composite actin-vimentin networks to test for mechanical synergy. Below we present the data, first for vimentin, then actin, and finally vimentin-actin composites.

5.2.1. IMPACT OF ACTIF ON VIMENTIN NETWORKS

LINEAR MECHANICS OF VIMENTIN NETWORKS

We compared the rheological properties of vimentin networks (18 μM) crosslinked with different ACTIF-vimentin monomer molar ratios of 1:100 (0.18 μM ACTIF), 1:50 (0.36 μM ACTIF), 1:25 (0.72 μM ACTIF), and 1:10 (1.8 μM ACTIF) to control vimentin networks formed in absence of ACTIF. Time-dependent monitoring of network formation by small amplitude oscillatory measurements showed that the control networks reached a steady-state elastic modulus G' of approximately 2 Pa over a time period of 1-1.5 hours (lightest curve in Figure 5.1A). Crosslinked networks with the lowest (1:100) or highest (1:10) ACTIF:vimentin ratio reached a comparable stiffness as the control networks (Figure 5.1). Interestingly, networks crosslinked at intermediate ACTIF:vimentin ratios (1:50 and 1:25) reached a higher stiffness of ~ 5 Pa on average. These findings suggest that ACTIF provides crosslinks between vimentin filaments with a measurable impact on network stiffness for sufficiently high ACTIF-vimentin ratios. The observation that the stiffening impact is lost at the highest ACTIF:vimentin ratio could potentially reflect a competition with ionic crosslinks mediated by the C-terminal tail domains that decorate the surface of vimentin filaments. It has been established in earlier work that the tails crosslink vimentin networks even in absence of crosslinker proteins [315, 199, 202]. We speculate that high concentrations of ACTIF may perturb this crosslinking mechanism. Alternatively, it is conceivable that ACTIF generates network inhomogeneities by bundling vimentin filaments. Theoretical models suggest that bundling of semiflexible polymers may lower the elastic modulus by causing the network deformation to become more nonaffine [164]. Future confocal imaging will be needed to test this alternative explanation.

We then proceeded to measure the linear viscoelastic response of the fully formed networks by applying small amplitude oscillatory shear with a strain amplitude of 1% while varying the frequency logarithmically between 0.001 and 10 Hz (frequency sweep protocol). We determined the network elastic (storage) shear modulus, G' , and viscous (loss) modulus, G'' , from the stress response (Figure 5.1B). Consistent with the time sweep data discussed above, the elastic modulus showed a nonmonotonic dependence on ACTIF concentration (Figure 5.1C). Networks with the lowest (1:100) and highest (1:10) ACTIF:vimentin ratios had an elastic modulus of ~ 2 Pa (at a frequency of 1 Hz) comparable to that of control networks. By contrast, networks with intermediate crosslink densities (1:50 and 1:25 ACTIF:vimentin ratios) were stiffer, with an elastic modulus of ~ 4 Pa. All networks behaved as soft elastic solids, with $G' > G''$ over the entire frequency range and a weak power law dependence of G' on frequency, characteristic of soft matter systems with a wide range of relaxation time scales (see Figure 5.1B top). All networks showed a power-law dependence of G' on frequency with an exponent of ~ 0.081 . The loss tangents $\tan(\delta) = \frac{G''}{G'}$ were slightly smaller for the networks with intermediate ACTIF:vimentin crosslink ratios (1:100 and 1:50) as compared to the other networks (see Figure 5.1B bottom), indicating a slightly more solid-like character consistent with their larger elastic modulus. The most highly crosslinked networks (1:25 and 1:10 ACTIF:vimentin ratios) had comparable loss tangents as control networks. However, we note that the loss tangent data were quite noisy since the stress was close to the sen-

sitivity limit of the rheometer. In conclusion, ACTIF is capable of crosslinking vimentin networks, but with a nonmonotonic concentration dependence.

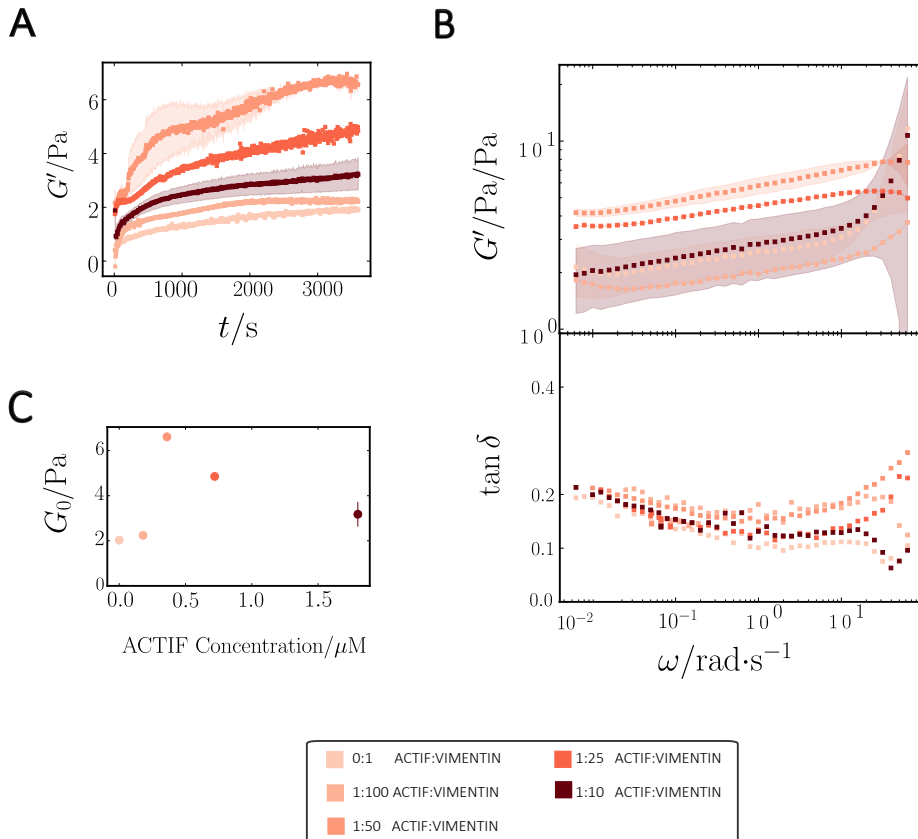


Figure 5.1: (A) Polymerization curves for vimentin (18 μM) polymerized without or with ACTIF (left), colored by ACTIF:vimentin molar ratio. Plots show the evolution of the linear storage moduli, G' , as a function of polymerization time, measured by time-resolved small strain amplitude oscillations. (B) Frequency sweep showing the dependence of the linear elastic modulus (Top) and loss tangent (Bottom) on oscillation frequency for the same networks. (C) Elastic modulus G_0 at $6.28 \text{ rad} \cdot \text{s}^{-1}$ (i.e. 1 Hz) of the vimentin networks as a function of the ACTIF concentration. The color code is the same for all panels (legend at the bottom).

NONLINEAR MECHANICS OF VIMENTIN NETWORKS

To probe the nonlinear response of the vimentin networks to large shear loads, we performed stress ramps with a constant loading rate of $1 \cdot 10^{-3}$ decades of stress per second. We determined the tangent modulus K' by differentiating the stress-strain curves and normalized it by the linear modulus K'_0 (Figure 5.2A). The control vimentin networks without ACTIF showed a linear regime of constant elastic modulus up to an onset strain γ_0 of ~ 0.5 , followed by a pronounced two-stage strain-stiffening response. An initial steep stiffening regime was followed by a regime of slightly less steep stiffening. This

strain-dependence is consistent with previous studies showing that the first regime represents entropic strain-stiffening, where thermal bending undulations of the vimentin filaments are pulled out, while the second regime represents an enthalpic regime, where the vimentin filament backbones are stretched out [197]. Replotting the data in terms of K' versus stress (Figure 5.2B), we find that K' initially increases as a power law in stress with a power law exponent close to 3/2 (indicated by the dashed line), consistent with entropically driven stiffening [197, 403, 164]. We can furthermore observe that the control vimentin network stiffens by an impressive factor of ~ 100 before rupturing at a stress of ~ 120 Pa (see Figure 5.1C), highlighting the elastomeric character of vimentin filaments.

Interestingly, the corresponding networks crosslinked via ACTIF over the whole range of ACTIF:vimentin ratios (1:100 to 1:10), all showed an initial shear-softening response before undergoing strain-stiffening (Figure 5.2A). Since the control network does not show this softening response, we suspect that this initial softening originates from unbinding of ACTIF-mediated crosslinks between vimentin filaments. If true, this would indicate that ACTIF forms crosslinks that are more likely to dissociate than crosslinks mediated by the C-terminal vimentin tails at this specific loading rate. We furthermore observe in Figure 5.2A that, once the crosslinked networks start to strain-stiffen, the K' -strain curves overlap for all crosslinker ratios. Replotting the data in terms of K' versus stress (Figure 5.2B), we see that K' increases as $\sigma^{3/2}$, as for the control network. The rupture stress where the networks fail shows an interesting nonmonotonic dependence on the ACTIF concentration (Figure 5.2C). In the presence of ACTIF, the rupture stress initially increases with increasing ACTIF concentration, but eventually it falls back to the same low value measured at the lowest ACTIF concentration. This nonmonotonic concentration dependence mirrors the nonmonotonic dependence of the linear modulus on ACTIF concentration and again suggests an interesting competition between ACTIF-mediated versus vimentin tail-mediated crosslinks to the mechanical integrity of the networks. Interestingly, in the presence of ACTIF, the rupture stress is always smaller than for uncrosslinked networks. This observation suggests that tail-mediated crosslinks dominate the network strength at high strains.

EFFECT OF C-TERMINAL VIMENTIN TAILS ON THE MECHANICAL RESPONSE

To test our hypothesis that ACTIF competes with vimentin tail-mediated crosslinking, we turned to tail-truncated vimentin where the C-terminal region starting from residue 411, considered the last one in the central α -helical rod domain, is removed. [404, 315]). Earlier studies showed that tail-truncated vimentin can still form elastic self-supporting networks [315] with an identical linear elastic modulus to full-length vimentin [200], but it has largely lost the strain-stiffening ability of full-length vimentin [200]. Hence this work concluded that tail-mediated crosslinking is essential for maintaining network integrity and mediating strain-stiffening under large shear. We note that since tail-truncated vimentin forms thicker filaments than full length vimentin [405], it is important to perform these rheological comparisons at vimentin concentrations adjusted such that the networks have the same filament length per volume. Specifically, we reconstituted tail-truncated vimentin networks at a protein concentration of $63\ \mu\text{M}$, which corresponds to a filament length per volume of $2.34 \cdot 10^{13}\ \text{m}^{-2}$ given a mass-length ratio

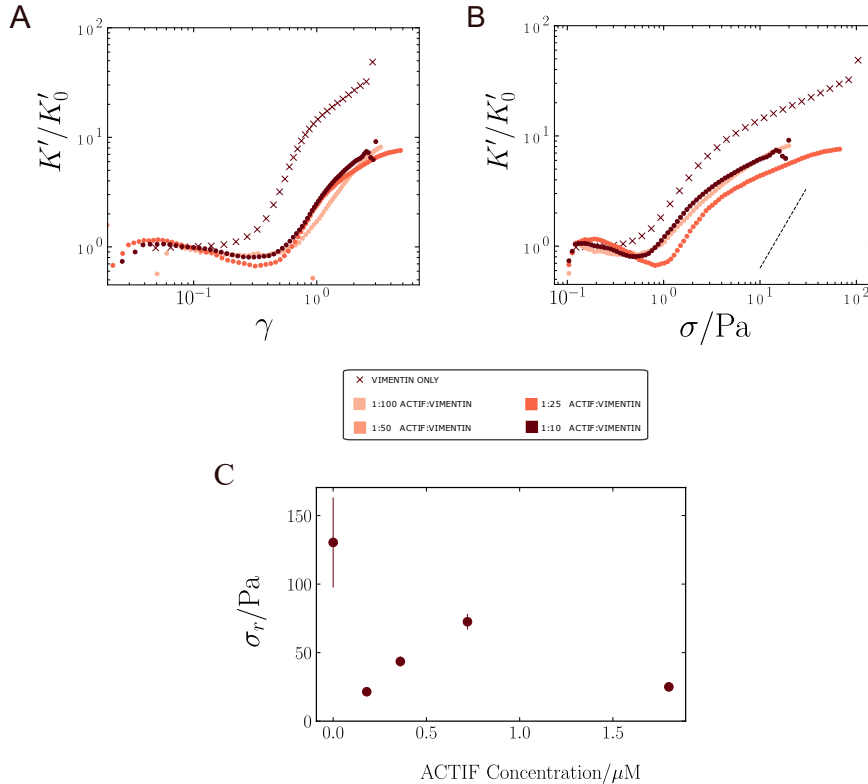


Figure 5.2: (A) Strain-dependence of the differential modulus K' normalized by the linear modulus, determined by stress ramp measurements with a constant loading rate of $1 \cdot 10^{-3}$ decades of stress per second. Legend in the square in the bottom, common with the next panel. (B) Same data, but plotted as a function of applied shear stress. The dashed line serves as a guideline for power law stiffening with an exponent of $3/2$, expected in case of entropically driven stiffening. Legend in the square in the bottom, common with the previous panel. (C) Rupture stress plotted against ACTIF concentration. The rupture stress corresponds to the stress where K' reaches its maximum value.

of $48 \text{ kDa} \cdot \text{nm}^{-1}$ [315], matching the filament length per volume reached by full length vimentin at $18 \mu\text{M}$ (which has a mass-length ratio of $53 \text{ kDa} \cdot \text{nm}^{-1}$ [315, 39]).

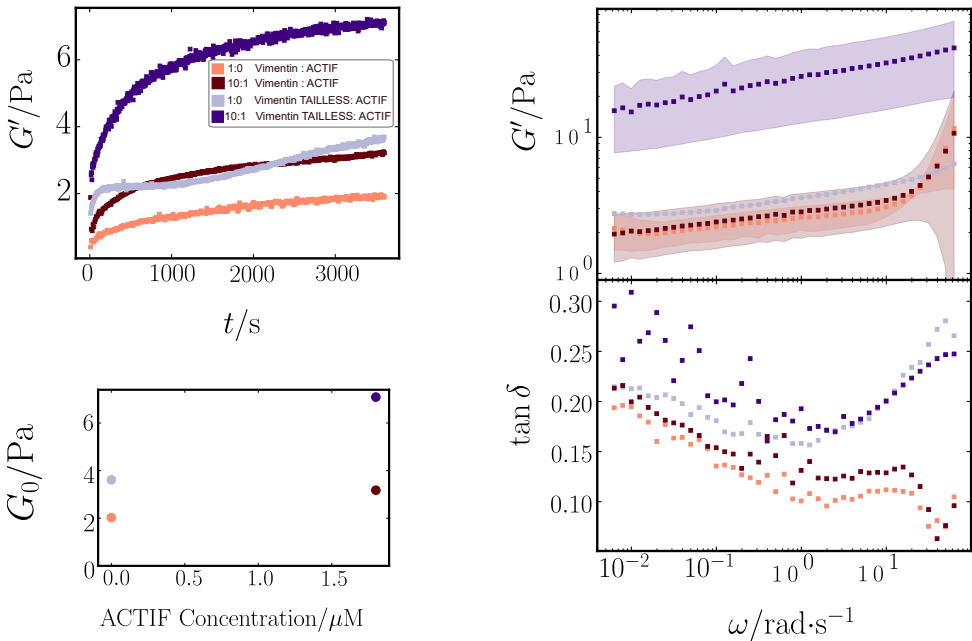


Figure 5.3: (A) Polymerization curves for tail-less vimentin ($63 \mu\text{M}$, blueish curves) and full length vimentin ($18 \mu\text{M}$, reddish curves) with ACTIF (darker curves) or without ACTIF (lighter curves). Plots show the evolution of the linear storage moduli as a function of polymerization time, measured by time-resolved small amplitude oscillations. (B) Frequency sweep showing the dependence of the linear elastic modulus (Top) and loss tangent (Bottom) on oscillation frequency for the same networks. (C) Elastic modulus G_0 at $6.28 \text{ rad} \cdot \text{s}^{-1}$ (i.e. 1 Hz) of the vimentin and tail-less vimentin networks as a function of the ACTIF concentration. The color code is the same for all panels (see legend in panel A).

The networks of full length and tail-truncated (tail-less) vimentin were polymerized for one hour at 37°C , in presence or absence of ACTIF (see Figure 5.3A). In absence of ACTIF, networks of full length vimentin (orange curve) and tail-less vimentin (light blue curve) reached a similar final stiffness of $\sim 2 \text{ Pa}$, as expected based on prior studies. Full length vimentin crosslinked with ACTIF at a 10:1 vimentin:ACTIF ratio reached the same stiffness (dark red curve). Interestingly, however, tail-less vimentin networks crosslinked with ACTIF (dark blue curve) reached a larger final modulus of $\sim 6 \text{ Pa}$.

All networks showed a power-law dependence of G' on frequency with an exponent of ~ 0.08 (Figure 5.3B (top)). Crosslinked tail-less vimentin networks were more solid-like ($\tan \delta < 0.2$, dark violet curve in Figure 5.3B(bottom)) than their non-crosslinked counterpart and than full length vimentin with/without ACTIF ($\tan \delta > 0.15$, light green curve in Figure 5.3B(bottom)). Note that the loss tangent is noisy because the applied strain and the shear moduli (especially G'') are small, so the stress is close to the sensitivity limit of the rheometer. The higher stiffness and more solid-like nature of crosslinked tail-less vimentin networks as compared to crosslinked full length vimentin networks is

consistent with our hypothesis that ACTIF competes with tail-mediated crosslinks: in absence of tails, ACTIF becomes the dominant crosslinker.

Finally we also compared the nonlinear response of full length and tail-less vimentin network in absence and presence of ACTIF. Figure 5.8A shows the strain dependence of K'/K_0 , while Figure 5.8B shows the same data plotted as a function of stress. In absence of ACTIF, the tail-less vimentin network strain-softened, in contrast to its strain-stiffening full-length counterpart. Surprisingly, in presence of ACTIF, the crosslinked tail-less vimentin network still did not stress-stiffen (violet curve, see Figure 5.4B), unlike full length vimentin with and without ACTIF (see orange and red curve in Figure 5.4B). This observation suggests that the vimentin tails are important for strain-stiffening of full length vimentin, and that ACTIF-mediated crosslinkers alone are unable to support strain-stiffening, either because they dissociate under load or because the causing bundling and hence a nonaffine strain-weakening response. Future confocal imaging will be needed to help distinguish between these scenarios by revealing the impact of ACTIF on the network microstructure.

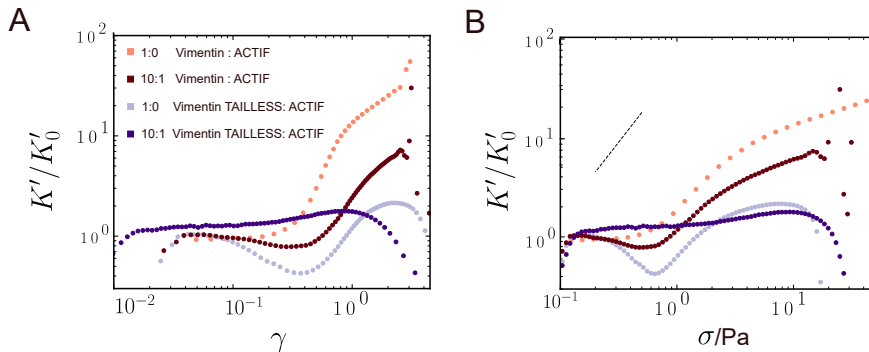


Figure 5.4: (A) Normalized differential modulus K' of tail-less vimentin ($63 \mu\text{M}$, blueish curves) and full length vimentin ($18 \mu\text{M}$, reddish curves) polymerized with ACTIF (darker curves) or without ACTIF (lighter curves) as a function of shear strain, determined by stress ramp experiments. (B) Same data replotted as a function of applied shear stress. The dashed line serves as a guideline for power law stress-stiffening with an exponent of $3/2$.

5.2.2. IMPACT OF ACTIF ON F-ACTIN NETWORKS

LINEAR MECHANICS OF F-ACTIN NETWORKS

We next tested whether ACTIF is also capable of crosslinking F-actin networks. We reconstituted control F-actin network at a concentration of $24 \mu\text{M}$ and compared it to networks assembled in the presence of ACTIF at different ACTIF:actin ratios. Specifically, we tested ACTIF:actin ratios of 1:60 ($0.4 \mu\text{M}$ ACTIF), 1:30 ($0.8 \mu\text{M}$ ACTIF) and 1:10 ($2.4 \mu\text{M}$ ACTIF). As shown in Figure 5.5A, control networks reached a modulus of $\sim 2 \text{ Pa}$ after 2 hours. The elastic modulus of the crosslinked networks progressively increased with increasing ACTIF concentration, from $\sim 2.5 \text{ Pa}$ (1:60 ACTIF:actin ratio) to $\sim 4 \text{ Pa}$ (1:30

ACTIF:actin ratio) to ~ 15 Pa (1:10 ACTIF:actin ratio). This dose-dependent stiffening provides clear evidence that ACTIF is capable of crosslinking actin filaments.

The final elastic modulus showed weak power-law scaling with frequency (see Figure 5.5B(top)) with an exponent $\alpha \sim 0.189$ for control networks. In presence of ACTIF, the exponent decreased in a dose-dependent manner, from $\alpha \sim 0.135$ (1:60 ACTIF:actin), to $\alpha \sim 0.073$ (1:30 ACTIF:actin), to $\alpha \sim 0.0346$ (1:10 ACTIF:actin). This observation indicates that ACTIF slows down stress relaxation through crosslinking of actin filaments. Interestingly, the elastic modulus G_0 (extracted as the modulus at $6.28 \text{ rad} \cdot \text{s}^{-1}$) increased monotonically with ACTIF concentration in a stronger than linear fashion (Figure 5.5C). We fitted the data with $G(cActif) = G(0) + A * [ACTIF]^x$ and obtained a concentration exponent of $x = 1.92$ and the free parameter in the feet, $G(0)$, $G(0) = 5.68 \text{ Pa}$ (dashed line in Figure 5.5C). At the same time, the crosslinked network with the highest actin:ACTIF ratio (10:1) was significantly more solid-like (with $\tan\delta \sim 0.1$) as compared to more weakly crosslinked and uncrosslinked networks ($\tan\delta \sim 0.2$) (see Figure 5.5B(bottom)). Together, these observations confirm that ACTIF is capable of crosslinking actin filaments.

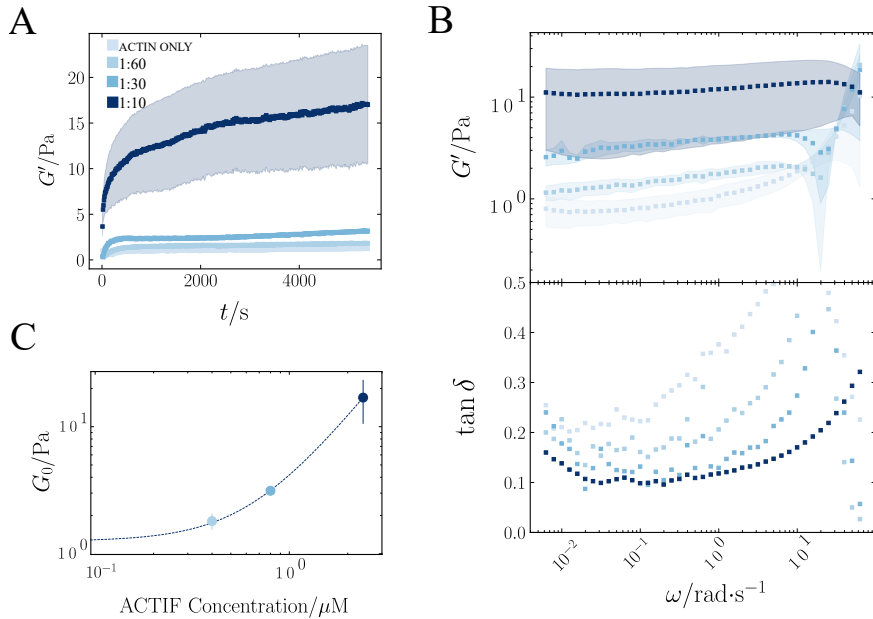


Figure 5.5: (A) Polymerization curves for actin ($24 \mu\text{M}$) polymerized with or without ACTIF, color-coded by ACTIF:actin ratio as indicated in the legend (which applies to all panels). Plots show the evolution of the linear storage moduli as a function of polymerization time, measured by time-resolved small amplitude oscillations. (B) Frequency sweep showing the dependence of the linear elastic modulus (Top) and loss tangent (Bottom) on oscillation frequency for the same networks. (C) Elastic modulus G_0 at $6.28 \text{ rad} \cdot \text{s}^{-1}$ (i.e. 1 Hz) of the actin networks as a function of the ACTIF concentration. Dashed line shows a fit to the equation $G(cActif) = G(0) + A * [ACTIF]^x$ with $x = 1.92$ and $G(0) = 5.68 \text{ Pa}$.

NONLINEAR MECHANICS OF F-ACTIN NETWORKS

To test the impact of ACTIF on the nonlinear elastic response of actin networks, we again performed stress ramps. The control (non-crosslinked) actin networks had a small modulus and fluidized when the strain increased (crosses in Figure 5.6A). By contrast, the crosslinked networks displayed strain-stiffening behavior, albeit only over a narrow strain regime (circles in Figure 5.6A, color-coded by ACTIF:actin ratio). Crosslinking by ACTIF is indeed expected to prevent actin network fluidization and to introduce a strain-stiffening response. Replotting the data in terms of K' versus stress (Figure 5.6B), we see that when the ACTIF:actin ratio increases, the networks tolerate larger shear stresses and stiffen more. This trend is summarized in Figure 5.6C, which shows that the rupture stress significantly increases with increasing ACTIF concentration.

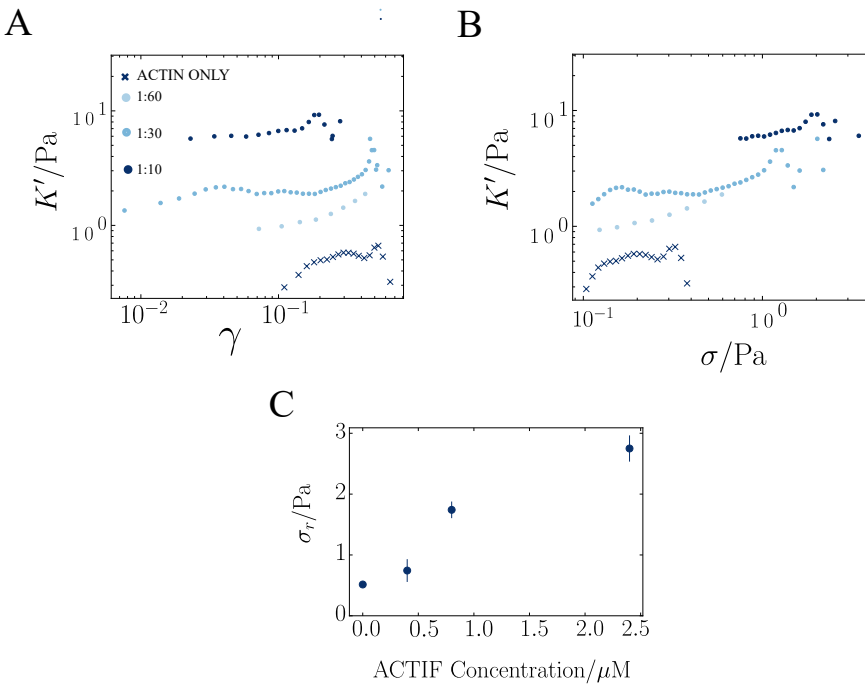


Figure 5.6: (A) Differential elastic modulus of actin networks with and without ACTIF as a function of shear strain, determined by stress ramp experiments. (B) Same data replotted as a function of shear stress. (C) Rupture stress (crosslinked networks) and fluidization stress (control network) plotted against ACTIF concentration.

5.2.3. IMPACT OF ACTIF ON COMPOSITE F-ACTIN-VIMENTIN NETWORKS

Having established that ACTIF is capable of crosslinking F-actin and vimentin individually, we then proceeded to study the mechanical properties of composites of F-actin and vimentin crosslinked via ACTIF. We studied composites with constant concentrations of 24 μM actin and 18 μM vimentin, crosslinked with ACTIF at different concentrations of

ACTIF. We explored different protein:ACTIF ratios, where 'protein' stands for the total concentration of G-actin and vimentin monomers (details in Appendix Table 5.1).

LINEAR MECHANICS OF COMPOSITE F-ACTIN-VIMENTIN NETWORKS

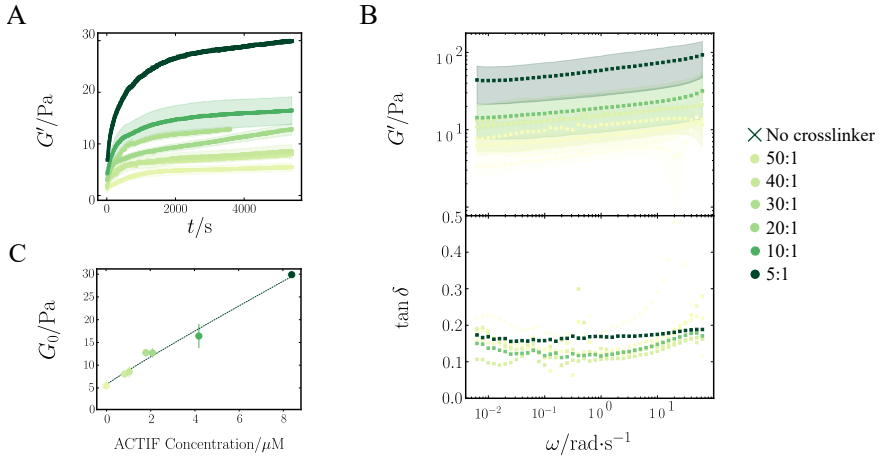


Figure 5.7: (A) Polymerization curves for composite networks of actin (24 μ M) and vimentin (18 μ M) co-polymerized in the presence or absence of ACTIF. The curves are color-coded by ACTIF:protein ratio as indicated in the legend on the far-right. Note that 'protein' stands for the total concentration of actin + vimentin (42 μ M). Plots show the evolution of the linear storage moduli as a function of polymerization time measured by time-resolved small amplitude oscillations. (B) Frequency sweep showing the dependence of the linear elastic modulus (Top) and loss tangent (Bottom) on oscillation frequency for the same networks. (C) Elastic modulus G_0 at 6.28 rad·s⁻¹ (i.e. 1 Hz) of the composite F-actin-vimentin networks as a function of the ACTIF concentration. The line shows a linear fit according to $G(cActif) = G(0) + A * [ACTIF]^x$, with $x = 0.98$ and $G(0) = 1.25$ Pa.

To test whether ACTIF crosslinkers can stiffen F-actin-vimentin composites, we first monitored the evolution of the linear elastic modulus during network formation. As shown in Figure 5.7A, the actin-vimentin networks were soft (~ 5 Pa) in absence of ACTIF but 6-fold stiffer (~ 30 Pa) at the highest protein:ACTIF ratio of 5:1, confirming crosslinking activity of ACTIF. Both non-crosslinked and crosslinked composite networks showed a weak power law increase of the linear elastic modulus with frequency with an exponent of ~ 0.077 (Figure 5.7B(top)). This value is comparable to the power law exponents we observed for single-polymer networks of F-actin and vimentin, indicating all networks present similar stress relaxation dynamics over the studied frequency range. However, crosslinked composites at the highest (5:1) protein:ACTIF ratio were significantly more solid-like ($\tan \delta < 0.2$, dark green curve in Figure 5.7B(bottom)) than their non-crosslinked counterpart ($\tan \delta > 0.2$, light green curve in Figure 5.7B(bottom))). The elastic modulus G_0 extracted at a single frequency (1 Hz) shows an interesting linear dependence on ACTIF concentration (see Figure 5.7C), different from the nonmonotonic dependence observed for vimentin and the near-quadratic dependence observed for F-actin.

NONLINEAR MECHANICS OF F-ACTIN-VIMENTIN COMPOSITE NETWORKS

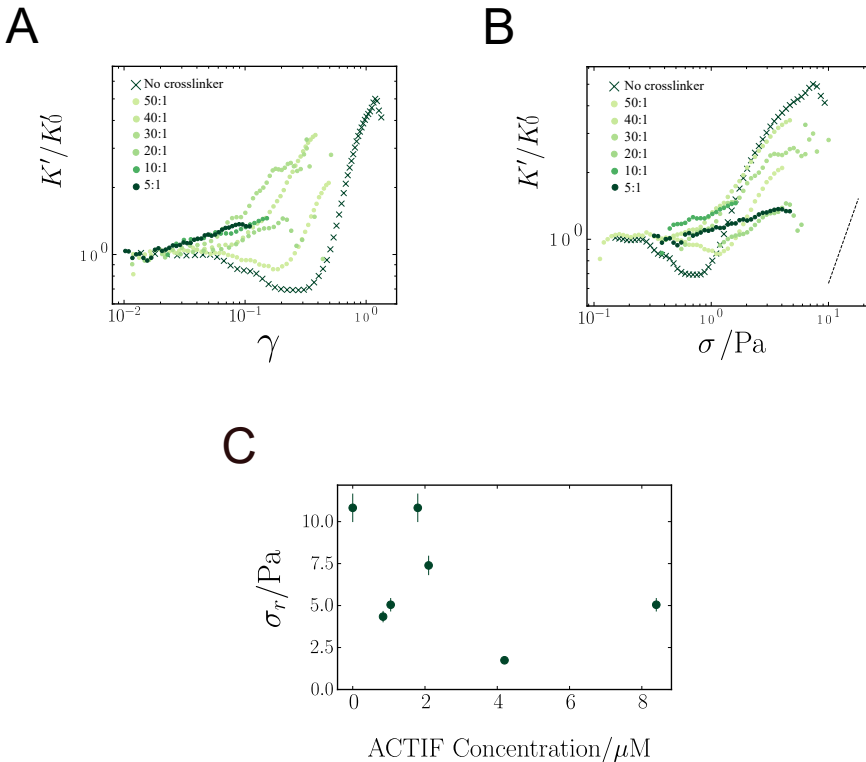


Figure 5.8: (A) Normalized differential modulus K' of F-actin-vimentin composite networks as a function of shear strain, determined by stress ramp experiments. (B) Same data replotted as a function of shear stress. The dashed line serves as a guideline for power law stress-stiffening with an exponent of 3/2. (C) Rupture stress plotted against ACTIF concentration.

When probed by stress ramps, we found that control (non-crosslinked) F-actin-vimentin composite networks initially softened, followed by a stiffening regime (crosses in Figure 5.8A). When we replot the data as a function of shear stress (crosses in Figure 5.8B), we observe that the control networks reach a final modulus of ~ 70 Pa before rupturing at a stress of ~ 10 Pa. When ACTIF is added, we observe a complex dependence on the protein:ACTIF ratio. At lower ratios (50:1, 40:1, 30:1, and 20:1), the networks gradually lose the initial softening response and strain-stiffening sets in at smaller strain than for the control networks (circles in Figure 5.8A, color-coded by protein-ACTIF ratio). Both effects indicate that ACTIF is capable of crosslinking the networks. At the highest protein:ACTIF ratios (10:1 and 5:1), the networks show only weak strain-stiffening (the two darkest curves in Figure 5.8A). When we replot these data in terms of K' as a function of shear stress, we see that at lower protein:ACTIF ratios (50:1, 40:1, 30:1, and 20:1), the networks tolerate progressively larger shear stresses before rupture as the ACTIF concentration increases (circles in Figure 5.8B). They stress-stiffen according to the $\sigma^{3/2}$ power law

stiffening expected for entropic networks (dashed line). By contrast, at the highest protein:ACTIF ratios (10:1 and 5:1), small shear stresses already induce network rupture (the two darkest curves in Figure 5.8B). This nonmonotonic dependence of the rupture stress on the ACTIF concentration is summarized in Figure 5.8C. When a small concentration of ACTIF is added (protein:ACTIF ratio of 50:1), the rupture stress drastically decreases compared to the control network. This could potentially be an effect of the competition between ACTIF and the vimentin tails in vimentin crosslinking that we noted earlier. Then, as the ACTIF concentration is increased, the rupture stress increases, reaching a maximum value comparable to that of the control network for a protein:ACTIF ratio of 30:1. Apparently, ACTIF is introducing sufficient crosslinks to confer mechanical protection on the networks. However, as the ACTIF concentration is increased even more, the rupture stress decreases again, while finally, at the highest ACTIF concentration (5:1 ratio), the rupture stress slightly increases again. The complex behavior in this regime suggests that the relative contributions of F-actin crosslinking, vimentin crosslinking, and F-actin-vimentin crosslinking to the overall network mechanics may be varying.

5.3. DISCUSSION

In this chapter we investigated the influence of crosslinking between actin and vimentin filaments on the mechanical properties of composite F-actin-vimentin networks. For this purpose, we used an engineered crosslinker called ACTIF, which mimics the crosslinking functionality of plectin, one of the main crosslinkers in the cell. We showed in Chapter 4 by biochemical and single-molecule imaging assays that ACTIF is capable of binding, crosslinking and bundling vimentin and F-actin, both individually and together. We attributed this to the fact that ACTIF is a dimer, so it has two binding domains for F-actin as well as for vimentin. Based on these observations we anticipated complex effects of ACTIF on the mechanics of composite F-actin-vimentin networks, and therefore systematically compared the effect of ACTIF on single-polymer networks of F-actin or vimentin versus composite networks. Our data shows that ACTIF is indeed capable of crosslinking vimentin as well as F-actin networks, confirming that ACTIF has two binding domains available for both polymers. We furthermore found that ACTIF is capable of crosslinking F-actin-vimentin composite networks, thereby introducing strong mechanical synergy. We furthermore uncovered several interesting unanticipated effects pointing to a competition of ACTIF-mediated crosslinking with vimentin tail-mediated crosslinking.

When vimentin was polymerized in the presence of ACTIF, we observed a striking nonmonotonic dependence of the network elastic modulus on ACTIF concentration, with an optimum at intermediate ACTIF concentrations. Similarly, the rupture stress of the networks showed an optimum at intermediate ACTIF concentrations and networks crosslinked with ACTIF were always weaker (i.e., having a lower rupture stress) than control networks. Together, these observations strongly hint that ACTIF provides crosslinks by forming ACTIF-mediated bonds between vimentin filaments, but at the same time disrupts crosslinks formed by vimentin's C-terminal tail domains [200]. Interestingly, we found that ACTIF much more strongly enhanced the elastic modulus of tail-less vimentin networks than of full length vimentin networks, suggesting that

conversely, tail-mediated crosslinking also interferes with ACTIF-mediated crosslinking. This further reinforces the notion of a competition between ACTIF- versus tail-mediated crosslinking. The observation that ACTIF-crosslinked vimentin networks have a smaller rupture stress than control networks suggests that ACTIF crosslinkers dissociate more easily under tensile loading than tail-tail crosslinks. This idea is reinforced by the observation that tail-less vimentin networks crosslinked with ACTIF did not stress-stiffen. Indeed tail-mediated crosslinking has the benefit of high avidity, with bonds being individually weak but collectively strong [200]. In future it will be interesting to dissect the crosslinking competition between ACTIF and the vimentin tails by performing stress ramps at different loading rates, potentially coupled with single-molecule measurements of the loading-rate dependent binding affinities [406]. In addition, it will be important to test whether ACTIF introduces any changes in network structure through confocal fluorescence imaging. Higher ACTIF concentrations may cause vimentin filament bundling, which is expected to repress strain-stiffening by causing a nonaffine mechanical response.

When actin was polymerized in the presence of ACTIF, we observed a clear dose-dependent increase of both the linear modulus and the rupture stress of the networks with ACTIF concentration. This provides strong evidence that ACTIF is capable of crosslinking actin filaments. The networks stress-stiffened only weakly and only over a narrow window of shear stress (and strain), which is reminiscent of the behavior of F-actin networks crosslinked with fascin [407]. Fascin was shown to cause F-actin bundling, hence causing a highly nonaffine mechanical response characterized by weak (enthalpic) stiffening, in contrast to the strong (entropic) stiffening seen for isotropically crosslinked actin networks [400, 190, 401]. To test this interpretation, it will be important to perform confocal imaging of the actin networks as a function of ACTIF concentration.

When F-actin-vimentin composite networks were polymerized in the presence of ACTIF, we observed a linear increase of the elastic modulus with increasing ACTIF concentration, reflecting a dose-dependent increase in network connectivity. By contrast, the rupture stress showed a much more complex, nonmonotonic dependence on ACTIF concentration. We conclude that ACTIF is capable of crosslinking the composite networks and introducing mechanical synergy, but in a complex concentration-dependent manner. There are likely different crosslinking mechanisms at play: ACTIF can crosslink F-actin-to-vimentin, but also F-actin to F-actin, and vimentin-to-vimentin. The relative contributions of these three crosslinking mechanisms will depend on the (load-dependent) binding affinities associated with these interactions. Our kinetic measurements under stress-free conditions reported in Chapter 4 showed that ACTIF has a 700 times higher binding affinity for vimentin as compared to F-actin [217]. This would suggest that the stiffness and mechanical resilience of the composites is dominated by vimentin, and that F-actin should only come into play at high crosslinker and/or F-actin concentrations. Consistent with this idea, the stress ramp data show that the strain-stiffening response of composite networks transforms from a more vimentin-like response at low ACTIF concentration to a more actin-like response at high ACTIF concentration. Our working hypothesis is that the majority of the filament-bound ACTIF pool resides on vimentin filaments. The ACTIF-coated vimentin filaments can engage in crosslinks with either F-actin and vimentin filaments that are in close proximity, depen-

dent on the relative proportions of F-actin and vimentin in the composites. In future, we plan to test this idea by measuring the impact of the F-actin and vimentin concentrations on the rheology of the composites. We note that competition between ACTIF and tail-mediated crosslinking makes the behavior of the composites even more complex. To pinpoint this particular effect, it would be interesting to perform rheological tests on composite networks of F-actin with tail-less vimentin. We further note that it will be important to test the impact of ACTIF on the microstructure of the networks. Prior work showed that F-actin and vimentin composites in absence of any crosslinker form an isotropic and homogeneous network [326]. We anticipate that ACTIF causes bundling of F-actin and vimentin (on their own or in mixed bundles), especially at higher concentrations [217].

5.4. CONCLUSION

In this chapter we characterized the impact of crosslinking on the mechanical properties of F-actin-vimentin composite networks, using an engineered ACTIF crosslinker that mimics the physiological function of plectin. We showed that ACTIF is capable of crosslinking vimentin as well as F-actin networks, implying that ACTIF has two binding domains available for both polymers. We furthermore found that ACTIF is capable of crosslinking F-actin-vimentin composite networks, thereby introducing strong mechanical synergy. We uncovered several interesting unanticipated effects that arise from differences in the binding affinity of ACTIF for vimentin versus F-actin and from a likely competition between ACTIF-mediated versus vimentin tail-mediated interactions. These results form an exciting basis for understanding the mechanical properties of F-actin-vimentin composites, but we acknowledge that more information (especially regarding the network microstructure) is needed to draw firm conclusions. At the same time, this work also provides basis for understanding the contribution of crosslinker-mediated cytoskeletal crosstalk to cell mechanics (see Chapter 7).

5.5. METHODS

5.5.1. PROTEIN PURIFICATION AND RECONSTITUTION

Protein purification and characterization (in terms of purity and - in case of ACTIF - oligomerization status) as well as sample preparation were performed as reported in the Methods section of Chapter 4.

5.5.2. RHEOLOGY

Rheological measurements were conducted using a stress-controlled Malvern Kinexus Pro rheometer and TA HR-2 rheometer, both equipped with a stainless steel cone-plate geometry. For both, the cone had a radius of 20 mm and an angle of 1°. The temperature was maintained at ~37°C by Peltier plates. Networks were polymerized between the plates of the rheometer by loading 40 μ l of the sample directly after mixing the proteins

in F-buffer; we always added the protein mix last (i.e G-actin, vimentin, or pre-mixed composite of G-actin and vimentin; with or without ACTIF). To prevent solvent evaporation during the experiment, a thin layer of mineral oil Type A (Sigma Aldrich, #8042475) was carefully applied around the sample edge with a 200 μL pipette tip by placing some drops around the top geometry and letting the oil flow and cover the geometry contour. Progress of network formation was monitored by applying a small strain amplitude (0.5%) oscillatory shear with an oscillation frequency of 0.5 Hz for a duration of 1.5 to 2 hours. Following this polymerization period, a frequency sweep was conducted in the range of 0.01 to 10 Hz at a small strain amplitude of 1%, sampling 10 data points per decade. Data taken at frequencies exceeding 3 Hz had to be discarded because they were dominated by inertial effects from the rheometer. For each curve, we took an average over $N = 3$ independently prepared samples (except for crosslinked tail-less vimentin sample (dark violet curve) in Figures 5.3 and 5.4, where $N=2$. For nonlinear rheology experiments, we implemented a stress ramp protocol following earlier work on vimentin [200], where the stress was steadily increased from 10 to 1000 Pa at a loading rate of $1 * 10^{-3}$ decades of stress per second. The differential elastic modulus K' was obtained by differentiating the stress-strain curve with a custom-written python script.

5.6. ACKNOWLEDGEMENTS

I would like to thank Quang Duc Tran, Cécile Leduc and Jeffrey den Haan for their invaluable help with wild-type and tail-less vimentin purification. I furthermore thank Fred MacKintosh for valuable discussions about the rheology data.

5.7. APPENDIX

Protein:ACTIF ratio	ACTIF concentration (μM)
No crosslinker	0
50:1	0.84
40:1	1.05
30:1	1.4
20:1	2.1
10:1	4.2
5:1	8.4

Table 5.1: ACTIF concentrations and corresponding protein:ACTIF ratios in experiments on reconstituted composite networks of $24\mu\text{M}$ actin and $18\mu\text{M}$ vimentin. "protein" refers to actin+vimentin.

6

ENGINEERING A LIBRARY OF TENSION-SENSING ACTIN CROSSLINKERS FOR MOLECULAR-SCALE FORCE MAPPING WITHIN RECONSTITUTED ACTIN NETWORKS

Cells in our body are constantly subjected to a wide range of mechanical forces that regulate essential cellular functions. The cytoskeleton controls the mechanical response of the cell to external forces, actively generates internal forces to deform the cell, and contributes to mechanotransduction. The main component of the cytoskeleton responsible for these functions is the actin cytoskeleton. Actin filaments form various structures, including the cortex and stress fibers, but how these actin structures contribute to the generation and transmission of mechanical forces is unclear. In order to understand these processes better, it would be advantageous to be able to measure the molecular tension distribution within the actin cytoskeleton in cells and in cell-free systems. This Chapter presents a new library of engineered actin crosslinking proteins with embedded FRET-force sensors. Although the purity of the crosslinking proteins is suboptimal, likely due to protein degradation, we were able to prove by rheology that they are mechanically functional, being able to stiffen reconstituted actin network. We end the chapter with a perspective on future applications of the tension-sensing crosslinkers to measure the response of reconstituted actin networks to myosin motor activity.

6.1. INTRODUCTION

The cells in our body are subjected to a wide range of mechanical forces. They sense and respond to those forces in a process known as mechanotransduction [408]. Mechanotransduction is mediated by different subcellular structures, including the plasma membrane and ion channels and adhesion receptors embedded therein [409, 410, 411], the nucleus [412], and the cytoskeleton [408]. Disentangling the contributions of each of these structures to cellular mechanotransduction is a complex task, since it is difficult to map force propagation within the crowded interior of the cell. Nevertheless, there is consensus that the cytoskeleton plays a central role, given its inherent mechanosensitivity (with cytoskeletal proteins being able to undergo force-induced conformational changes) and its connections to all the other mechanosensitive structures. While all four cytoskeletal polymers (filamentous (F)-actin, microtubules, intermediate filaments and septins) contribute to mechanotransduction [413], the role of F-actin has been most widely studied.

The actin cytoskeleton is a complex biopolymer network essential for many cellular processes, including cell division [342], locomotion [20], and cell shape alterations [414]. Its architecture and mechanical properties are finely tuned by dozens of actin-binding proteins that influence the (de)polymerization dynamics and interactions of actin filaments [415]. Among the actin-binding proteins, crosslinking proteins have a particularly strong impact on the architecture and mechanics of the actin cytoskeleton [416]. By connecting pairs of actin filaments, they create crosslinked elastic gels [417, 418] or bundled structures such as stress fibers [11]. Crosslinker proteins also influence the level of contractile prestress in the actin cytoskeleton by tuning the range over which forces generated by myosin motor proteins can propagate [419].

Measuring forces across the actin cytoskeleton requires methods with picoNewton (pN) force sensitivity given that both myosin motors [420] and growing actin filaments [421] exert pN-level forces. Several techniques have been developed to quantitatively measure these forces in cells, including atomic force microscopy (AFM) and optical- and magnetic-tweezer based force spectroscopy [422]. However, it is much less straightforward to measure forces on individual molecules in the crowded interior of the cell than it is *in vitro* [423, 138].

To address this challenge, about 15 years ago a complementary approach was introduced, based on molecular tension sensors. These are force-sensitive molecules whose extension can be detected by Förster Resonance Energy Transfer (FRET) [424]. The basic idea of this method is that fluorophores can non-radiatively transfer energy to each other with a strong (inverse sixth-power) dependence on their separation distance. By connecting a donor fluorophore and an acceptor fluorophore via a deformable linker with known compliance, molecular tension across the linker can be measured from the donor-to-acceptor FRET signal. By incorporating this tension sensing module into a protein of choice, one can then specifically probe the load-bearing role of this protein. This principle was first demonstrated for the actin-crosslinking protein alpha-actinin in 2008 [425]. Since then, a wide range of tension modules based on synthetic molecules, proteins, or nucleic acids have been developed, which have been incorporated into different

mechanosensitive proteins found in focal adhesions, cell-cell contacts, and the nuclear membrane.

Attempts to measure molecular tension related to the actin cytoskeleton have mainly been limited to indirect measurements on tension sensors incorporated in proteins associated with integrin adhesions. It is difficult to infer from these traction forces on the substrate what are the internal forces inside the cell. There have been a few papers where FRET-based tension sensors were physically embedded in the actin cytoskeleton by equipping actin crosslinkers with a molecular tension sensor module [426, 427, 425, 311, 428]. However, it remains challenging to interpret these data because of the enormous molecular and structural complexity of the cytoskeleton.

In vitro (cell-free) studies on networks reconstituted from purified cytoskeletal proteins can greatly facilitate the interpretation of data obtained in cells, as reviewed in Chapter 2. Rheological studies of crosslinked actin networks have for instance helped delineate the mechanical impact of F-actin's semiflexible filament properties and of the binding kinetics of crosslinker proteins [400, 190, 429]. Despite their compositional simplicity, *in vitro* actin networks have complex mechanical properties because actin filaments are semiflexible polymers. Theoretical models predict that semiflexible polymer networks deform nonaffinely and nonlinearly [403]. FRET-based tension sensors in combination with reconstituted actin networks provide an opportunity to test these models experimentally, which could eventually help interpret molecular tension measurements in cells.

In this chapter, we engineered actin crosslinker proteins equipped with a FRET tension sensor module to enable molecular tension measurements in reconstituted F-actin networks. We generated a library of crosslinkers, all with the same F-actin-binding domains (taken from ACF7/MACF [359]) and donor and acceptor fluorophores, but with different mechanosensitive linker peptides. We created crosslinkers with four distinct modules (i.e., two tension sensors and two control modules), developed and calibrated by the Grashoff lab [430, 1, 431]. The two tension sensor modules have different peptide linkers with force sensitivities in the range of 1-6 pN (F40) and 3-5 pN (FL), respectively. We targeted this wide range in order to make sensors available for a range of force-sensing applications, from reconstituted F-actin networks to composite cytoskeletal networks combining actin filaments with microtubules and/or intermediate filaments. We demonstrate by rheology measurements that the engineered crosslinkers stiffen F-actin networks, proving their crosslinking functionality. We end the chapter with a perspective on future applications of the tension-sensing crosslinkers to measure the response of cytoskeletal networks to myosin motor activity or external forces in cell-free systems.

6.2. MEASURING THE FRET EFFICIENCY OF MOLECULAR TENSION SENSORS

Molecular tension sensor modules consist of a donor and an acceptor fluorophore connected by an elastic linker (see Fig. 6.1A). The fluorophores are chosen such that the emission spectrum of the donor overlaps with the absorption spectrum of the acceptor. Upon excitation with light of the right wavelength, the donor can therefore non-

radiatively transfer energy to the acceptor. A popular donor/acceptor fluorophore pair for tension sensors is the combination of the yellow fluorescent protein Ypet¹ and the red fluorescent protein mCherry [432], also used in this Chapter.

The efficiency of non-radiative energy transfer strongly depends on the separation distance r between the fluorophores, hence providing a sensitive readout of force-induced elongation or compression of the linker. The FRET efficiency, E , defined as the fraction of donor molecules that effectively transfer excitation energy to the acceptor, depends on r as:

$$E = \frac{R_0^6}{R_0^6 + r^6} \quad (6.1)$$

R_0 is the Förster distance, which is the distance where the FRET efficiency is 50% (see dashed lines in Fig. 6.1B). In a tension sensor, the separation distance R of the donor and acceptor fluorophores, and hence the FRET efficiency E , will be modulated by the force applied to the tension sensor and the compliance of the linker, as shown in Fig. 6.1B. These two parameters are therefore critical for designing tension sensors for *in vitro* reconstituted networks. We note that R_0 also depends on the relative orientation of the donor and acceptor dipoles. A brief summary of further theoretical considerations to guide the design of FRET sensors can be found in Appendix 6.8.1.

Experimentally, the FRET efficiency is often measured by intensity measurements. Here the donor fluorophore is excited and the FRET ratio is computed from the measured fluorescence emission intensities of both the donor and the acceptor. The advantage of this method is that it can be carried out with standard wide-field or confocal microscopes. An alternative is to use Fluorescence Lifetime Imaging, which requires more specialized equipment but has the benefit of providing a readout of FRET efficiency that is independent of the fluorophore concentrations.

6.3. RESULTS

6.3.1. ENGINEERING, PURIFICATION AND TESTING OF THE HOST ACTIN-CROSSLINKER VECTOR

The first step in creating the library of tension-sensing actin crosslinkers was the engineering and testing of the actin-crosslinker vector in which to host the sensors. We based the design of the crosslinkers on the architectural plan of typical actin crosslinkers such as filamin and α -actinin, which have two F-actin-binding domains (ABDs) separated by a spacer domain. By analogy, we coupled two ABDs by a spacer that contained the tension sensor module. For the F-actin binding functionality, we decided to use the tandem calponin homology domains (CH1-CH2) of ACF7/MACF7 [433] that we already characterized extensively in Chapter 4. We note that calponin-homology domains are ubiquitous actin-binding domains found in many actin-crosslinkers [434]. We obtained the

¹We by default will refer to Ypet as Ypet(short), due to the terminology specified in the plasmid sequence provided for the here implemented FRET cassettes used in [430, 431].

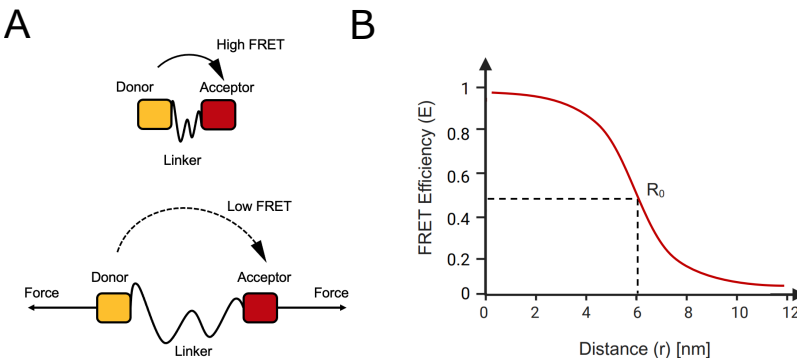


Figure 6.1: (A) The FRET efficiency for a donor-acceptor fluorophore pair connected by an elastic linker region depends on the linker extension. For the relaxed linker, the fluorophores are in close proximity, leading to a high FRET efficiency (top). Upon stretching, the fluorophores are separated and the FRET efficiency decreases (bottom). (B) The FRET efficiency has an inverse sixth power dependence on the donor-acceptor separation distance. The dashed lines indicate the Förster distance R_0 where the FRET efficiency is 50%.

ABP from the actin-microtubule crosslinker protein TipAct previously developed by our lab [359].

We first engineered a host vector for the tension sensors, which we refer to as GFP-ABD-ABD. This protein contained an enhanced green fluorescent protein (GFP) followed by two sets of the CH1-CH2 tandem domains (ABDs) separated by a 4 amino acid linker (Figure 6.2A) and terminating with a 6xHis tag allowing for His-tag affinity purification (see sequence in Appendix Table 6.8). SDS-PAGE gel electrophoresis showed successful recovery of the protein at the expected molecular weight of 84 kDa, although some lower molecular weight bands (\approx 55 kDa, 43 kDa, and 34 kDa) were also present, indicative of proteolytic degradation (Figure 6.2B). Interferometric scattering (iSCAT) measurements on dilute (50 nM) solutions of the GFP-ABD-ABD protein showed the presence of proteins of different molecular weights (Figure 6.2C). The monomer peak at a molar mass of 71 ± 13 kDa contained only 18% of the total counts. We observed three additional peaks, two smaller ones at a molecular weight of 132 ± 23 kDa (19% of the counts) and 257 ± 56 kDa (12% of the counts), and a larger third peak at a molecular weight of 408 ± 36 kDa (49% of the counts). This finding surprised us, since the protein lacks any known oligomerization domains.

To test the F-actin-binding functionality of the GFP-ABD-ABD protein, we first performed total internal reflection fluorescence microscopy of a mixture of 2 μ M actin co-polymerized with 0.5 μ M GFP-ABD-ABD. As shown in Figure 6.2D, the GFP-ABD-ABD crosslinker (green, bottom panel) co-localized with F-actin bundles (blue, middle panel), indicating that the crosslinker indeed binds actin filaments. F-actin bundles were also present in the no-crosslinker actin control sample (Figure 6.2E), indicating that the observed bundling was (at least in part) caused by the methylcellulose (0.15%) we used as a crowding agent. Previous reports showed methylcellulose-induced bundling at similar concentrations [435, 436].

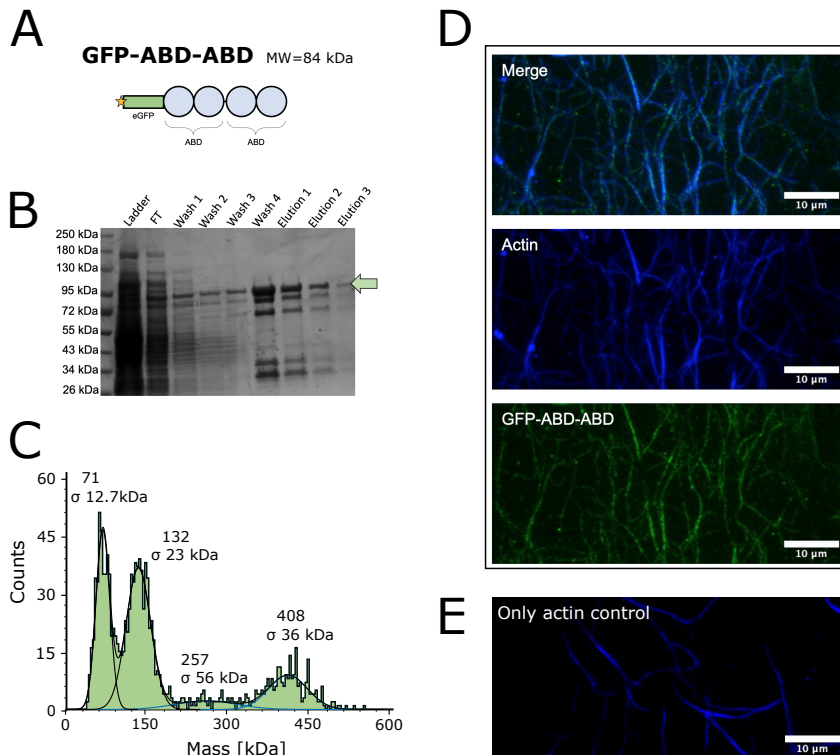


Figure 6.2: Design, purification and functional testing of the host actin-crosslinker vector for the FRET tension sensors. (A) Domain structure of the engineered GFP-tagged actin-crosslinker protein, GFP-ABD-ABD. (B) SDS-PAGE gel analysis of the purified protein, showing a major band at the expected molecular weight (84 kDa, marked with an arrow) together with smaller molecular weight bands indicative of some proteolytic degradation. Lanes from left to right: Ladder (molecular weight marker), FT (Flowthrough), Wash 1 to 4 (consecutive washing steps), Elution 1 to Elution 3 (consecutive elution steps). (C) Interferometric scattering (iSCAT) microscopy histogram for a 50 nM GFP-ABD-ABD solution in 20 mM Tris-HCl [pH 7.4], 50 mM KCl, 2 mM MgCl₂, 0.5 mM ATP. The first peak corresponds to the expected monomer molecular weight. The three higher molecular weight peaks indicate multimerization or aggregation of the protein. (D) Total internal reflection fluorescence (TIRF) images of F-actin (2 μ M) polymerized in the presence of 0.5 μ M GFP-ABD-ABD. F-actin forms bundles (bottom) and the crosslinker (middle) co-localizes with the bundles (merge image, top), confirming the crosslinker's ability to bind F-actin. (E) Corresponding TIRF image of F-actin polymerized in the absence of GFP-ABD-ABD. We observe similar bundles as in (D), indicating that the methylcellulose crowding agent present in the buffer is likely responsible for the bundling.

6.3.2. DESIGN, CLONING AND OPTIMIZATION OF FORCE-SENSING ACTIN CROSSLINKERS

CHOICE OF TENSION SENSOR MODULES

For the mechanosensitive peptides, we aimed at a force sensitivity corresponding to typical forces exerted on the actin cytoskeleton by myosin motors, which have been reported to be on the order of $\sim 3\text{-}4$ pN [420]. From an extensive literature research, we identified several candidate tension sensor cassettes with a suitable force sensitivity, as summarized in Table 6.1. Of these, we decided to pick a set of well-characterized mechanosensitive peptides developed and calibrated by the group of Dr. Carsten Grashoff (University of Münster). Specifically, we chose the modules TSMod and FLMod, which we refer to as **F40** and **FL**, respectively, following the terminology in the literature [1, 430].

Name	Sensing element	Sensor sensitivity	Source
MTFM	PEG_n^a	0–20 pN	Stabley et al. [437]
TSMod	Flagelliform (GPGGA_8)	1–6 pN	Grashoff et al. [1]
FLMod	Ferrodoxin(FL)-peptide	3–5 pN	Ringer et al. [430]
sstFRET	Spectrin repeat	5–7 pN	Meng and Sachs [438]
stFRET	α -helix	pN range	Meng et al. [425]
PriSSM	AS(GGS)_9	pN range	Iwai et al. [439]
cpYFPc ^c	Chromophore	pN range	Ichimura et al. [440]
cpstFRET	circularly permuted Cerulean and Venus,	5–7 pN	Meng and Sachs [441]
AuNP-MTFM	PEG	0–25 pN	Liu et al. [442]
MTS	Flagelliform (GPGGA_8)	1–6 pN	Morimatsu et al [443]

Table 6.1: Candidate molecular tension sensors of interest for *in vitro* cytoskeletal reconstitution based on their <10 pN force sensitivity range. Abbreviations: MTFM = Molecular Tension-Based Fluorescence Microscopy, PEG = Poly-Ethylene Glycol. Others: TSMod (tension sensor module), TS (tension sensor), sstFRET (single stranded stretch-sensitive FRET), PriSSM (PRIM-based strain sensor module, where PRIM stands for proximity imaging technique), cpYFPc (circularly permuted yellow fluorescent protein chromophore), cpstFRET (circularly permuted stretch sensitive FRET), AuNP-MTFM (MTFM (molecular tension-based fluorescence microscopy) tagged with a gold nanoparticle), dsDNA (double-stranded DNA).

The library of FRET-actin crosslinkers we developed based on the TS and FL modules is shown in Figure 6.3. In all cases, the donor fluorophore was YPet(short) and the acceptor fluorophore was mCherry, chosen for their optimal spectral overlap, needed for a good FRET efficiency, as explained in Section 6.2. First, we engineered two variants of an actin crosslinker with the F40 peptide, namely **ABD-F40-ABD** (Figure 6.3A) and **ABD-F40 (control donor only)-ABD** (Figure 6.3B). In the latter case, the mCherry acceptor had a truncation after residue 1353, known as the Y72L mutation, which disrupts chromophore formation [444]. The F40 module is derived from the elastic spider silk protein flagelliform [1]. The 40-amino-acid long F40 peptide responds to forces between 1–6 pN with a gradual length increase (Figure 6.3C), resulting in a gradual FRET response (Figure 6.3D), which is of particular interest for us since the resolution of forces below 6 pN has proven to be challenging in prior studies [1].

Second, we engineered an actin crosslinker with the FL peptide, which we refer to as **ABD-FL-ABD** (Fig. 6.3E). The **FL module** is an 82 amino-acid long peptide that adopts a ferrodoxin (FL)-like fold in the absence of load [430] (Figure 6.3F). Under a mechanical

load of 3-5 pN, the peptide undergoes an unfolding transition, which results in a sharp FRET loss (Figure 6.3G). Furthermore, this peptide is insensitive to forces of 1-2 pN, rendering it less susceptible to mechanical noise than F40. In Figure 6.3D and Figure 6.3G, the force-dependent FRET efficiencies of the F40 and FL modules are compared with those of the HP35 and HPst modules, also developed by the Grashoff group [431]. Those modules are 35 amino acids long and consist of a villin headpiece peptide (HP). The wild type HP35 peptide is sensitive to 6-8 pN forces (see Appendix Figure 6.14B, orange curve) while the mutant variant HP35st is sensitive to 9-11 pN forces (see Appendix Figure 6.14B, red curve). We decided to not consider these modules for the moment since these force sensitivity ranges exceed our range of interest.

Finally, we also engineered an actin crosslinker with a no-force control module (F7), containing a flexible 7-aa-long peptide (F7) that cannot be significantly elongated under force. The resulting actin-crosslinker **ABD-F7-ABD** is therefore force-insensitive (Fig. 6.3H).

CLOTHING AND PURIFICATION OF FORCE-SENSING ACTIN CROSSLINKERS

In order to clone the force-sensing actin crosslinker constructs, we first removed the GFP domain from GFP-ABD-ABD, obtaining a simple ABD-ABD construct, which we did not purify but only used as a vector in which to insert the FRET cassettes in order to obtain sensors. To this end, we amplified the fragments of interest via PCR and used Gibson Assembly with the primers in Table 6.4) (for a detailed explanation see Section 6.7 and Appendix Figure 6.15). We initially attempted to insert the FRET cassettes into the ABD-ABD vector by Gibson Assembly (data not shown). However, this strategy was unsuccesfull because the Gibson assembly primers for the insert FRET-module, which were targeted to bind to the ABDs, bound in an aleatory manner to the two consecutive ABD binding sites in the ABD-ABD construct, interfering with proper primer ligation and thus resulting in the wrong fragments getting amplified. We therefore decided to amplify the fragments (insert FRET-module and vector) via PCR but then merge the correct fragments with Golden Gate Assembly instead (detailed protocol explained in the Methods section 6.7) using the primers in Table 6.3. With Golden Gate Assembly, we were able to target specific binding sites for the primers using Type IIS Restriction Enzymes. Details on the cloning optimization are shown in Appendix Figure 6.15A. The constructs were expressed in *E. Coli* cells and the proteins were purified with a His-tag purification column (see SDS-PAGE gel in Fig. 6.16A and protocol in Methods section). The fractions of interest were pooled and cleaned up by gel filtration (Fig. 6.16B), in an attempt to remove any truncated proteins (non-fully expressed or degraded) that could affect the FRET efficiency in our assays.

⁰²Optical tweezer measurements were performed by the Grashoff lab [1]. The peptides were connected on one end to a polymer-coated glass surface via an 18 bp double-stranded (ds) DNA strand and on the other end to a microsphere held in optical tweezers via a ~50 kbp dsDNA tether. The DNA tethers presented the fluorophores in close proximity to terminal cysteine residues of the peptides, allowing estimation of the linker end-to-end distance as a function of force from FRET measurements. The authors numerically converted their experimental data and fitted the data to a fourth order polynomial (see Supplementary Note III in [1]).

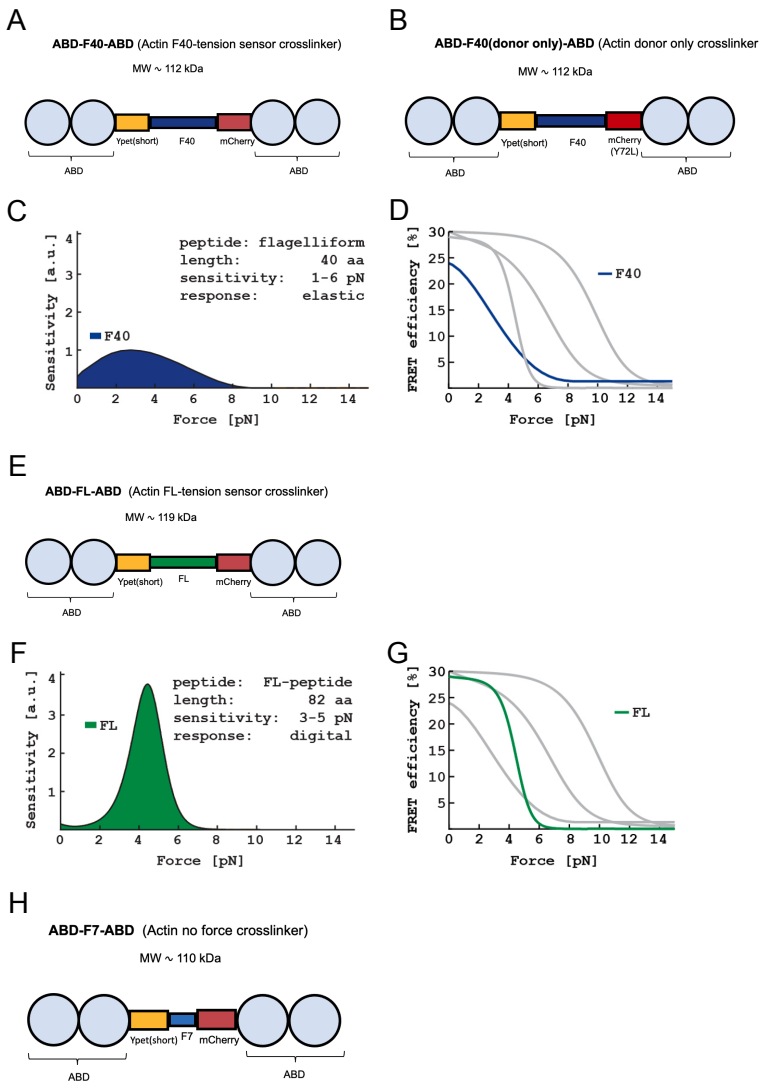


Figure 6.3: Library of engineered force-sensing actin crosslinkers. (A) Domain structure of the ABD-F40-ABD crosslinker, comprising an actin binding domain (consisting of two calponin homology (CH) domains), a donor fluorophore (Ypet(short)), the F40 tension module, an acceptor fluorophore (mCherry) and a second actin binding domain (again consisting of two calponin homology domains). (B) Domain structure of the ABD-F40 (donor only control)-ABD crosslinker, which is the same as ABD-F40-ABD but with a nonfluorescent mutant variant of the acceptor fluorophore (mCherry with Y72L mutation). (C) Sensitivity curve for the F40 tension module, showing sensitivity to forces between 1-6 pN (adapted from [430]). (D) FRET efficiency for the F40 tension module, compared with other tension sensors (Hp35 and HP35st) not used in this chapter but shown for possible follow-up experiments (see Appendix Figure 6.14). All curves were measured by the Grashoff lab using optical tweezer force spectroscopy². Panels F and G are adapted from Ref. [430]. (E) Domain structure of the ABD-FL-ABD crosslinker, which is the same as for ABD-F40-ABD but with the FL tension module. (F) Sensitivity curve for the FL linker (adapted from Ref. [430]). (G) FRET efficiency for the FL tension module, compared with other tension sensors (Hp35 and HP35st) (see Appendix Figure 6.14). Panels F and G are adapted from Ref. [430]. (H) Domain structure of the ABD-F7-ABD crosslinker, which is the same as for ABD-F40-ABD but with the F7 no force control module.

6.3.3. CHARACTERIZATION OF THE ACTIN-CROSSLINKING FRET SENSORS

To test the protein purity, we performed SDS-PAGE analysis after the final gel filtration chromatography step. As shown in Figure 6.4A, the SDS-PAGE gel shows a major band localized at the expected molecular weight for each protein. However, we also observe additional weaker bands of smaller molecular weight (indicative of protein degradation or incomplete translation) and in some cases higher molecular weight (indicative of aggregation). To estimate the purity of the protein preparations, we performed a densitometry analysis for the most prominent bands on the SDS-PAGE gels (see Appendix Figure 6.13). We normalized the band intensities by the intensity of the darkest (most intense) band and finally calculated the fraction of each constituent by dividing by the sum of all band intensities. As summarized in Appendix Table 6.5, the bands corresponding to intact monomer comprised 24% of the total protein amount for ABD-F40-ABD, 10% for ABD-F7-ABD, 31% for ABD-F40 (control only)-ABD, and 37% for ABD-FL-ABD. In all cases, we observed that the majority fraction consisted of contaminants with molecular weight smaller than the intact monomer mass (see Appendix Table 6.5). To check the oligomeric state of the proteins in solution, we performed interferometric scattering (iSCAT) microscopy. As shown in Fig. 6.4B-E), the mass histograms showed only a single peak centered around a molecular weight corresponding to the value expected value for the monomers, indicating that there is little aggregation in solution, at least under the conditions of iSCAT (50 nM protein).

For all proteins, we next checked the optical absorbance spectrum across a wavelength range spanning the absorbance spectra of the donor and acceptor fluorophores (Figure 6.4F). Note that we compare only relative absorbance (normalized by the maximal absorbance) since the different actin-crosslinking FRET sensors differ in purity and in concentration. In the SDS-PAGE gel in Figure 6.4A we for instance see that, although the proteins were loaded at the same nominal concentration, the lane of ABD-FL-ABD was overloaded. For the donor only construct (ABD-F40(donor only control)-ABD, yellow curve in Figure 6.4F), we see an absorbance peak at the donor wavelength ($\lambda=500$ nm) but no absorbance at the acceptor wavelength ($\lambda=610$ nm). This is in agreement with the fact that the mCherry acceptor cannot absorb any light as a consequence of the Y72L point mutation [444]. For the other constructs, we do observe both a donor and acceptor peak, but the peak absorbance of the donor at $\lambda=500$ nm was always higher than the peak absorbance of the acceptor at $\lambda=610$ nm. The difference between the donor and acceptor absorbance at the peak wavelengths was ~60% for the protein with the FL module (ABD-FL-ABD, blue curve in Figure 6.4F), ~75% for the F40 module (ABD-F40-ABD, salmon curve in Figure 6.4F), and ~70% for the no force control module ((BD-F7-ABD, orange curve in Figure 6.4F). It appears therefore that the most efficient absorbance at 610 nm is obtained with the ABD-FL-ABD and that not much difference, in this setting, is measured between the no force control and the F40 module.

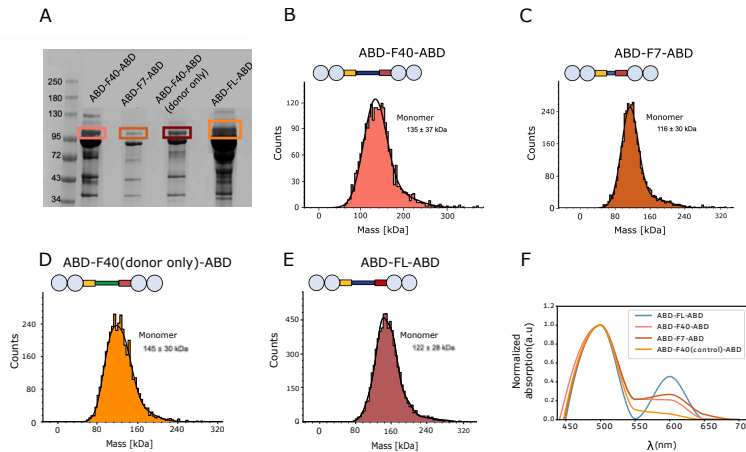


Figure 6.4: Characterization of the purity, oligomerization status, and optical properties of the actin-crosslinking FRET sensors. (A) SDS-PAGE gel of all 4 proteins (see legend), purified by His-tag affinity purification followed by gel filtration. Left-most lane: molecular weight marker. Rectangles mark the band of the full-length protein. In all cases we observe additional bands of higher and lower molecular weight (see Appendix Figure 6.13). (B-E) iSCAT measurements of the molecular mass distribution of the purified proteins (50 nM solutions in 20 mM Tris-HCl, pH 7.4, 50 mM KCl, 2 mM MgCl₂, 0.5 mM ATP) for (B) ABD-F40-ABD, (C) ABD-F7-ABD, (D) ABD-F40(control)-ABD, and (E) ABD-FL-ABD. In all cases we observed a single peak centered around a molecular mass corresponding to the full length monomer masses expected from the protein sequence. (F) UV-VIS absorption spectra for the proteins at a concentration of 5 μ M in F-buffer (20 mM Tris-HCl, pH 7.4, 50 mM KCl, 2 mM MgCl₂, 0.5 mM ATP) normalized by the maximal registered absorption. We all constructs except the ABD-F40(donor only control)-ABD construct we observe two absorption peaks, one for the donor (Ypet) centered around 500 nm and another for the acceptor (mCherry) centered around 610 nm.

6.3.4. THE ACTIN-CROSSLINKING FRET SENSORS INDEED HAVE CROSSLINKING ACTIVITY

MECHANICS OF CROSSLINKED ACTIN NETWORKS AT LOW SHEAR STRAINS

In order to determine the actin-crosslinking functionality of the sensors, we performed shear rheology on actin networks polymerized with and without the FRET-crosslinkers. For all samples, the G-actin concentration was fixed at 24 μ M and the concentration of crosslinker was set at 2.4 μ M. Figure 6.5A shows the polymerization curves of a control actin network (blue curve) compared with networks polymerizing in the presence of the actin-crosslinking FRET sensors. We show two repeat curves for each condition to portray the variability. All crosslinked networks reached a plateau elastic shear modulus G' of \sim 7 Pa, whereas the control entangled actin networks stabilized at a modulus of 2 Pa after 1h30 of polymerization at 25 °C. This significant stiffening effect clearly shows that all FRET sensors are capable of crosslinking actin filaments.

The linear elastic modulus exhibited a weak power law dependence on the shear oscillation frequency characterized by a small exponent of \sim 0.1 for both the control and the crosslinked networks (see Figure 6.5B). The loss tangent, which is the ratio of the viscous over the elastic modulus, was indistinguishable between networks crosslinked

with different actin-crosslinking FRET sensors ($\tan(\delta) \sim 0.6$, see Figure 6.5C). The loss tangent for the crosslinked networks was slightly higher than for the control network ($\tan(\delta) \sim 0.75$), consistent with the crosslinked networks being more solid-like than the control network. However, we note that the loss tangents are noisy because the applied strain and the shear moduli (especially G'') were small, so the stress was close to the sensitivity limit of the rheometer. We furthermore caution that there are limited statistics ($N=2$). Nevertheless, we can conclude from the linear rheology that the FRET sensor proteins are capable of crosslinking actin filaments.

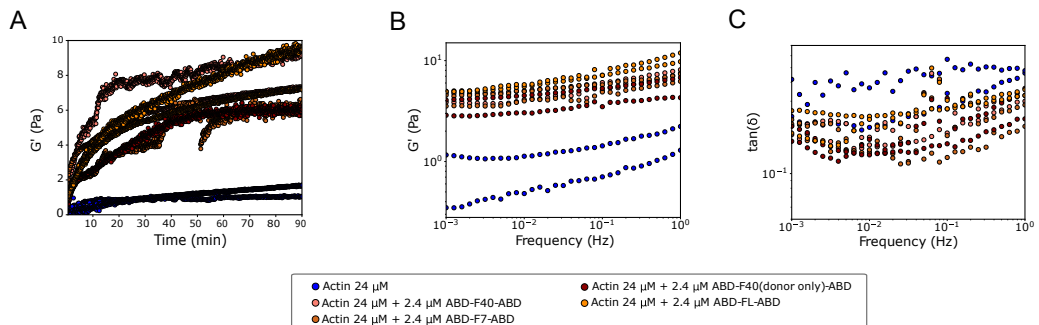


Figure 6.5: Linear viscoelastic behaviour of actin networks reveals that the FRET sensor constructs function as crosslinkers. (A) Polymerization of 24 μ M actin in the absence and presence of 2.4 μ M of the four different FRET sensors crosslinkers (see legend) observed as an increase in the elastic shear modulus, G' , over time. The crosslinkers cause network stiffening compared to control networks, indicative of crosslinking activity. Two repeat curves are shown per condition. Artifacts of the rheometer measurement can cause some curves to 'break', but yet being valid due to immediately the modulus coming to its original value. (B) Frequency dependence of G' for the actin networks obtained after steady state polymerization is reached. (C) Corresponding loss tangents. Note that the loss tangent is noisy due to the stress being close to the rheometer sensitivity limit. The data shown for each sample corresponds the separate independent $N=2$ repeats.

MECHANICS OF CROSSLINKED ACTIN AT HIGH SHEAR STRAINS

To elucidate the influence of the engineered crosslinkers on the high strain response of the networks, we implemented a stress ramp protocol (see Methods) to measure the tangent elastic modulus K' of the actin networks as a function of shear stress in the absence or presence of the crosslinkers. Since the nonlinear response of entangled F-actin solutions strongly depends on the strain rate [193], we made sure to compare all systems at the same stress rate of 10⁻¹ decades of stress (in units of Pascal) per second. As shown in Fig. A, crosslinked actin networks strain-stiffened, in strong contrast to the fluidization response of the control networks. Since strain-stiffening requires the filaments to be crosslinked, this response again confirms that the FRET sensor proteins are functional as crosslinking proteins. Interestingly, networks crosslinked with the force-sensing constructs (ABD-F40-ABD, salmon curve; or ABD-FL-ABD, orange curve) showed monotonic stress-stiffening, whereas the networks crosslinked with the no force control sensor (ABD-F7-ABD, red curve) or the donor-only control sensors (ABD-F40(donor only)-ABD) showed initial stress-softening before stress-stiffening set in. The no-force control mod-

ule, being shorter, has a smaller compliance than the F40 and FL modules, which could explain this difference. However the donor-only control is expected to have an identical mechanical compliance as the ABD-F40-ABD tension sensor since they only differ in a single residue in the YPet fluorophore. It is therefore likely that the differences are primarily caused by varying levels of degraded proteins in the solution that may occupy binding sites on actin filaments without forming productive crosslinks.

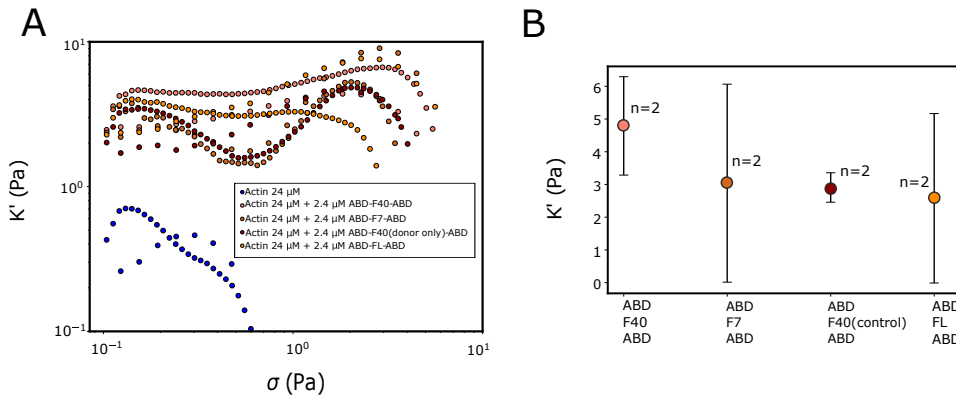


Figure 6.6: Nonlinear elastic behaviour of actin networks probed by stress ramp experiments (using a stress rate of 10^{-1} decades of stress (in units of Pascal) per second) confirms that the FRET sensor constructs function as crosslinkers. (A) Actin networks (24 μ M) polymerized with or without 2.4 μ M of FRET sensor crosslinker (see legend). The control network fluidizes, whereas the crosslinked networks show stress-stiffening, a clear signature of crosslinking. (B) Small-stress elastic modulus of the networks extracted from the small-stress plateau in the stress-stiffening data. The data shown for each sample corresponds the separate independent $N=2$ repeats

6.4. DISCUSSION

In this chapter we presented a carefully designed library of actin crosslinkers for FRET experiments. The purpose of this chapter is to provide the reader the needed tools to further implement these engineered sensors within reconstituted cytoskeletal networks. The cytoskeleton regulates the shape and function of animal cells. In particular, the actin cytoskeleton and F-actin architecture contribute to force generation and transmission within the cell, but the underlying mechanisms remain unclear. Therefore, tension sensors that can be embedded within the cytoskeleton can help understand better F-actin's role in force generation and transmission.

Our library of engineered crosslinkers consists of different tension sensors embedded in between two actin binding domains. The tension sensors fall within the range of relevant force sensitivity, since measuring across the actin cytoskeleton requires methods with picoNewton (pN) force sensitivity: myosin motors exert forces in the range of 3-4 pN [420] and growing actin filaments also exert pN-level forces [421]. Specifically, we designed tension sensors harboring either the F40 tension sensor [1], sensitive to 1-6 pN

range, or the FL tension sensor [430], sensitive to 3-5 pN. We aimed to achieve maximal purity by combining His-tag purification with subsequent gel filtration, but we achieved only 10-37% purity. The majority of contaminants in the final protein preparations were of molecular weight smaller than that of the full length proteins, suggesting that significant proteolysis occurs. Both SDS-PAGE gels and iSCAT measurements showed that the actin-crosslinking FRET sensors were largely (over 95%) monomeric, as expected from their sequence, which lacks any known domains capable of inducing oligomerization.

To validate the actin-crosslinking functionality of the engineered FRET sensors, we performed shear rheology tests on actin networks polymerized in presence of the sensors. We observed significant stiffening of the actin networks upon crosslinking and a slight decrease in the loss tangent, consistent with a more solid-like behavior. Moreover, the sensors caused the networks to stress-stiffen, as expected for crosslinked actin networks due to the entropic elasticity of the semiflexible filaments [445]. We did not yet test the FRET efficiencies of the sensors. The next steps in this project will be to test the FRET efficiency for the sensors, first in solution, using fluorescence excitation spectroscopy, and next within F-actin networks, using FRET/FLIM microscopy. Once the load-free conditions are well-characterized, it will be interesting to test whether the sensors are capable of reporting changes in tension when a mechanical load is applied. We are aware of only one previous study where F-actin-binding FRET sensor proteins were used to measure force transmission in reconstituted F-actin networks [446]. In this work, forces were introduced by embedding myosin II motors, which generate contractile forces. Actin-myosin II networks are indeed an attractive choice as a model system because the amplitude and range of forces can be controlled by changes in myosin II concentration and in the network crosslinking density [447]. We therefore re-established this system, previously studied in our research group [448, 234]. To this end, actin networks were reconstituted together with fascin crosslinkers and muscle myosin II motors in a buffer containing 0.1 mM MgATP (see Figure 6.7A). As shown in Figure 6.7B, time-lapse confocal imaging showed that the motors macroscopically contracted the fascin-crosslinked actin network contraction over a time course of 12 minutes. Note that the images are time projections of movies, with the color scale representing time. We think such a system could be of strong interest to test our library of engineered crosslinkers. Given their force sensitivity range of 1-7 pN, we hope to be able to map forces across crosslinks during motor-driven contraction from changes in the FRET signal or fluorescence lifetime of the FRET sensors. Unfortunately, due to time constraints, we leave this exciting experiment for the future.

6.5. CONCLUSION

FRET-force sensors have become a valuable tool for measuring forces in living cells, but they have not yet been implemented to study force propagation in reconstituted biopolymer gels. In this chapter we engineered FRET-based sensors as a tool to study force propagation within reconstituted actin networks. We engineered actin-crosslinker proteins by sandwiching actin-binding domains around a FRET cassette based on two different tension sensors selected for their optimal force sensitivities in the pN range,

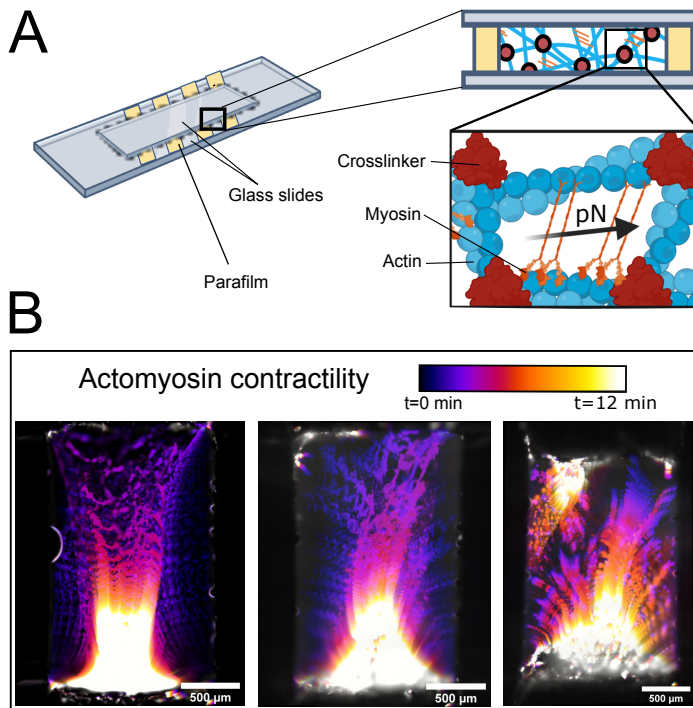


Figure 6.7: Proposed test system for the tension-sensing actin crosslinkers. (A) We propose to incorporate the FRET sensors as crosslinkers in reconstituted F-actin networks formed in the presence of myosin II motors that drive contraction. These networks can be formed inside glass chambers to allow for FRET/FLIM imaging. (B) Time projections of confocal time lapse movies of actin networks (15 μ M) crosslinked with fascin (in a 20:1 G-actin:fascin molar ratio) and skeletal muscle myosin II (in a 100:1 G-actin:myosin II molar ratio). Scale bar is 500 μ m, color bar encodes the time elapsed since the start of observation.

taken from previous work, since myosin motors exert forces in the range of 3-4 pN [420] and growing actin filaments also exert pN-level forces [421]. We demonstrated that our newly engineered actin crosslinkers with integrated FRET-sensors (which have been previously studied in terms of FRET efficiency [1, 430]) are functional in terms of actin-crosslinking activity. We propose to test these sensors in future in an already established acto-myosin contraction assay where myosin motors generate contractile forces.

6.6. ACKNOWLEDGEMENTS

I thank Carsten Grashoff for generously sharing his FRET-sensing constructs and providing all the relevant information. I thank Zima Kabir for taking the first steps with me in engineering the sensor vectors, and I thank Angeliki Goutou for all the precious help in the engineering with Golden Gate assembly and optimization of the purification of

the sensors. Finally I thank Kabir Razack and Lucia Baldauf for extensive joint efforts to (re-)establish the actomyosin contraction assay.

6.7. METHODS

GFP-ABD-ABD AND ABD-ABD SENSOR ENGINEERING

GFP-ABD-ABD was designed to contain an enhanced Green Fluorescent Protein (GFP) tag followed by two copies of the actin binding domain (ABD) from the actin-microtubule crosslinker protein MACF/ACF7. We inserted additional residues for flexibility between the different domains, as shown in Appendix Figure 6.8. As a vector, we used the TipAct construct previously developed in our lab [359]. For the ABD insert we used the same plasmid (actin-microtubule crosslinker protein MACF/ACF7 from [359]). The two fragments (vector and insert) were amplified using the primers indicated in Appendix Table 6.4. PCR amplification was performed using KOD Xtreme Hot start DNA polymerase (#1975). The PCR products were run on a 1% agarose gel (Biorad #1613100EDU) and cleaned using the Wizard® SV Gel and PCR Clean-Up System A9281. For electrophoresis, samples were prepared with TrackIt™ Cyan/Yellow Loading Buffer (Invitrogen #10482035), using TrackIt™ 1 Kb Plus DNA Ladder (Invitrogen #10488085) as a ladder. The electrophoresis gel was run at 100V for 20 minutes (Biorad #1613100EDU). Next, the fragments were assembled using Gibson Assembly, following the instructions of the NEB-uilder HiFi DNA Assembly Cloning Kit (#E5520S). Afterward, the sample was transformed into *Dh5 α* competent *E. coli* cells (#C2987). To determine if the plasmid contained the insert, a miniprep was performed using the PureYield™ Plasmid Miniprep System A1222 for sequencing via Macrogen. After sequencing, the plasmid was transformed into *E. coli* BL21 (NEB #C2527).

FRET SENSORS ENGINEERING

The actin-crosslinking FRET sensors were constructed by Golden Gate Assembly. All Golden Gate assemblies were performed in a total volume of 20 μ L using the NEB Golden Gate Assembly Kit (BsaI-HFv2, NEB# E1601S/L). The final reaction volume contained 10x T-ligase buffer, 1 μ L Golden Gate enzyme mix (BsaI), 50 ng of destination vector and a 2:1 molar ratio (insert:vector backbone) of insert. We prepared reaction mixtures (ligase buffer, acceptor plasmid, insert) and adjusted with ddH₂O. In a final step, the corresponding enzymes were quickly added. First, a volume of 0.5 μ L of the restriction enzyme BsaI (10 units; New England Biolabs, Ipswich, US) and then T4 ligase was added. Golden Gate reactions were carried out by default under the following conditions: a) Enzymatic restriction at 37 °C (1 min, 30 passes); b) Ligation 16 °C (1 min, 30 passes) and c) enzyme inactivation: 60 °C (10 min). In parallel, we thawed the bacteria before the last reaction step and we transformed immediately after taking the samples out of the PCR reaction.

GFP-ABD-ABD PROTEIN PURIFICATION

A pre-culture of *E. coli* BL21 cells expressing the construct of interest was grown from a glycerol stock in Luria-Bertani (LB) medium containing 1:1000 diluted kanamycin at 37 °C. Growth was upscaled to a total of 12 liters (separated in 4 cultures of 3 L each),

adding 1:1000 diluted kanamycin, and 25 mL of preculture. This large volume was necessary because we obtained rather small yields, and wanted to make sure enough protein would be obtained for microscopy and rheology. The cultures were incubated at 37 °C in flasks on a shaker platform at 200 rpm. When the Optical Density (OD) at 600 nm reached 0.9, we cooled the 4 cultures down in an ice bath for 30 minutes, then induced overnight expression with 1 mM Isopropyl β -D-1-thiogalactopyranoside (IPTG #11411446001) at 16 °C. The cultures were harvested by a 15 min centrifugation in the Avanti JLA8.1000 fixed angle rotor at 4000 rpm at 25 °C. The supernatant was discarded, and the cell pellets for each sensor were combined in one 50 mL falcon tube. The cells were resuspended with lysis buffer (20 mM sodium phosphate pH 7.4, 10 % glycerol, 5 mM 2-mercaptoethanol, 500 mM NaCl, 45 mM imidazole), supplemented with cCompleteTM EDTA-free protease inhibitor cocktail (SigmaAldrich, St. Louis, MO, USA #11836153001) and 1 mg/mL of lysozyme from chicken egg white (Sigma Aldrich #10837059001). The cell solution was incubated on ice for 30 minutes. The lysate was passed through the French press three times at 20 kpsi and next centrifuged at 17,000 \times g for 80 minutes at 4 °C (Avanti JXN-26).

The supernatant was collected and incubated with 1 mL pre-washed nickel-IMAC resin (Thermo Fisher Scientific #88221) overnight at 4 °C to allow protein binding to the resin. The beads were pre-washed with wash buffer (20 mM sodium phosphate pH 7.4, 10% glycerol, 5 mM 2-mercaptoethanol, 500 mM NaCl, 45 mM imidazole) in an empty column (Econo-Pac® Chromatography Columns #7321010). The lysate was passed through the disposable column for gravity flow purification. The flow-through was collected and kept at 4 °C. The column was washed three times with wash buffer. To elute the protein from the column, the column was incubated with elution buffer (20 mM sodium phosphate pH 7.4, 10% glycerol, 5 mM 2-mercaptoethanol, 500 mM NaCl, 200 mM imidazole) for 20 minutes at 4 °C. Afterward, an analysis of protein yield and purity for the eluate was performed by SDS-PAGE analysis. The sample was aliquoted at the desired molar concentration, calculated using values for the molecular weight and extinction coefficient determined on the basis of the sequence using the Expasy analysis tool [388]. Values are shown in Table 6.2.

FRET SENSOR PROTEIN PURIFICATION

The initial steps of the purification of the FRET sensors was performed in the same way as described above for GFP-ABD-ABD. Next, we added an additional purification step consisting of size exclusion chromatography on a Superdex 200 10/300 prep grade (Cytiva) column. The column, which was stored in ethanol, was first washed with 1.5 \times column volumes of MilliQ water and then with 1.5 \times column volumes of MRB40 buffer (40mM piperazine-N,N'-bis(2-ethanesulfonic acid) (PIPES) pH 7.0, 4 mM MgCl₂, and 1 mM ethylene glycol tetraacetic acid (EGTA)). After the column was equilibrated, we injected the sample through the 5 mL loop and ran it at a flow rate of 0.5 mL/min, while collecting 0.3 mL fractions. The fractions of interest, as judged from the absorbance at 280 nm, were pooled and analyzed by SDS-PAGE gel electrophoresis. The samples were aliquotted at the desired molar concentration, calculated using values for the molecular weight and extinction coefficient shown in Table 6.2.

ACTIN RECONSTITUTION

For TIRF and rheology experiments, lyophilized rabbit alpha-skeletal muscle actin was purchased from Hypermol EK. Actin was dialyzed against G-buffer (pH 7.8) comprising 5 mM Tris-HCl, 0.1 mM MgCl₂, 0.2 mM Na₂ATP and 5 mM DTT. After dialysis, G-actin was aliquotted, flash-frozen in liquid nitrogen and stored at -80 °C. The final actin concentration was measured by UV-VIS absorbance measurements using an extinction coefficient at 290 nm of 26,600 M⁻¹ cm⁻¹ and molecular weight of G-actin of 42 kDa [335].

TOTAL INTERNAL REFLECTION FLUORESCENCE MICROSCOPY

Actin samples assembled by polymerizing G-actin with or without GFP-ABD-ABD in F-buffer (20 mM Tris-HCl, pH 7.4, 50 mM KCl, 2 mM MgCl₂, 0.5 mM ATP) at room temperature were imaged using a Nikon Ti2-E microscope complemented with a Gataca iLAS2 azimuthal TIRF illumination system. The sample was illuminated with lasers of 488 nm and 647 nm lasers (Gataca laser combiner iLAS2) to visualize the crosslinker and the actin signals, respectively. The fluorescence signal was split with a CairnResearch Optosplit II ByPass containing a Chroma ZT 543 rdc dichroic mirror and filtered with either a 525/50 or a 700/50 chroma bandpass filter. The images were recorded with an Andor iXon Ultra 897 EM-CCD camera using an exposure time of 100 ms, gain of 250 and 10 % laser power for 488 nm, and at a 100 ms exposure time, gain of 250 and 8.2 % laser power for 647 nm. Reference images for image registration were acquired using 200 nm multifluorescent beads mounted on a microscope slide (Cat. #10505593, Invitrogen), and registration was performed using the ImageJ plugin *2D descriptor based registration*.

INTERFEROMETRIC SCATTERING MICROSCOPY

Interferometric Scattering Microscopy (iSCAT) experiments were conducted with a OneMP Mass Photometer (Refeyn). The instrument was equipped with a 525 nm laser for illumination. iSCAT measurements were carried out using CultureWell gaskets (Cat. #GBL103250, Grace Biolabs) affixed to #1.5 coverslips (Cat. #13296788, Corning). To prepare the coverslips for optimal protein adhesion, a meticulous stepwise sonication cleaning process was employed. The coverslips were sonicated sequentially in MilliQ water, 50% isopropanol, and again in MilliQ water, each for a duration of 5 minutes. Following the cleaning process, the coverslips were incubated with a poly-L-lysine solution (PLL, Cat. #P4832, Merck) for 30 seconds. Subsequently, the coverslips were rinsed with MilliQ water and dried under a stream of N₂ gas. The treated coverslips were stored upright in a Teflon rack within a covered beaker to protect them from dust. They were utilized within a week to maintain their cleanliness.

During the iSCAT measurements, videos were recorded with a field of view measuring 10 × 10 μm. The recording duration ranged from 6000 to 15000 frames, with a frame rate of 300 frames per second. This ensured a minimum count of 1000 particles per video. Maintaining a dilute solution of proteins is crucial to ensure well-separated scattering patterns. Hence protein concentrations in the range of 10 nM to 50 nM in F-buffer were chosen to achieve adequate separation of landing events while still collecting sufficient statistics within a maximum of 15000 frames to limit the data volume. The iS-

CAT video analysis was executed using the DiscoverMP software, a commercial software package provided by Refeyn.

RHEOLOGY

Rheological measurements were conducted using a stress-controlled KinexusMalvern Pro rheometer or a TA rheometer, both equipped with a stainless steel cone-plate geometry. In both cases, the cone had a radius of 20 mm and an angle of 1°. The temperature was maintained at 25 °C by Peltier plates. F-actin networks were polymerized between the plates of the rheometer by loading 40 μ l of the sample directly after mixing G-actin with the FRET sensors in the polymerization buffer (F-buffer). To prevent solvent evaporation during the experiment, a thin layer of mineral oil Type A (Sigma, #18602) was carefully applied around the sample edge with a 200 μ L pipette tip by placing some drops around the top geometry and letting the oil flow and cover the geometry contour.

Progress of network formation was monitored by applying a small oscillatory shear with a fixed strain amplitude of 0.5% and oscillation frequency of 0.5 Hz for a duration of 2 hours. Following the 2-hour polymerization period [449], a frequency sweep was conducted in the range of 0.01 to 10 Hz at a small strain amplitude of 1%, sampling 10 data points per decade. Data taken at frequencies exceeding 3 Hz had to be discarded because they were dominated by inertial effects from the rheometer. For each curve, we took an average over $N = 2$ independently prepared samples. For nonlinear rheology experiments, we implemented a stress ramp protocol [200] with a loading rate of 10^{-1} decades of stress per second from 0 to 1000 Pa. The rheology data sets had different total number of datapoints per sample recording because the two rheometers had different sampling rates. To average data obtained with the different rheometers, we implemented a custom-written spline interpolation in Python.

6.8. APPENDIX

6.8.1. THEORETICAL CONSIDERATIONS FOR FRET PAIR DESIGN

We here provide brief additional information regarding the impact of FRET pair design on the FRET efficiency, to aid future researchers following up on this work. R_0 is the Förster distance, and it is dependent on the dipole orientation factor k^2 , on the donor quantum yield, Q_D , and on the overlap integral of the donor emission spectrum with the acceptor absorption spectrum, J :

$$R_0^6 \sim \kappa^2 Q_D J \quad (6.2)$$

The orientation factor, κ^2 , is often assumed to remain constant throughout an experiment, but this may not always hold true. The relative orientation of the donor and acceptor dipoles has been used in orientation-dependent FRET biosensors (see Ref. [450, 451]). The spectral overlap integral (J) is a function of the wavelength, λ , and depends on the acceptor's molar extinction coefficient, ϵ_A , and on the donor fluorescence intensity, F_D :

$$J(\lambda) = \int \epsilon_A(\lambda) \lambda^4 F_D(\lambda) d\lambda \quad (6.3)$$

6.8.2. TABLES AND FIGURES

	Molecular weight (kDa)	Extinction coefficient ($M^{-1} cm^{-1}$)
GFP-ABD-ABD	84	84145
ABD-F40-ABD	112	118525
ABD-F40 (control donor only)-ABD	112	118525
ABD-F7-ABD	110	117035
ABD-FL-ABD	119	121505

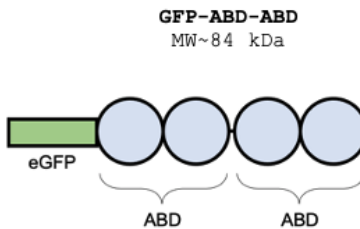
Table 6.2: List of molecular weights and extinction coefficients for the actin-crosslinking engineered constructs determined on the basis of the sequence using the Expasy analysis tool [388].

Fragment	Forward Primer	Reverse Primer
ABD-ABD Vector	GCTCGTTAGAGAGTAGCAAAAT	CCCTTCTCCACCCTCAGGAACCTT

Table 6.3: Primers used for Gibson Assembly for the actin-crosslinking vector (ABD-ABD).

Fragment	Primer
Forward Primer	aaagttcctgagggtggagaaggggCTCGAGATGGTGAGCAAAGGCGAA
Reverse Primer	attttgctactctaaacgagcAGCGGCCGCTTGTACAGCTCGTC

Table 6.4: Primers used for the insertion of the FRET-cassettes into the ABD-ABD vector by Golden Gate Assembly, using Golden Gate enzyme BsaI



MGSSHHHHHHSSGLVPRGSHMASMTGGQQMGR**MVSKGEEELFTGVVPILVELGDGVNGHKF** 60
 SVSGEGEGDATYGKLTGKFLCTTGKLPVPWPTLVTTLTGVQCFARYPDHMKQHDFFKSA 120
 MPEGYVQERTIFFKDDGNYKTRAEVKFEGDTLVNRIELKGIDFKEDGNILGHKLEYNYNS 180
 HKVYITADKQKNGIKVNFKTRHNIEDGSVQLADHYQQNTPIGDGPVLLPDNHYLSTQSAL 240
 SKDPNEKRDHMVLL**EVTAAAGITLGMDELYKVQKKTFTKVNKLMKVRKHINDLYEDLR** 300
 DGHNLISLLEVLSGIKLPREKGRMRFHRLQNVQIALDFLKQRQVKLVNIRNDDITDGNPK 360
 LTLGLIWTIILHFQ**ISDIYISGESGDMSAKEKLLLWTQKVTAGYTGIKCTNFSSCWSDGK** 420
 MFNALIHRYRPDLVDMERVQIQSNRENLEQAF**EVAAERLGVTTRLDAEDVDVPSPDEKSVI** 480
 TYVSS**IYDAIPKVPEVQKKTFTKVNKLMKVRKHINDLYEDLRDGHNLISLLEVLSGIK** 540
 LPREKGRMRFHRLQNVQIALDFLKQRQVKLVNIRNDDITDGNPKL**TGLIWTIILHFQIS** 600
 DIYISGESGDMSAKEKLLLWTQKVTAGYTGIKCTNFSSCWSDGKMFNALIHRYRPD**LVD** 660
 ERVQIQSNRENLEQAF**EVAAERLGVTTRLDAEDVDVPSPDEKSVITYVSSIIYDAFF** 715

Figure 6.8: Domain organization and amino acid sequence of GFP-ABD-ABD. (Top) GFP-ABD-ABD domain organization with the amino acid numbers indicated from the sequence below. GFP, enhanced green fluorescent protein; ABD, actin-binding domain (from MACF/ACF7). (Bottom) Amino acid sequence of GFP-ABD-ABD. The color code corresponds to the domains indicated on the diagram above and the spacers between domains are indicated in black letters. The purple amino acid region corresponds to the 6xHis-tag for protein purification.

	Relative abundance (%)	
	Protein of interest	Darkest band
ABD-F40-ABD	24	38
ABD-F7-ABD	10	54
ABD-F40 (donor only)-ABD	31	50
ABD-FL-ABD	37	58

Table 6.5: Densitometry analysis of the protein bands observed by SDS-PAGE analysis. Percentages correspond to the intensities of the bands (either the "protein of interest", which is the full length monomer, or the "darkest band", which refers to the most intense band observed on the gel), divided by the summed intensities of all analyzed bands. Data are shown for ABD-F40-ABD, ABD-F7-ABD, ABD-F40 (control donor only)-ABD and ABD-FL-ABD.

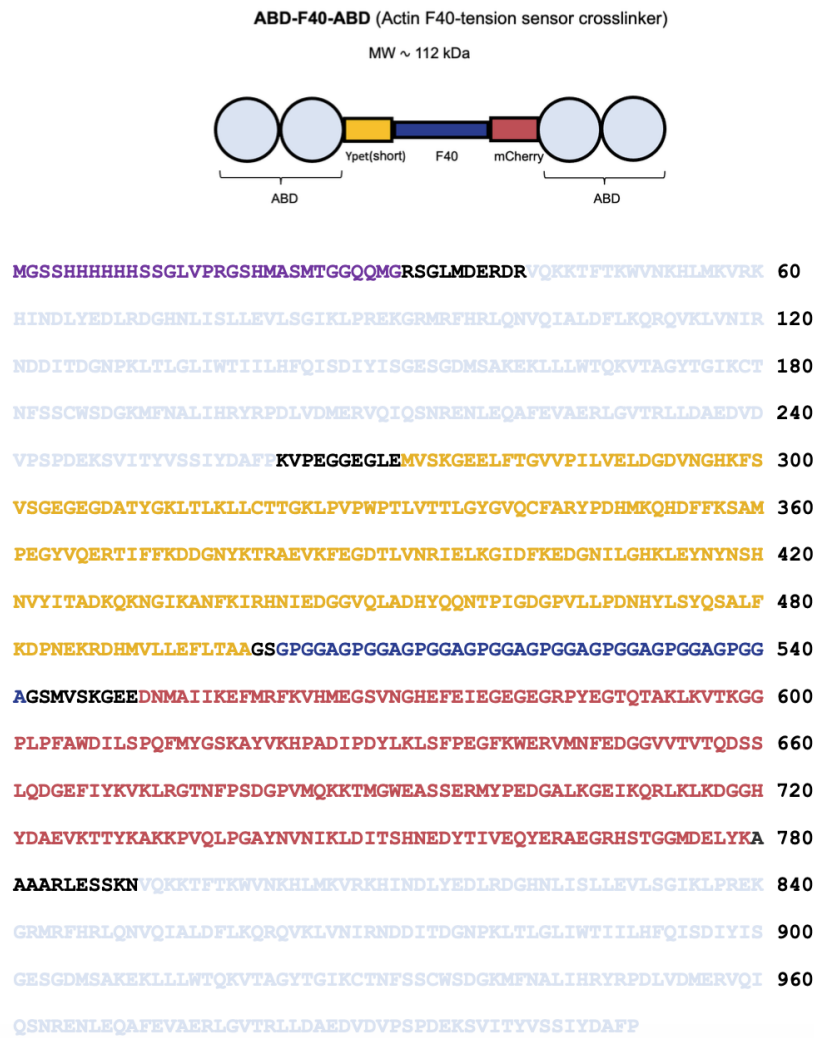


Figure 6.9: Domain organization and amino acid sequence of ABD-F40-ABD (Actin F40-tension sensor crosslinker). (Top) Domain organization of ABD-F40-ABD with the amino-acid numbers indicated from the sequence below. ABD, actin-binding domain; Ypet; F40-tension sensor, mCherry. (Bottom) Amino acid sequence of ABD-F40-ABD. The color code corresponds to the domains indicated on the diagram above and the spacers between domains are indicated in black letters. The purple amino-acid region corresponds to the 6xHis-tag for protein purification.

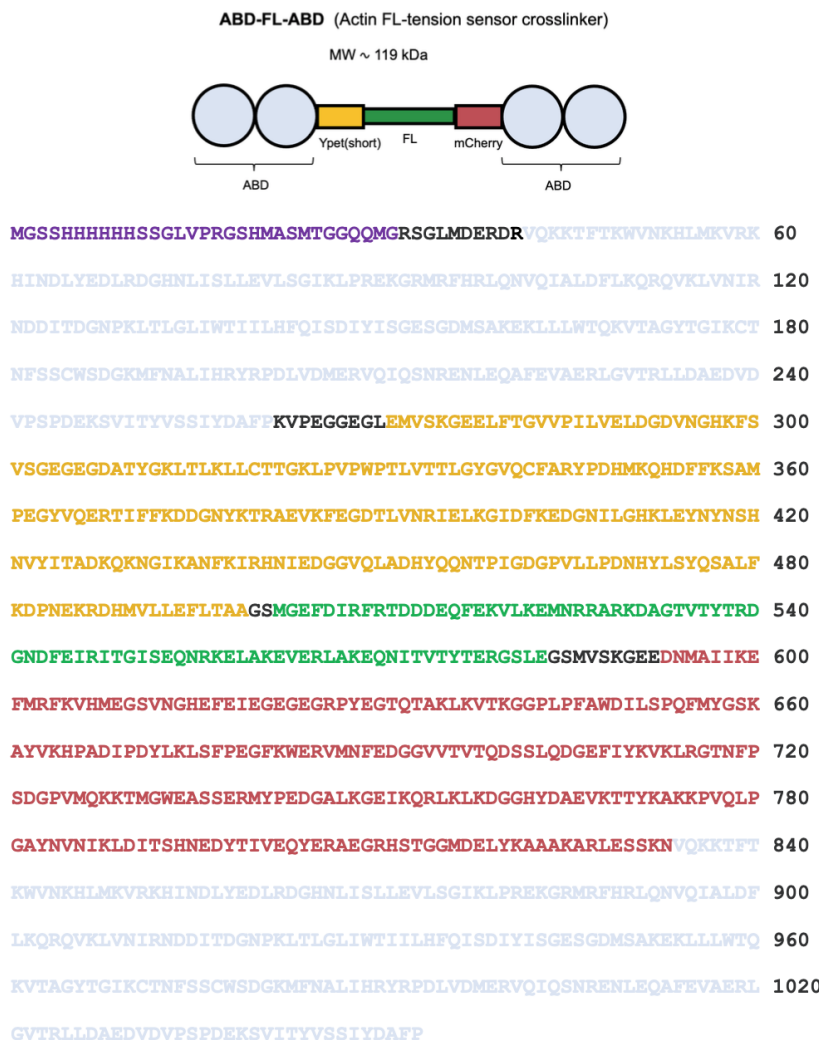


Figure 6.10: Domain organization and amino acid sequence of ABD-FL-ABD (Actin FL-tension sensor crosslinker). (Top) Domain organization of ABD-FL-ABD with the amino acid numbers indicated from the sequence below. ABD, actin-binding domain; Ypet; FL-tension sensor, mCherry. (Top) Amino acid sequence of ABD-FL-ABD. The color code corresponds to the domains indicated on the diagram above and the spacers between domains are indicated in black letters. The purple amino acid region corresponds to the 6xHis-tag for protein purification.

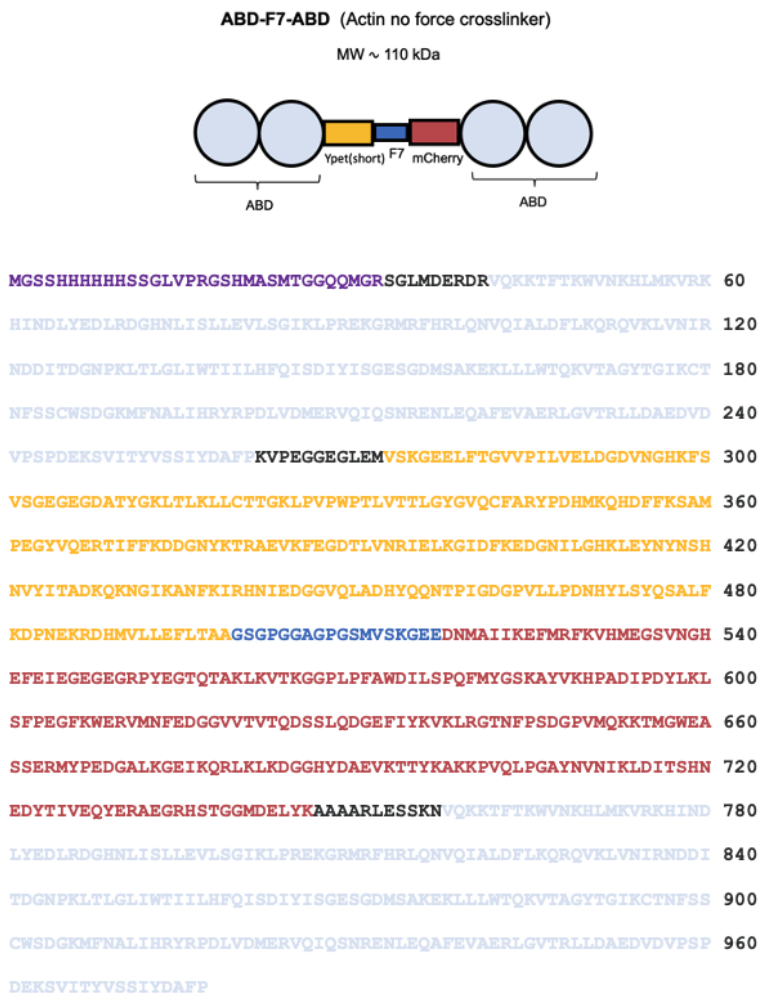


Figure 6.11: Domain organization and amino acid sequence of ABD-F7-ABD (Actin crosslinker no force control). (Top) Domain organization of ABD-F7-ABD with the amino acid numbers indicated from the sequence below. ABD, actin-binding domain; Ypet; F7 no force linker, mCherry. (Bottom) Amino acid sequence of ABD-F7-ABD. The color code corresponds to the domains indicated on the diagram above and the spacers between domains are indicated in black letters. The purple amino acid region corresponds to the 6xHis-tag for protein purification.

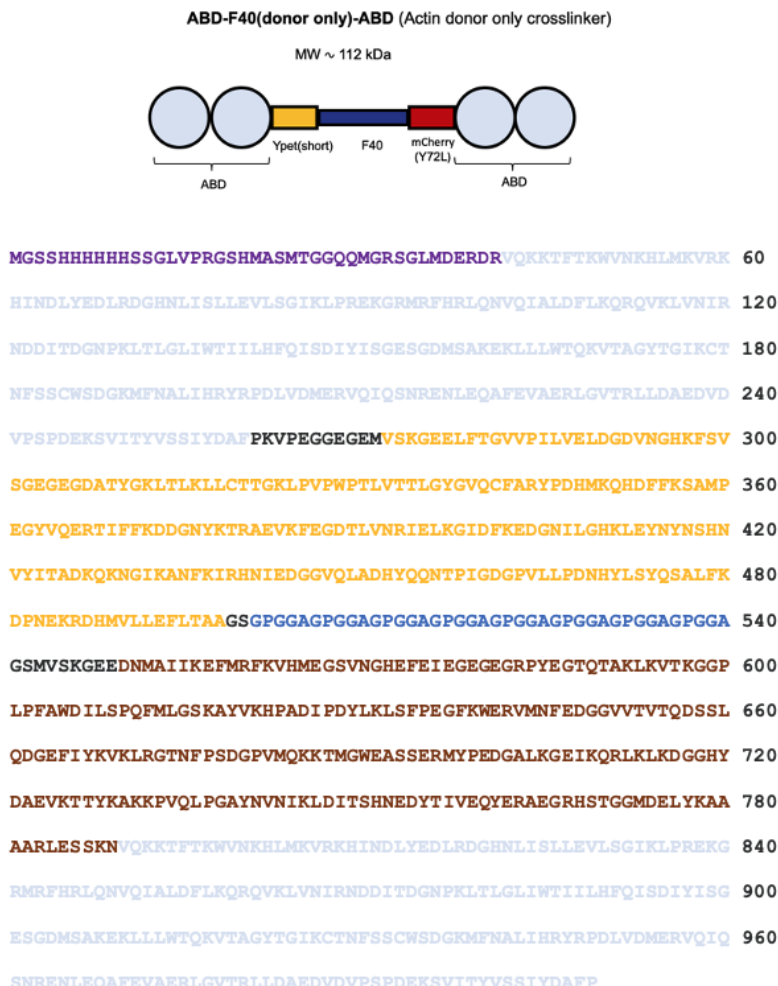


Figure 6.12: Domain organization and amino acid sequence of ABD-F40 (donor only-ABD (Actin F40(donor only)-tension sensor crosslinker). (Top) Domain organization of ABD-F40 (donor only)-ABD with the amino acid numbers indicated from the sequence below. ABD, actin-binding domain; Ypet; F40(donor only)-tension sensor, mCherry. (Bottom) Amino acid sequence of ABD-F40 (donor only)-ABD. The color code corresponds to the domains indicated on the diagram above and the spacers between domains are indicated in black letters. The purple amino-acid region corresponds to the 6xHis-tag for protein purification.

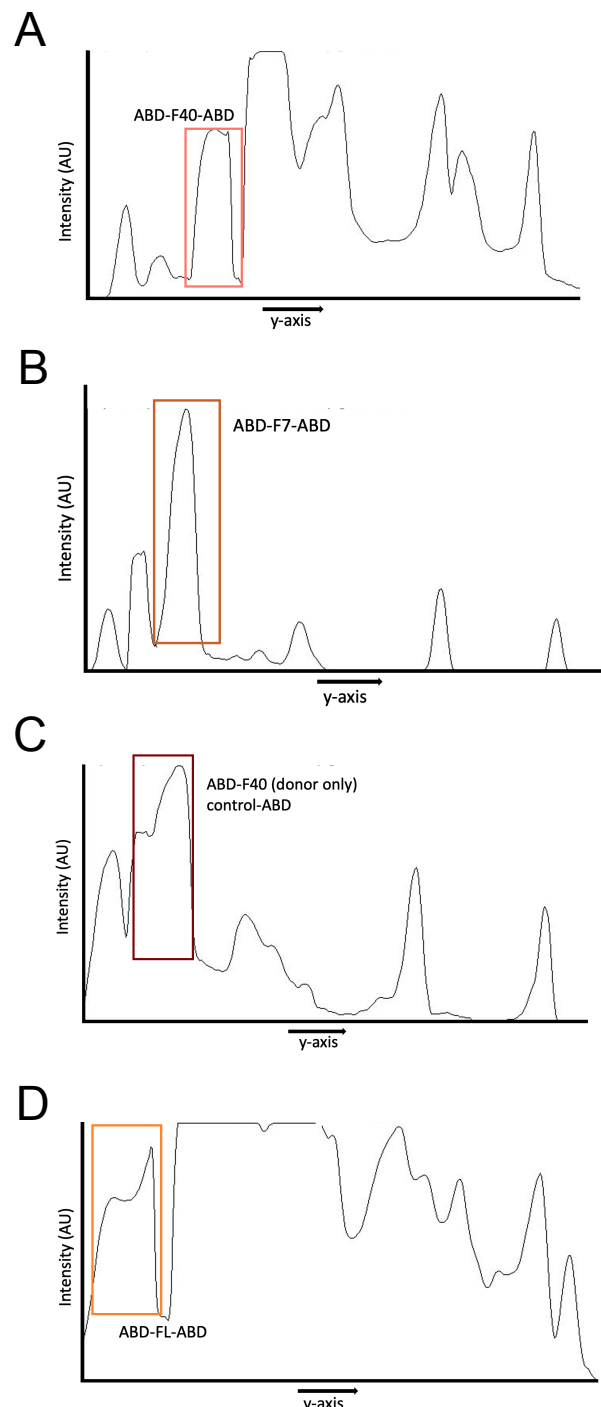


Figure 6.13: Densitometry analysis of the protein bands observed by SDS-PAGE analysis in Figure ??A. Plots show the measured pixel intensity (UA) versus distance (y-axis), where the peaks along the y-axis correspond to the different gel bands. Densitometry of (A) ABD-F40-ABD, (B) ABD-F7-ABD, (C) ABD-F40 (control donor only)-ABD, and (D) ABD-FL-ABD. Colored squares indicate the full length monomer.

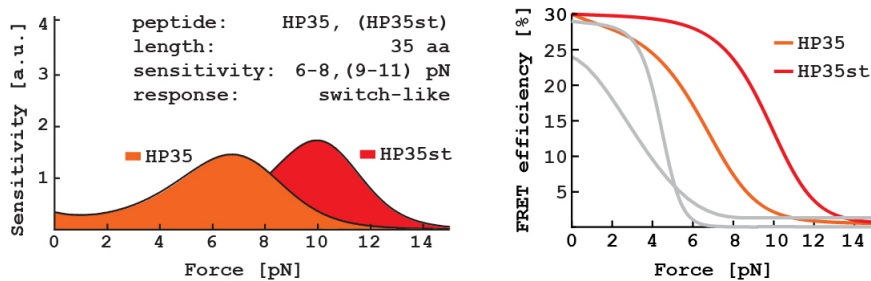


Figure 6.14: Tension sensing modules engineered by the group of Carsten Grashoff[430, 1, 431] that were not implemented in our engineered crosslinkers for the time being. (A) The HP35 module uses the 35 aa-long villin headpiece peptide (HP), which is characterized by an unfolding response at 6–8 pN (orange distribution). The mutant HP35st module is sensitive to 9–11 pN (red distribution). (B) Comparison of the force-dependent FRET efficiency of the HP35 and HP35st modules with the F40 and FL modules (grey curves, discussed in Figure 6.3). Data are taken from [431].

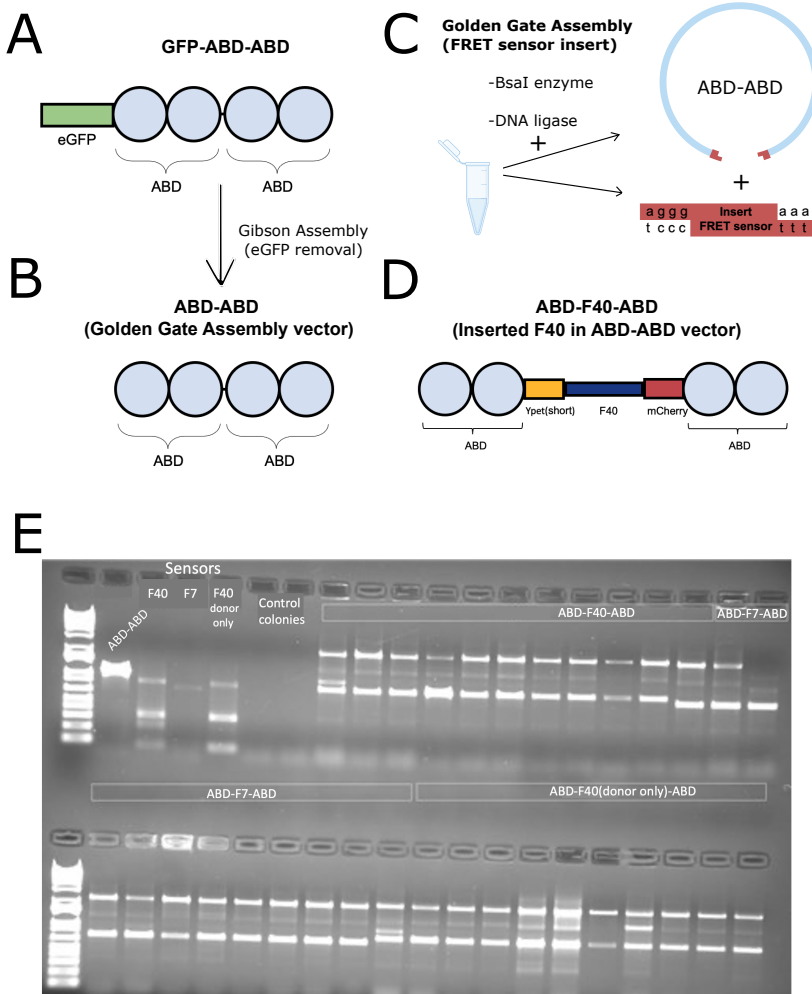


Figure 6.15: (A) GFP-ABD-ABD construct, developed for testing the actin crosslinking vector functionality. (B) ABD-ABD vector obtained by removal of GFP from the construct in A. Note that this construct was not purified. (C) Golden Gate assembly strategy to insert each FRET sensor in the ABD-ABD vector. Engineering strategy for all vectors starting with YPet and finishing with mCherry in the linearized insert vector. (D) Example force sensor construct based on the F40 module. (E) Colony amplification control for the assembled constructs via Golden Gate Assembly. For each sample (ABD-F40-ABD, ABD-F7-ABD, ABD-F40(donor only)-ABD), several copies were picked (corresponding to all the lanes below the construct reference). The ladder did not run well enough to quantify the DNA size, but qualitative comparison can be established with the actin crosslinker vector for the sensors (ABD-ABD) and the inserted fragments (F40, F7 and F40-donor only tension sensors).

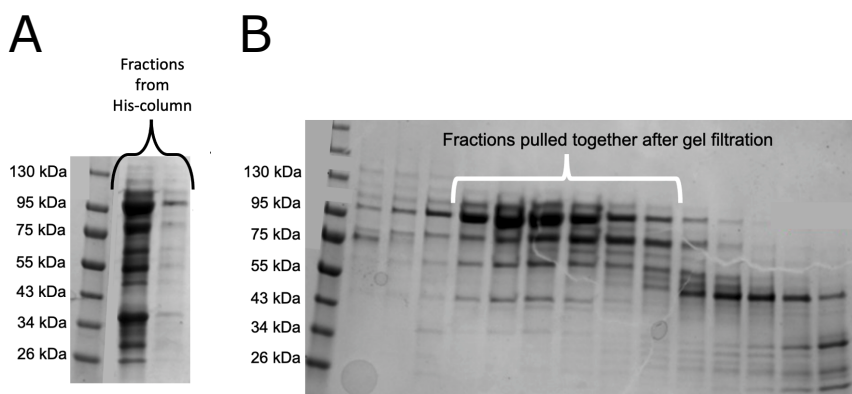


Figure 6.16: Example of optimized purification for ABD-FL-ABD. (A) SDS-PAGE gel showing the fractions from the His-column purification that were selected for further purification. The first lane shows the molecular weight marker for reference. (B) SDS-PAGE gel showing the fractions collected from subsequent gel filtration. Left lane shows the molecular weight marker. The white bracket shows the fractions that were pooled together for the final protein sample.

7

OUTLOOK

In this thesis, I have explored the interactions and mechanical synergy of actin and vimentin, providing a basis for understanding the physical origins of cytoskeletal crosstalk and its impact on cell mechanics. In Chapter 2, I first reviewed prior work on the role of cytoskeletal crosstalk in cell mechanics and migration, with a focus on confronting live cell versus cell-free reconstitution studies. Next in Chapter 3, I demonstrated the cell-free reconstitution of composite networks of F-actin and vimentin and characterized their microscopic dynamics and macroscopic rheology. In Chapter 4, I extended this system with tunable crosslinking by engineering crosslinkers that mimic natural crosslinker proteins such as plectin. In Chapter 5, I demonstrated that the resulting crosslinked composite networks exhibit intriguing synergistic mechanical properties. Finally, in Chapter 6, I introduced engineered F-actin crosslinker proteins with embedded FRET-based force sensors, which can in future be modified to also report on force transmission between F-actin and vimentin. Despite these advances, many questions still remain open: How can we better understand the functional consequences of crosstalk for cell mechanics? Can we do so by combining cell-free and cell-based studies? How can we better understand the tissue-specific roles of the different intermediate filament proteins in different cell types? In this Outlook chapter, I present exploratory work addressing these questions. While this thesis has an experimental focus on cell-free studies, I hope, through this Outlook chapter, to stimulate efforts to bring together cell-free and cell-based approaches to understand cytoskeletal crosstalk.

7.1. INTRODUCTION

THE cells that make up our bodies exhibit remarkable capabilities to undergo shape changes needed for essential processes such as cell division and movement. These shape changes are mainly mediated by the dynamics of the cytoskeleton, which comprises three distinct networks of protein polymers: filamentous actin (F-actin), microtubules, and intermediate filaments. Of these, intermediate filaments are the least studied cytoskeletal constituent. Each polymeric system possesses unique dynamical and mechanical properties that cells leverage in various physiological processes like migration, division, polarization, and intracellular transport. Moreover, an ensemble of proteins is involved in coordinating the activities of the three cytoskeletal systems, either through direct physical crosslinks or through indirect biochemical regulation.

Despite our comprehensive understanding of the individual functions of the three cytoskeletal subsystems through cell-free and cell-based studies, a detailed comprehension of how their activities are coordinated within cells remains elusive. In this thesis, our main focus is on extending cell-free reconstitution to composite networks of actin and vimentin, with the aim to understand the mechanical synergy of these two cytoskeletal networks. In order to mechanically couple them, we engineered a library of bifunctional crosslinkers based on natural crosslinking proteins (plectin and APC), and we characterized their binding kinetics and their effects on network organization and mechanics (Chapters 4 and 5). As reviewed in Chapter 2, we believe that such cell-free (or bottom-up) studies are an important complement to cell-based studies to understand the role of cytoskeletal crosstalk in fundamental cellular processes like cell migration. We therefore hope that the work presented in this thesis forms a basis for further explorations of cytoskeletal crosstalk in future.

In this Outlook chapter, I discuss several directions for future work, illustrated with pilot data. First, I propose follow-up research on crosslinker-mediated cytoskeletal crosstalk. I show that the engineered ACTIF crosslinker can be expressed in cells to study its function as an actin-vimentin crosslinker within the full complexity of the cellular environment. This approach will in future enable us to test the physiological relevance of our cell-free findings. I furthermore present an alternative reconstituted cytoskeletal system where actin is crosslinked to microtubules using anillin, which is relevant in the context of cell division. Second, I propose follow-up research deepening the central role of intermediate filaments in cytoskeletal crosstalk. Intermediate filaments have been much more challenging to study than actin filaments and microtubules because the field lacks experimental tools to fluorescently tag intermediate filaments or to interfere with their assembly. I show preliminary data which demonstrate that coiled-coil peptides designed to mimic the central coiled coil domain of vimentin can interfere with *in vitro* vimentin filament assembly. Third, I discuss the need for studying different intermediate filament proteins. Throughout this thesis, the importance of intermediate filaments in cell mechanics and resilience has been recurrently highlighted. In humans, intermediate filaments are a large family with around 70 genes encoding different proteins [452]. Each cell type in the body expresses a specific combination of intermediate filament proteins and isoforms thereof, which changes during development and in disease. This thesis fo-

cused on vimentin, which is mainly present in mesenchymal cells and stem cells. In this chapter, I show preliminary data on the viscoelastic properties of networks reconstituted from purified glial fibrillary acidic protein (GFAP), which is specifically expressed in astrocytes (with 10 distinct isoforms) in conjunction with vimentin, nestin, and synemin.

7.2. BRIDING CELL-FREE AND CELL-BASED STUDIES OF CROSSLINKER-MEDIATED CYTOSKELETAL CROSSTALK

7.2.1. EXPRESSING THE ENGINEERED ACTIN-VIMENTIN CROSSLINKER ACTIF IN CELLS

Plectin plays a crucial role in crosslinking vimentin intermediate filaments to a diverse range of intracellular structures (reviewed in [453]). Its C-terminal domain binds to vimentin [454, 376], while its N-terminal domain targets different binding partners depending on the plectin splice isoform [61]. Various plectin isoforms have the capability to establish crosslinks between vimentin and F-actin through their N-terminal calponin homology domains [73, 74]. Plectin is a giant cytolinker with a multidomain structure and a molecular weight of \sim 500 kDa, which complicates recombinant expression and purification. In Chapters 4 and 5, I introduced a novel plectin-mimicking crosslinker which we called ACTIF and demonstrated its actin-vimentin crosslinking functionality through bottom-up reconstitution. Since reconstituted systems are highly simplified, it will be important to complement this approach with cell-based studies to test how our findings carry over to the cellular environment.

In order to assess the functionality of ACTIF directly in cells, we decided to express ACTIF in wild type (plectin $+/+$) mouse embryonic fibroblasts¹. After transfection, we

¹Cell transfection and imaging experiments were performed by our collaborator, Dr. Lilli Winter (Medical University of Vienna). The cells were provided by Dr. Gerhard Wiche (University of Vienna). We used FuGENE 4K, a widely used transfection reagent effective for a wide range of cell types. Cells were seeded on glass coverslips at a density of 80,000 cells per well in either 6-well or 24-well plates. The cells were allowed to grow overnight to achieve optimal confluence. Transfection Reagent Preparation: The FuGENE 4K transfection reagent and DMEM were equilibrated to room temperature before use. Next, 100 μ L DMEM was combined with 2 μ g of plasmid DNA, followed by thorough vortexing. To this mixture, 4 μ L of FuGENE 4K was added, taking care not to pipette directly against the tube wall to ensure proper mixing and minimize adhesion to the plastic. The mixture was then left at room temperature for 15-20 minutes to allow for complex formation. After removing the medium from the cells, a minimal volume of fresh medium (300-500 μ L) was added to cover the cells. The transfection mixture was added dropwise to the cells, followed by gentle plate swinging for thorough mixing. The cells were then placed in the incubator overnight to facilitate successful transfection.

performed immunostaining² and observed the cells by fluorescence microscopy³. As shown in Figure 7.1A, we observed a strong overlap of the GFP-tagged ACTIF signal with the vimentin cytoskeleton, but not much overlap with the actin cytoskeleton. This observation is consistent with our *in vitro* observation in Chapter 4 that ACTIF has a much (70-fold) higher binding affinity for vimentin as compared to F-actin. We nevertheless do observe three-way co-localization of ACTIF, vimentin and actin at some actin stress fibers, as shown in Figure 7.1B (see arrow).

Next, we also tested the potential of ACTIF to restore actin-vimentin crosslinking in plectin-deficient fibroblasts (plectin-/-). These cells had a similar morphology as plectin +/+ cells and ACTIF again mainly co-localized with the vimentin cytoskeleton (Figure 7.1C), although we also observed some three-way colocalization of ACTIF, actin and vimentin at actin stress fibers (Figure 7.1D, see arrows). These findings suggest that ACTIF has actin- and vimentin-binding activity in cells, but more quantitative analysis of co-localization is needed to firmly establish its crosslinking functionality.

Transfection of plectin-deficient fibroblasts with expression plasmids encoding full-length rat plectin (pBN60) or carboxy-terminal fragments of plectin [455, 364] have previously been shown to cause a collapse of the vimentin network into a perinuclear aggregate [456]. We did not observe clear indications of perinuclear aggregate formation upon ACTIF transfection, neither in the plectin +/+ nor the plectin -/- cells, but clearly more careful comparisons with untransfected cells will be needed. Moreover, it will be interesting to test phenotypic consequences of ACTIF transfection, such as effects on cell motility and stiffness. Excitingly, the modular design of the ACTIF crosslinker should make it possible to test how molecular features of actin-vimentin crosslinkers such as the identity of the binding domains, length and flexibility of the spacer, and dimerization affect cell functions.

7.2.2. ANILLIN-MEDIATED CROSSLINKING OF ACTIN AND MICROTUBULES

Anillin is a highly conserved scaffolding protein that plays a key role as a regulator of cytokinesis [457] and of the activity of the actomyosin cortex of epithelial cells [458]. Its involvement in the formation and stabilization of the cytokinetic ring and in intercel-

²Cells grown on coverslips were washed with 1x PBS, fixed in 4% paraformaldehyde (PFA) in PBS for 20 minutes at room temperature, and again washed with PBS. Coverslips were incubated with 100 mM glycine in PBS for 15 minutes and washed twice with PBS for 5 minutes. Next, the cells were permeabilized in PBS containing 0.1% Triton X-100 for 5 minutes. For blocking of unspecific binding sites, the coverslips were incubated with 4% Bovine Serum Albumin (BSA) in PBS for 60 minutes at room temperature. Primary antibody dilutions were prepared in PBS, and dishes were incubated with antibody solution for 60 minutes at room temperature. After washing with PBS thrice for 5 minutes, fluorescently tagged secondary antibodies, diluted in PBS, were added and incubated for 60 minutes at room temperature under light protection. Cells were stained with the actin-specific toxin phalloidin (CoraLite 594 Phalloidin, ProteinTech, 1:1000), goat-anti Vimentin antibodies (P. Traub, University of Bonn, Bonn, Germany; 1:400; with biotin-conjugated Affinipure donkey-anti goat IgG (H+L), 1:100, in combination with streptavidin Alexa 647, 1:500). Cells were washed twice with PBS for 5 minutes, stained with 4,6-diamidino-2-phenylindole (DAPI, Sigma Aldrich, 10236276001; 2 µg/ml) for 10 minutes, and rinsed with milliQ water. Coverslips were mounted by placing them onto a small drop of Mowiol on a glass slide. Samples were dried overnight at room temperature in the dark.

³Imaging was performed using an Olympus FLUOVIEW FV3000 confocal microscope equipped with PlanApo N 60x 1.4 NA and UPLAN FLN 40x 1.3 NA objective lenses (Olympus, Japan). Z-stacks were recorded using the Olympus Fluoview software and processed with ImageJ software to generate maximum intensity projections.

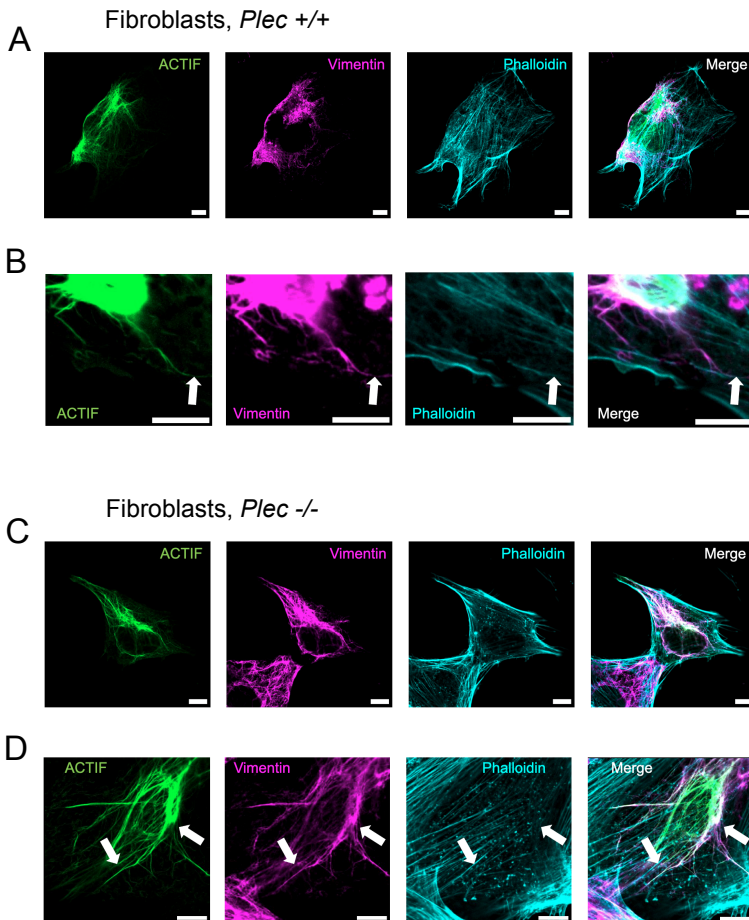


Figure 7.1: (A) Confocal fluorescence images of wild-type mouse embryonic fibroblasts (*plec* $+/+$) transfected with eGFP-tagged ACTIF and immunostained for vimentin and actin. Panels from left to right show ACTIF, vimentin, F-actin, and the merge image. The merge image shows mainly co-localization of ACTIF with vimentin. (B) Zoomed-in images (same order) showing co-localization of ACTIF with both vimentin and actin at actin stress fibers (see arrow). (C) Confocal fluorescence images of plectin-knockout cells (*plec* $-/-$) transfected with ACTIF. (D) Zoomed-in images showing co-localization of ACTIF with vimentin and actin at actin stress fibers (see arrows). All scale bars are 10 μ m.

lular bridge maturation has been well-established in the literature [459, 460, 461]. In epithelial monolayers, anillin impacts tissue mechanics by regulating the medial-apical actin-myosin network and cell-cell junction integrity [458, 462].

Anillin is a large (124 kDa) multidomain protein with many different interaction partners (see schematic representation in Figure 7.2A). Its N-terminal half contains three domains that bind formin (an actin-nucleator protein), F-actin, and nonmuscle myosin 2, respectively. The C-terminal half of anillin contains the anillin-homology domain, which binds RhoA, septins, myosins and lipids. The N- and C-terminal halves are separated by a spacer region of undefined fold which is predicted to contain a coiled coil domain that may facilitate multimerisation [457].

The actin-binding domain of anillin has been demonstrated to bind F-actin by *in vitro* reconstitution experiments [463, 464, 465]. Several studies observed co-localization of anillin with microtubules during cytokinesis by fluorescence imaging and attributed this to an indirect interaction mediated by the spindle-associated component RacGAP50C [466] and/or to direct interactions evident from co-sedimentation assays with purified proteins [467, 468]. Based on these interactions, anillin could potentially regulate actin-microtubule crosstalk during cell division by crosslinking. However, it has not yet been definitively demonstrated that anillins binds microtubules nor that it can actually serve as a crosslinker for actin and microtubules.

To address these open questions, we performed cell-free experiments using full-length human anillin (isoform 2, 1087 amino acids) purified from insect cells by our collaborators Dr. Zdenek Lansky and Dr. Marcus Braun (BIOCEV, Prague) [465]. To visualize actin-microtubule interactions at high spatial resolution, we used Transmission Electron Microscopy (EM) on negatively stained cytoskeletal proteins deposited on Formvar-coated grids. For all experiments, we used microtubules stabilized with the nonhydrolyzable GTP-analog GMPCPP, F-actin (1 μ M) and/or anillin (100 nM).

First, we tried to recapitulate earlier findings [463, 464, 465] that anillin interacts with F-actin. When G-actin was polymerized on its own, we observed entangled F-actin filaments with a diameter of around 8 nm (see arrows in Figure 7.2B(left)). When pre-polymerized F-actin was mixed with anillin, we observed F-actin bundling (Figure 7.2B (right, see arrows)). This observation confirms that anillin binds F-actin and serves as an F-actin crosslinker. By contrast, anillin did not obviously bundle microtubules, as shown by comparing images of microtubules in the absence (Figure 7.2C (left)) and presence (Figure 7.2C (right)) of anillin. From these data alone it is unclear whether or not anillin can bind microtubules. However, our collaborator Dr. Ilina Bareja found by fluorescence imaging that anillin does bind microtubules (data not shown).

Finally, we combined F-actin and microtubules. In the absence of anillin we did not observe any bundling or other visible signs of interactions between F-actin and microtubules (see Figure 7.2D(left)). By contrast, we observed large bundles when F-actin was mixed with GMPCPP-microtubules and anillin (see Figure 7.2D(right), where blue arrows point out actin filaments and yellow arrows point out microtubules). A zoomed-in image of the actin-microtubule composite co-assembled in presence of anillin is shown in Figure 7.2E. The red squares highlight regions where aligned filaments in close proximity or contact within the bundles show a coexistence of actin filaments (recognizable by their width of \sim 7 nm) and microtubules (recognizable by their width of \sim 25 nm). We

also observe microtubules aligned together within these bundles. These observations strongly suggest that anillin can bind microtubules and crosslink them to other microtubules and to actin filaments.

The potential role of anillin as a crosslinker between F-actin and microtubules raises interesting questions to explore in the future: what are the consequences of this crosslinking functionality for actin-microtubule co-organization? How does this crosslinking impact the mechanical properties of *in vitro* reconstituted networks (bottom-up) and dividing cells or epithelial cells (top-down)? In addition, I strongly encourage readers that come from a more synthetic biology perspective to consider the use of anillin as a tool to build a minimal divisome to divide synthetic cells [469].

7.3. INTERMEDIATE FILAMENTS: A LONG ROAD OF DISCOVERIES AHEAD

7.3.1. PEPTIDES FOR TARGETING VIMENTIN AND INTERFERING WITH ITS ASSEMBLY

Intermediate filament research is still in an early stage compared to actin and microtubules research. Actin was first mentioned explicitly in 1983 [470] but it was actually already first isolated from acetone-dried muscle powder in the early 1940's in the laboratory of Albert Szent-Gyorgyi at the Institute of Medical Chemistry in Hungary [471]) (for a historical overview see ref. [472, 471]). Microtubule studies can be traced back to the 1940's as well: the first biophysical evidence for their dynamic structure and function in mitosis was obtained through polarizing microscopy [473]. Interestingly, intermediate filaments were actually observed even earlier by cytologists and histologists, in 1925 in a period when silver staining was used to generate contrast for observations with bright-field microscopy [474]. Keratin, an intermediate filament protein present in hair and nails, was discussed by Francis Crick in 1952 [475]. From then onwards, intermediate filaments gained more attention in the literature [35] due to their impact in skin diseases [476] and in brain-related disorders such as glioblastoma [477] and Alexander disease [478]. In recent years there has been growing attention for the basic mechanisms by which intermediate filaments influence essential cellular processes such as cell migration and division, but many questions remain. In particular, the tissue-specific functions of different intermediate filament proteins in cell differentiation and tissue-specific cell functions are largely unexplored.

Intermediate filaments share a tripartite monomer structure: an intrinsically disordered N-terminal head, a central α -helical rod and a disordered C-terminal tail (see schematic representation in Figure 7.3A). These domains have different roles in filament formation: the rods drive monomer assembly into dimers via the α -helical rod, while the dimers in turn assemble into antiparallel tetramers. Subsequently, the head domains mediate sideways and end-to-end association of the tetramers into filaments. The tails are exposed on the filament surface and mediate interactions between intermediate filaments [392]. Recent cryo-electron microscopy data showed that in case of vimentin, this hierarchical assembly process results in an intertwined and flexible helical structure

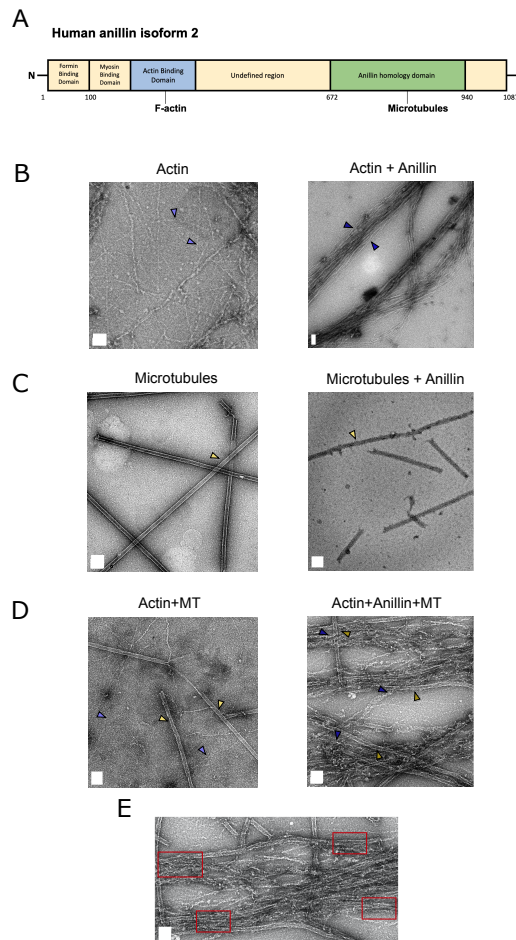


Figure 7.2: A) Domain structure of human anillin isoform 2. The actin-binding domain (blue) has previously been shown to directly bind F-actin by *in vitro* experiments. The anillin homology domain has previously been proposed, but not yet definitively proven, to bind microtubules. The numbers underneath the domain structure denote amino acid residue numbers. (B) Electron micrographs of 1 μ M F-actin (left) and 1 μ M pre-polymerized F-actin mixed with 100 nM anillin (right). (C) Electron micrographs of GMPCPP-stabilized microtubules (exact concentration not known) (left) and microtubules + 100 nM anillin (right). (D) A mixture of pre-formed F-actin and microtubules without anillin shows no visible signs of interactions (left) whereas the same mixture with anillin shows large bundles of aligned filaments. (E) Closer view of bundle formation upon mixing actin, microtubules and anillin. Red squares show areas indicative of actin-microtubule and microtubule-microtubule crosslinking, recognizable from the widths of filaments in close contact (~ 7 nm for F-actin and ~ 25 nm for microtubules). All scale bars are 100 nm.

of 40 α -helices in cross-section, organized into five protofibrils [39]. The head domains were seen to form a fiber in the lumen of the filaments, while the tail domains form lateral connections between the protofibrils.

Structure-based design of peptides that bind intermediate filaments tightly and specifically is challenging given the complexity of the structure of the filaments and their component monomers described above. Motivated by the essential role of coiled-coil dimerization in filament assembly, our collaborators Prof. Dek Woolfson, Dr Selma Crecente Garcia and Dr. Reece King (University of Bristol) decided to design coiled-coil peptides to target this domain. From a design perspective, protein coiled-coils have the advantage that they are defined by a small number of parameters that can be changed systematically [479]. Moreover, the rod domain of vimentin has an α -helical subdomain termed coil 1A (CC1A) that forms less stable coiled-coil assemblies than other parts of the α -helical rod domain [480]; moreover, this subdomain is also part of a sequence implicated in head-to-tail assembly of vimentin [481]. This region could therefore provide a region in the filament that is amenable to infiltration and binding of α -helical peptides with a complementary sequence. Using a bioinformatics approach, our collaborators designed three different *de novo* peptides targeting CC-1A of human vimentin (see Figure 7.3B): the parent CC1A peptide and an arginized version (Arg-CC1A) that has some of its solvent-exposed residues (identified from the X-ray crystal structure of vimentin's helical domain [482]) replaced by arginines to facilitate cell penetration [483]. Moreover, our collaborators also designed a peptide targeting CC-2B of human vimentin (see Figure 7.3B).

To test the functionality of the peptides, we tested two scenarios. In the first scenario, vimentin filaments (0.1 mg/mL) were co-polymerized with the peptides by mixing vimentin tetramers with the peptides and incubating in F-buffer (20 mM Tris-HCl, pH 7.4, 50 mM KCl, 2 mM MgCl₂, 0.5 mM ATP) at room temperature for 1 hour (Figure 7.3C). Transmission electron microscopy of the negatively stained preparation revealed that the parent CC1A peptide does not alter the filaments (Figure 7.3C (left)), whereas the Arg-CC1A peptides do. The Arg-CC1A peptides appear to aggregate on top of filamentous-like structures that look more packed and less entangled than vimentin filaments assembled in the absence of the peptides (Figure 7.3D, E). In the second scenario, the peptides were added to a solution of preformed vimentin filaments obtained by a one-hour polymerization (Figure 7.3D). Adding the peptides after filament formation qualitatively had a similar effect on the vimentin filaments when we compare the morphology of filaments mixed with the control parent sequence (Figure 7.3D (left)) to filaments mixed with binders (consecutive panels in Figure 7.3D for addition of Binder Coil 1, Binder Coil 2 and Arginized Coil 1, respectively).

Our findings provide a first proof of concept that the peptides can target and interfere with vimentin filaments in a purified context. The labs of Prof. Sandrine Etienne-Manneville (Institut Pasteur) and Prof. Elly Hol (UMCU) simultaneously demonstrated that the Arg-CC 1A peptide can penetrate into U251 cells and brain organoids, respectively (personal communication). It will be interesting to thoroughly test and compare the ability of the peptides to label and interfere with the vimentin cytoskeleton *in vitro* and in cells. Besides providing a much-needed tool for vimentin control, this will add fundamental knowledge regarding intermediate filament structure, dynamics and for-

mation in the cell. Eventually it will also be interesting to target the N- and C-terminal head and tail domains given the large variation in their sequence and length between different intermediate filament types and isoforms. I believe that peptides designed to target intermediate filaments will provide powerful tools to systematically and in a controlled manner track the different interactions of intermediate filaments with their surroundings (e.g., with the cytoskeleton, focal adhesions, signalling pathways, and the nuclear envelope).

7.3.2. *In vitro* RECONSTITUTION OF GLIAL FIBRILLARY ACIDIC PROTEIN (GFAP)

Intermediate filament proteins are a large family expressed from 70 genes in humans [452]. Different intermediate filaments are expressed in different areas of the body. In this thesis we focused on vimentin, which is one of the more ubiquitously expressed intermediate filament proteins, being present in all mesenchymal cells. By contrast, Glial fibrillary acidic protein (GFAP) is the hallmark intermediate filament protein specific to astrocytes, a major type of glial cell in the central nervous system with many regulatory functions [484].

Like vimentin, GFAP is classified as a type III intermediate filament and it has a similar tripartite monomer structure (Figure 7.4A). With the exception of a few missense mutations residing in either the head or the tail domain, most pathogenic GFAP mutations discovered to date are located in the rod domain [485]. The mechanical properties of GFAP are still unknown. Moreover, only a handful of studies have reconstituted GFAP filaments *in vitro* [486, 487, 485]. Thus many fundamental questions are open: What are the mechanical properties of GFAP networks and are they, like other intermediate filaments, crosslinked via salt-dependent tail-tail interactions? Is there synergy between GFAP and other intermediate filaments and can we pinpoint the role of each intermediate filament protein in cytoskeletal crosstalk in astrocytes? I here present our preliminary work on these matters, hoping this can lay the basis for future experiments.

Previous studies of purified GFAP used an imidazole-based buffer containing 20 mM imidazole [pH 6.8], 100 mM NaCl, and 1 mM DTT [486, 487, 485]. We decided to reproduce reconstitution in this buffer using recombinant GFAP expressed from a plasmid kindly provided by Prof. Ming-Der Perng (National Tsing Hua University). Transmission electron microscopy of negatively stained GFAP reconstituted in this imidazole buffer showed well-formed filaments with a diameter of 10 nm (Figure 7.4B), consistent with previous literature [486, 487, 485]. Aiming to eventually co-polymerize vimentin and GFAP, we also tested GFAP reconstitution in the buffer that we used throughout this thesis for vimentin assembly (25 mM 1,4-Piperazinediethanesulfonic acid [PIPES] [pH 7.0], 100 mM KCl, 4 mM $MgCl_2$, 1 mM EGTA, 1 mM DTT). We again observed 10-nm GFAP filaments, but the structures were variable in length and irregular in width and we observed some aggregates (data not shown). We therefore recommend to do buffer optimization in future studies.

We then turned to the mechanical properties of the reconstituted GFAP networks. Before addressing the results, it is important to remind the reader that similar studies for vimentin showed that its C-terminal tail domains cause noncovalent crosslinking (see

[200] and Chapter 5 of this thesis). Networks of full-length vimentin strain-stiffen under shear, whereas tail-truncated vimentin networks do not strain-stiffen. Several studies showed that multivalent cations crosslink vimentin's tail domains in a dose-dependent manner [197, 202, 198, 199]. Since GFAP is from the same type III family as vimentin, we expected the viscoelastic properties of GFAP networks to be fairly similar to those of vimentin networks. Interestingly, however, we found that reconstituted networks of 1 mg/mL GFAP (Figure 7.4C (red curve)) were significantly softer than networks of 1 mg/mL vimentin (Figure 7.4C (violet curve)), with linear elastic moduli of 1 Pa versus 2 Pa. However, the addition of divalent cations to GFAP (5 mM ZnCl₂) (Figure 7.4C (scarlet curve)) increased the stiffness of the GFAP networks about two-fold across the entire frequency range and made the 'crosslinked' GFAP stiffer than the vimentin network. This finding suggests that GFAP is also ionically crosslinked, similar to vimentin networks [197, 202]. However, our results are inconclusive at this point because the loss tangents, defined as $(\tan(\delta) = \frac{G''}{G})$, are similar within experimental error for all networks (Figure 7.4C (bottom)).

When we compared the nonlinear elastic response of vimentin and GFAP networks, we found very surprising results: vimentin networks strain-stiffened after an initial fluidization (see Figure 7.4D (violet curve)), whereas GFAP networks did not strain-stiffen (see Figure 7.4D (red curve)). When we added divalent cations, the GFAP network still did not strain-stiffen (Figure 7.4D (scarlet curve)). One interpretation could be that the GFAP filaments are significantly shorter than vimentin filaments, causing a lower network connectivity. Yet our EM data do not support this (Figure 7.4B). We therefore also consider the option that crosslinking might be less effective for GFAP than for vimentin due to a difference in the length and sequence of their C-terminal tail domains.

To investigate this hypothesis, we contacted Prof. Roy Beck (Tel Aviv University) and built on his previous bioinformatic research [488, 489] to evaluate possible differences in the tail interactions of vimentin versus GFAP. Specifically, his group established a bioinformatic analysis called 'Handshake analysis of short-range electrostatic interactions', which was applied to neurofilaments. This analysis calculates the energy matrices for all possible segment pairs of opposing tails in order to locate pairs of amino acid segments that interact via electrostatic bridges. We imported the protein sequences of human vimentin and GFAP from the UniProt database and tried to identify which sequence regions were more attractive with each other. For both full-length protein and only the C-terminal tail domain, we tried to identify the polypeptide segments involved in such attraction. In order to do this, the unscreened Coulomb energy of two interacting segments is calculated, where each segment is centered at a specific tail amino acid (Figure 7.4E) and the segment length is on the order of the polypeptide persistence length (we consider $\sim 1 \mu\text{m}$; and for intermediate filaments one may consider 0.2–3 μm , depending on the IF composition and measurement conditions [490]). We thus obtain a 2D matrix that points at the most electrostatically viable cross-linking pairs. The handshake analysis of the tails of vimentin (Figure 7.4F) and GFAP (Figure 7.4G) revealed multiple potential attractive sites located among their last amino acids, as shown in blue. For vimentin, blue patches appear at the edges of the matrices, whereas for GFAP the patches are not as blue (i.e., less attractive) and less at the edges. This preliminary analysis suggests that there may indeed be differences in the crosslinking efficiency of GFAP versus

vimentin. However, we hold off from a definitive conclusion. A more refined analysis will be needed in future, accounting for more neighbours and for phosphorylation. Further, we will need to explore alternative hypotheses, such as a difference in filament length (as mentioned above) or filament structure. It is known that so-called kick-start assembly by rapid dilution of intermediate filaments into assembly buffer, as used here, can result in different filament structures as compared to slower assembly achieved by overnight dialysis assembly [315], used in previous GFAP studies [486, 487]. It will therefore be interesting to compare different filament assembly protocols.

By reconstituting GFAP under different buffer conditions, we paved the way for future co-polymerization of different intermediate filaments. Moreover, if we find the right environmental conditions for co-assembly of GFAP and vimentin, what are the arrangements that will emerge? Intermediate filaments have a hierarchical assembly: if we copolymerize these proteins, will we have mixed populations of unit-length-filaments (ULFs) within a filament or mixed monomers within the ULF? Eventually, can we also understand the co-assembly process in cells? These questions remains open and I really hope future work will unravel these intricacies.

7.4. ACKNOWLEDGEMENTS

Concerning the intermediate filament work, we thank Ming-Der Perng for providing the GFAP plasmid. We also thank Roy Beck for providing software and valuable advise regarding the handshake analysis. We also thank Dek Woolfson, Selma Crecente Garcia and Reece King for providing the *de novo* designed vimentin-targeting peptides. Thank you as well to Johan Kramer and Jeffrey den Haan for investing a major effort to develop the GFAP purification protocol. Thanks to Jeffrey den Haan for purification of actin and vimentin and thank you to Cecile Leduc and Quang Tran for their invaluable help with the vimentin purification. Concerning anillin, thank you to Ilina Bareja for the great collaboration and thank you to Zdenek Lansky and Marcus Braun for providing full length anillin. Last but not least, a big thank you to Lilli Winter and Gerhard Wiche for performing the cell-based experiments with ACTIF and providing the beautiful confocal images of the cells shown in this chapter.

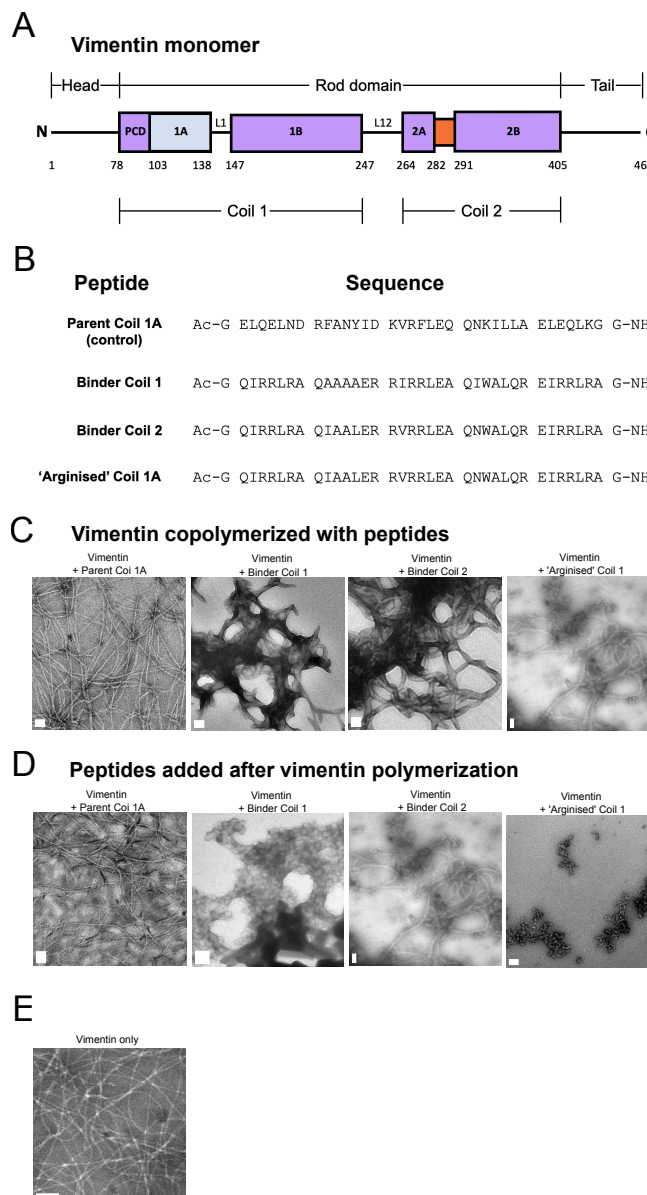


Figure 7.3: (A) Domain structure of a vimentin monomer, portraying its tripartite domain architecture with an N-terminal head and a C-terminal tail separated by an α -helical rod domain. The rod domain comprises two equally sized subdomains termed coil 1 and coil 2, which are connected by a non- α -helical linker segment L12. Both coil regions in turn consist of several subdomains. Numbers underneath the domain structure denote amino acid residue numbering [452]. (B) Overview of the synthetic peptides designed to bind to the coil 1 and coil 2 subdomains of vimentin monomers. The "parent coil 1A" and its arginised variant Arg-CC1A should target coil A; Arg-CC1A should additionally be able to penetrate cells. The binder coil 2 should target the coil 2B (specifically sections 368-401). (C) TEM images of vimentin (0.1 mg/mL) that has been co-polymerized with 0.1 mg/mL peptide, with (from left to right): the "parent coil 1A", the binder coil 1, the binder coil 2 and the "arginised" coil 1A. (D) TEM images of vimentin that was pre-polymerized for 1 hr before mixing with the different peptides. From left to right, vimentin was combined with the "parent coil 1A", the binder coil 1, the binder coil 2 and the "arginised" coil 1A. Same concentrations as in C. (E) Representative TEM image of a control sample of vimentin filaments assembled in absence of peptides at 0.1 mg/mL. All scale bars are 100 nm.

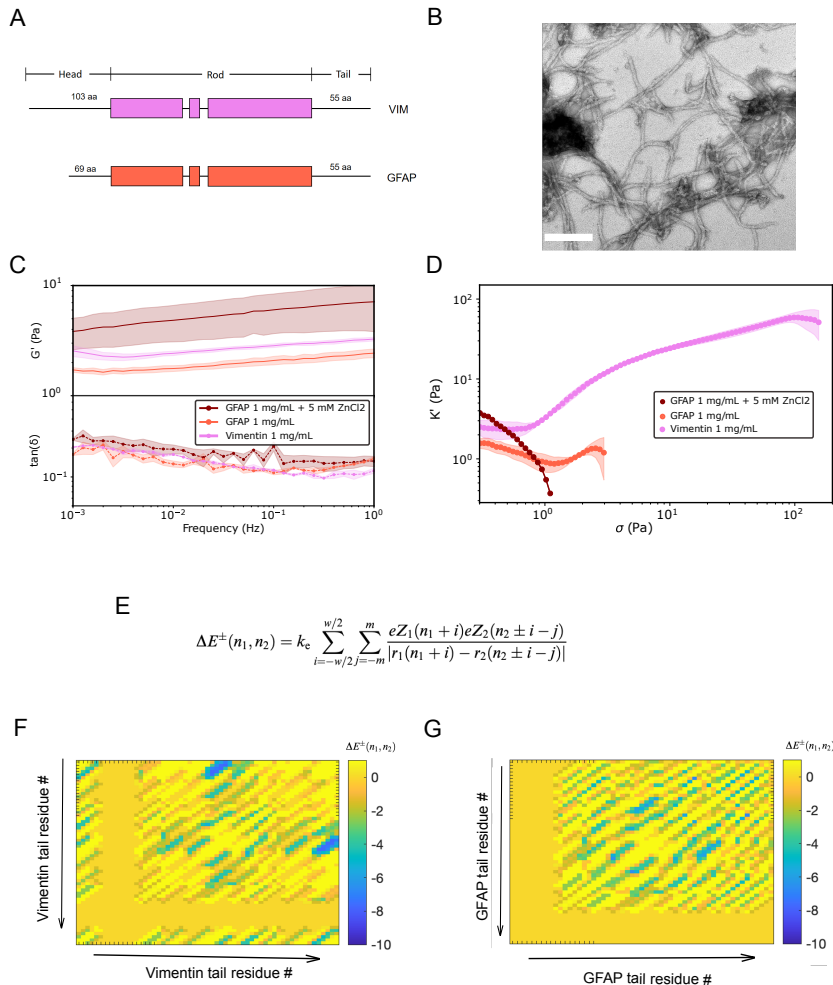


Figure 7.4: (A) Schematic representation of the tripartite domain structure of vimentin (top, violet) and GFAP (bottom, red) monomers. Both monomers have a head, rod and tail domain. (B) Reconstituted GFAP filaments at 0.1 mg/mL imaged with transmission electron microscopy. (C) (Top) Frequency dependence of the elastic shear modulus of networks of vimentin (violet), GFAP (red) and 'GFAP crosslinked' using 5 mM ZnCl₂ (scarlet), measured by cone-and-plate rheology. The protein concentrations were 1 mg/mL. (Bottom) Corresponding loss tangents, defined as the ratio of the loss modulus G'' to the storage modulus G' (same color code). Note that the loss tangent is noisy because the applied strain and the shear moduli (especially G'') are small, so the stress is close to the sensitivity limit of the rheometer. (D) Dependence of the tangent elastic modulus K' on shear stress, measured by stress ramp experiments with a constant loading rate of $1 * 10^{-3}$ decades of stress per second. (E) Coulomb Energy equation used for the handshake analysis of tail-to-tail interactions, where n_1 and n_2 refer to residue numbers on tail 1 and 2, respectively. Charge eZ and location $r(n)$ of amino acid residue n on each tail are indexed. The calculation includes $2m + 1$ next-nearest neighbors and is coarse grained over w amino acids ($w = 10$, $m = 5$). We then obtain the matrices of the tails aligned in an anti-parallel configuration, showing interactions of ionic crosslinking sites on two anti-parallel tails for (F) vimentin and (G) GFAP. The scales separate the consecutive tail residues. The colors in the handshake matrices are given by Coulomb's law in E. Blue color indicates attractive interactions (see color bar on the right) in units of energy (Joules).

REFERENCES

- [1] Carsten Grashoff, Brenton D. Hoffman, Michael D. Brenner, Ruobo Zhou, Maddy Parsons, Michael T. Yang, Mark A. McLean, Stephen G. Sligar, Christopher S. Chen, Taekjip Ha, and Martin A. Schwartz. Measuring mechanical tension across vinculin reveals regulation of focal adhesion dynamics. *Nature*, 466(7303):263–266, 2010.
- [2] Robert Hooke, Allestry James, and Martyn John. *Micrographia, or, Some physiological descriptions of minute bodies made by magnifying glasses. With observations and inquiries thereupon*. 1665.
- [3] Christina H. Stuelten, Carole A. Parent, and Denise J. Montell. Cell motility in cancer invasion and metastasis: insights from simple model organisms. *Nature reviews. Cancer*, 18:296, 2018.
- [4] Allison T. Ryan, Minsoo Kim, and Kihong Lim. Immune cell migration to cancer. *Cells* 2024, 13:844, 2024.
- [5] Serge Mostowy and Pascale Cossart. Septins: the fourth component of the cytoskeleton. *Nature reviews. Molecular cell biology*, 13(3):183–194, 2012.
- [6] Vitold E. Galkin, Albina Orlova, Matthijn R. Vos, Gunnar F. Schröder, and Edward H. Egelman. Near-atomic resolution for one state of f-actin. *Structure (London, England : 1993)*, 23:173–182, 2015.
- [7] Hyeran Kang, Michael J. Bradley, Brannon R. McCullough, Anaëlle Pierre, Elena E. Grintsevich, Emil Reisler, and Enrique M. De La Cruz. Identification of cation-binding sites on actin that drive polymerization and modulate bending stiffness. *Proceedings of the National Academy of Sciences of the United States of America*, 109:16923–16927, 2012.
- [8] Peter J Carman, Kyle R Barrie, Grzegorz Rebowski, and Roberto Dominguez. Structures of the free and capped ends of the actin filament. *science*, 380(6651):1287–1292, 2023.
- [9] Naoki Watanabe and Timothy J Mitchison. Single-molecule speckle analysis of actin filament turnover in lamellipodia. *Science*, 295(5557):1083–1086, 2002.
- [10] Marco Fritzsche, Alexandre Lewalle, Tom Duke, Karsten Kruse, and Guillaume Charras. Analysis of turnover dynamics of the submembranous actin cortex. *Molecular Biology of the Cell*, 24(6):757, 2013.

- [11] Sari Tojkander, Gergana Gateva, and Pekka Lappalainen. Actin stress fibers - assembly, dynamics and biological roles. *Journal of Cell Science*, 125(8):1855–1864, 2012.
- [12] Seema Khurana and Sudeep P. George. The role of actin bundling proteins in the assembly of filopodia in epithelial cells. *Cell Adhesion Migration*, 5:409, 2011.
- [13] Andrew W. Schaefer, Nurul Kabir, and Paul Forscher. Filopodia and actin arcs guide the assembly and transport of two populations of microtubules with unique dynamic parameters in neuronal growth cones. *The Journal of Cell Biology*, 158:139, 2002.
- [14] Jamis McGrath, Chun Yu Tung, Xiayi Liao, Inna A. Belyantseva, Pallabi Roy, Oisorjo Chakraborty, Jinan Li, Nicolas F. Berbari, Christian C. Faaborg-Andersen, Melanie Barzik, Jonathan E. Bird, Bo Zhao, Lata Balakrishnan, Thomas B. Friedman, and Benjamin J. Perrin. Actin at stereocilia tips is regulated by mechanotransduction and adf/cofilin. *Current biology : CB*, 31:1141–1153.e7, 2021.
- [15] Michael Murrell, Patrick W. Oakes, Martin Lenz, and Margaret L. Gardel. Forcing cells into shape: the mechanics of actomyosin contractility. *Nature reviews. Molecular cell biology*, 16:486, 2015.
- [16] Daniel V. Iwamoto, Andrew Huehn, Bertrand Simon, Clotilde Huet-Calderwood, Massimiliano Baldassarre, Charles V. Sindelar, and David A. Calderwood. Structural basis of the filamin a actin-binding domain interaction with f-actin. *Nature structural molecular biology*, 25:918, 2018.
- [17] Alexandre J.S. Ribeiro, Payal Khanna, Aishwarya Sukumar, Cheng Dong, and Kris Noel Dahl. Nuclear stiffening inhibits migration of invasive melanoma cells. *Cellular and Molecular Bioengineering*, 7(4):544–551, 2014.
- [18] Shigeko Yamashiro, Yoshihiko Yamakita, Shoichiro Ono, and Fumio Matsumura. Fascin, an actin-bundling protein, induces membrane protrusions and increases cell motility of epithelial cells. *Molecular Biology of the Cell*, 9:993, 1998.
- [19] Colleen T. Skau, David S. Courson, Andrew J. Bestul, Jonathan D. Winkelman, Ronald S. Rock, Vladimir Sirotnik, and David R. Kovar. Actin filament bundling by fimbrin is important for endocytosis, cytokinesis, and polarization in fission yeast. *The Journal of Biological Chemistry*, 286:26964, 2011.
- [20] Geoffrey M Cooper. The cytoskeleton and cell movement. 2000.
- [21] John Kolega. The role of myosin ii motor activity in distributing myosin asymmetrically and coupling protrusive activity to cell translocation. *Molecular Biology of the Cell*, 17:4435, 2006.
- [22] Miguel Vicente-Manzanares, Xuefei Ma, Robert S. Adelstein, and Alan Rick Horwitz. Non-muscle myosin ii takes centre stage in cell adhesion and migration. *Nature reviews. Molecular cell biology*, 10:778–790, 2009.

- [23] Ulrike Rölleke, Pallavi Kumari, Ruth Meyer, and Sarah Köster. The unique biomechanics of intermediate filaments - from single filaments to cells and tissues. *Current Opinion in Cell Biology*, 85(102263):102263, 2023.
- [24] Justin T. Jacob, Pierre A. Coulombe, Raymond Kwan, and M. Bishr Omary. Types i and ii keratin intermediate filaments. *Cold Spring Harbor Perspectives in Biology*, 10, 2018.
- [25] Pierre A. Coulombe and M. Bishr Omary. 'hard' and 'soft' principles defining the structure, function and regulation of keratin intermediate filaments. *Current Opinion in Cell Biology*, 14:110–122, 2002.
- [26] Miriam S Weber, Matthias Eibauer, Suganya Sivagurunathan, Thomas M Magin, Robert D Goldman, and Ohad Medalia. Structural heterogeneity of cellular k5/k14 filaments as revealed by cryo-electron microscopy. *Elife*, 10, 2021.
- [27] Robert C. Marshall. Nail, claw, hoof and horn keratin. *Biology of the Integument*, pages 722–738, 1986.
- [28] Denise Paulin and Zhenlin Li. Desmin: a major intermediate filament protein essential for the structural integrity and function of muscle. *Experimental cell research*, 301:1–7, 2004.
- [29] Elly M. Hol and Milos Pekny. Glial fibrillary acidic protein (gfap) and the astrocyte intermediate filament system in diseases of the central nervous system. *Current opinion in cell biology*, 32:121–130, 2015.
- [30] Aidong Yuan, Mala V. Rao, Veeranna, and Ralph A. Nixon. Neurofilaments at a glance. *Journal of Cell Science*, 125:3257–3263, 2012.
- [31] Aidong Yuan, Mala V. Rao, Veeranna, and Ralph A. Nixon. Neurofilaments and neurofilament proteins in health and disease. *Cold Spring Harbor Perspectives in Biology*, 9, 2017.
- [32] Aidong Yuan, Mala V. Rao, Takahiro Sasaki, Yuanxin Chen, Asok Kumar, Veeranna, Ronald K.H. Liem, Joel Eyer, Alan C. Peterson, Jean Pierre Julien, and Ralph A. Nixon. -internexin is structurally and functionally associated with the neurofilament triplet proteins in the mature cns. *The Journal of Neuroscience*, 26:10006, 2006.
- [33] Oliver I. Wagner, Sebastian Rammensee, Neha Korde, Qi Wen, Jean Francois Leterrier, and Paul A. Janmey. Softness, strength and self-repair in intermediate filament networks. *Experimental Cell Research*, 313(10):2228, 2007.
- [34] Yosef Gruenbaum and Roland Foisner. Lamins: nuclear intermediate filament proteins with fundamental functions in nuclear mechanics and genome regulation. *Annual review of biochemistry*, 84:131–164, 2015.

- [35] John E. Eriksson, Thomas Dechat, Boris Grin, Brian Helfand, Melissa Mendez, Hanna Mari Pallari, and Robert D. Goldman. Introducing intermediate filaments: from discovery to disease. *The Journal of Clinical Investigation*, 119(7):1763–1771, 2009.
- [36] Saima Usman, Naushin H. Waseem, Thuan Khanh Ngoc Nguyen, Sahar Mohsin, Ahmad Jamal, Muy Teck Teh, and Ahmad Waseem. Vimentin is at the heart of epithelial-mesenchymal transition (EMT) mediated metastasis. *Cancers* 2021, Vol. 13, Page 4985, 13(19):4985, 2021.
- [37] Ching Yi Liu, Hsi Hui Lin, Ming Jer Tang, and Yang Kao Wang. Vimentin contributes to epithelial-mesenchymal transition cancer cell mechanics by mediating cytoskeletal organization and focal adhesion maturation. *Oncotarget*, 6:15966, 2015.
- [38] Harald Herrmann and Ueli Aebi. Intermediate filaments: Structure and assembly. *Cold Spring Harbor Perspectives in Biology*, 8, 2016.
- [39] Matthias Eibauer, Miriam S Weber, Rafael Kronenberg-Tenga, Charlie T Beales, Rajaa Boujemaa-Paterski, Yagmur Turgay, Suganya Sivagurunathan, Julia Kraxner, Sarah Koester, Robert D Goldman, et al. Vimentin filaments integrate low complexity domains in a highly complex helical structure. *bioRxiv*, pages 2023–05, 2023.
- [40] Bernd Nöding, Harald Herrmann, and Sarah Köster. Direct observation of sub-unit exchange along mature vimentin intermediate filaments. *Biophysical Journal*, 107(12):2923–2931, 2014.
- [41] Quang D. Tran, Valerio Sorichetti, Gerard Pehau-Arnaudet, Martin Lenz, and Céline Leduc. Fragmentation and entanglement limit vimentin intermediate filament assembly. *Physical Review X*, 13(1):011014, 2023.
- [42] Amélie Robert, Molly J Rossow, Caroline Hookway, Stephen A Adam, and Vladimir I Gelfand. Vimentin filament precursors exchange subunits in an ATP-dependent manner. *Proceedings of the National Academy of Sciences*, 112(27):E3505–14, 2015.
- [43] Caroline Hookway, Liya Ding, Michael W Davidson, Joshua Z Rappoport, Gaudenz Danuser, and Vladimir I Gelfand. Microtubule-dependent transport and dynamics of vimentin intermediate filaments. *Molecular Biology of the Cell*, 26(9):1675–1686, 2015.
- [44] Hyeran Kang, Michael J. Bradley, Wenxiang Cao, Kaifeng Zhou, Elena E. Grintsevich, Alphée Michelot, Charles V. Sindelar, Mark Hochstrasser, and Enrique M. De La Cruz. Site-specific cation release drives actin filament severing by vertebrate cofilin. *Proceedings of the National Academy of Sciences*, 111(50):17821–17826, 2014.
- [45] Roy Beck, Joanna Deek, Myung Chul Choi, Taiji Ikawa, Osamu Watanabe, Erwin Frey, Philip Pincus, and Cyrus R Safinya. Unconventional salt trend from soft to stiff in single neurofilament biopolymers. *Langmuir*, 26(24):18595–18599, 2010.

[46] Bernd Nöding and Sarah Köster. Intermediate filaments in small configuration spaces. *Physical Review Letters*, 108(8):088101, 2012.

[47] Paul Pawelzyk, Norbert Mücke, Harald Herrmann, and Norbert Willenbacher. Attractive interactions among intermediate filaments determine network mechanics in vitro. *PLoS One.*, 9(4):e93194, 2014.

[48] Michael Schopferer, Harald Bär, Bernhard Hochstein, Sarika Sharma, Norbert Mücke, Harald Herrmann, and Norbert Willenbacher. Desmin and vimentin intermediate filament networks: their viscoelastic properties investigated by mechanical rheometry. *Journal of Molecular Biology*, 388(1):133–143, 2009.

[49] N Mücke, L Kreplak, R Kirmse, T Wedig, H Herrmann, U Aebi, and J Langowski. Assessing the flexibility of intermediate filaments by atomic force microscopy. *Journal of Molecular Biology*, 335(5):1241–1250, 2004.

[50] Marcel Knossow, Valérie Campanacci, Liza Ammar Khodja, and Benoît Gigant. The mechanism of tubulin assembly into microtubules: Insights from structural studies. *iScience*, 23, 2020.

[51] Didier Job, Odile Valiron, and Berl Oakley. Microtubule nucleation. *Current Opinion in Cell Biology*, 15:111–117, 2003.

[52] Lewis G. Tilney, Joseph Bryan, Doris J. Bush, Keigi Fujiwara, Mark S. Mooseker, Douglas B. Murphy, and Daniel H. Snyder. Microtubules: Evidence for 13 protofilaments. *The Journal of Cell Biology*, 59:267, 1973.

[53] Ju Zhou, Anhui Wang, Yinlong Song, Nan Liu, Jia Wang, Yan Li, Xin Liang, Guohui Li, Huiying Chu, and Hong Wei Wang. Structural insights into the mechanism of gtp initiation of microtubule assembly. *Nature Communications* 2023 14:1, 14:1–17, 2023.

[54] Felipe Andrés Piedra, Tae Kim, Emily S. Garza, Elisabeth A. Geyer, Alexander Burns, Xuecheng Ye, and Luke M. Rice. Gdp-to-gtp exchange on the microtubule end can contribute to the frequency of catastrophe. *Molecular Biology of the Cell*, 27:3515, 2016.

[55] Gennady Margolin, Ivan V. Gregoretti, Trevor M. Cickovski, Chunlei Li, Wei Shi, Mark S. Alber, and Holly V. Goodson. The mechanisms of microtubule catastrophe and rescue: implications from analysis of a dimer-scale computational model. *Molecular Biology of the Cell*, 23:642, 2012.

[56] K. A. Akhmetova, I. N. Chesnokov, and S. A. Fedorova. Functional characterization of septin complexes. *Molekuliarnaya biologiya*, 52:155, 2018.

[57] Italo A Cavini, Diego A Leonardo, Higor VD Rosa, Danielle KSV Castro, Humberto D'Muniz Pereira, Napoleão F Valadares, Ana PU Araujo, and Richard C Garratt. The structural biology of septins and their filaments: an update. *Frontiers in Cell and Developmental Biology*, 9:765085, 2021.

[58] Lin Li, Xue Ming Zhu, Zhen Zhu Su, Maurizio Del Poeta, Xiao Hong Liu, and Fu Cheng Lin. Insights of roles played by septins in pathogenic fungi. *Virulence*, 12:1550, 2021.

[59] Jamal-Eddine Bouameur, Bertrand Favre, Lionel Fontao, Prakash Lingasamy, Nadja Begré, and Luca Borradori. Interaction of plectin with keratins 5 and 14: dependence on several plectin domains and keratin quaternary structure. *Journal of Investigative Dermatology*, 134(11):2776–2783, 2014.

[60] Fiyaz Mohammed, Catharine Trieber, Michael Overduin, and Martyn Chidgey. Molecular mechanism of intermediate filament recognition by plakin proteins. *Biochim. Biophys. Acta Mol. Cell Res.*, 1867(11):118801, 2020.

[61] Gerhard Wiche and Lilli Winter. Plectin isoforms as organizers of intermediate filament cytoarchitecture. *Bioarchitecture*, 1(1):14, 2011.

[62] Gerhard Wiche and Margaret A Baker. Cytoplasmic network arrays demonstrated by immunolocalization using antibodies to a high molecular weight protein present in cytoskeletal preparations from cultured cells. *Experimental Cell Research*, 138(1):15–29, 1982.

[63] R Foisner, FE Leichtfried, H Herrmann, JV Small, D Lawson, and G Wiche. Cytoskeleton-associated plectin: in situ localization, in vitro reconstitution, and binding to immobilized intermediate filament proteins. *Journal of Cell Biology*, 106(3):723–733, 1988.

[64] R Foisner, W Bohn, K Mannweiler, and G Wiche. Distribution and ultrastructure of plectin arrays in subclones of rat glioma c6 cells differing in intermediate filament protein (vimentin) expression. *Journal of Structural Biology*, 115(3):304–17, 1995.

[65] Tatyana M Svitkina, Alexander B Verkhovsky, and Gary G Borisy. Plectin sidearms mediate interaction of intermediate filaments with microtubules and other components of the cytoskeleton. *Journal of Cell Biology*, 135(4):991–1007, 1996.

[66] Pragati C. Marks, Breanne R. Hewitt, Michelle A. Baird, Gerhard Wiche, and Ryan J. Petrie. Plectin linkages are mechanosensitive and required for the nuclear piston mechanism of three-dimensional cell migration. *Molecular Biology of the Cell*, 33(12):ar104, 2022.

[67] Huayin Wu, Yinan Shen, Suganya Sivagurunathan, Miriam Sarah Weber, Stephen A Adam, Jennifer H Shin, Jeffrey J Fredberg, Ohad Medalia, Robert Goldman, David A Weitz, and Jennifer Lippincott-Schwartz. Vimentin intermediate filaments and filamentous actin form unexpected interpenetrating networks that redefine the cell cortex. *Proceedings of the National Academy of Sciences*, 119(10):2115217119, 2022.

[68] Yaming Jiu, Jaakko Lehtimäki, Sari Tojkander, Fang Cheng, Harri Jäälinnoja, Xiaonan Liu, Markku Varjosalo, John E. Eriksson, and Pekka Lappalainen. Bidirectional interplay between vimentin intermediate filaments and contractile actin stress fibers. *Cell Reports*, 11(10):1511–1518, 2015.

[69] Marie Schoumacher, Robert D Goldman, Daniel Louvard, and Danijela M Vignjevic. Actin, microtubules, and vimentin intermediate filaments cooperate for elongation of invadopodia. *Journal of Cell Biology*, 189(3):541–556, 2010.

[70] Mihoko Sutoh Yoneyama, Shingo Hatakeyama, Tomonori Habuchi, Takamitsu Inoue, Toshiya Nakamura, Tomihisa Funyu, Gerhard Wiche, Chikara Ohyama, and Shigeru Tsuboi. Vimentin intermediate filament and plectin provide a scaffold for invadopodia, facilitating cancer cell invasion and extravasation for metastasis. *European Journal of Cell Biology*, 93(4):157–169, 2014.

[71] Murielle P Serres, Matthias Samwer, Binh An Truong Quang, Geneviève Lavoie, Upamali Perera, Dirk Görlich, Guillaume Charras, Mark Petronczki, Philippe P Roux, and Ewa K Paluch. F-actin interactome reveals vimentin as a key regulator of actin organization and cell mechanics in mitosis. *Developmental Cell*, 52(2):210–222, 2020.

[72] Lilli Winter, Christina Abrahamsberg, and Gerhard Wiche. Plectin isoform 1b mediates mitochondrion–intermediate filament network linkage and controls organelle shape. *Journal of Cell Biology*, 181(6):903–911, 2008.

[73] Lionel Fontao, Dirk Geerts, Ingrid Kulkman, Jan Koster, Duco Kramer, and Arnoud Sonnenberg. The interaction of plectin with actin: evidence for cross-linking of actin filaments by dimerization of the actin-binding domain of plectin. *Journal of cell science*, 114(Pt 11):2065–2076, 2001.

[74] B. García-Alvarez, A. Bobkov, A. Sonnenberg, J.M. De Pereda, B. García-Alvarez, A. Bobkov, A. Sonnenberg, and J.M. De Pereda. Structural and functional analysis of the actin binding domain of plectin suggests alternative mechanisms for binding to f-actin and integrin $\beta 4$. *Structure*, 11(6):615–625, 2003.

[75] Hee-Jung Choi, Shaun Park-Snyder, Lauren T Pascoe, Kathleen J Green, and William I Weis. Structures of two intermediate filament-binding fragments of desmoplakin reveal a unique repeat motif structure. *Nature Structural Molecular Biology*, 9(8):612–620, 2002.

[76] Bertrand Favre, Yann Schneider, Prakash Lingasamy, Jamal-Eddine Bouameur, Nadja Begré, Yves Gontier, Marie-France Steiner-Champliaud, Miguel A Frias, Luca Borradori, and Lionel Fontao. Plectin interacts with the rod domain of type iii intermediate filament proteins desmin and vimentin. *European Journal of Cell Biology*, 90(5):390–400, 2011.

[77] Claudia Fogl, Fiyaz Mohammed, Caezar Al-Jassar, Mark Jeeves, Timothy J Knowles, Penelope Rodriguez-Zamora, Scott A White, Elena Odintsova, Michael Overduin, and Martyn Chidgey. Mechanism of intermediate filament recognition by plakin repeat domains revealed by envoplakin targeting of vimentin. *Nature Communications*, 7(1):10827, 2016.

[78] Hyunook Kang, Thomas M Weiss, Injin Bang, William I Weis, and Hee-Jung Choi. Structure of the intermediate filament-binding region of desmoplakin. *PLOS One*, 11(1):e0147641, 2016.

[79] Sungsoo Na, Farhan Chowdhury, Bernard Tay, Mingxing Ouyang, Martin Gregor, Yingxiao Wang, Gerhard Wiche, and Ning Wang. Plectin contributes to mechanical properties of living cells. *American Journal of Physiology-Cell Physiology*, 296(4):C868–C877, 2009.

[80] Navid Bonakdar, Achim Schilling, Marina Spörer, Pablo Lennert, Astrid Mainka, Lilli Winter, Gernot Walko, Gerhard Wiche, Ben Fabry, and Wolfgang H Goldmann. Determining the mechanical properties of plectin in mouse myoblasts and keratinocytes. *Experimental Cell Research*, 331(2):331–337, 2015.

[81] Marcin Moch, Reinhard Windoffer, Nicole Schwarz, Raphaela Pohl, Andreas Omenzetter, Uwe Schnakenberg, Fabian Herb, Kraisorn Chaisaowong, Dorit Merhof, Lena Ramms, et al. Effects of plectin depletion on keratin network dynamics and organization. *PLOS One*, 11(3):e0149106, 2016.

[82] Ines Martin, Marcin Moch, Tobias Neckernuss, Stephan Paschke, Harald Hermann, and Othmar Marti. Both monovalent cations and plectin are potent modulators of mechanical properties of keratin k8/k18 networks. *Soft Matter*, 12(33):6964–6974, 2016.

[83] Michaela M Zrelska, Sabrina Hösele, Monika Kustermann, Petra Fichtinger, Delf Kah, Ioannis Athanasiou, Philipp R Esser, Anja Wagner, Rebecca Herzog, Klaus Kratochwill, et al. Plectin deficiency in fibroblasts deranges intermediate filament and organelle morphology, migration, and adhesion. *Journal of Investigative Dermatology*, 2023.

[84] Selma Osmanagic-Myers, Stefanie Rus, Michael Wolfram, Daniela Brunner, Wolfgang H. Goldmann, Navid Bonakdar, Irmgard Fischer, Siegfried Reipert, Aurora Zuzuarregui, Gernot Walko, and Gerhard Wiche. Plectin reinforces vascular integrity by mediating crosstalk between the vimentin and the actin networks. *Journal of Cell Science*, 128(22):4138–4150, 2015.

[85] Magdalena Prechova, Zuzana Adamova, Anna-Lena Schweizer, Miloslava Mananova, Andreas Bauer, Delf Kah, Samuel M Meier-Menches, Gerhard Wiche, Ben Fabry, and Martin Gregor. Plectin-mediated cytoskeletal crosstalk controls cell tension and cohesion in epithelial sheets. *Journal of Cell Biology*, 221(3):202105146, 2022.

[86] Dirk Geerts, Lionel Fontao, Mirjam G Nievers, Roel QJ Schaapveld, Patricia E Purkis, Grant N Wheeler, E Birgitte Lane, Irene M Leigh, and Arnoud Sonnenberg. Binding of integrin $\alpha 6\beta 4$ to plectin prevents plectin association with f-actin but does not interfere with intermediate filament binding. *Journal of Cell Biology*, 147(2):417–434, 1999.

[87] Ramona Bhattacharya, Annette M Gonzalez, Phillip J DeBiase, Humberto E Trejo, Robert D Goldman, Frederick W Flitney, and Jonathan CR Jones. Recruitment of vimentin to the cell surface by $\beta 3$ integrin and plectin mediates adhesion strength. *Journal of Cell Science*, 122(9):1390–1400, 2009.

[88] Gernot Walko, Maria J Castañón, and Gerhard Wiche. Molecular architecture and function of the hemidesmosome. *Cell Tissue Res.*, 360:363–378, 2015.

[89] Chiara De Pascalis, Carlos Pérez-González, Shailaja Seetharaman, Batiste Boëda, Benoit Vianay, Mithila Burute, Cécile Leduc, Nicolas Borghi, Xavier Trepat, and Sandrine Etienne-Manneville. Intermediate filaments control collective migration by restricting traction forces and sustaining cell-cell contacts. *Journal of Cell Biology*, 217(9):3031–3044, 2018.

[90] Zachary T Colburn and Jonathan CR Jones. Complexes of $\alpha 6\beta 4$ integrin and vimentin act as signaling hubs to regulate epithelial cell migration. *Journal of Cell Science*, 131(14):214593, 2018.

[91] Kevin Wilhelmsen, Sandy HM Litjens, Ingrid Kuikman, Ntambua Tshimbalanga, Hans Janssen, Iman van den Bout, Karine Raymond, and Arnoud Sonnenberg. Nesprin-3, a novel outer nuclear membrane protein, associates with the cytoskeletal linker protein plectin. *Journal of Cell Biology*, 171(5):799–810, 2005.

[92] Zhuo Gan, Liya Ding, Christoph J Burckhardt, Jason Lowery, Assaf Zaritsky, Karlyndsay Sitterley, Andressa Mota, Nancy Costigliola, Colby G Starker, Daniel F Voytas, Jessica Tytell, Robert D Goldman, and Gaudenz Danuser. Vimentin intermediate filaments template microtubule networks to enhance persistence in cell polarity and directed migration. *Cell Syst.*, 3(3):252–263.e8, 2016.

[93] Nancy Costigliola, Liya Ding, Christoph J. Burckhardt, Sangyoong J. Han, Edgar Gutierrez, Andressa Mota, Alex Groisman, Timothy J. Mitchison, and Gaudenz Danuser. Vimentin fibers orient traction stress. *Proceedings of the National Academy of Sciences*, 114(20):5195–5200, 2017.

[94] Yaming Jiu, Johan Peränen, Niccole Schaible, Fang Cheng, John E. Eriksson, Ramaswamy Krishnan, and Pekka Lappalainen. Vimentin intermediate filaments control actin stress fiber assembly through gef-h1 and rhoa. *Journal of Cell Science*, 130(5):892–902, 2017.

[95] Emma J. van Bodegraven and Sandrine Etienne-Manneville. Intermediate filaments against actomyosin: the david and goliath of cell migration. *Current Opinion in Cell Biology*, 66:79–88, 2020.

[96] Sofia Duarte, Álvaro Viedma-Poyatos, Elena Navarro-Carrasco, Alma E. Martínez, María A. Pajares, and Dolores Pérez-Sala. Vimentin filaments interact with the actin cortex in mitosis allowing normal cell division. *Nature communications*, 10(1):1–19, 2019.

[97] Kristin Seltmann, Anatol W Fritsch, Josef A Käs, and Thomas M Magin. Keratins significantly contribute to cell stiffness and impact invasive behavior. *Proceedings of the National Academy of Sciences*, 110(46):18507–18512, 2013.

[98] Lena Ramms, Gloria Fabris, Reinhard Windoffer, Nicole Schwarz, Ronald Springer, Chen Zhou, Jaroslav Lazar, Simone Stiefel, Nils Hersch, Uwe Schnakenberg, et al.

Keratins as the main component for the mechanical integrity of keratinocytes. *Proceedings of the National Academy of Sciences*, 110(46):18513–18518, 2013.

[99] Jiliang Hu, Yiwei Li, Yukun Hao, Tianqi Zheng, Satish K Gupta, German Alberto Parada, Huayin Wu, Shaoting Lin, Shida Wang, Xuanhe Zhao, et al. High stretchability, strength, and toughness of living cells enabled by hyperelastic vimentin intermediate filaments. *Proceedings of the National Academy of Sciences*, 116(35):17175–17180, 2019.

[100] Osigwe Esue, Ashley A. Carson, Yiider Tseng, and Denis Wirtz. A direct interaction between actin and vimentin filaments mediated by the tail domain of vimentin. *Journal of Biological Chemistry*, 281(41):30393–30399, 2006.

[101] Tom Golde, Constantin Huster, Martin Glaser, Tina Händler, Harald Herrmann, Josef A. Käs, and Jörg Schnauß. Glassy dynamics in composite biopolymer networks. *Soft Matter*, 14(39):7970–7978, 2018.

[102] Elena Scarpa and Roberto Mayor. Collective cell migration in development. *Journal of Cell Biology*, 212(2):143–155, 2016.

[103] Laurent Lamalice, Fabrice Le Boeuf, and Jacques Huot. Endothelial cell migration during angiogenesis. *Cir. Res.*, 100(6):782–794, 2007.

[104] Peihong Su, Ye Tian, Chaofei Yang, Xiaoli Ma, Xue Wang, Jiawei Pei, and Airong Qian. Mesenchymal stem cell migration during bone formation and bone diseases therapy. *International Journal of Molecular Sciences*, 19(8):2343, 2018.

[105] Xiaorong Fu, Ge Liu, Alexander Halim, Yang Ju, Qing Luo, and Guanbin Song. Mesenchymal stem cell migration and tissue repair. *Cells*, 8(8):784, 2019.

[106] Maria-Graciela Delgado and Ana Maria Lennon-Duménil. How cell migration helps immune sentinels. *Frontiers in Cell and Developmental Biology*, 10:932472, 2022.

[107] Juan Liu, Xiaomin Zhang, Yujie Cheng, and Xuetao Cao. Dendritic cell migration in inflammation and immunity. *Cell. Mol. Immunol.*, 18(11):2461–2471, 2021.

[108] Claudia Tanja Mierke. The matrix environmental and cell mechanical properties regulate cell migration and contribute to the invasive phenotype of cancer cells. *Rep. Prog. Phys.*, 82(6):064602, 2019.

[109] Klemens Rottner and Matthias Schaks. Assembling actin filaments for protrusion. *Current Opinion in Cell Biology*, 56:53–63, 2019.

[110] Maria F Ullo and Jeremy S Logue. ADF and cofilin-1 collaborate to promote cortical actin flow and the leader bleb-based migration of confined cells. *eLife*, 10:67856, 2021.

[111] Anna Akhmanova and Lukas C Kapitein. Mechanisms of microtubule organization in differentiated animal cells. *Nature Reviews Molecular Cell Biology*, 23(8):541–558, 2022.

[112] Alison E. Patteson, Amir Vahabikashi, Katarzyna Pogoda, Stephen A. Adam, Kalpana Mandal, Mark Kittisopikul, Suganya Sivagurunathan, Anne Goldman, Robert D. Goldman, and Paul A. Janmey. Vimentin protects cells against nuclear rupture and dna damage during migration. *Journal of Cell Biology*, 218(12):4079–4092, 2019.

[113] Sandrine B Lavenus, Sara M Tudor, Maria F Ullo, Karl W Vosatka, and Jeremy S Logue. A flexible network of vimentin intermediate filaments promotes migration of amoeboid cancer cells through confined environments. *Journal of Biological Chemistry*, 295(19):6700–6709, 2020.

[114] Shailaja Seetharaman and Sandrine Etienne-Manneville. Cytoskeletal crosstalk in cell migration. *Trends Cell Biol.*, 30(9):720–735, 2020.

[115] Byung Min Chung, Jeremy D. Rotty, and Pierre A. Coulombe. Networking galore: Intermediate filaments and cell migration. *Current Opinion in Cell Biology*, 25(5):600–612, 2013.

[116] Morgan L Pimm and Jessica L Henty-Ridilla. New twists in actin-microtubule interactions. *Molecular Biology of the Cell*, 32(3):211–217, 2021.

[117] CJ Schmidt and SJ Stehbens. Microtubule control of migration: Coordination in confinement. *Current Opinion in Cell Biology*, 86:102289, 2023.

[118] Andreas Buttenschön and Leah Edelstein-Keshet. Bridging from single to collective cell migration: A review of models and links to experiments. *PLoS Comput. Biol.*, 16(12):e1008411, 2020.

[119] Shiladitya Banerjee and M Cristina Marchetti. Continuum models of collective cell migration. *Adv. Exp. Med. Biol.*, 1146:45–66, 2019.

[120] Brittany MacTaggart and Anna Kashina. Posttranslational modifications of the cytoskeleton. *Cytoskeleton*, 78(4):142–173, 2021.

[121] Shailaja Seetharaman, Benoit Vianay, Vanessa Roca, Aaron J. Farrugia, Chiara De Pascalis, Batiste Boëda, Florent Dingli, Damarys Loew, Stéphane Vassilopoulos, Alexander Bershadsky, Manuel Théry, and Sandrine Etienne-Manneville. Microtubules tune mechanosensitive cell responses. *Nature Materials*, 21(3):366–377, 2022.

[122] Veronika Te Boekhorst, Luigi Preziosi, and Peter Friedl. Plasticity of cell migration in vivo and in silico. *Annu. Rev. Cell Dev. Biol.*, 32:491–526, 2016.

[123] James P Conboy, Irene Istúriz Petitjean, Anouk van der Net, and Gijsje H Koen-derink. How cytoskeletal crosstalk makes cells move: Bridging cell-free and cell studies. *Biophysics Reviews*, 5(2), 2024.

[124] Katarina Wolf, Stephanie Alexander, Vivien Schacht, Lisa M Coussens, Ulrich H von Andrian, Jacco van Rheenen, Elena Deryugina, and Peter Friedl. Collagen-based cell migration models in vitro and in vivo. *Semin. Cell Dev. Biol.*, 20(8):931–941, 2009.

[125] Jochen Guck, Franziska Lautenschläger, Stephan Paschke, and Michael Beil. Critical review: cellular mechanobiology and amoeboid migration. *Integr. Biol.*, 2(11-12):575–583, 2010.

[126] Zhenhui Liu, Se Jong Lee, Seungman Park, Konstantinos Konstantopoulos, Kristine Glunde, Yun Chen, and Ishan Barman. Cancer cells display increased migration and deformability in pace with metastatic progression. *FASEB J.*, 34(7):9307–9315, 2020.

[127] Blanca González-Bermúdez, Gustavo V Guinea, and Gustavo R Plaza. Advances in micropipette aspiration: Applications in cell biomechanics, models, and extended studies. *Biophysical Journal*, 116(4):587–594, 2019.

[128] J Guck, R Ananthakrishnan, H Mahmood, T J Moon, C C Cunningham, and J Käs. The optical stretcher: a novel laser tool to micromanipulate cells. *Biophysical Journal*, 81(2):767–784, 2001.

[129] O Thoumine and A Ott. Time scale dependent viscoelastic and contractile regimes in fibroblasts probed by microplate manipulation. *Journal of Cell Science*, 110 (Pt 17)(17):2109–2116, 1997.

[130] Marta Urbanska, Hector E. Muñoz, Josephine Shaw Bagnall, Oliver Otto, Scott R. Manalis, Dino Di Carlo, and Jochen Guck. A comparison of microfluidic methods for high-throughput cell deformability measurements. *Nature Methods*, 17(6):587–593, 2020.

[131] P Fernandez, L Heymann, A Ott, N Aksel, and PA Pullarkat. Shear rheology of a cell monolayer. *New Journal of Physics*, 9:419, 2007.

[132] Amy A Sutton, Clayton W Molter, Ali Amini, Johanan Idicula, Max Furman, Pouria Tirgar, Yuanyuan Tao, Ajinkya Ghagre, Newsha Koushki, Adele Khavari, and Allen J Ehrlicher. Cell monolayer deformation microscopy reveals mechanical fragility of cell monolayers following EMT. *Biophysical Journal*, 121(4):629–643, 2022.

[133] Khawaja Muhammad Imran Bashir, Suhyang Lee, Dong Hee Jung, Santanu Kumar Basu, Man-Gi Cho, and Andreas Wierschem. Narrow-gap rheometry: A novel method for measuring cell mechanics. *Cells*, 11(13):2010, 2022.

[134] Kellie Beicker, E Timothy O'Brien, 3rd, Michael R Falvo, and Richard Superfine. Vertical light sheet enhanced side-view imaging for AFM cell mechanics studies. *Sci. Rep.*, 8(1):1504, 2018.

[135] Katarzyna Pogoda, Fitzroy Byfield, Piotr Deptuła, Mateusz Cieśluk, Łukasz Suprawicz, Karol Skłodowski, Jordan L Shivers, Anne van Oosten, Katrina Cruz, Ekaterina Tarasovetc, Ekaterina L Grishchuk, Fred C Mackintosh, Robert Bucki, Alison E Patteson, and Paul A Janmey. Unique role of vimentin networks in compression stiffening of cells and protection of nuclei from compressive stress. *Nano Lett.*, 22(12):4725–4732, 2022.

[136] B Fabry, G N Maksym, J P Butler, M Glogauer, D Navajas, and J J Fredberg. Scaling the microrheology of living cells. *Physical Review Letters*, 87(14):148102, 2001.

[137] Sajedeh Kerdegari, Paolo Canepa, Davide Odino, Reinier Oropesa-Nuñez, Annalisa Relini, Ornella Cavalleri, and Claudio Canale. Insights in cell biomechanics through atomic force microscopy. *Materials*, 16(8):2980, 2023.

[138] Frederic Català-Castro, Erik Schäffer, and Michael Krieg. Exploring cell and tissue mechanics with optical tweezers. *Journal of Cell Science*, 135(15):259–355, 2022.

[139] A R Bausch, F Ziemann, A A Boulbitch, K Jacobson, and E Sackmann. Local measurements of viscoelastic parameters of adherent cell surfaces by magnetic bead microrheometry. *Biophysical Journal*, 75(4):2038–2049, 1998.

[140] A W C Lau, B D Hoffman, A Davies, J C Crocker, and T C Lubensky. Microrheology, stress fluctuations, and active behavior of living cells. *Physical Review Letters*, 91(19):198101, 2003.

[141] Porntula Panorchan, Jerry S H Lee, Thomas P Kole, Yiider Tseng, and Denis Wirtz. Microrheology and ROCK signaling of human endothelial cells embedded in a 3D matrix. *Biophysical Journal*, 91(9):3499–3507, 2006.

[142] Jack R Staunton, Bryant L Doss, Stuart Lindsay, and Robert Ros. Correlating confocal microscopy and atomic force indentation reveals metastatic cancer cells stiffen during invasion into collagen I matrices. *Sci. Rep.*, 6(1):19686, 2016.

[143] Joe Swift, Irena L Ivanovska, Amnon Buxboim, Takamasa Harada, P C Dave P Dingal, Joel Pinter, J David Pajerowski, Kyle R Spinler, Jae-Won Shin, Manorama Tewari, Florian Rehfeldt, David W Speicher, and Dennis E Discher. Nuclear lamin-a scales with tissue stiffness and enhances matrix-directed differentiation. *science*, 341(6149):1240104, 2013.

[144] Fitzroy Byfield, Behnaz Eftekhari, Kaeli Kaymak-Loveless, Kalpana Mandal, David Li, Rebecca G Wells, Wenjun Chen, Jasna Brujic, Giulia Bergamasschi, Gijs G wuite, et al. Metabolically intact nuclei are fluidized by the activity of the chromatin remodeling motor brg1. *bioRxiv*, pages 2024–04, 2024.

[145] Jan Lammerding, Loren G. Fong, Julie Y. Ji, Karen Reue, Colin L. Stewart, Stephen G. Young, and Richard T. Lee. Lamins a and c but not lamin b1 regulate nuclear mechanics. *Journal of Biological Chemistry*, 281(35):25768–25780, 2006.

[146] Andrew D Stephens, Edward J Banigan, Stephen A Adam, Robert D Goldman, and John F Marko. Chromatin and lamin a determine two different mechanical response regimes of the cell nucleus. *Molecular Biology of the Cell*, 28(14):1984–1996, 2017.

[147] Emily S Bell, Pragya Shah, Noam Zuela-Sopilniak, Dongsung Kim, Alice-Anais Varlet, Julien L P Morival, Alexandra L McGregor, Philipp Isermann, Patricia M Davidson, Joshua J Elacqua, Jonathan N Lakins, Linda Vahdat, Valerie M Weaver,

Marcus B Smolka, Paul N Span, and Jan Lammerding. Low lamin a levels enhance confined cell migration and metastatic capacity in breast cancer. *Oncogene*, 41(36):4211–4230, 2022.

[148] Haijiao Liu, Jun Wen, Yun Xiao, Jun Liu, Sevan Hopyan, Milica Radisic, Craig A Simmons, and Yu Sun. In situ mechanical characterization of the cell nucleus by atomic force microscopy. *ACS Nano*, 8(4):3821–3828, 2014.

[149] Alexandra Lynn McGregor, Chieh Ren Hsia, and Jan Lammerding. Squish and squeeze — the nucleus as a physical barrier during migration in confined environments. *Current Opinion in Cell Biology*, 40:32–40, 2016.

[150] Katarina Wolf, Mariska te Lindert, Marina Krause, Stephanie Alexander, Joost te Riet, Amanda L. Willis, Robert M. Hoffman, Carl G. Figgdr, Stephen J. Weiss, and Peter Friedl. Physical limits of cell migration: control by ecm space and nuclear deformation and tuning by proteolysis and traction force. *Journal of Cell Biology*, 201(7):1069–1084, 2013.

[151] Patricia M Davidson, Celine Denais, Maya C Bakshi, and Jan Lammerding. Nuclear deformability constitutes a rate-limiting step during cell migration in 3-D environments. *Cell. Mol. Bioeng.*, 7(3):293–306, 2014.

[152] Franziska Lautenschläger, Stephan Paschke, Stefan Schinkinger, Arlette Bruel, Michael Beil, and Jochen Guck. The regulatory role of cell mechanics for migration of differentiating myeloid cells. *Proceedings of the National Academy of Sciences*, 106(37):15696–15701, 2009.

[153] C Rotsch and M Radmacher. Drug-induced changes of cytoskeletal structure and mechanics in fibroblasts: an atomic force microscopy study. *Biophysical Journal*, 78(1):520–535, 2000.

[154] Jan Christian Martens and Manfred Radmacher. Softening of the actin cytoskeleton by inhibition of myosin II. *Pflugers Arch.*, 456(1):95–100, 2008.

[155] Elisabeth Fischer-Friedrich, Yusuke Toyoda, Cedric J Cattin, Daniel J Müller, Anthony A Hyman, and Frank Jülicher. Rheology of the active cell cortex in mitosis. *Biophysical Journal*, 111(3):589–600, 2016.

[156] Ming Guo, Allen J Ehrlicher, Saleemulla Mohammad, Hilary Fabich, Mikkel H Jensen, Jeffrey R Moore, Jeffrey J Fredberg, Robert D Goldman, and David A Weitz. The role of vimentin intermediate filaments in cortical and cytoplasmic mechanics. *Biophysical Journal*, 105(7):1562–1568, 2013.

[157] M J Brown, J A Hallam, E Colucci-Guyon, and S Shaw. Rigidity of circulating lymphocytes is primarily conferred by vimentin intermediate filaments. *Journal of Immunology*, 166(11):6640–6646, 2001.

[158] Kristin Seltmann, Anatol W. Fritsch, Josef A. Käs, and Thomas M. Magin. Keratins significantly contribute to cell stiffness and impact invasive behavior. *Proceedings of the National Academy of Sciences*, 110(46):18507–18512, 2013.

[159] Alison E. Patteson, Katarzyna Pogoda, Fitzroy J. Byfield, Kalpana Mandal, Zofia Ostrowska-Podhorodecka, Elisabeth E. Charrier, Peter A. Galie, Piotr Deptuła, Robert Bucki, Christopher A. McCulloch, and Paul A. Janmey. Loss of vimentin enhances cell motility through small confining spaces. *Small.*, 15(50):e1903180, 2019.

[160] N Wang. Mechanical interactions among cytoskeletal filaments. *Hypertension.*, 32(1):162–165, 1998.

[161] Yuhui Li, Ondřej Kučera, Damien Cuvelier, David M Rutkowski, Mathieu Deygas, Dipti Rai, Tonja Pavlovič, Filipe Nunes Vicente, Matthieu Piel, Grégoire Giannone, Dimitrios Vavylonis, Anna Akhmanova, Laurent Blanchoin, and Manuel Théry. Compressive forces stabilize microtubules in living cells. *Nature Materials*, 22(7):913–924, 2023.

[162] Benjamin P Bouchet, Ivar Noordstra, Miranda van Amersfoort, Eugene A Katrakha, York-Christoph Ammon, Natalie D Ter Hoeve, Louis Hodgson, Marileen Dogterom, Patrick W B DerkSEN, and Anna Akhmanova. Mesenchymal cell invasion requires cooperative regulation of persistent microtubule growth by SLAIN2 and CLASP1. *Developmental Cell*, 39(6):708–723, 2016.

[163] Jan Maarten van Doorn, Luuk Lageschaar, Joris Sprakel, and Jasper van der Gucht. Criticality and mechanical enhancement in composite fiber networks. *Physical Review E*, 95(4-1):042503, 2017.

[164] Sihan Chen, Tomer Markovich, and Fred C MacKintosh. Nonaffine deformation of semiflexible polymer and fiber networks. *Physical Review Letters*, 130(8):088101, 2023.

[165] Yuan-Chen Chang, Perihan Nalbant, Jörg Birkenfeld, Zee-Fen Chang, and Gary M Bokoch. GEF-H1 couples nocodazole-induced microtubule disassembly to cell contractility via RhoA. *Molecular Biology of the Cell*, 19(5):2147–2153, 2008.

[166] Ernest Latorre, Sohan Kale, Laura Casares, Manuel Gómez-González, Marina Uroz, Léo Valon, Roshna V Nair, Elena Garreta, Nuria Montserrat, Aránzazu Del Campo, Benoit Ladoux, Marino Arroyo, and Xavier Trepat. Active superelasticity in three-dimensional epithelia of controlled shape. *Nature.*, 563(7730):203–208, 2018.

[167] Moumita Das and F C Mackintosh. Poisson's ratio in composite elastic media with rigid rods. *Physical Review Letters*, 105(13):138102, 2010.

[168] M Dogterom and B Yurke. Measurement of the force-velocity relation for growing microtubules. *Science*, 278(5339):856–860, 1997.

[169] Clifford P Brangwynne, Frederick C MacKintosh, Sanjay Kumar, Nicholas A Geisse, Jennifer Talbot, L Mahadevan, Kevin K Parker, Donald E Ingber, and David A Weitz. Microtubules can bear enhanced compressive loads in living cells because of lateral reinforcement. *Journal of Cell Biology*, 173(5):733–741, 2006.

[170] Patrick Robison, Matthew A Caporizzo, Hossein Ahmadzadeh, Alexey I Bogush, Christina Yingxian Chen, Kenneth B Margulies, Vivek B Shenoy, and Benjamin L Prosser. Detyrosinated microtubules buckle and bear load in contracting cardiomyocytes. *science*, 352(6284):aaf0659, 2016.

[171] N Wang, K Naruse, D Stamenović, J J Fredberg, S M Mijailovich, I M Tolić-Nørrelykke, T Polte, R Mannix, and D E Ingber. Mechanical behavior in living cells consistent with the tensegrity model. *Proceedings of the National Academy of Sciences*, 98(14):7765–7770, 2001.

[172] Pei Hsun Wu, Dikla Raz Ben Aroush, Atef Asnacios, Wei Chiang Chen, Maxim E. Dokukin, Bryant L. Doss, Pauline Durand-Smet, Andrew Ekpenyong, Jochen Guck, Nataliia V. Guz, Paul A. Janmey, Jerry S.H. Lee, Nicole M. Moore, Albrecht Ott, Yeh Chuin Poh, Robert Ros, Mathias Sander, Igor Sokolov, Jack R. Staunton, Ning Wang, Graeme Whyte, and Denis Wirtz. A comparison of methods to assess cell mechanical properties. *Nature Methods*, 15:491–498, 2018.

[173] Johanna Block, Hannes Witt, Andrea Candelli, Jordi Cabanas Danes, Erwin J.G. Peterman, Gijs J.L. Wuite, Andreas Janshoff, and Sarah Köster. Viscoelastic properties of vimentin originate from nonequilibrium conformational changes. *Sci. Adv.*, 4(6):aat1161, 2018.

[174] Joost van Mameren, Karen C Vermeulen, Fred Gittes, and Christoph F Schmidt. Leveraging single protein polymers to measure flexural rigidity. *J. Phys. Chem. B*, 113(12):3837–3844, 2009.

[175] R Yasuda, H Miyata, and K Kinosita, Jr. Direct measurement of the torsional rigidity of single actin filaments. *Journal of Molecular Biology*, 263(2):227–236, 1996.

[176] Jeffrey P Bibeau, Nandan G Pandit, Shawn Gray, Nooshin Shatery Nejad, Charles V Sindelar, Wenxiang Cao, and Enrique M De La Cruz. Twist response of actin filaments. *Proceedings of the National Academy of Sciences*, 120(4):e2208536120, 2023.

[177] L. Kreplak, H. Bär, J. F. Leterrier, H. Herrmann, and U. Aebi. Exploring the mechanical behavior of single intermediate filaments. *Journal of Molecular Biology*, 354(3):569–577, 2005.

[178] A Kis, S Kasas, B Babić, A J Kulik, W Benoît, G A D Briggs, C Schönenberger, S Caticas, and L Forró. Nanomechanics of microtubules. *Physical Review Letters*, 89(24):248101, 2002.

[179] Laura Schaedel, Karin John, Jérémie Gaillard, Maxence V Nachury, Laurent Blanchoin, and Manuel Théry. Microtubules self-repair in response to mechanical stress. *Nature Materials*, 14(11):1156–1163, 2015.

[180] Y Tsuda, H Yasutake, A Ishijima, and T Yanagida. Torsional rigidity of single actin filaments and actin-actin bond breaking force under torsion measured directly by *in vitro* micromanipulation. *Proceedings of the National Academy of Sciences*, 93(23):12937–12942, 1996.

[181] Sharyn A Endow and Piotr E Marszalek. An estimate to the first approximation of microtubule rupture force. *Eur. Biophysical Journal*, 48(6):569–577, 2019.

[182] Charlotta Lorenz, Johanna Forsting, Robert W Style, Stefan Klumpp, and Sarah Köster. Keratin filament mechanics and energy dissipation are determined by metal-like plasticity. *Matter*, 6(6):2019–2033, 2023.

[183] Filipe Nunes Vicente, Mickael Lelek, Jean-Yves Tinevez, Quang D Tran, Gerard Pehau-Arnaudet, Christophe Zimmer, Sandrine Etienne-Manneville, Gregory Giannone, and Cécile Leduc. Molecular organization and mechanics of single vimentin filaments revealed by super-resolution imaging. *Sci. Adv.*, 8(8):eabm2696, 2022.

[184] Margaret L Gardel, Karen E Kasza, Clifford P Brangwynne, Jiayu Liu, and David A Weitz. Chapter 19: Mechanical response of cytoskeletal networks. *Methods Cell Biol.*, 89:487–519, 2008.

[185] Daphne Weihns, Thomas G Mason, and Michael A Teitell. Bio-microrheology: a frontier in microrheology. *Biophysical Journal*, 91(11):4296–4305, 2006.

[186] Yali Yang, Mo Bai, William S Klug, Alex J Levine, and Megan T Valentine. Microrheology of highly crosslinked microtubule networks is dominated by force-induced crosslinker unbinding. *Soft Matter*, 9(2):383–393, 2013.

[187] Yi Chia Lin, Gijsje H. Koenderink, Frederick C. MacKintosh, and David A. Weitz. Viscoelastic properties of microtubule networks. *Macromolecules*, 40(21):7714–7720, 2007.

[188] Yali Yang, Jun Lin, Bugra Kaytanli, Omar A. Saleh, and Megan T. Valentine. Direct correlation between creep compliance and deformation in entangled and sparsely crosslinked microtubule networks. *Soft Matter*, 8(6):1776–1784, 2012.

[189] Inka Kirchenbuechler, Donald Guu, Nicholas A Kurniawan, Gijsje H Koenderink, and M Paul Lettinga. Direct visualization of flow-induced conformational transitions of single actin filaments in entangled solutions. *Nature Communications*, 5(1):5060, 2014.

[190] M. L. Gardel, J. H. Shin, F. C. MacKintosh, L. Mahadevan, P. Matsudaira, and D. A. Weitz. Elastic behavior of cross-linked and bundled actin networks. *science*, 304(5675):1301–1305, 2004.

[191] F C MacKintosh, J Käs, and P A Janmey. Elasticity of semiflexible biopolymer networks. *Physical Review Letters*, 75(24):4425–4428, 1995.

[192] K. E. Kasza, C. P. Broedersz, G. H. Koenderink, Y. C. Lin, W. Messner, E. A. Millman, F. Nakamura, T. P. Stossel, F. C. MacKintosh, and D. A. Weitz. Actin filament length tunes elasticity of flexibly cross-linked actin networks. *Biophysical Journal*, 99(4):1091–1100, 2010.

[193] Chase P. Broedersz, Karen E. Kasza, Louise M. Jawerth, Stefan Münster, David A. Weitz, and Frederick C. MacKintosh. Measurement of nonlinear rheology of cross-linked biopolymer gels. *Soft Matter*, 6(17):4120–4127, 2010.

[194] Jan Wilhelm and Erwin Frey. Elasticity of stiff polymer networks. *Physical Review Letters*, 91(10):108103, 2003.

[195] David A Head, Alex J Levine, and F C MacKintosh. Deformation of cross-linked semiflexible polymer networks. *Physical Review Letters*, 91(10):108102, 2003.

[196] Ovijit Chaudhuri, Sapun H Parekh, and Daniel A Fletcher. Reversible stress softening of actin networks. *Nature*, 445(7125):295–298, 2007.

[197] Yi Chia Lin, Norman Y. Yao, Chase P. Broedersz, Harald Herrmann, Fred C. MacKintosh, and David A. Weitz. Origins of elasticity in intermediate filament networks. *Physical Review Letters*, 104(5):058101, 2010.

[198] Norman Y. Yao, Chase P. Braedersz, Yi Chia Lin, Karen E. Kasza, Frederick C. MacKintosh, and David A. Weitz. Elasticity in ionically cross-linked neurofilament networks. *Biophysical Journal*, 98(10):2147–2153, 2010.

[199] Yi Chia Lin, Chase P. Broedersz, Amy C. Rowat, Tatjana Wedig, Harald Herrmann, Frederick C. MacKintosh, and David A. Weitz. Divalent cations crosslink vimentin intermediate filament tail domains to regulate network mechanics. *Journal of Molecular Bio*, 399(4):637–644, 2010.

[200] Anders Aufderhorst-Roberts and Gisje H. Koenderink. Stiffening and inelastic fluidization in vimentin intermediate filament networks. *Soft Matter*, 15(36):7127–7136, 2019.

[201] Harald Bär, Michael Schopferer, Sarika Sharma, Bernhard Hochstein, Norbert Mücke, Harald Herrmann, and Norbert Willenbacher. Mutations in desmin's carboxy-terminal “tail” domain severely modify filament and network mechanics. *Journal of Molecular Biology*, 397(5):1188–1198, 2010.

[202] Huayin Wu, Yinan Shen, Dianzhuo Wang, Harald Herrmann, Robert D Goldman, David A Weitz, and John A Paulson. Effect of divalent cations on the structure and mechanics of vimentin intermediate filaments. *Biophysical Journal*, 119:55–64, 2020.

[203] Kimie Fukuyama, Takashi Murozuka, Russell Caldwell, and William L Epstein. Divalent cation stimulation of in vitro fibre assembly from epidermal keratin protein. *Journal of Cell Science*, 33:255–263, 1978.

[204] Anna V. Schepers, Charlotta Lorenz, Peter Nietmann, Andreas Janshoff, Stefan Klumpp, and Sarah Köster. Multiscale mechanics and temporal evolution of vimentin intermediate filament networks. *Proceedings of the National Academy of Sciences*, 118(27):2102026118, 2021.

[205] Manuela Denz, Manuel Marschall, Harald Herrmann, and Sarah Köster. Ion type and valency differentially drive vimentin tetramers into intermediate filaments or higher order assemblies. *Soft Matter*, 17(4):870–878, 2021.

[206] J. Deek, R. Maan, E. Loiseau, and A. R. Bausch. Reconstitution of composite actin and keratin networks in vesicles. *Soft Matter*, 14(10):1897–1902, 2018.

[207] Iman Elbalasy, Paul Mollenkopf, Cary Tutmarc, Harald Herrmann, and Jörg Schnauß. Keratins determine network stress responsiveness in reconstituted actin-keratin filament systems. *Soft Matter*, 17(14):3954–3962, 2021.

[208] Vincent Pelletier, Naama Gal, Paul Fournier, and Maria L Kilfoil. Microrheology of microtubule solutions and actin-microtubule composite networks. *Physical Review Letters*, 102(18):188303, 2009.

[209] I.K. Piechocka. Biopolymers: from structural hierarchy to nonlinear rheology. 2011.

[210] Laura Schaedel, Charlotta Lorenz, Anna V. Schepers, Stefan Klumpp, and Sarah Köster. Vimentin intermediate filaments stabilize dynamic microtubules by direct interactions. *Nature Communications*, 12(1):1–12, 2021.

[211] Mikkel H Jensen, Eliza J Morris, Robert D Goldman, and David A Weitz. Emergent properties of composite semiflexible biopolymer networks. *Bioarchitecture*, 4(4-5):138–143, 2014.

[212] Yi-Chia Lin, Gijsje H. Koenderink, Frederick C. MacKintosh, and David A. Weitz. Control of non-linear elasticity in f-actin networks with microtubules. *Soft Matter*, 7:902–906, 2011.

[213] Shea N Ricketts, Jennifer L Ross, and Rae M Robertson-Anderson. Co-entangled actin-microtubule composites exhibit tunable stiffness and power-law stress relaxation. *Biophysical Journal*, 115(6):1055–1067, 2018.

[214] Shea N Ricketts, Madison L Francis, Leila Farhadi, Michael J Rust, Moumita Das, Jennifer L Ross, and Rae M Robertson-Anderson. Varying crosslinking motifs drive the mesoscale mechanics of actin-microtubule composites. *Sci. Rep.*, 9(1):12831, 2019.

[215] Yinan Shen, Huayin Wu, Peter J. Lu, Dianzhuo Wang, Marjan Shayegan, Hui Li, Weichao Shi, Zizhao Wang, Li Heng Cai, Jing Xia, Meng Zhang, Ruihua Ding, Harald Herrmann, Robert Goldman, Fred C. Mackintosh, Arturo Moncho-Jordá, and David A. Weitz. Effects of vimentin intermediate filaments on the structure and dynamics of in vitro multicomponent interpenetrating cytoskeletal networks. *Physical Review Letters*, 127(10):108101, 2021.

[216] Magdalena Preciado López, Florian Huber, Ilya Grigoriev, Michel O Steinmetz, Anna Akhmanova, Gijsje H Koenderink, and Marileen Dogterom. Actin-microtubule coordination at growing microtubule ends. *Nature Communications*, 5(1):4778, 2014.

[217] Irene Istúriz Petitjean, Quang D Tran, Angeliki Goutou, Zima Kabir, Gerhard Wiche, Cécile Leduc, and Gijsje H Koenderink. Reconstitution of cytolinker-mediated crosstalk between actin and vimentin. *European Journal of Cell Biology*, 103(2):151403, 2024.

[218] Shuvasree SenGupta, Carole A Parent, and James E Bear. The principles of directed cell migration. *Nature Reviews Molecular Cell Biology*, 22(8):529–547, 2021.

[219] Ryan J Petrie and Kenneth M Yamada. Multiple mechanisms of 3D migration: the origins of plasticity. *Current Opinion in Cell Biology*, 42:7–12, 2016.

[220] Sean P. Palecek, Anna Huttenlocher, Alan F. Horwitz, and Douglas A. Lauffenburger. Physical and biochemical regulation of integrin release during rear detachment of migrating cells. *Journal of Cell Science*, 111(7):929–940, 1998.

[221] Robert W. Style, Rostislav Boltyanskiy, Guy K. German, Callen Hyland, Christopher W. Macminn, Aaron F. Mertz, Larry A. Wilen, Ye Xu, and Eric R. Dufresne. Traction force microscopy in physics and biology. *Soft Matter*, 10(23):4047–4055, 2014.

[222] Ryan J Petrie, Hyun Koo, and Kenneth M Yamada. Generation of compartmentalized pressure by a nuclear piston governs cell motility in a 3D matrix. *science*, 345(6200):1062–1065, 2014.

[223] Ewa K Paluch and Erez Raz. The role and regulation of blebs in cell migration. *Current Opinion in Cell Biology*, 25(5):582–590, 2013.

[224] Yan-Jun Liu, Maël Le Berre, Franziska Lautenschlaeger, Paolo Maiuri, Andrew Callan-Jones, Mélina Heuzé, Tohru Takaki, Raphaël Voituriez, and Matthieu Piel. Confinement and low adhesion induce fast amoeboid migration of slow mesenchymal cells. *Cell*, 160(4):659–672, 2015.

[225] Kimberly M Stroka, Hongyuan Jiang, Shih-Hsun Chen, Ziqiu Tong, Denis Wirtz, Sean X Sun, and Konstantinos Konstantopoulos. Water permeation drives tumor cell migration in confined microenvironments. *Cell*, 157(3):611–623, 2014.

[226] Mira Krendel, Frank T Zenke, and Gary M Bokoch. Nucleotide exchange factor GEF-H1 mediates cross-talk between microtubules and the actin cytoskeleton. *Nature Cell Biology*, 4(4):294–301, 2002.

[227] Andrew Rape, Wei Hui Guo, and Yu Li Wang. Microtubule depolymerization induces traction force increase through two distinct pathways. *Journal of Cell Science*, 124(24):4233–4240, 2011.

[228] Mihai L Azoitei, Jungsik Noh, Daniel J Marston, Philippe Roudot, Christopher B Marshall, Timothy A Daugird, Sidney L Lisanza, María-José Sandí, Mitsu Ikura, John Sondek, Robert Rottapel, Klaus M Hahn, and Gaudenz Danuser. Spatiotemporal dynamics of GEF-H1 activation controlled by microtubule- and src-mediated pathways. *Journal of Cell Biology*, 218(9):3077–3097, 2019.

[229] Jessica N Heck, Suzanne M Ponik, Maria G Garcia-Mendoza, Carolyn A Pehlke, David R Inman, Kevin W Eliceiri, and Patricia J Keely. Microtubules regulate GEF-H1 in response to extracellular matrix stiffness. *Molecular Biology of the Cell*, 23(13):2583–2592, 2012.

[230] Aglaja Kopf, Jörg Renkawitz, Robert Hauschild, Irute Girkontaite, Kerry Tedford, Jack Merrin, Oliver Thorn-Seshold, Dirk Trauner, Hans Häcker, Klaus-Dieter Fischer, Eva Kiermaier, and Michael Sixt. Microtubules control cellular shape and coherence in amoeboid migrating cells. *Journal of Cell Biology*, 219(6), 2020.

[231] Csaba Daday, Katra Kolšek, and Frauke Gräter. The mechano-sensing role of the unique sh3 insertion in plakin domains revealed by molecular dynamics simulations. *Sci. Rep.*, 7:11669, 2017.

[232] Michael Murrell, Patrick W Oakes, Martin Lenz, and Margaret L Gardel. Forcing cells into shape: the mechanics of actomyosin contractility. *Nature Reviews Molecular Cell Biology*, 16(8):486–498, 2015.

[233] Michael P Murrell and Margaret L Gardel. F-actin buckling coordinates contractility and severing in a biomimetic actomyosin cortex. *Proceedings of the National Academy of Sciences*, 109(51):20820–20825, 2012.

[234] Viktoria Wollrab, Julio M Belmonte, Lucia Baldauf, Maria Leptin, François Nédélec, and Gijsje H Koenderink. Polarity sorting drives remodeling of actin-myosin networks. *Journal of Cell Science*, 132(4):jcs219717, 2018.

[235] José Alvarado, Michael Sheinman, Abhinav Sharma, Fred C. MacKintosh, and Gijsje H. Koenderink. Force percolation of contractile active gels. *Soft Matter*, 13(34):5624–5644, 2017.

[236] Poul M Bendix, Gijsje H Koenderink, Damien Cuvelier, Zvonimir Dogic, Bernard N Koeleman, William M Brieher, Christine M Field, L Mahadevan, and David A Weitz. A quantitative analysis of contractility in active cytoskeletal protein networks. *Bioophysical Journal*, 94(8):3126–3136, 2008.

[237] Kevin Carvalho, Feng C. Tsai, Edouard Lees, Raphaël Voituriez, Gijsje H. Koenderink, and Cecile Sykes. Cell-sized liposomes reveal how actomyosin cortical tension drives shape change. *Proceedings of the National Academy of Sciences*, 110(41):16456–16461, 2013.

[238] Etienne Loiseau, Jochen A M Schneider, Felix C Keber, Carina Pelzl, Gladys Massiera, Guillaume Salbreux, and Andreas R Bausch. Shape remodeling and blebbing of active cytoskeletal vesicles. *Sci. Adv.*, 2(4):e1500465, 2016.

[239] William M McFadden, Patrick M McCall, Margaret L Gardel, and Edwin M Munro. Filament turnover tunes both force generation and dissipation to control long-range flows in a model actomyosin cortex. *PLoS Comput. Biol.*, 13(12):e1005811, 2017.

[240] Sven K Vogel, Christian Wölfer, Diego A Ramirez-Diaz, Robert J Flassig, Kai Sundmacher, and Petra Schwille. Symmetry breaking and emergence of directional flows in minimal actomyosin cortices. *Cells*, 9(6):1432, 2020.

[241] Sonal, Kristina A. Ganzinger, Sven K. Vogel, Jonas Mücksch, Philipp Blumhardt, and Petra Schwille. Myosin-ii activity generates a dynamic steady state with continuous actin turnover in a minimal actin cortex. *Journal of Cell Science*, 132(4):jcs219899, 2019.

[242] Tzer Han Tan, Maya Malik-Garbi, Enas Abu-Shah, Junang Li, Abhinav Sharma, Fred C MacKintosh, Kinneret Keren, Christoph F Schmidt, and Nikta Fakhri. Self-organized stress patterns drive state transitions in actin cortices. 4(6):eaar2847, 2018.

[243] Mathieu Pinot, Villier Steiner, Benoit Dehapiot, Byung-Kuk Yoo, Franck Chesnel, Laurent Blanchoin, Charles Kervrann, and Zoher Gueroui. Confinement induces actin flow in a meiotic cytoplasm. *Proceedings of the National Academy of Sciences*, 109(29):11705–11710, 2012.

[244] Maya Malik-Garbi, Niv Ierushalmi, Silvia Jansen, Enas Abu-Shah, Bruce L Goode, Alex Mogilner, and Kinneret Keren. Scaling behaviour in steady-state contracting actomyosin networks. *Nature Physics*, 15(5):509–516, 2019.

[245] Ryota Sakamoto, Ziane Izri, Yuta Shimamoto, Makito Miyazaki, and Yusuke T Maeda. Geometric trade-off between contractile force and viscous drag determines the actomyosin-based motility of a cell-sized droplet. *Proceedings of the National Academy of Sciences*, 119(30):e2121147119, 2022.

[246] Gloria Lee, Gregor Leech, Michael J Rust, Moumita Das, Ryan J McGorty, Jennifer L Ross, and Rae M Robertson-Anderson. Myosin-driven actin-microtubule networks exhibit self-organized contractile dynamics. *Sci. Adv.*, 7(6):eabe4334, 2021.

[247] Louise P Cramer. Forming the cell rear first: breaking cell symmetry to trigger directed cell migration. *Nature Cell Biology*, 12(7):628–632, 2010.

[248] Ju M Vasiliev, I M Gelfand, L V Domnina, O Y Ivanova, S G Komm, and L V Olshevskaja. Effect of colcemid on the locomotory behaviour of fibroblasts. *Development*, 24:625–640, 1970.

[249] Nadia Efimova, Changsong Yang, Jonathan X Chia, Ning Li, Christopher J Lengner, Kristi L Neufeld, and Tatyana M Svitkina. Branched actin networks are assembled on microtubules by adenomatous polyposis coli for targeted membrane protrusion. *Journal of Cell Biology*, 219(9):e202003091, 2020.

[250] Jessica L Henty-Ridilla, Aneliya Rankova, Julian A Eskin, Katelyn Kenny, and Bruce L Goode. Accelerated actin filament polymerization from microtubule plus ends. *Science*, 352(6288):1004–1009, 2016.

[251] Marileen Dogterom and Gijsje H Koenderink. Actin–microtubule crosstalk in cell biology. *Nature reviews Molecular cell biology*, 20(1):38–54, 2019.

[252] Atsuko Kodama, Iakowos Karakesisoglou, Ellen Wong, Alec Vaezi, and Elaine Fuchs. Acf7: An essential integrator of microtubule dynamics. *Cell Press.*, 115:343–354, 2003.

[253] Ksenija Drabek, Marco van Ham, Tatiana Stepanova, Katharina Draegestein, Remco van Horssen, Carmen Laura Sayas, Anna Akhmanova, Timo ten Hagen, Ron Smits, Riccardo Fodde, Frank Grosveld, and Niels Galjart. Role of clasp2 in microtubule stabilization and the regulation of persistent motility. *Curr. Biol.*, 16(22):2259–2264, 2006.

[254] Benjamin P Bouchet, Rosemarie E Gough, York-Christoph Ammon, Dieudonné van de Willige, Harm Post, Guillaume Jacquemet, Af Maarten Altelaar, Albert Heck, Jr, Benjamin T Goult, and Anna Akhmanova. Talin-KANK1 interaction controls the recruitment of cortical microtubule stabilizing complexes to focal adhesions. *eLife.*, 5:e18124, 2016.

[255] Elvira Infante, Alessia Castagnino, Robin Ferrari, Pedro Monteiro, Sonia Agüera-González, Perrine Paul-Gilloteaux, Mélanie J Domingues, Paolo Maiuri, Matthew Raab, Catherine M Shanahan, Alexandre Baffet, Matthieu Piel, Edgar R Gomes, and Philippe Chavrier. LINC complex-lis1 interplay controls MT1-MMP matrix digest-on-demand response for confined tumor cell migration. *Nature Communications*, 9(1):2443, 2018.

[256] Brian T. Helfand, Melissa G. Mendez, S. N. Prasanna Murthy, Dale K. Shumaker, Boris Grin, Saleemulla Mohammad, Ueli Aebi, Tatjana Wedig, Yi I. Wu, Klaus M. Hahn, Masaki Inagaki, Harald Herrmann, and Robert D. Goldman. Vimentin organization modulates the formation of lamellipodia. *Molecular Biology of the Cell*, 22(8):1274–1289, 2011.

[257] Yasuhisa Sakamoto, Batiste Boëda, and Sandrine Etienne-Manneville. APC binds intermediate filaments and is required for their reorganization during cell migration. *Journal of Cell Biology*, 200(3):249–258, 2013.

[258] Shagufta H. Shabbir, Megan M. Cleland, Robert D. Goldman, and Milan Mrksich. Geometric control of vimentin intermediate filaments. *Biomaterials.*, 35(5):1359–1366, 2014.

[259] Cécile Leduc and Sandrine Etienne-Manneville. Regulation of microtubule-associated motors drives intermediate filament network polarization. *Journal of Cell Biology*, 216(6):1689–1703, 2017.

[260] Rudolf E Leube, Marcin Moch, and Reinhard Windoffer. Intermediate filaments and the regulation of focal adhesion. *Current Opinion in Cell Biology*, 32:13–20, 2015.

[261] Magdalena Preciado López, Florian Huber, Ilya Grigoriev, Michel O Steinmetz, Anna Akhmanova, Marileen Dogterom, and Gijsje H Koenderink. In vitro reconstitution of dynamic microtubules interacting with actin filament networks. *Methods Enzymol.*, 540:301–320, 2014.

[262] Daisuke Inoue, Dorian Obino, Judith Pineau, Francesca Farina, Jérémie Gaillard, Christophe Guerin, Laurent Blanchoin, Ana-Maria Lennon-Duménil, and Manuel Théry. Actin filaments regulate microtubule growth at the centrosome. *EMBO J.*, 38(11):e99630, 2019.

[263] Matthieu Gélin, Alexandre Schaeffer, Jérémie Gaillard, Christophe Guérin, Benoit Vianay, Magali Orhant-Prioux, Marcus Braun, Christophe Leterrier, Laurent Blanchoin, and Manuel Théry. Microtubules under mechanical pressure can breach dense actin networks. *Journal of Cell Science*, 136(22), 2023.

[264] Dieudonné van de Willige, Jessica Ja Hummel, Celine Alkemade, Olga I Kahn, Franco Kc Au, Robert Z Qi, Marileen Dogterom, Gijsje H Koenderink, Casper C Hoogenraad, and Anna Akhmanova. Cytolinker Gas2L1 regulates axon morphology through microtubule-modulated actin stabilization. *EMBO Rep.*, 20(11):e47732, 2019.

[265] Auréliane Elie, Elea Prezel, Christophe Guérin, Eric Denarier, Sacnicte Ramirez-Rios, Laurence Serre, Annie Andrieux, Anne Fourest-Lievin, Laurent Blanchoin, and Isabelle Arnal. Tau co-organizes dynamic microtubule and actin networks. *Sci. Rep.*, 5(1):9964, 2015.

[266] Celine Alkemade. *Reconstituting microtubule-actin coordination by cytolinkers*. PhD thesis, Delft University of Technology, 2021.

[267] N C Rodgers, E J Lawrence, A V Sawant, N Efimova, G Gonzalez-Vasquez, T T Hickman, I Kaverina, and M Zanic. CLASP2 facilitates dynamic actin filament organization along the microtubule lattice. *Molecular Biology of the Cell*, 34(3):261a, 2023.

[268] Celine Alkemade, Harmen Wierenga, Vladimir A. Volkov, Magdalena Preciado López, Anna Akhmanova, Pieter Rein ten Wolde, Marileen Dogterom, and Gijsje H. Koenderink. Cross-linkers at growing microtubule ends generate forces that drive actin transport. *Proceedings of the National Academy of Sciences*, 119(11):1-12, 2022.

[269] Brett J Roberts, Anjeza Pashaj, Keith R Johnson, and James K Wahl Iii. Desmosome dynamics in migrating epithelial cells requires the actin cytoskeleton. *Exp. cell research*, 317(20):2814–2822, 2011.

[270] Pooja R Sonavane, Chong Wang, Bette Dzamba, Gregory F Weber, Ammasi Periasamy, and Douglas W DeSimone. Mechanical and signaling roles for keratin intermediate filaments in the assembly and morphogenesis of xenopus mesendoderm tissue at gastrulation. *Development*, 144(23):4363–4376, 2017.

[271] Ekaterina Vasileva and Sandra Citi. The role of microtubules in the regulation of epithelial junctions. *Tissue Barriers*, 6(3):1539596, 2018.

[272] Marta N. Shahbazi, Diego Megias, Carolina Epifano, Anna Akhmanova, Gregg G. Gundersen, Elaine Fuchs, and Mirna Perez-Moreno. Clasp2 interacts with p120-catenin and governs microtubule dynamics at adherens junctions. *Journal of Cell Biology*, 203(6):1043–1061, 2013.

[273] Samantha J. Stehbens, Andrew D. Paterson, Matthew S. Crampton, Annette M. Shewan, Charles Ferguson, Anna Akhmanova, Robert G. Parton, and Alpha S. Yap. Dynamic microtubules regulate the local concentration of e-cadherin at cell-cell contacts. *Journal of Cell Science*, 119(9):1801–1811, 2006.

[274] Xinyu Chen, Shin-Ichiro Kojima, Gary G Borisy, and Kathleen J Green. P120 catenin associates with kinesin and facilitates the transport of cadherin-catenin complexes to intercellular junctions. *Journal of Cell Biology*, 163(3):547–557, 2003.

[275] Lee A. Ligon and Erika L.F. Holzbaur. Microtubules tethered at epithelial cell junctions by dynein facilitate efficient junction assembly. *Traffic*, 8(7):808–819, 2007.

[276] Kazuto Tsukita, Manabu Kitamata, Hiroka Kashihara, Tomoki Yano, Ikuko Fujiwara, Timothy F Day, Tatsuya Katsuno, Jaewon Kim, Fumiko Takenaga, Hiroo Tanaka, Sungsu Park, Makoto Miyata, Hitomi Watanabe, Gen Kondoh, Ryosuke Takahashi, Atsushi Tamura, and Sachiko Tsukita. Phase separation of an actin nucleator by junctional microtubules regulates epithelial function. *Sci. Adv.*, 9(7):eadf6358, 2023.

[277] Céline Revenu, Sebastian Streichan, Erika Donà, Virginie Lecaudey, Lars Hufnagel, and Darren Gilmour. Quantitative cell polarity imaging defines leader-to-follower transitions during collective migration and the key role of microtubule-dependent adherens junction formation. *Development*, 141(6):1282–1291, 2014.

[278] Robert A Law, Alexander Kiepas, Habben E Desta, Emiliano Perez Ipiña, Maria Parlani, Se Jong Lee, Christopher L Yankaskas, Runchen Zhao, Panagiotis Mistriotis, Nianchao Wang, Zhizhan Gu, Petr Kalab, Peter Friedl, Brian A Camley, and Konstantinos Konstantopoulos. Cytokinesis machinery promotes cell dissociation from collectively migrating strands in confinement. *Sci. Adv.*, 9(2):eabq6480, 2023.

[279] Jeffrey W Brown, Charles J Cho, and Jason C Mills. Paligenesis: Cellular remodeling during tissue repair. *Annu. Rev. Physiol.*, 84:461–483, 2021.

[280] Pierre Savagner. Epithelial–mesenchymal transitions: From cell plasticity to concept elasticity. *Curr. Top. Dev. Biol.*, 112:273–300, 2015.

[281] V Poltavets, M Kochetkova, Pitson Sm, and M S Samuel. The role of the extracellular matrix and its molecular and cellular regulators in cancer cell plasticity. *Cancer Cell Plasticity. Front. Oncol.*, 8:431, 2018.

[282] Tyler D. Ross, Brian G. Coon, Sanguk Yun, Nicolas Baeyens, Keiichiro Tanaka, Mingxing Ouyang, and Martin A. Schwartz. Integrins in mechanotransduction. *Current Opinion in Cell Biology*, 25(5):613–618, 2013.

[283] David A Calderwood, Iain D Campbell, and David R Critchley. Talins and kindlins: partners in integrin-mediated adhesion. *Nature Reviews Molecular Cell Biology*, 14(8):503–517, 2013.

[284] Julieann I Puleo, Sara S Parker, Mackenzie R Roman, Adam W Watson, Kiarash Rahmani Eliato, Leilei Peng, Kathylynn Saboda, Denise J Roe, Robert Ros, Frank B Gertler, and Ghassan Mouneimne. Mechanosensing during directed cell migration requires dynamic actin polymerization at focal adhesions. *Journal of Cell Biology*, 218(12):4215–4235, 2019.

[285] Peter Friedl and Katarina Wolf. Plasticity of cell migration: A multiscale tuning model. *Journal of Cell Biology*, 188(1):11–19, 2010.

[286] Jennifer M Mataraza, Michael W Briggs, Zhigang Li, Alan Entwistle, Anne J Ridley, and David B Sacks. Iqgap1 promotes cell motility and invasion. *Journal of Biological Chemistry*, 278:41237–41245, 2003.

[287] Barbara Belletti, Milena S Nicoloso, Monica Schiappacassi, Stefania Berton, Francesca Lovat, Katarina Wolf, Vincenzo Canzonieri, Antonella Zucchetto, Peter Friedl, Alfonso Colombatti, and Gustavo Baldassarre. Stathmin activity influences sarcoma cell shape, motility, and metastatic potential. *Molecular Biology of the Cell*, 19:2003–2013, 2003.

[288] Karen M Ridge, John E Eriksson, Milos Pekny, and Robert D Goldman. Roles of vimentin in health and disease. *Genes Dev.*, 36(7-8):391–407, 2022.

[289] Lei Qi, Teresa Knifley, Min Chen, and Kathleen L. O'Connor. Integrin $\alpha 6\beta 4$ requires plectin and vimentin for adhesion complex distribution and invasive growth. *Journal of Cell Science*, 135(2):jcs258471, 2022.

[290] Ya-Jun Wang, Hong Liang, Yixin Liu, Qiyuan Bao, Shuang Yang, Xin-Xin Xu, Yu-Chen Chen, Wei Liu, Xuemeng Shi, Yuheng Shi, Xiaohui Liu, Baohong Liu, Hai Gao, Yaming Jiu, and Yan-Jun Liu. Lamin a/c and vimentin as a coordinated regulator during amoeboid migration in microscale confined microenvironments. *Nano Lett.*, 23:6735, 2023.

[291] Herbert B Schiller, Caroline C Friedel, Cyril Boulegue, and Reinhard Fässler. Quantitative proteomics of the integrin adhesome show a myosin II-dependent recruitment of LIM domain proteins. *EMBO Rep.*, 12(3):259–266, 2011.

[292] Corina Ciobanasu, Bruno Faivre, and Christophe Le Clainche. Actomyosin-dependent formation of the mechanosensitive talin-vinculin complex reinforces actin anchoring. *Nature Communications*, 5:3095, 2014.

[293] Florian Franz, Rafael Tapia-Rojo, Sabina Winograd-Katz, Rajaa Boujemaa-Paterski, Wenhong Li, Tamar Unger, Shira Albeck, Camilo Aponte-Santamaria, Sergi Garcia-Manyes, Ohad Medalia, Benjamin Geiger, and Frauke Gräter. Allosteric activation of vinculin by talin. *Nature Communications*, 14(1):4311, 2023.

[294] Rajaa Boujemaa-Paterski, Bruno Martins, Matthias Eibauer, Charlie T. Beales, Benjamin Geiger, and Ohad Medalia. Talin-activated vinculin interacts with branched actin networks to initiate bundles. *eLife.*, 9:1–26, 2020.

[295] Derek L. Huang, Nicolas A. Bax, Craig D. Buckley, William I. Weis, and Alexander R. Dunn. Vinculin forms a directionally asymmetric catch bond with f-actin. *science*, 357(6352):703–706, 2017.

[296] Julien Pernier, Marcelina Cardoso Dos Santos, Mariem Souissi, Adrien Joly, Hemalatha Narassimprakash, Olivier Rossier, Grégory Giannone, Emmanuèle Helfer, Kheya Sengupta, and Christophe Le Clainche. Talin and kindlin cooperate to control the density of integrin clusters. *Journal of Cell Science*, 136(8):jcs260746, 2023.

[297] Charlotte F Kelley, Thomas Litschel, Stephanie Schumacher, Dirk Dedden, Petra Schwille, and Naoko Mizuno. Phosphoinositides regulate force-independent interactions between talin, vinculin, and actin. *eLife.*, 9:e56110, 2020.

[298] A J Ehrlicher, F Nakamura, J H Hartwig, D A Weitz, and T P Stossel. Mechanical strain in actin networks regulates filgap and integrin binding to filamin a. *Nature.*, 478:260–263, 2011.

[299] Elias T Spiliotis and Michael A McMurray. Masters of asymmetry - lessons and perspectives from 50 years of septins. *Molecular Biology of the Cell*, 31(21):2289–2297, 2020.

[300] Konstantinos Nakos, Md Noor A Alam, Megan R Radler, Ilona A Kesisova, Changsong Yang, Joshua Okletsey, Meagan R Tomasso, Shae B Padrick, Tatyana M Svitkina, and Elias T Spiliotis. Septins mediate a microtubule-actin crosstalk that enables actin growth on microtubules. *Proceedings of the National Academy of Sciences*, 119(50):e2202803119, 2022.

[301] AS Zhovmer, A Manning, C Smith, A Nguyen, O Prince, PJ Sáez, X Ma, D Tsygankov, AX Cartagena-Rivera, NA Singh, RK Singh, and ED Tabdanov. Septins provide microenvironment sensing and cortical actomyosin partitioning in motile amoeboid t lymphocytes. *Sci Adv.*, 10:ead1788, 2024.

[302] Joanna Kim, Olivia L. Mooren, Michael D. Onken, and John A. Cooper. Septin and actin contributions to endothelial cell–cell junctions and monolayer integrity. *Cytoskeleton*, 80(8):228–241, 2022.

[303] Xueying Wang, Wenwen Wang, Xiwei Wang, Ming Wang, Lijuan Zhu, Fatima Garba, Chuanhai Fu, Barbara Zieger, Xu Liu, Xing Liu, and Xuebiao Yao. The septin complex links the catenin complex to the actin cytoskeleton for establishing epithelial cell polarity. *Journal of Molecular Cell Biology*, 13(6):395, 2021.

[304] Kim J A Vendel, Celine Alkemade, Nemo Andrea, Gisje H Koenderink, and Marileen Dogterom. In vitro reconstitution of dynamic co-organization of microtubules and actin filaments in emulsion droplets. *Methods Mol. Biol.*, 2101:53–75, 2020.

- [305] Orit Siton-Mendelson and Anne Bernheim-Groswasser. Toward the reconstitution of synthetic cell motility. *Cell Adhes. Migr.*, 10(5):461–474, 2016.
- [306] Andreas Fink, Charlotte R Doll, Ana Yagüe Relimpio, Yannik Dreher, Joachim P Spatz, Kerstin Göpfrich, and Elisabetta Ada Cavalcanti-Adam. Extracellular cues govern shape and cytoskeletal organization in giant unilamellar lipid vesicles. *ACS Synth. Biol.*, 12(2):369–374, 2023.
- [307] Torsten Wittmann, Alessandro Dema, and Jeffrey van Haren. Lights, cytoskeleton, action: Optogenetic control of cell dynamics. *Current Opinion in Cell Biology*, 66:1–10, 2020.
- [308] Jessica G Bermudez, Alexander Deiters, and Matthew C Good. Patterning microtubule network organization reshapes cell-like compartments. *ACS Synth. Biol.*, 10(6):1338–1350, 2021.
- [309] David B Brückner, Nicolas Arlt, Alexandra Fink, Pierre Ronceray, Joachim O Rädler, and Chase P Broedersz. Learning the dynamics of cell-cell interactions in confined cell migration. *Proceedings of the National Academy of Sciences*, 118(7):e2016602118, 2021.
- [310] Rebecca C Adikes, Ryan A Hallett, Brian F Saway, Brian Kuhlman, and Kevin C Slep. Control of microtubule dynamics using an optogenetic microtubule plus end-f-actin cross-linker. *Journal of Cell Biology*, 217(2):779–793, 2018.
- [311] Sorosh Amiri, Camelia Muresan, Xingbo Shang, Clotilde Huet-Calderwood, Martin A Schwartz, David A Calderwood, and Michael Murrell. Intracellular tension sensor reveals mechanical anisotropy of the actin cytoskeleton. *Nature Communications*, 14(1):8011, 2023.
- [312] Paul A. Janmey. Mechanical properties of cytoskeletal polymers. *Current Opinion in Cell Biology*, 3(1):4–11, 1991.
- [313] Ulrike Rölleke, Pallavi Kumari, Ruth Meyer, and Sarah Köster. The unique biomechanics of intermediate filaments—from single filaments to cells and tissues. *Current Opinion in Cell Biology*, 85:102263, 2023.
- [314] AV Vakhrusheva, AV Murashko, ES Trifonova, Yu M Efremov, PS Timashev, and OS Sokolova. Role of actin-binding proteins in the regulation of cellular mechanics. *European Journal of Cell Biology*, 101(3):151241, 2022.
- [315] Harald Herrmann, Markus Häner, Monika Brettel, Shirley A Müller, Kenneth N Goldie, Bettina Fedtke, Ariel Lustig, Werner W Franke, and Ueli Aebi. Structure and assembly properties of the intermediate filament protein vimentin: the role of its head, rod and tail domains. *Journal of molecular biology*, 264(5):933–953, 1996.
- [316] Chase P Broedersz and Fred C MacKintosh. Modeling semiflexible polymer networks. *Reviews of Modern Physics*, 86(3):995–1036, 2014.

[317] Michael Meleties, Rhett L Martineau, Maneesh K Gupta, and Jin Kim Montclare. Particle-based microrheology as a tool for characterizing protein-based materials. *ACS Biomaterials Science & Engineering*, 8(7):2747–2763, 2022.

[318] Maayan Levin, Raya Sorkin, David Pine, Rony Granek, Anne Bernheim-Groswasser, and Yael Roichman. Kinetics of actin networks formation measured by time resolved particle-tracking microrheology. *Soft matter*, 16(33):7869–7876, 2020.

[319] Roberto Cerbino and Veronique Trappe. Differential dynamic microscopy: probing wave vector dependent dynamics with a microscope. *Physical review letters*, 100(18):188102, 2008.

[320] Roberto Cerbino, Fabio Giavazzi, and Matthew E Helgeson. Differential dynamic microscopy for the characterization of polymer systems. *Journal of Polymer Science*, 60(7):1079–1089, 2022.

[321] SJ Anderson, Jonathan Garamella, S Adalbert, RJ McGorty, and RM Robertson-Anderson. Subtle changes in crosslinking drive diverse anomalous transport characteristics in actin–microtubule networks. *Soft Matter*, 17(16):4375–4385, 2021.

[322] Devynn M Wulstein, Kathryn E Regan, Jonathan Garamella, Ryan J McGorty, and Rae M Robertson-Anderson. Topology-dependent anomalous dynamics of ring and linear dna are sensitive to cytoskeleton crosslinking. *Science Advances*, 5(12):eaay5912, 2019.

[323] Maik Drechsler, Fabio Giavazzi, Roberto Cerbino, and Isabel M Palacios. Active diffusion and advection in drosophila oocytes result from the interplay of actin and microtubules. *Nature communications*, 8(1):1520, 2017.

[324] Hannah N Verwei, Gloria Lee, Gregor Leech, Irene Istúriz Petitjean, Gijsje H Koenderink, Rae M Robertson-Anderson, and Ryan James McGorty. Quantifying cytoskeleton dynamics using differential dynamic microscopy. *JoVE (Journal of Visualized Experiments)*, (184):e63931, 2022.

[325] Alexandra V Bayles, Todd M Squires, and Matthew E Helgeson. Dark-field differential dynamic microscopy. *Soft Matter*, 12(8):2440–2452, 2016.

[326] Julie Pinchiaroli Pinchiaroli, Renita Saldanha Saldanha, Alison E Patteson, Rae M Robertson-Anderson, and Bekele J Gurmessa. Switchable microscale stress response of actin–vimentin composites emerges from scale-dependent interactions. *bioRxiv*, pages 2024–06, 2024.

[327] David Germain, Mathieu Leocmach, and Thomas Gibaud. Differential dynamic microscopy to characterize brownian motion and bacteria motility. *American Journal of Physics*, 84(3):202–210, 2016.

[328] ML Gardel, MT Valentine, John C Crocker, Andreas R Bausch, and DA Weitz. Microrheology of entangled f-actin solutions. *Physical review letters*, 91(15):158302, 2003.

[329] Ian Y Wong, Margaret L Gardel, David R Reichman, Eric R Weeks, Megan T Valentine, Andreas R Bausch, and David A Weitz. Anomalous diffusion probes microstructure dynamics of entangled f-actin networks. *Physical review letters*, 92(17):178101, 2004.

[330] Christina Cruickshank Miller. The stokes-einstein law for diffusion in solution. *Proceedings of the Royal Society of London. Series A, Containing Papers of a Mathematical and Physical Character*, 106(740):724–749, 1924.

[331] Pietro Cicuta and Athene M Donald. Microrheology: a review of the method and applications. *Soft matter*, 3(12):1449–1455, 2007.

[332] Fabio Giavazzi, Paolo Edera, Peter J Lu, and Roberto Cerbino. Image windowing mitigates edge effects in differential dynamic microscopy. *The European Physical Journal E*, 40:1–9, 2017.

[333] Inês Barreira Santarino, Severino Carlos B Oliveira, and Ana Maria Oliveira-Brett. Protein reducing agents dithiothreitol and tris (2-carboxyethyl) phosphine anodic oxidation. *Electrochemistry Communications*, 23:114–117, 2012.

[334] Clémentine Rouyère, Thomas Serrano, Stéphane Frémont, and Arnaud Echard. Oxidation and reduction of actin: Origin, impact in vitro and functional consequences in vivo. *European journal of cell biology*, 101(3):151249, 2022.

[335] T William Houk Jr and Kathleen Ue. The measurement of actin concentration in solution: a comparison of methods. *Anal. Biochem.*, 62(1):66–74, 1974.

[336] KA Jansen. Extracellular matrix mechanics and implications for cellular mechanosensing. 2016.

[337] Anthony J Kim, Vinothan N Manoharan, and John C Crocker. Swelling-based method for preparing stable, functionalized polymer colloids. *Journal of the American Chemical Society*, 127(6):1592–1593, 2005.

[338] Christoph F Schmidt, Michael Baermann, Gerhard Isenberg, and Erich Sackmann. Chain dynamics, mesh size, and diffusive transport in networks of polymerized actin: a quasielastic light scattering and microfluorescence study. *Macromolecules*, 22(9):3638–3649, 1989.

[339] Ute Wickert, Norbert Mücke, Tatjana Wedig, Shirley A Müller, Ueli Aebi, and Harald Herrmann. Characterization of the in vitro co-assembly process of the intermediate filament proteins vimentin and desmin: mixed polymers at all stages of assembly. *European journal of cell biology*, 84(2-3):379–391, 2005.

[340] Daniel A. Fletcher and R. Dyche Mullins. Cell mechanics and the cytoskeleton. *Nature*, 463(7280):485, 2010.

[341] Adrian F. Pegoraro, Paul Janmey, and David A. Weitz. Mechanical properties of the cytoskeleton and cells. *Cold Spring Harb. Perspect. Biol.*, 9(11), 2017.

[342] Y. Nakaseko and M. Yanagida. Cytoskeleton in the cell cycle. *Nature* 2001 412:6844, 412(6844):291–292, 2001.

[343] Matthew K. Hoelzle and Tatyana Svitkina. The cytoskeletal mechanisms of cell-cell junction formation in endothelial cells. *Molecular Biology of the Cell*, 23(2):310–323, 2012.

[344] Paul A Janmey. The cytoskeleton and cell signaling: component localization and mechanical coupling. *Physiological reviews*, 78(3):763–781, 1998.

[345] P. A. Janmey, U. Euteneuer, P. Traub, and M. Schliwa. Viscoelastic properties of vimentin compared with other filamentous biopolymer networks. *Journal of Cell Biology*, 113(1):155, 1991.

[346] Johanna Block, Hannes Witt, Andrea Candelli, Erwin J.G. Peterman, Gijs J.L. Wuite, Andreas Janshoff, and Sarah Köster. Nonlinear loading-rate-dependent force response of individual vimentin intermediate filaments to applied strain. *Physical Review Letters*, 118(4):048101, 2017.

[347] Johanna Forsting, Julia Kraxner, Hannes Witt, Andreas Janshoff, and Sarah Köster. Vimentin intermediate filaments undergo irreversible conformational changes during cyclic loading. *Nano Lett.*, 19(10):7349–7356, 2019.

[348] Alison E. Patteson, Amir Vahabikashi, Robert D. Goldman, and Paul A. Janmey. Mechanical and non-mechanical functions of filamentous and non-filamentous vimentin. *BioEssays*, 42(11):2000078, 2020.

[349] Melanie L. Styers, Gloria Salazar, Rachal Love, Andrew A. Peden, Andrew P. Kowalczyk, and Victor Faundez. The endo-lysosomal sorting machinery interacts with the intermediate filament cytoskeleton. *Molecular Biology of the Cell*, 15(12):5369, 2004.

[350] Ivan S. Chernoivanenko, Elena A. Matveeva, Vladimir I. Gelfand, Robert D. Goldman, and Alexander A. Minin. Mitochondrial membrane potential is regulated by vimentin intermediate filaments. *FASEB J.*, 29(3):820–827, 2015.

[351] Marika Sjöqvist, Daniel Antfolk, Freddy Suarez-Rodriguez, and Cecilia Sahlgren. From structural resilience to cell specification — intermediate filaments as regulators of cell fate. *FASEB J.*, 35(1):e21182, 2021.

[352] Alok Tomar and David D. Schlaepfer. Focal adhesion kinase: switching between gaps and gefs in the regulation of cell motility. *Current Opinion in Cell Biology*, 21(5):676, 2009.

[353] Nayana Tusamda Wakhloo, Sebastian Anders, Florent Badique, Melanie Eichhorn, Isabelle Brigaud, Tatiana Petithory, Maxime Vassaux, Jean-Louis Milan, Jean-Noël Freund, Jürgen Rühe, Patricia M. Davidson, Laurent Pieuchot, and Karine Anselme. Actomyosin, vimentin and linc complex pull on osteosarcoma nuclei to deform on micropillar topography. *Biomaterials*, 234:119746, 2020.

[354] Laurent Blanchoin, Rajaa Boujema-Paterski, Cécile Sykes, and Julie Plastino. Actin dynamics, architecture, and mechanics in cell motility. *Physiological reviews*, 94(1):235–263, 2014.

[355] Mathijs Vleugel, Maurits Kok, and Marileen Dogterom. Understanding force-generating microtubule systems through in vitro reconstitution. *Cell adhesion & migration*, 10(5):475–494, 2016.

[356] M. Yusuf Ali, Elena B. Krementsova, Guy G. Kennedy, Rachel Mahaffy, Thomas D. Pollard, Kathleen M. Trybus, and David M. Warshaw. Myosin va maneuvers through actin intersections and diffuses along microtubules. *Proceedings of the National Academy of Sciences*, 104(11):4332–4336, 2007.

[357] Harry W. Schroeder, Chris Mitchell, Henry Shuman, Erika L.F. Holzbaur, and Yale E. Goldman. Motor number controls cargo switching at actin-microtubule intersections in vitro. *Curr. Biol.*, 20(8):687–696, 2010.

[358] Dennis Breitsprecher, Richa Jaiswal, Jeffrey P. Bombardier, Christopher J. Gould, Jeff Gelles, and Bruce L. Goode. Rocket launcher mechanism of collaborative actin assembly defined by single-molecule imaging. *Science*, 336(6085):1164–1168, 2012.

[359] Magdalena Preciado López, Florian Huber, Ilya Grigoriev, Michel O. Steinmetz, Anna Akhmanova, Gijsje H. Koenderink, and Marileen Dogterom. Actin–microtubule coordination at growing microtubule ends. *Nature Communications* 2014 5:1, 5(1):1–9, 2014.

[360] Janet Y Sheung, Daisy H Achiriloae, Christopher Currie, Karthik Peddireddy, Aaron Xie, Jessalyn Simon-Parker, Gloria Lee, Michael J Rust, Moumita Das, Jennifer L Ross, and Rae M Robertson-Anderson. Motor-driven restructuring of cytoskeleton composites leads to tunable time-varying elasticity. *ACS Macro Lett.*, 10(9):1151–1158, 2021.

[361] Arnoud Sonnenberg, Ana M Rojas, and José M de Pereda. The structure of a tandem pair of spectrin repeats of plectin reveals a modular organization of the plakin domain. *Journal of Molecular Biology*, 368(5):1379–1391, 2007.

[362] Caezar Al-Jassar, Pau Bernadó, Martyn Chidgey, and Michael Overduin. Hinged plakin domains provide specialized degrees of articulation in envoplakin, periplakin and desmoplakin. *PLOS One*, 8(7):e69767, 2013.

[363] Esther Ortega, José A Manso, Rubén M Buey, Ana M Carballido, Arturo Carabias, Arnoud Sonnenberg, and Jose M de Pereda. The structure of the plakin domain of plectin reveals an extended rod-like shape. *Journal of Biological Chemistry*, 291(36):18643–18662, 2016.

[364] Branislav Nikolic, Elisabeth Mac Nulty, Birgit Mir, and Gerhard Wiche. Basic amino acid residue cluster within nuclear targeting sequence motif is essential for cytoplasmic plectin-vimentin network junctions. *The Journal of cell biology*, 134(6):1455–1467, 1996.

[365] Marie-France Steiner-Champliaud, Yann Schneider, Bertrand Favre, Frédérique Paulhe, Silke Praetzel-Wunder, Georgine Faulkner, Patryk Konieczny, Marianne Raith, Gerhard Wiche, Adijat Adebola, et al. Bpag1 isoform-b: Complex distribution pattern in striated and heart muscle and association with plectin and α -actinin. *Experimental Cell Research*, 316(3):297–313, 2010.

[366] L'ubica Urbániková, Lubomír Janda, Alexander Popov, Gerhard Wiche, and Jozef Ševčík. Purification, crystallization and preliminary x-ray analysis of the plectin actin-binding domain. *Acta Crystallogr. D*, 58(8):1368–1370, 2002.

[367] Jozef Sevcik, L'ubica Urbanikova, Julius Kost'an, Lubomir Janda, and Gerhard Wiche. Actin-binding domain of mouse plectin. crystal structure and binding to vimentin. *European Journal of Biochemistry*, 271(10):1873–1884, 2004.

[368] Jan Faix, Michel Steinmetz, Heike Boves, Richard A. Kammerer, Friedrich Lottspeich, Ursula Mintert, John Murphy, Alexander Stock, Ueli Aebi, and Günther Gerisch. Cortexillins, major determinants of cell shape and size, are actin-bundling proteins with a parallel coiled-coil tail. *Cell*, 86(4):631–642, 1996.

[369] Gavin Young, Nikolas Hundt, Daniel Cole, Adam Fineberg, Joanna Andrecka, Andrew Tyler, Anna Olerinyova, Ayla Ansari, Erik G. Marklund, Miranda P. Collier, Shane A. Chandler, Olga Tkachenko, Joel Allen, Max Crispin, Neil Billington, Yasuharu Takagi, James R. Sellers, Cédric Eichmann, Philipp Selenko, Lukas Frey, Roland Riek, Martin R. Galpin, Weston B. Struwe, Justin L. P. Benesch, and Philipp Kukura. Quantitative mass imaging of single biological macromolecules. *Science*, 360(6387):423–427, 2018.

[370] J. Chloe Bulinski, David J. Odde, Bonnie J. Howell, Ted D. Salmon, and Clare M. Waterman-Storer. Rapid dynamics of the microtubule binding of ensconsin in vivo. *Journal of Cell Science*, 114(21):3885–3897, 2001.

[371] Qi Wen and Paul A Janmey. Polymer physics of the cytoskeleton. *Curr. Opin. Solid State Mater. Sci.*, 15(5):177–182, 2011.

[372] Sabine M Volkmer Ward, Astrid Weins, Martin R Pollak, and David A Weitz. Dynamic viscoelasticity of actin cross-linked with wild-type and disease-causing mutant α -actinin-4. *Biophysical Journal*, 95(10):4915–4923, 2008.

[373] Andreas Bremer, Robert C Millonig, Rosmarie Sütterlin, Andreas Engel, Thomas D Pollard, and Ueli Aebi. The structural basis for the intrinsic disorder of the actin filament: the " lateral slipping" model. *Journal of Cell Biology*, 115(3):689–703, 1991.

[374] Radovan Spurny, Kamaran Abdoulrahman, Lubomir Janda, Dominik Ruönzler, Gottfried Koöhler, Maria J Castanon, and Gerhard Wiche. Oxidation and nitrosylation of cysteines proximal to the intermediate filament (if)-binding site of plectin: effects on structure and vimentin binding and involvement in if collapse. *Journal of Biological Chemistry*, 282(11):8175–8187, 2007.

[375] Mario Gimona and Steven J Winder. Single calponin homology domains are not actin-binding domains. *Curr. Biol.*, 8(19):R673–R675, 1998.

[376] Ferdinand A. Steinböck, Branislav Nikolic, Pierre A. Coulombe, Elaine Fuchs, Peter Traub, and Gerhard Wiche. Dose-dependent linkage, assembly inhibition and disassembly of vimentin and cytokeratin 5/14 filaments through plectin's intermediate filament-binding domain. *Journal of cell science*, 113 (Pt 3(3):483–491, 2000.

[377] Julia Kraxner, Charlotta Lorenz, Julia Menzel, Iwan Parfentev, Ivan Silbern, Manuela Denz, Henning Urlaub, Blanche Schwappach, and Sarah Köster. Post-translational modifications soften vimentin intermediate filaments. *Nanoscale*, 13(1):380–387, 2021.

[378] Heather J Tarbet, Lee Dolat, Timothy J Smith, Brett M Condon, E Timothy O'Brien III, Raphael H Valdivia, and Michael Boyce. Site-specific glycosylation regulates the form and function of the intermediate filament cytoskeleton. *eLife*, 7:e31807, 2018.

[379] Patricia González-Jiménez, Sofía Duarte, Alma E Martínez, Elena Navarro-Carrasco, Vasiliki Lalioti, María A Pajares, and Dolores Pérez-Sala. Vimentin single cysteine residue acts as a tunable sensor for network organization and as a key for actin remodeling in response to oxidants and electrophiles. *Redox Biol.*, page 102756, 2023.

[380] Jamal-Eddine Bouameur, Yann Schneider, Nadja Begré, Ryan P Hobbs, Prakash Lingasamy, Lionel Fontao, Kathleen J Green, Bertrand Favre, and Luca Borradori. Phosphorylation of serine 4642 in the c-terminus of plectin by mnk2 and pka modulates its interaction with intermediate filaments. *Journal of Cell Science*, 126(18):4195–4207, 2013.

[381] Roland Foisner, Nicole Malecz, Nicoline Dressel, Christine Stadler, and Gerhard Wiche. M-phase-specific phosphorylation and structural rearrangement of the cytoplasmic cross-linking protein plectin involve p34cdc2 kinase. *Molecular Biology of the Cell*, 7(2):273–288, 1996.

[382] Roland Foisner, Peter Traub, and Gerhard Wiche. Protein kinase a-and protein kinase c-regulated interaction of plectin with lamin b and vimentin. *Proceedings of the National Academy of Sciences*, 88(9):3812–3816, 1991.

[383] Csaba Daday, Katra Kolšek, and Frauke Gräter. The mechano-sensing role of the unique sh3 insertion in plakin domains revealed by molecular dynamics simulations. *Sci. Rep.*, 7(1):11669, 2017.

[384] Tim Sanchez, Daniel TN Chen, Stephen J DeCamp, Michael Heymann, and Zvonimir Dogic. Spontaneous motion in hierarchically assembled active matter. *Nature*, 491(7424):431–434, 2012.

[385] John Berezney, Bruce L Goode, Seth Fraden, and Zvonimir Dogic. Extensile to contractile transition in active microtubule–actin composites generates layered asters with programmable lifetimes. *Proceedings of the National Academy of Sciences*, 119(5):e2115895119, 2022.

[386] Yuval Mulla, Anders Aufderhorst-Roberts, and Gijsje H Koenderink. Shaping up synthetic cells. *Phys. Biol.*, 15(4):041001, 2018.

[387] Marian Weiss, Johannes Patrick Frohnmaier, Lucia Theresa Benk, Barbara Haller, Jan-Willi Janiesch, Thomas Heitkamp, Michael Börsch, Rafael B Lira, Rumiana Dimova, Reinhard Lipowsky, et al. Sequential bottom-up assembly of mechanically stabilized synthetic cells by microfluidics. *Nature Materials*, 17(1):89–96, 2018.

[388] John M Walker. *The proteomics protocols handbook*. 2005.

[389] Hugo Wioland, Berengere Guichard, Yosuke Senju, Sarah Myram, Pekka Lappalainen, Antoine Jégou, and Guillaume Romet-Lemonne. Adf/cofilin accelerates actin dynamics by severing filaments and promoting their depolymerization at both ends. *Curr. Biol.*, 27(13):1956–1967, 2017.

[390] James A Spudich and Susan Watt. The regulation of rabbit skeletal muscle contraction: I. biochemical studies of the interaction of the tropomyosin-troponin complex with actin and the proteolytic fragments of myosin. *Journal of Biological Chemistry*, 246(15):4866–4871, 1971.

[391] Guillaume Romet-Lemonne, Bérengère Guichard, and Antoine Jégou. Using microfluidics single filament assay to study formin control of actin assembly. pages 75–92, 2018.

[392] Harald Herrmann and Ueli Aebi. Intermediate filaments: molecular structure, assembly mechanism, and integration into functionally distinct intracellular scaffolds. *Annual review of biochemistry*, 73:749–789, 2004.

[393] Stefan Winheim, Aaron R. Hieb, Marleen Silbermann, Eva-Maria Surmann, Tatjana Wedig, Harald Herrmann, Jörg Langowski, and Norbert Mücke. Deconstructing the late phase of vimentin assembly by total internal reflection fluorescence microscopy (tirfm). *PLOS One*, 6(4), 2011.

[394] Quang D. Tran, Valerio Sorichetti, Gerard Pehau-Arnaudet, Martin Lenz, and Céline Leduc. Fragmentation and entanglement limit vimentin intermediate filament assembly. *Physical Review X*, 13:011014, 2023.

[395] Johannes Schindelin, Ignacio Arganda-Carreras, Erwin Frise, Verena Kaynig, Mark Longair, Tobias Pietzsch, Stephan Preibisch, Curtis Rueden, Stephan Saalfeld, Benjamin Schmid, et al. Fiji: an open-source platform for biological-image analysis. *Nature methods*, 9(7):676–682, 2012.

[396] Laurent Lignieres, Véronique Legros, Manel Khelil, Nicolas Seneca, Matthew A Lauber, Jean-Michel Camadro, and Guillaume Chevreux. Capillary liquid chromatography coupled with mass spectrometry for analysis of nanogram protein

quantities on a wide-pore superficially porous particle column in top-down proteomics. *Journal of Chromatography B*, 1214:123566, 2023.

[397] Antoine Jégou, Thomas Niedermayer, József Orbán, Dominique Didry, Reinhard Lipowsky, Marie-France Carlier, and Guillaume Romet-Lemonne. Individual actin filaments in a microfluidic flow reveal the mechanism of atp hydrolysis and give insight into the properties of profilin. *PLoS biology*, 9(9):e1001161, 2011.

[398] Cécile Leduc, Kathrin Padberg-Gehle, Vladimir Varga, Dirk Helbing, Stefan Diez, and Jonathon Howard. Molecular crowding creates traffic jams of kinesin motors on microtubules. *Proceedings of the National Academy of Sciences*, 109(16):6100–6105, 2012.

[399] Rachel A Battaglia, Samed Delic, Harald Herrmann, and Natasha T Snider. Vimentin on the move: new developments in cell migration. *F1000Research*, 7, 2018.

[400] ML Gardel, Jennifer Hyunjong Shin, FC MacKintosh, L Mahadevan, PA Matsudaira, and DA Weitz. Scaling of f-actin network rheology to probe single filament elasticity and dynamics. *Physical review letters*, 93(18):188102, 2004.

[401] Margaret L Gardel, Fumihiko Nakamura, John H Hartwig, John C Crocker, Thomas P Stossel, and David A Weitz. Prestressed f-actin networks cross-linked by hinged filamins replicate mechanical properties of cells. *Proceedings of the National Academy of Sciences*, 103(6):1762–1767, 2006.

[402] KE Kasza, GH Koenderink, YC Lin, CP Broedersz, W Messner, F Nakamura, TP Stossel, FC MacKintosh, and DA Weitz. Nonlinear elasticity of stiff biopolymers connected by flexible linkers. *Physical Review E—Statistical, Nonlinear, and Soft Matter Physics*, 79(4):041928, 2009.

[403] C. P. Broedersz and F. C. Mackintosh. Modeling semiflexible polymer networks. *Reviews of Modern Physics*, 86(3):995–1036, 2014.

[404] KR Rogers, A Eckelt, V Nimmrich, KP Janssen, M Schliwa, H Herrmann, and WW Franke. Truncation mutagenesis of the non-alpha-helical carboxyterminal tail domain of vimentin reveals contributions to cellular localization but not to filament assembly. *European journal of cell biology*, 66(2):136–150, 1995.

[405] Martha E Brennich, Ulla Vainio, Tatjana Wedig, Susanne Bauch, Harald Herrmann, and Sarah Köster. Mutation-induced alterations of intra-filament subunit organization in vimentin filaments revealed by sachs. *Soft matter*, 15(9):1999–2008, 2019.

[406] Yuval Mulla, Mario J Avellaneda, Antoine Roland, Lucia Baldauf, Wonyeong Jung, Taeyoon Kim, Sander J Tans, and Gijsje H Koenderink. Weak catch bonds make strong networks. *Nature materials*, 21(9):1019–1023, 2022.

[407] Oliver Lieleg, Mireille MAE Claessens, Claus Heussinger, Erwin Frey, and Andreas R Bausch. Mechanics of bundled semiflexible polymer networks. *Physical review letters*, 99(8):088102, 2007.

[408] Fabiana Martino, Ana R. Perestrelo, Vladimír Vinarský, Stefania Pagliari, and Giancarlo Forte. Cellular mechanotransduction: From tension to function. *Frontiers in Physiology*, 9(JUL):378185, 2018.

[409] Iván P. Uray and Karen Uray. Mechanotransduction at the plasma membrane-cytoskeleton interface. *International Journal of Molecular Sciences*, 22(21):11566, 2021.

[410] Alba Zuidema, Wei Wang, and Arnoud Sonnenberg. Crosstalk between cell adhesion complexes in regulation of mechanotransduction. *BioEssays : news and reviews in molecular, cellular and developmental biology*, 42(11), 2020.

[411] Jenny Z Kechagia, Johanna Ivaska, and Pere Roca-Cusachs. Integrins as biomechanical sensors of the microenvironment. *Nature Reviews Molecular Cell Biology*, 20(8):457–473, 2019.

[412] Cátia S. Janota, Francisco Javier Calero-Cuenca, and Edgar R. Gomes. The role of the cell nucleus in mechanotransduction. *Current opinion in cell biology*, 63:204–211, 2020.

[413] Anne-Betty Ndiaye, Gijsje H Koenderink, and Michal Shemesh. Intermediate filaments in cellular mechanoresponsiveness: mediating cytoskeletal crosstalk from membrane to nucleus and back. *Frontiers in cell and developmental biology*, 10:882037, 2022.

[414] Thomas D. Pollard and John A. Cooper. Actin, a central player in cell shape and movement. *Science (New York, N.Y.)*, 326(5957):1208, 2009.

[415] Thomas D. Pollard. Actin and actin-binding proteins. *Cold Spring Harbor perspectives in biology*, 8(8), 2016.

[416] Daniel Krueger, Theresa Quinkler, Simon Arnold Mortensen, Carsten Sachse, and Stefano de Renzis. Cross-linker-mediated regulation of actin network organization controls tissue morphogenesis. *The Journal of Cell Biology*, 218(8):2743, 2019.

[417] D. H. Wachsstock, W. H. Schwarz, and T. D. Pollard. Cross-linker dynamics determine the mechanical properties of actin gels. *Biophysical journal*, 66(3 Pt 1):801–809, 1994.

[418] P. A. Janmey, S. Hvidt, J. Kas, D. Lerche, A. Maggs, E. Sackmann, M. Schliwa, and T. P. Stossel. The mechanical properties of actin gels. elastic modulus and filament motions. *Journal of Biological Chemistry*, 269(51):32503–32513, 1994.

[419] Gijsje H Koenderink and Ewa K Paluch. Architecture shapes contractility in actomyosin networks. *Current Opinion in Cell Biology*, 50:79–85, 2018.

[420] Bin Guo and William H. Guilford. Mechanics of actomyosin bonds in different nucleotide states are tuned to muscle contraction. *Proceedings of the National Academy of Sciences of the United States of America*, 103(26):9844–9849, 2006.

[421] Matthew J. Footer, Jacob W.J. Kerssemakers, Julie A. Theriot, and Marileen Dogterom. Direct measurement of force generation by actin filament polymerization using an optical trap. *Proceedings of the National Academy of Sciences of the United States of America*, 104(7):2181–2186, 2007.

[422] Pere Roca-Cusachs, Vito Conte, and Xavier Trepat. Quantifying forces in cell biology. *Nature Cell Biology* 2017 19:7, 19(7):742–751, 2017.

[423] Claudia Arbore, Laura Perego, Marios Sergides, and Marco Capitanio. Probing force in living cells with optical tweezers: from single-molecule mechanics to cell mechanotransduction. *Biophysical reviews*, 11(5):765–782, 2019.

[424] Andrea Freikamp, Alexander Mehlich, Christoph Klingner, and Carsten Grashoff. Investigating piconewton forces in cells by fret-based molecular force microscopy. *Journal of Structural Biology*, 197(1):37–42, 2017.

[425] Fanjie Meng, Thomas M. Suchyna, and Frederick Sachs. A fluorescence energy transfer-based mechanical stress sensor for specific proteins in situ. *The FEBS journal*, 275(12):3072–3087, 2008.

[426] Sayuki Hirano, Takayoshi Yamamoto, and Tatsuo Michiue. Fret-based tension measurement across actin-associated mechanotransductive structures using lima1. *The International journal of developmental biology*, 62(9-10):631–636, 2018.

[427] Jun Guo, Yuexiu Wang, Frederick Sachs, and Fanjie Meng. Actin stress in cell re-programming. *Proceedings of the National Academy of Sciences of the United States of America*, 111(49):5252–5261, 2014.

[428] T Curtis Shoyer, Kasie L Collins, Trevor R Ham, Aaron T Blanchard, Juilee N Malavade, L West, Brenton D Hoffman, and Brenton Hoffman. Detection of fluorescent protein mechanical switching in cellulo. *bioRxiv*, page 2024.01.10.575065, 2024.

[429] Yuval Mulla, Mario J. Avellaneda, Antoine Roland, Lucia Baldauf, Wonyeong Jung, Taeyoon Kim, Sander J. Tans, and Gisje H. Koenderink. Weak catch bonds make strong networks. *Nature Materials* 2022 21:9, 21(9):1019–1023, 2022.

[430] Pia Ringer, Andreas Weißl, Anna Lena Cost, Andrea Freikamp, Benedikt Sabass, Alexander Mehlich, Marc Tramier, Matthias Rief, and Carsten Grashoff. Multiplexing molecular tension sensors reveals piconewton force gradient across talin-1. *Nature methods*, 14(11):1090–1096, 2017.

[431] Katharina Austen, Pia Ringer, Alexander Mehlich, Anna Chrostek-Grashoff, Carleen Kluger, Christoph Klingner, Benedikt Sabass, Roy Zent, Matthias Rief, and Carsten Grashoff. Extracellular rigidity sensing by talin isoform-specific mechanical linkages. *Nature cell biology*, 17(12):1597–1606, 2015.

[432] Bryce T. Bajar, Emily S. Wang, Shu Zhang, Michael Z. Lin, and Jun Chu. A guide to fluorescent protein fret pairs. *Sensors (Basel, Switzerland)*, 16(9), 2016.

[433] Conrad L. Leung, Dongming Sun, Min Zheng, David R. Knowles, and Ronald K.H. Liem. Microtubule actin cross-linking factor (macf): a hybrid of dystonin and dystrophin that can interact with the actin and microtubule cytoskeletons. *The Journal of cell biology*, 147(6):1275–1285, 1999.

[434] Sonia Bañuelos, Matti Saraste, and Kristina Djinović Carugo. Structural comparisons of calponin homology domains: implications for actin binding. *Structure*, 6(11):1419–1431, 1998.

[435] Simone Köhler, Oliver Lieleg, and Andreas R. Bausch. Rheological characterization of the bundling transition in f-actin solutions induced by methylcellulose. *PLoS one*, 3(7), 2008.

[436] Nicholas Castaneda, Jinho Park, and Ellen Hyeran Kang. Regulation of actin bundle mechanics and structure by intracellular environmental factors. *Frontiers in Physics*, 9:227, 2021.

[437] Daniel R. Stabley, Carol Jurchenko, Stephen S. Marshall, and Khalid S. Salaita. Visualizing mechanical tension across membrane receptors with a fluorescent sensor. *Nature Methods* 2011 9:1, 9(1):64–67, 2011.

[438] Fanjie Meng and Frederick Sachs. Visualizing dynamic cytoplasmic forces with a compliance-matched fret sensor. *Journal of Cell Science*, 124(2):261–269, 2011.

[439] Sosuke Iwai and Taro Q.P. Uyeda. Visualizing myosin-actin interaction with a genetically-encoded fluorescent strain sensor. *Proceedings of the National Academy of Sciences of the United States of America*, 105(44):16882–16887, 2008.

[440] Taro Ichimura, Hideaki Fujita, Keiko Yoshizawa, and Tomonobu M. Watanabe. Engineering strain-sensitive yellow fluorescent protein. *Chemical Communications*, 48(63):7871–7873, 2012.

[441] Fanjie Meng and Frederick Sachs. Orientation-based fret sensor for real-time imaging of cellular forces. *Journal of Cell Science*, 125(3):743–750, 2012.

[442] Yang Liu, Kevin Yehl, Yoshie Narui, and Khalid Salaita. Tension sensing nanoparticles for mechano-imaging at the living/nonliving interface. *Journal of the American Chemical Society*, 135(14):5320–5323, 2013.

[443] Masatoshi Morimatsu, Armen H. Mekhdjian, Arjun S. Adhikari, and Alexander R. Dunn. Molecular tension sensors report forces generated by single integrin molecules in living cells. *Nano Letters*, 13(9):3985–3989, 2013.

[444] Sonya Lee, Cynthia N Okoye, Devin Biesbrock, Emily C Harris, Katelyn F Miyasaki, Ryan G Rilinger, Megalan Tso, and Kathryn M Hart. Natural and synthetic suppressor mutations defy stability–activity tradeoffs. *Biochemistry*, 61(5):398–407, 2022.

[445] Tyler D. Jorgenson, Kashmeera D. Baboolall, Cristian Suarez, David R. Kovar, Margaret L. Gardel, and Stuart J. Rowan. Highly flexible peg-lifeact constructs act as tunable biomimetic actin crosslinkers. *Soft Matter*, 20(5):971–977, 2024.

[446] Muneaki Nakamura, Lu Chen, Stuart C. Howes, Tony D. Schindler, Eva Nogales, and Zev Bryant. Remote control of myosin and kinesin motors using light-activated gearshifting. *Nature Nanotechnology* 2014 9:9, 9(9):693–697, 2014.

[447] José Alvarado and Gijsje H. Koenderink. Reconstituting cytoskeletal contraction events with biomimetic actin–myosin active gels. *Methods in Cell Biology*, 128:83–103, 2015.

[448] José Alvarado, Michael Sheinman, Abhinav Sharma, Fred C. Mackintosh, and Gijsje H. Koenderink. Molecular motors robustly drive active gels to a critically connected state. *Nature Physics*, 9(9):591–597, 2013.

[449] Yuval Mulla, Harmen Wierenga, Celine Alkemade, Pieter Rein Ten Wolde, and Gijsje H. Koenderink. Frustrated binding of biopolymer crosslinkers. *Soft matter*, 15(14):3036–3042, 2019.

[450] Elizabeth A. Jares-Erijman and Thomas M. Jovin. Fret imaging. *Nature Biotechnology* 2003 21:11, 21(11):1387–1395, 2003.

[451] Anna Lena Cost, Pia Ringer, Anna Chrostek-Grashoff, and Carsten Grashoff. How to measure molecular forces in cells: A guide to evaluating genetically-encoded fret-based tension sensors. *Cellular and Molecular Bioengineering*, 8(1):96–105, 2015.

[452] Harald Herrmann, Sergei V. Strelkov, Peter Burkhard, and Ueli Aebi. Intermediate filaments: Primary determinants of cell architecture and plasticity. *Journal of Clinical Investigation*, 119(7):1772–1783, 2009.

[453] Gerhard Wiche. Plectin-mediated intermediate filament functions: Why isoforms matter. *Cells*, 10(8), 2021.

[454] Konstantinos Tsilafakis and Manolis Mavroidis. Are the head and tail domains of intermediate filaments really unstructured regions? *Genes 2024, Vol. 15, Page 633*, 15(5):633, 2024.

[455] Gerhard Wiche, Dmitri Gromov, Adriana Donovan, María J. Castañón, and Elaine Fuchs. Expression of plectin mutant cdna in cultured cells indicates a role of cooh-terminal domain in intermediate filament association. *Journal of Cell Biology*, 121(3):607–619, 1993.

[456] Kerstin Andrä, Branislav Nikolic, Markus Stöcher, Detlev Drenckhahn, and Gerhard Wiche. Not just scaffolding: plectin regulates actin dynamics in cultured cells. *Genes Development*, 12(21):3442–3451, 1998.

[457] Alisa J. Piekny and Amy Shaub Maddox. The myriad roles of anillin during cytokinesis. *Seminars in cell developmental biology*, 21(9):881–891, 2010.

[458] Torey R. Arnold, Joseph H. Shawky, Rachel E. Stephenson, Kayla M. Dinshaw, Tomohito Higashi, Farah Huq, Lance A. Davidson, and Ann L. Miller. Anillin regulates epithelial cell mechanics by structuring the medial-apical actomyosin network. *eLife*, 8, 2019.

[459] Gilles R.X. Hickson and Patrick H. O'Farrell. Rho-dependent control of anillin behavior during cytokinesis. *The Journal of cell biology*, 180(2):285–294, 2008.

[460] Li Zhang and Amy Shaub Maddox. Anillin. *Current biology : CB*, 20(4), 2010.

[461] Christos Panagiotou, Iossif Papadakis, Erin Kara, Elias Kammoun, and Michal Dovčiak. A physical model for the uv/optical power spectra of agn. *The Astrophysical Journal*, 935(2):93, 2022.

[462] Ciara C. Reyes, Meiyang Jin, Elaina B. Breznau, Rhogelyn Espino, Ricard Delgado-Gonzalo, Andrew B. Goryachev, and Ann L. Miller. Anillin regulates cell-cell junction integrity by organizing junctional accumulation of rho-gtp and actomyosin. *Current biology : CB*, 24(11):1263–1270, 2014.

[463] Silvana Jananji, Cristina Risi, Indeewari K.S. Lindamulage, Louis Philippe Picard, Robert Van Sciver, Guillaume Laflamme, Abe Albaghjati, Gilles R.X. Hickson, Benjamin H. Kwok, and Vitold E. Galkin. Multimodal and polymorphic interactions between anillin and actin: Their implications for cytokinesis. *Journal of molecular biology*, 429(5):715–731, 2017.

[464] Kyohei Matsuda, Mitsuhiro Sugawa, Masahiko Yamagishi, Noriyuki Kodera, and Junichiro Yajima. Visualizing dynamic actin cross-linking processes driven by the actin-binding protein anillin. *FEBS letters*, 594(8):1237–1247, 2020.

[465] Ondřej Kučera, Valerie Siahaan, Daniel Janda, Sietske H. Dijkstra, Eliška Pilátová, Eva Zatecká, Stefan Diez, Marcus Braun, and Zdenek Lansky. Anillin propels myosin-independent constriction of actin rings. *Nature Communications*, 12(1), 2021.

[466] Stephen L. Gregory, Saman Ebrahimi, Joanne Milverton, Whitney M. Jones, Amy Bejsovec, and Robert Saint. Cell division requires a direct link between microtubule-bound racgap and anillin in the contractile ring. *Current biology : CB*, 18(1):25–29, 2008.

[467] Chloe van Oostende Triplet, Melina Jaramillo Garcia, Husni Haji Bik, Daniel Beaudet, and Alisa Piekny. Anillin interacts with microtubules and is part of the astral pathway that defines cortical domains. *Journal of cell science*, 127(Pt 17):3699–3710, 2014.

[468] Yu Chung Tse, Alisa Piekny, and Michael Glotzera. Anillin promotes astral microtubule-directed cortical myosin polarization. *Molecular biology of the cell*, 22(17):3165–3175, 2011.

[469] Lucia Baldauf, Lennard Van Buren, Federico Fanalista, and Gisje Hendrika Koenderink. Actomyosin-driven division of a synthetic cell. *ACS synthetic biology*, 11(10):3120–3133, 2022.

[470] Thomas D Pollard. Measurement of rate constants for actin filament elongation in solution. *Analytical biochemistry*, 134(2):406–412, 1983.

[471] I Banga and A Szent-Györgyi. Preparation and properties of myosin a and b. *Stud. Inst. Med. Chem. Univ. Szeged*, 1:5–15, 1942.

[472] Beáta Bugyi and Miklós Kellermayer. The discovery of actin: “to see what everyone else has seen, and to think what nobody has thought”*. *Journal of Muscle Research and Cell Motility*, 41(1):3–9, 2020.

[473] WJ Schmidt. Doppelbrechung der kernspindel und zugfasertheorie der chromosomenbewegung. *Zeitschrift für Zellforschung und Mikroskopische Anatomie Abt. B Chromosoma*, 1:253–264, 1939.

[474] Edmund Beecher Wilson. *The cell in development and heredity*. 1925.

[475] F. H.C. Crick. Is alpha-keratin a coiled coil? *Nature*, 170(4334):882–883, 1952.

[476] M. Bishr Omary, Pierre A. Coulombe, and W.H. Irwin McLean. Intermediate filament proteins and their associated diseases. *New England Journal of Medicine*, 351(20):2087–2100, 2004.

[477] Rebeca Uceda-Castro, Jessy V. van Asperen, Claire Vennin, Jacqueline A. Sluijs, Emma J. van Bodegraven, Andreia S. Margarido, Pierre A.J. Robe, Jacco van Rheeën, and Elly M. Hol. Gfap splice variants fine-tune glioma cell invasion and tumour dynamics by modulating migration persistence. *Scientific Reports*, 12(1), 2022.

[478] Roy A. Quinlan, Michael Brenner, James E. Goldman, and Albee Messing. Gfap and its role in alexander disease. *Experimental cell research*, 313(10):2077, 2007.

[479] Derek N. Woolfson. The design of coiled-coil structures and assemblies. *Advances in Protein Chemistry*, 70:79–112, 2005.

[480] Markus Meier, G. Pauline Padilla, Harald Herrmann, Tatjana Wedig, Michaela Hergt, Trushar R. Patel, Jörg Stetefeld, Ueli Aebi, and Peter Burkhard. Vimentin coil 1a—a molecular switch involved in the initiation of filament elongation. *Journal of Molecular Biology*, 390(2):245–261, 2009.

[481] Raja Dey and Peter Burkhard. A proposed atomic model of the head-to-tail interaction in the filament structure of vimentin. *Journal of Biomolecular Structure and Dynamics*, 38(16):4921–4927, 2020.

[482] Anastasia A. Chernyatina, Stefan Nicolet, Ueli Aebi, Harald Herrmann, and Sergei V. Strelkov. Atomic structure of the vimentin central α -helical domain and its implications for intermediate filament assembly. *Proceedings of the National Academy of Sciences of the United States of America*, 109(34):13620–13625, 2012.

[483] Minglu Hao, Lei Zhang, and Pu Chen. Membrane internalization mechanisms and design strategies of arginine-rich cell-penetrating peptides. *International Journal of Molecular Sciences*, 23(16), 2022.

[484] Zhihui Yang and Kevin K.W. Wang. Glial fibrillary acidic protein: From intermediate filament assembly and gliosis to neurobiomarker. *Trends in neurosciences*, 38(6):364, 2015.

[485] Ai Wen Yang, Ni Hsuan Lin, Ting Hung Yeh, Natasha Snider, and Ming Der Perng. Effects of alexander disease-associated mutations on the assembly and organization of gfap intermediate filaments. *Molecular Biology of the Cell*, 33(8), 2022.

[486] Ming Der Perng, Mu Su, Shu Fang Wen, Rong Li, Terry Gibbon, Alan R. Prescott, Michael Brenner, and Roy A. Quinlan. The alexander disease-causing glial fibrillary acidic protein mutant, r416w, accumulates into rosenthal fibers by a pathway that involves filament aggregation and the association of alpha b-crystallin and hsp27. *American journal of human genetics*, 79(2):197–213, 2006.

[487] Ming Der Perng, Shu Fang Wen, Terry Gibbon, Jinte Middeldorp, Jacqueline Sluijs, Elly M. Hol, and Roy A. Quinlan. Glial fibrillary acidic protein filaments can tolerate the incorporation of assembly-compromised gfap-delta, but with consequences for filament organization and alphab-crystallin association. *Molecular biology of the cell*, 19(10):4521–4533, 2008.

[488] M. Kornreich, E. Malka-Gibor, A. Laser-Azogui, O. Doron, H. Herrmann, and R. Beck. Composite bottlebrush mechanics: α -internexin fine-tunes neurofilament network properties. *Soft Matter*, 11(29):5839–5849, 2015.

[489] Eti Malka-Gibor, Micha Kornreich, Adi Laser-Azogui, Ofer Doron, Irena Zingerman-Koladko, Jan Harapin, Ohad Medalia, and Roy Beck. Phosphorylation-induced mechanical regulation of intrinsically disordered neurofilament proteins. *Biophysical Journal*, 112(5):892, 2017.

[490] Johanna Block, Viktor Schroeder, Paul Pawelzyk, Norbert Willenbacher, and Sarah Köster. Physical properties of cytoplasmic intermediate filaments. *Biochimica et Biophysica Acta (BBA)-Molecular Cell Research*, 1853(11):3053–3064, 2015.

PUBLICATIONS

Istúriz Petitjean, I¹, Tran, Q. D.¹, Goutou, A., Kabir, Z., Wiche, G., Leduc, C., Koenderink, G. H. (2024). Reconstitution of cytolinker-mediated crosstalk between actin and vimentin. *European Journal of Cell Biology*, 103(2), 151403.

Conboy, J. P.², **Istúriz Petitjean, I**², van der Net, A.², Koenderink, G. H.² (2024). How cytoskeletal crosstalk makes cells move: Bridging cell-free and cell studies. *Biophysics Reviews*, 5(2), 021307

Istúriz Petitjean, I³, Muntz I.³, Koenderink, G. H. Mechanical crosstalk of actin and vimentin (Manuscript in preparation)

Bareja I., Kucera O., **Istúriz Petitjean, I**, Sabo J., Braun M., Lánsky Z., Koenderink, G. H. Dogterom M. Anillin as a microtubule-actin crosslinker (Manuscript in preparation)

Verwei, H. N., Lee, G., Leech, G., **Istúriz Petitjean, I**, Koenderink, G. H., Robertson-Anderson, R. M., McGorty, R. J. (2022). Quantifying cytoskeleton dynamics using differential dynamic microscopy. *JoVE (Journal of Visualized Experiments)*, (184), e63931.

¹These authors contributed equally to this work.

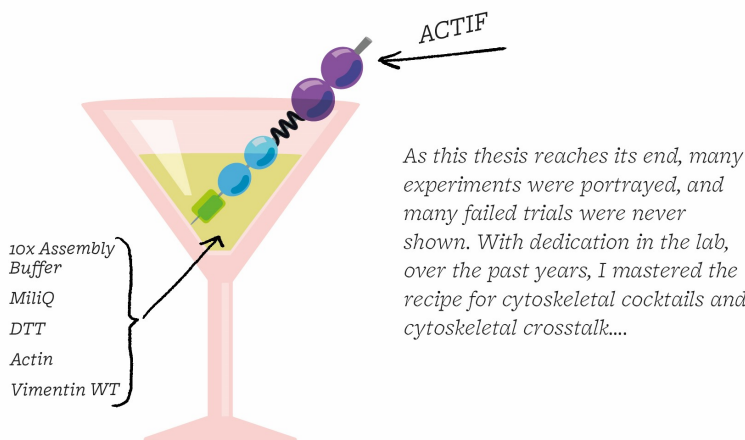
²These authors contributed equally to this work.

³These authors contributed equally to this work.

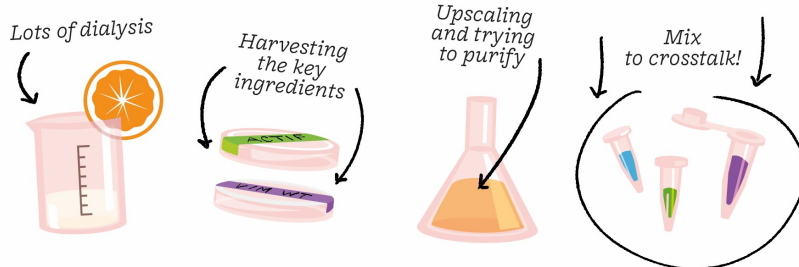
CURRICULUM VITAE

Irene Istúriz Petitjean was born in Barcelona on February 16, 1993. She lived until age 18 in Vilanova i la Geltrú. She obtained her high school diploma in 2011 at Institut Francesc Xavier Lluch i Rafecas and then moved to Barcelona, where she started her studies in Physics at the University of Barcelona, graduating with a Bachelor's thesis entitled "The EPR Paradox". During her studies, in 2016, she spent a semester abroad studying some courses of the Master's of Biophysics and Biophotonics at the Vrije Universiteit in Amsterdam. She obtained her Bachelor's degree in Physics in 2017 and moved to Copenhagen, where she started her Master's degree in Nanoscience and Nanotechnology at the University of Copenhagen. She graduated in 2019 with a Master's thesis entitled "Viscoelastic Properties of Embryonic Stem Cells Under Different Culturing Conditions", conducted at the Niels Bohr Institute in Copenhagen. She moved in October 2019 to Rotterdam to start working on her PhD at Delft University of Technology. She moved to Amsterdam in 2020 and worked on her PhD research until the end of 2024. The results of this work are presented in this thesis.

ACKNOWLEDGMENTS



*Some essential tools
were needed:*



.... but the tools are not enough. Mixing is fun, but it would have never been possible without the best support network, to enjoy the process and the final scientific and emotional cocktails.

To my colleagues and my beloved friends & family: Cheers to you!

Curious to read the most important chapter of all? For the full text and photos of the acknowledgments, check out the printed version!

Love and thanks!

Irene

